



HAL
open science

Design, fabrication and investigation of Interband Cascade structures for mid-IR VCSELs

Daniel Andrés Díaz Thomas

► **To cite this version:**

Daniel Andrés Díaz Thomas. Design, fabrication and investigation of Interband Cascade structures for mid-IR VCSELs. Electronics. Université Montpellier, 2020. English. NNT : 2020MONTs101 . tel-03383352

HAL Id: tel-03383352

<https://theses.hal.science/tel-03383352>

Submitted on 18 Oct 2021

HAL is a multi-disciplinary open access archive for the deposit and dissemination of scientific research documents, whether they are published or not. The documents may come from teaching and research institutions in France or abroad, or from public or private research centers.

L'archive ouverte pluridisciplinaire **HAL**, est destinée au dépôt et à la diffusion de documents scientifiques de niveau recherche, publiés ou non, émanant des établissements d'enseignement et de recherche français ou étrangers, des laboratoires publics ou privés.

THÈSE POUR OBTENIR LE GRADE DE DOCTEUR DE L'UNIVERSITÉ DE MONTPELLIER

Spécialité : Électronique

École doctorale : Information, Structures, Systèmes

Unité de recherche : Institut d'Électronique et des Systèmes – UMR 5214

Design, fabrication and investigation of Interband Cascade
structures for mid-IR VCSELs.

**Présentée par Daniel Andrés DIAZ THOMAS
Le 08 décembre 2020**

**Sous la direction de Laurent CERUTTI
et Alexei BARANOV**

Devant le jury composé de

Sophie BOUCHOULE, Directrice de recherche, CNRS, C2N - Université Paris-Saclay

Sukhdeep DHILLON, Directeur de recherche, CNRS, LPA, ENS

Guilhem ALMUNEAU, Directeur de recherche, CNRS, LAAS

Christophe LEVALLOIS, Maître de conférences, CNRS, FOTON – INSA Rennes

Alexei BARANOV, Directeur de recherche, CNRS, IES – Université de Montpellier

Laurent CERUTTI, Maître de conférences, CNRS, IES – Université de Montpellier

Rapportrice

Rapporteur

Examineur

Examineur

Co-directeur de thèse

Directeur de thèse



**UNIVERSITÉ
DE MONTPELLIER**

THÈSE POUR OBTENIR LE GRADE DE DOCTEUR DE L'UNIVERSITÉ DE MONTPELLIER

Spécialité : Électronique

École doctorale : Information, Structures, Systèmes

Unité de recherche : Institut d'Électronique et des Systèmes – UMR 5214

Design, fabrication and investigation of Interband Cascade
structures for mid-IR VCSELs.

Présentée par Daniel Andrés DIAZ THOMAS

Le 08 décembre 2020

Sous la direction de Laurent CERUTTI
et Alexei BARANOV

Devant le jury composé de

Sophie BOUCHOULE, Directrice de recherche, CNRS, C2N - Université Paris-Saclay

Sukhdeep DHILLON, Directeur de recherche, CNRS, LPA, ENS

Guilhem ALMUNEAU, Directeur de recherche, CNRS, LAAS

Christophe LEVALLOIS, Maître de conférences, CNRS, FOTON – INSA Rennes

Alexei BARANOV, Directeur de recherche, CNRS, IES – Université de Montpellier

Laurent CERUTTI, Maître de conférences, CNRS, IES – Université de Montpellier

Rapportrice

Rapporteur

Examineur

Examineur

Co-directeur de thèse

Directeur de thèse



UNIVERSITÉ
DE MONTPELLIER

Design, fabrication and investigation
of Interband Cascade structures for
mid-IR VCSELs

Index

ACKNOWLEDGMENTS	1
INTRODUCTION.....	3
CHAPTER I: MID – IR SEMICONDUCTOR LASER SOURCES	11
I.1 LASER CONCEPTS.....	12
I.1.1 Active medium of semiconductors.....	13
I.1.1.1 Quantum well configurations	14
I.1.1.2 Interband QW alignment	16
I.1.2 Resonant cavity.....	17
I.2 ACTIVE REGIONS FOR EMISSION IN THE MID INFRARED	18
I.2.1 Sb-based type-I QWs active regions	18
I.2.2 Auger effect.....	20
I.2.2.1 CHSH process	20
I.2.2.2 CHCC process:.....	21
I.2.3 Sb-based type-II QWs active regions	23
I.2.4 GaSb-based Interband Cascade active zone	24
I.3 VCSELS	30
I.3.1 Single mode lasers: DFB & VCSELS.....	30
I.3.2 Electro-optical confinement in VCSELS	32
I.3.3 MIR Sb-based VCSEL	34
I.4 CONCLUSION.....	37
CHAPTER II: INTERBAND CASCADE ACTIVE REGION	39
II.1 INTRODUCTION.....	39
II.2 DESIGN OF THE ACTIVE REGION	39
II.3 DESIGN, EPITAXY AND STRUCTURAL CHARACTERIZATION OF ICL STRUCTURES	41
II.3.1 Design of ICL for active stage studies	41
II.3.1 Growth temperature of the Type-II W QWs.....	41
II.3.2 Epitaxy and structural characterization of ICL	44
II.4 TECHNOLOGICAL PROCESS	45
II.4.1 Cleaning	46
II.4.2 Etching.....	46
II.4.2.1 Wet etching	46
II.4.2.2 Dry etching:.....	47
II.4.3 Passivation	48
II.4.4 Metallization.....	49
II.4.5 Polishing and bottom contact	52

II.4.6	<i>Mounting and top contacting</i>	53
II.5	CHARACTERIZATIONS OF ICLS	53
II.5.1	<i>Studies and improvement of the IC active region</i>	54
II.5.1.1	First ICL structure (ICL A).....	54
II.5.1.2	Voltage drop issue.....	55
II.5.1.1	ICL with improved voltage drop	57
II.5.1.2	Emission wavelength shift	58
II.5.1.3	Influence of the top cladding temperature.	61
II.5.1.4	Properties of broad area ICLs with optimized growth temperature.	63
II.5.1.5	Performances of narrow ridge ICL with optimized growth temperature.	65
II.5.1.6	ICL with InAs/AlSb superlattice cladding layers emitting at 3.6 μm	67
II.5.2	<i>ICL with new electron-injector design</i>	69
II.6	CONCLUSION.....	71
CHAPTER III: DISTRIBUTED BRAGG MIRRORS AND III-AS METAMORPHIC LAYER.		73
III.1	DISTRIBUTED BRAGG REFLECTORS (DBRs).....	73
III.1.1	<i>Bragg Mirror design parameters</i>	74
III.1.2	<i>Semiconductor AlAsSb\GaSb DBR</i>	75
III.1.2.1	Doping.....	76
III.1.3	<i>Dielectric DBR</i>	79
III.1.3.1	a-Si/SiNx dielectric DBR.....	79
III.1.4	<i>Ge/ZnS dielectric DBR</i>	81
III.2	ELECTRO-OPTICAL CONFINEMENT USING METAMORPHIC III-AS MATERIAL.....	83
III.2.1	<i>Doping of GaAs at optimized growth temperature</i>	83
III.2.2	<i>Electrical study of the GaAs/GaSb interface</i>	84
III.2.3	<i>VCSEL design for the metamorphic interface and the oxidation layer</i>	87
III.2.3.1	Position of the GaSb/GaAs metamorphic interface	87
III.2.3.2	Position of the AlAs oxidation layer in the structure.....	88
III.2.4	<i>Study of IC-Light Emitted Diode with metamorphic GaAs top layer</i>	90
III.2.5	<i>ICLs with metamorphic GaAs top cladding</i>	93
III.3	SUMMARY AND CONCLUSIONS OF THE METAMORPHIC ELECTRO-OPTICAL CONFINEMENT	96
CHAPTER IV: IC- VERTICAL CAVITY SURFACE EMITTING DEVICES.....		99
IV.1	SIMPLE IC-RESONANT CAVITY LIGHT EMITTING DIODES	99
IV.1.1	<i>Design of the RCLED-A</i>	99
IV.1.2	<i>Optical characterization of the RCLED-A</i>	100
IV.1.3	<i>RCLED-A processing and electro-optical characterizations</i>	101
IV.2	IC-RCLED WITH ALOX CONFINEMENT LAYER AND TOP GE/ZNS DBR.....	102
IV.2.1	<i>Design of the RCLED-B</i>	102
IV.2.2	<i>Structural and optical properties</i>	103

IV.2.2.1	TEM characterizations	103
IV.2.2.2	Reflectivity	104
IV.2.1	<i>RCLED-B Processing</i>	104
IV.2.1	<i>Electro-optical characterizations of RCLED-B</i>	108
IV.3	FIRST IC-VCSEL STRUCTURES	111
IV.3.1	<i>Design</i>	111
IV.3.2	<i>Optical properties</i>	112
IV.3.3	<i>Electro-optical properties</i>	113
IV.3.4	<i>Discussions on VCSEL-A issues</i>	115
IV.3.4.1	Current leakage	115
IV.3.4.2	Cavity-gain offset	117
IV.4	OPTIMIZED VCSEL STRUCTURE	117
IV.4.1	<i>Bragg mirror and W-MQW PL structure</i>	117
IV.4.2	<i>Characterization of the half VCSEL</i>	118
IV.4.3	<i>Process of the VCSEL-B</i>	119
IV.4.4	<i>Electro-optical properties of the VCSEL-B</i>	120
IV.5	CONCLUSIONS.....	122
CONCLUSION AND OUTLOOK		125
LIST OF PUBLICATIONS		129
BIBLIOGRAPHY		131

Acknowledgments

This thesis marks the end of a stage that began about four years ago and has been made possible thanks to the help of many people. In the following lines I would like to thank all these people who, in one way or another, helped in the realization of this thesis and forgive me if I forget someone. As you will notice there will be an alternation of English, French and Spanish as is what always happens in my head.

First of all, I want to thank God for allowing me to get here and my grandmother Ruth (may she rest in peace) for opening the way and the vision towards the education.

Thanks to my parents Yaneth and Ernesto, to my sisters Natalie and Karen my two great reasons (Do you wanna build a snow man?), to mi tía Ángela who has watched over my welfare since I was a child, mi tío Joseph and mi primo Eliot, to Camilo (hasta Pekin y un poquito mas depronto) and the beaux frèro because, in spite of not understanding very well this thing called doing a thesis and dedicating oneself to research, they have always understood it as something positive and have given me their support and affection. I don't think I will be able to find the words of gratitude for you, but since this thesis became a reality, it is thanks to you. Thanks to both of you, papás, for your education and because you have always convinced me that with effort everything is possible, in spite of the bumps that may arise.

Thanks to Mrs. Sophie BOUCHOULE, and Mr. Sukhdeep DHILLON for agreeing to be my reporters. I would also like to thank Mr. Guilhem ALMUNEAU and Mr. Christophe LEVALLOIS for participating in my jury.

I want to thank my thesis directors: Laurent CERUTTI and Alexeï BARANOV, for giving me this opportunity, for trusting me and for helping me. To you, together with Eric TOURNIÉ and Michaël BHRIZ thank you for teaching me to take my first steps in this world, for your patience, for putting up with my daily visits to deal with "my doubts" and for always having your office door open.

I would also like to thank our collaborators at the LAAS and FOTON laboratories, Oleksandr STEPANENKO, Stephane CALVEZ, Cyril PARANTHOEN and Thomas BATTE for all the enriching exchanges around our project.

Acknowledgments

Thanks to my NANOMIR team Thierry TALIERCIO, Jean-Baptiste RODRIGUEZ, Roland TESSIER, Aurore VICET, Ariane MEGUEKAM, Fernando GONZALEZ-POSADA-FLORES Jean-Philippe PEREZ, Philippe CHRISTOL, Richard ARINÉRO, Yves ROUILLARD, Jean-Marc ANIEL, Guilhem BOISSIER; to my PhD co-suffers Laura, Jie, Wioletta, Pierre, Diba, Rodolphe, Marta, Roman, Andrés, Melissa, Jordan, Kinjalk, Julien, Clara, Maxime, Michele, Nicolas, Kaim, Olivier, Ulises, Mario, Julie, Franziska, Eduardo, Rémi, Quentin; to the post-doc team Patricia, Dilek, Maria José and Hoang; and the new beginners Audray, Cécile and Julien.

A big thanks to you my favorite “poto” Zayneb, for having been with me through thick and thin and for having shared so many joys, fights and even tears, gracias cariño. To the parcerero Hadriano for all those shots during these three years; let’s go for that 3% buddy.

Thanks to my Roomies Bea, John, Magdis and even Lulo for all those meals, cakes that made us feel like family; To Cindy, Agata, Tam, Céline, Mario and Oswaldo for all the help given and for your friendship and to the whole THAÏ to BOX team, I will always be part of your team.

Thanks to Jean Marie PIERRIS, Frédéric PICHOT and all the CTM team, to my favorite team of the IES M2A (of course after the best one: NANOMIR) in special to Benjamin, Afaf, Audrey and Oramany.

To my teachers at the University of Montpellier Hervé PEYRE, Thierry GUILLET, Thierry BRETAGNON Sandrine JUILLAGET, Clément GALLO and Jerome DORIGNAC thank you for being my guides during my first steps in science; who would have thought that this student by day and sushi delivery man by nights would be a researcher today. It is thanks to you.

Finally, I must thank France, the University of Montpellier and the Institut d’Électronique et des Systèmes for allowing me to train there.

Thank you all for trusting and believing in me because a research work is also the result of the recognition and vital support offered by the people who esteem us, without which we would not have the strength and energy that encourages us to grow as people and as professionals.

A todos, muchas gracias.

Daniel

A mi abuelita Ruth ...

Introduction

Today, many aspects of our daily life originate from data collected with various sensors. Indeed, everyday considerations like food, healthcare, industrial and agricultural production, security, power production and consumption, the physical environment and human interaction are monitored using information collected, stored and analyzed through communications technologies. Wireless sensor network appears as a technology, which provides the basis for broad field applications. Although the interest in sensor network is increasing, it is needed to build large collections of sensors exchanging information with respect to their environment or their own state. Using the communications infrastructure of Internet, the widely distributed sensors will form an electronic ecosystem known as the “Internet of Things (IoT)”. In this context there is a strong driving force for the development of smart and compact biological and chemical sensors with increased autonomy, lifetime and connectivity with the mid-term goal of implementing global sensor networks. To have a better knowledge of our environment, one solution is to monitor trace of different molecules.

The presence of gas sensors continues to expand on the market. The sensitivity is high for many of them and future research should lead to their improvement. There are two main categories of existing gas detectors. On the one hand, those using a non-optical method and on the other hand, those using an optical method. Among those using a non-optical method, three families can be distinguished: electrochemical, thermal and classic detectors. Devices such as gas chromatography or mass spectrometry will not be taken into account because they are too voluminous. They are very efficient, sensitive and selective, but cumbersome and incompatible with portable system. Inversely, optical sensors based on Tunable Diode Laser Absorption Spectroscopy (TDLAS) are characterized by very good sensitivity, excellent selectivity and above all for its size that allows their integration into smart and small system for the new technologies.

Covering the wavelength range from approximately 2 to 5 μm (2000-5000 cm^{-1}), the mid-infrared (Mid-IR) is densely populated by important spectral characteristics in particular between 3 and 5 μm [1] as presented in figure Figure 0-1.

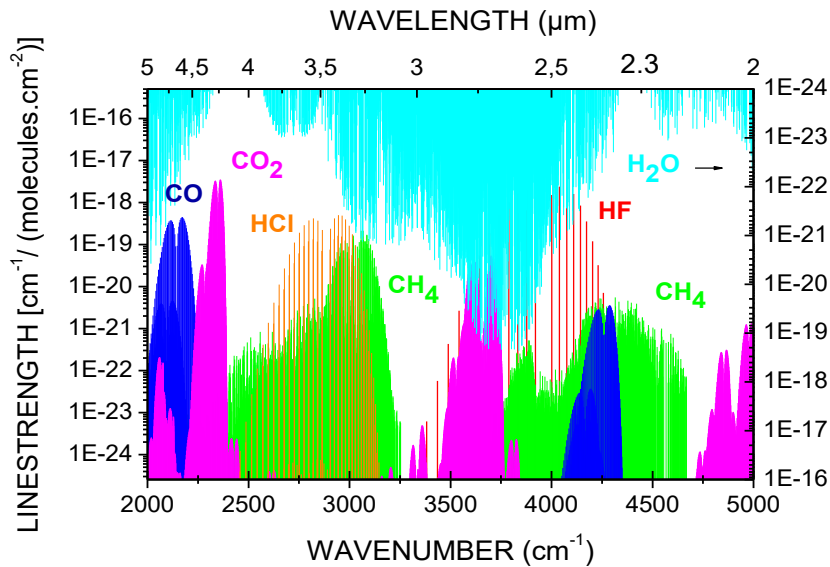


Figure 0-1 - Absorption spectral zones of several gaseous species between 2 and 5 μm of several gaseous species of military interest [1]

These include strong molecular absorption lines associated with the fundamental rotovibrational modes of many chemical functional groups that are vital for industrial and medical applications [2]–[8]. The MIR also contains several atmospheric transmission windows. These relatively high transparency regions are well positioned for atmospheric monitoring and have also attracted interest for open space communications, security and defense [9]–[12].

Based on the light-matter interaction, TDLAS measures the light absorption emitted by a laser source as it passes through a gaseous medium containing molecules capable of absorbing this radiation. The measurement is made directly with a suitable detector and is placed in the path of the light after the absorption zone. This laser source, has to be robust, powerful and operate under continuous electrical injection (CW) at near ambient temperature (for use in non-laboratory sensors). In addition, it must be sensitive to low concentrations on the order of ppmv (part per million) or ppbv (part per billion). The suffix “v” unit expresses the presence of a chemical species relative to a total volume of gas solution. Furthermore, and importantly for the selectivity feature, this laser source must emit in a single frequency. Indeed, each substance has absorption lines at specific wavelengths [13] but frequently, a gas in its natural state is composed of several species. Therefore, the discrimination and quantification of these species in the mixture is the main interest of a gas detection method. During the process, the absorption lines are scanned with a single frequency laser whose spectral width has to be much narrower than the gas line widths, especially at atmospheric pressure (MHz versus GHz) as illustrated in Figure 0-2.

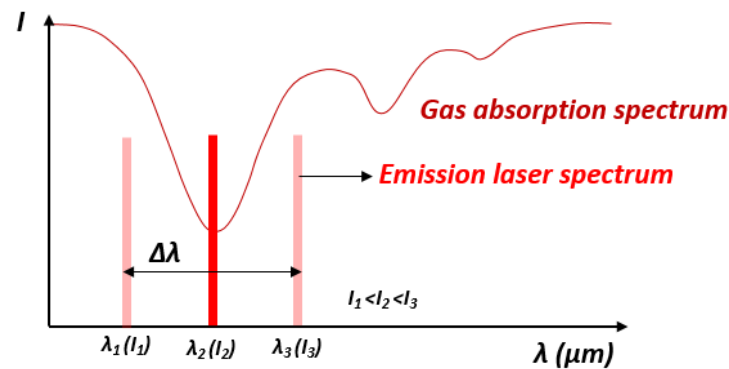


Figure 0-2 – Illustration of the principle of the tunable diode laser absorption spectroscopy with the laser linewidth much thinner than the gas absorption line

The main obstacle for a widespread use of the TDLAS is the lack of reliable and easy to use low cost laser devices in wavelength regions with strong absorption lines. TDLAS developments are thus intimately dependent on the availability of adequate Mid-IR sources. Emissions into single spectral mode and a low output power of 1 mW are usually sufficient. [14] Nowadays, only edge emitting GaSb-based interband-cascade lasers (ICLs) and InP-based quantum cascade laser (QCL) allow covering the 3- 5 μm spectral range [15], [16]. However, if their properties in term of optical power (> mW) and operating temperature (>300K) are compatible with TDLAS technology, complex and expensive distributed feedback (DFB) laser processing is used to achieve single mode emission which is required for TDLAS gas selectivity. Moreover, threshold currents higher than 100 mA combined with, notably for QCLs, high voltage polarization are a lock for the development of low power consumption and low cost integrated sensors.

In contrast, the electrically-pumped Vertical Cavity Surface Emitting Laser (VCSEL) is the only laser concept which intrinsically exhibits low threshold currents, low voltage operation, small footprint, easy fiber-coupling, on-wafer testing before packaging, and the most important single longitudinal mode emission. However, no VCSEL emitting above 3 μm in CW at room temperature (RT) has been demonstrated

This thesis is a part of the ANR (Agence Nationale de la Recherche) project MIMIC-SEL (Mid-Infrared Metamorphic Interband Cascade vertical cavity Surface Emitting Laser), whose the objective was to create the first electrically pumped VCSEL emitting above 3 μm in CW at RT. The starting point of this project was the complementary knowhow of the consortium with the

expertise of IES on the design, epitaxy and study of GaSb-based lasers and VCSELs, the capability of LAAS for VCSELs processing and of FOTON for their expertise in dielectric materials dedicated to Bragg mirror.

In the development of our work, we focused on two wavelengths, 3.3 and 3.6 μm for the detection of two types of gases. On one hand, 3.3 μm wavelength is targeted for the detection of methane CH_4 , because in addition to being a hydrocarbon which is a primary component of natural gas, it is also a greenhouse gas (GHG), so its presence in the atmosphere affects the earth's temperature and climate system. On the other hand, at 3.6 μm wavelength, there are strong absorption line of formaldehydes H_2CO . This material is used in manufacture of industrial and consumer products, especially in building materials. Formaldehyde escaping from these materials may lead to poor indoor air levels that adversely affect human health and has been identified by the International Agency of Research on Cancer (IARC) as carcinogenic since 2004.

The main scientific and technological goals of this thesis are to develop and investigate the technologies to demonstrate an electrically-pumped VCSELs offering the following properties:

- CW at RT and above
- Single frequency emission at 3.3 and 3.6 μm with a side mode suppression ratio of 30 dB
- Continuous electro-thermal tunability of 15 nm
- Optical output power higher than 1 mW
- Power consumption below 10 mW.

The challenges for the realization of such VCSELs are numerous and can be summarized as following:

- Investigate active material for emission at 3.3 and 3.6 μm region with high optical and structural quality.
- Develop low optical losses and high reflectivity dielectric and semiconductor distributed Bragg reflector (DBR)
- Control the electro-optical confinement of the VCSEL, which is the key parameter to obtain low threshold current and single frequency emission

Throughout this manuscript, I will describe the steps to fabricate and study such a device. For this purpose, the manuscript is divided in four chapters organized as follows:

- Chapter 1 is an introduction to laser concepts followed by a detailed state of the art of active regions for lasers emitting in the Mid-IR spectral range and electro-optical confinement in Mid-IR VCSELs. Based on these, it will be proposed a design for the VCSEL.
- Chapter 2 is dedicated to the study and optimization of the active region. For this purpose, we developed robust design, growth techniques and processing for obtaining high quality gain material, low threshold enabling above RT CW operation edge emitting lasers (EELs) at 3.3 and 3.6 μm . It will allow to determine the key parameters (voltage drop, efficiency, ...) of the active region in view of their implementation in VCSEL.
- Chapter 3 is devoted to the study and characterization of the semiconductor and dielectric distributed Bragg reflectors (DBR). Then, we studied the technology dedicated for the electro-optical confinement and its influence on the devices.
- Chapter 4 is related to the fabrication and study of vertical cavity surface emitting devices taking into account the technological development from chapter 2 and 3.

Chapter I: Mid – IR semiconductor laser sources

The development of the laser principles was first thought in 1951 at the Columbia University in New York with the idea of MASER (microwave amplification by stimulated emission of radiation) [17], [18]. Meanwhile, in the Soviet Union, the first report on the theoretical possibility of constructing a molecular generator was presented by Basov and Prokhorov (Nobel prize in 1964) in May 1952 at the Oscillations Laboratory of the Lebedev Institute in Moscow [19], [20]. They proposed a method to obtain negative absorption, named “the pumping method”.

Mixing the stimulated emission and negative absorption ideas, later in 1958, Bell Laboratories showed that masers could also operate in the visible and infrared regions [21]. This project was in charge of Charles Townes (Nobel prize in 1964). However, the first laser was demonstrated in 1960 based on a ruby pink crystal and was developed [22] at Hughes Research Laboratories by Theodore Maiman.

Afterwards, since the first experimental reports [23]–[26] of working semiconductor laser diodes in 1962 by the research groups at General Electric, IBM TJ Watson Center, General Electric in Syracuse, and MIT Lincoln Laboratory, the semiconductor material growth, device design, processing and characterization were one of the most rapid developments in the digital information industry.

Being able to reach an emission at a targeted wavelength, it is mostly a matter of finding appropriate materials. The Figure I-1 shows several semiconductor energy gaps as a function of their lattice constant.

In the laser industry, the most "established" industries are the GaAs (gallium arsenide) for visible and near infrared applications [7]–[8], and the InP (indium phosphide) industry for telecommunications at 1.3 and 1.55 μm [9]–[10]. The GaN (gallium nitride) research extended the wavelength application developing high-brightness blue light emitting diodes (LEDs) and laser diodes (LDs) for use in full-color displays [31]–[33]. The II-VI semiconductor family also displays many interesting features. The direct band gap of these materials makes them well-suited to high performance applications, such as LEDs and LDs for blue and ultraviolet applications [34], [35].

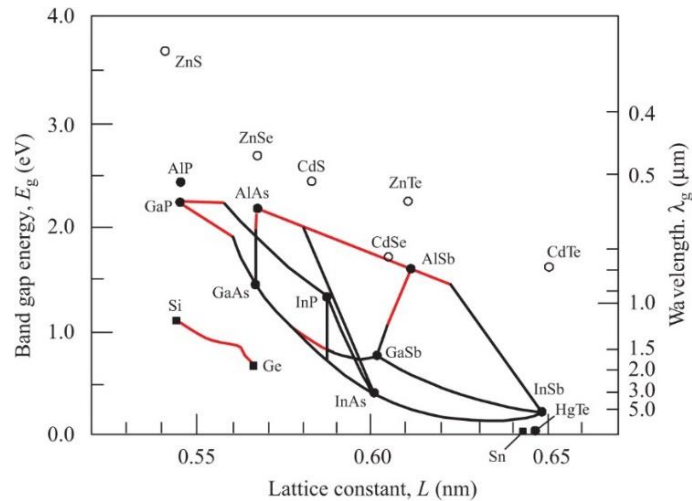


Figure I-1 - Room-temperature band gap energy E_g , as a function of lattice constant for several semiconductors. Lines connecting binary compounds represent alloy compositions. (red indirect band gap-black: direct bandgap)

Another material family, the so-called antimonides based compound semiconductors (ABCS) including GaSb (gallium antimonide), InAs (indium arsenide), InSb (indium antimonide), AlSb (aluminium antimonide) and their ternary, quaternary and quinary alloys, is specially well suited for light sources in the mid-infrared (MIR) spectral range. This family of materials refers to all III–V zinc-blend alloys that can be grown on GaSb or InAs substrates (with a lattice constant near 6.095 \AA).

Semiconductor lasers can be fabricated from different materials but their operation is based on several general principals which will be described below.

I.1 Laser concepts

So far, different lasers have been developed with different families of materials, but before continuing, I will describe several laser concepts and their operation; more specifically for semiconductor lasers.

Generally speaking, a laser structure consists of an active medium in a resonant cavity. The cavity is an optical resonator which amplifies the light produced in the active medium (Figure I-2). On the other hand, the active medium is typically a 4-level system producing optical gain by stimulated emission. The photon energy E will be defined by the energy difference between the 2nd and 1st level as shown in Figure I-2a.

The theoretical optical gain is characterized by a Lorentzian/Gaussian spectrum as depicted in Figure I-2b.

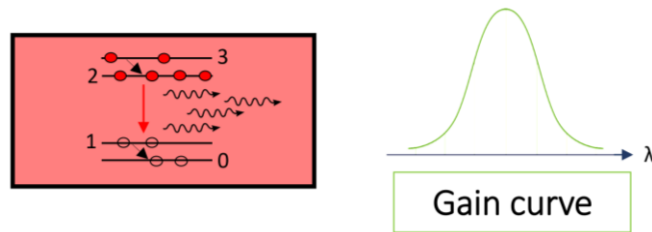


Figure I-2 - Photon emission process and gain curve

Laser performances are mainly defined by its active medium.

I.1.1 Active medium of semiconductors

In semiconductor lasers, the active medium (or gain media) is often composed of quantum wells (QWs).

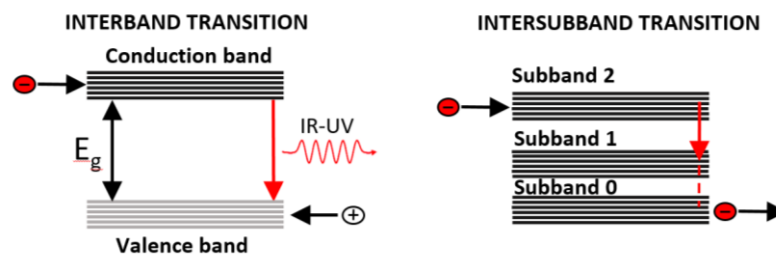


Figure I-3 - Type of transitions on a semiconductor quantum well. a) Interband transition. b) Intersubband transition

A transition from the conduction band to one of the valence bands is called an interband transition that involves electrons and holes; while if this occurs within the same band, it is named intersubband transition that requires only one type of carrier, as shown in Figure I-3. For an interband transition the emission is not only determined by the thickness of the well, as in the intersubband case, but also by the bandgap energy of the semiconductor.

Quantum selection rules governing transitions will define the optical polarization of the emitted photons. The polarizations can be TE (transverse electric), when \vec{E} oscillates in the layers plane or TM (transverse magnetic) when \vec{E} oscillates transversely to them. For interband transitions, both polarization modes are allowed whereas for intersubband transitions the only non-vanishing optical polarization is along the growth direction [36], leading to TM polarized emission.

Polarizations are decisive for the direction of light emission. For an in-plane emission, the two polarizations, TE and TM are possible, whereas for an emission perpendicular to the layers, the polarization is purely TE because in this case \vec{E} can oscillate only in the plane of the layers.

Therefore, to obtain a laser emission by the surface, interband transitions are mandatory.

I.1.1.1 Quantum well configurations

Generally, multiple identical QWs must be employed to provide sufficient gain at reasonable injection currents. Making an analogy with an electrical circuit, QWs can be connected in parallel or series configuration.

When the QW share a common quasi-Fermi level for each carrier type as depicted in Figure I-4, the QW organization is called parallel configuration. Here, carriers are injected from the n and p contacts into the conduction and the valence band. In an ideal case, they are distributed into M equal parts to feed the M different wells (with M being the number of wells) where the recombination and the emission process take place. Figure I-4 illustrates how this scheme is equivalent to a parallel circuit.

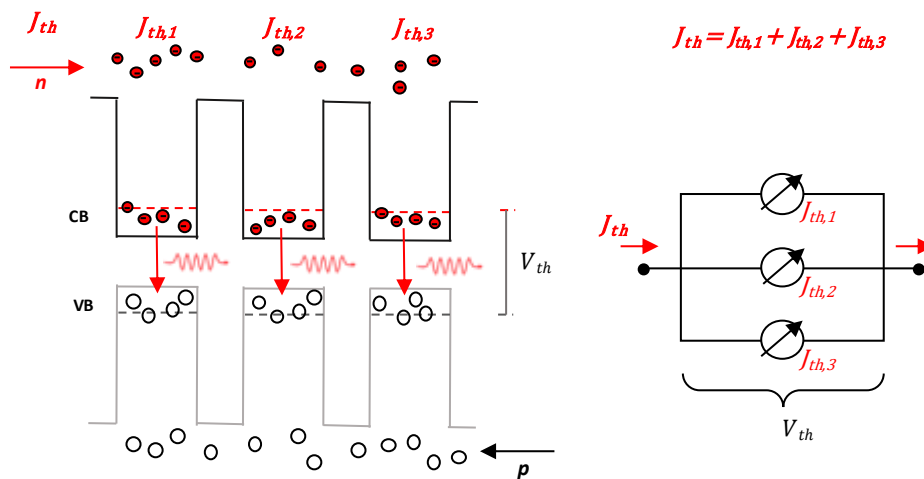


Figure I-4 - Parallel configuration in quantum wells - ideal case

In this configuration, $J_{th,m}$ is the current density needed to reach the threshold for each QW. Therefore, the current density required to reach the laser threshold can be written as follows:

$$J_{th} = M \cdot J_{th,m} \quad (1.1)$$

Concerning the voltage, at the lasing threshold the voltage drop V_{th} is equal to the energy gap $\frac{E_g}{q}$ plus a small margin $\frac{\Delta E}{q}$ linked to the internal losses [37] and is expressed by:

$$V_{th} = \frac{E_g + \Delta E}{q} \quad (1.2)$$

In a series configuration, the carriers are injected into the first well and then pass, by tunnel effect and thanks to the electric field, to the next well. During this process, in each QW, the carriers can perform either an interband or an intersubband transition generating a photon. This process is repeated in all quantum wells, producing what is commonly called the cascade effect [38] which is equivalent to a series circuit as depicted in Figure I-5.

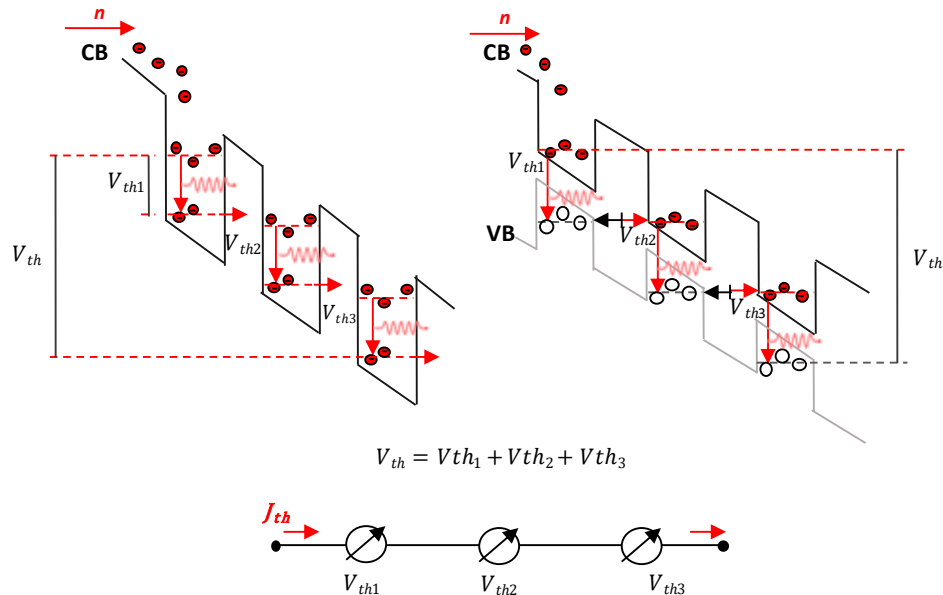


Figure I-5 - Series configuration in quantum wells - cascade effect

In this configuration the same current density feeds all QWs and is given by:

$$J_{th} = J_{th,m} \quad (1.3)$$

As showed in the figure 1-5, the electric field aligns the lower level of one well with the upper level of the next well. This suggests that several voltage drops are needed to align all wells and allow the current flow. Therefore, the required voltage drop is equal to the sum of each voltage drop of the corresponding well and can be deduced by:

$$V_{th} = M \cdot \frac{E_g + \Delta E}{q} \quad (1.4)$$

In general, the total power consumption of a semiconductor laser is defined as:

$$P_{th} = P_{th1} + P_{th2} \quad (1.5)$$

where P_{th1} is the power related to the total voltage drop in the active medium as a function of the current I .

$$P_{th1} = V_{th} \cdot I \quad (1.6)$$

and P_{th2} is the dissipated power related to the electrical resistance R of the whole device. If the series resistance is the same in both configurations, then we can write P_{th2} as a function of the square of the current:

$$P_{th2} = U \cdot I = R \cdot I^2 \quad (1.7)$$

If S is the surface of our device, the total power consumption for each QW configuration can be deduced as:

$$P_{th} = \frac{E_g + \Delta E}{q} \cdot M J_{th} S + R \cdot M^2 J_{th}^2 S \quad \text{Parallel configuration} \quad (1.8)$$

$$P_{th} = \frac{E_g + \Delta E}{q} \cdot M J_{th} S + R \cdot J_{th}^2 S \quad \text{Serial configuration} \quad (1.9)$$

In an ideal case, we can deduce that for QWs connected in the parallel configuration, the dissipated power will be quadratic in the number of wells. In series configuration, each injected electron goes through the entire circuit generating one photon per well traversed. It leads to a lower consumed power as there is more than one QW/branches. This strategy has driven the development of quantum cascade lasers (QCLs) [38] and bipolar cascade lasers [39].

1.1.1.2 Interband QW alignment

As shown in Figure I-6, there are 3 types of band alignment in QWs depending on the semiconductor material. The type-I alignment, the density of states is quasi-two-dimensional (2D) and both carriers are confined in the same layer. Therefore, the wavefunction overlap is close to 100 %. In the case of type-II and type-III alignment, the conduction band of the first material might lie between the gap or below the valence band of the adjacent layer respectively. In these two last designs, electrons and holes are confined within the adjacent layers reducing the electron-hole wavefunction overlap, however the energy gap can be lower

than the energy gap of each material.

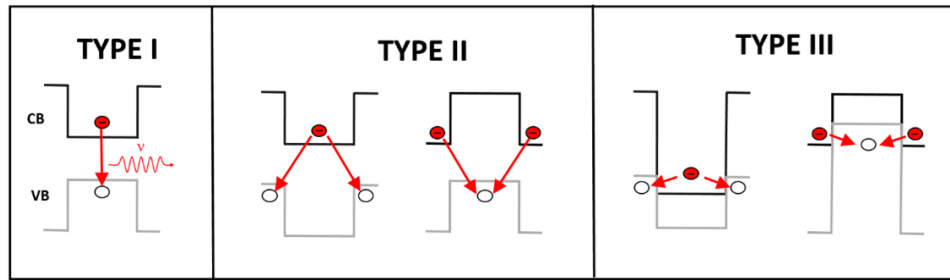


Figure I-6 - Types of band alignments in a semiconductor quantum well and their corresponding interband transitions

I.1.2 Resonant cavity

The simplest resonant cavity is the "Fabry-Perot" cavity which consists of two partially transmitting mirrors facing each other separated by a length L . The photons, generated by stimulated emission, undergo numerous reflections in the optical cavity causing multiple interferences. Just a small fraction of photons leaves the cavity by constructive interference forming the so-called longitudinal modes or "Fabry Perot" modes as explained in Figure I-7.

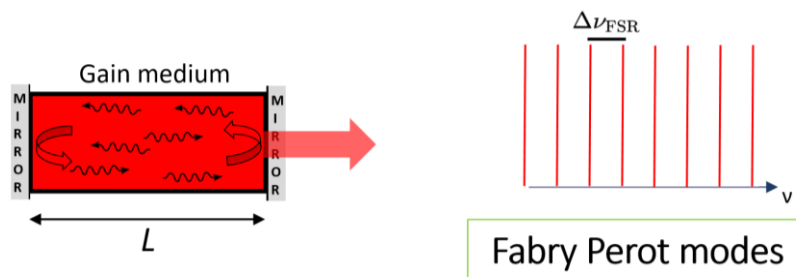


Figure I-7 - Fabry Perot resonant cavity and modes

The optical frequency spacing between two successive transmitted optical intensity maxima is called the free spectral range (FSR) and is given by:

$$\Delta\nu_{\text{FSR}} = \frac{c}{2n_g L} \quad (1.10)$$

Where n_g is the group index of the media and c the speed of light in the vacuum.

The convolution of the gain curve given by the gain medium with the Fabry-Perot modes, which are the contribution of the cavity, produces the emission spectra as explained, in a qualitative way, Figure I-8.

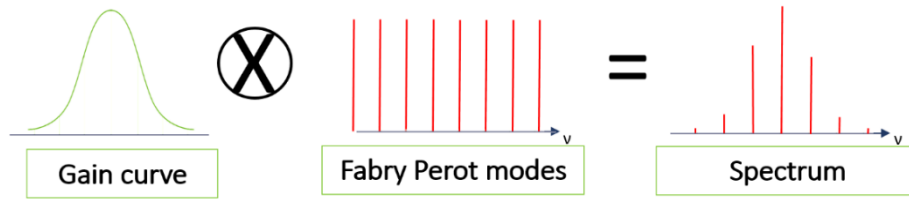


Figure I-8 - illustration of a longitudinal laser spectrum.

I.2 Active regions for emission in the mid infrared

In this paragraph, it will be presented the different configurations to obtain laser emission in the mid-infrared with their performances and limitations.

I.2.1 Sb-based type-I QWs active regions

As mentioned before, antimonides are the most relevant materials for interband emission at wavelengths longer than 1.6 μm . Figure I-9 shows the related position of band gap of III-V of antimonides among other III-V semiconductors. Indeed, all three band alignments can be obtained using the antimonides. [40] (see Section I.1.1).

The first GaSb laser was demonstrated by Kobayashi et al. at Nippon Telegraph and Telephone (NTT) Research Laboratories [41] in 1980. It was a double heterostructure (DH) laser grown by liquid phase epitaxy (LPE) emitting at 1.8 μm in pulsed mode. Then, the first MIR DH laser grown by molecular beam epitaxy (MBE) was reported by Bell Labs in 1983 with emission at 1.78 μm [42].

Over the next decade, the performance of Sb-based lasers was significantly improved with the use of strained quantum well structures.

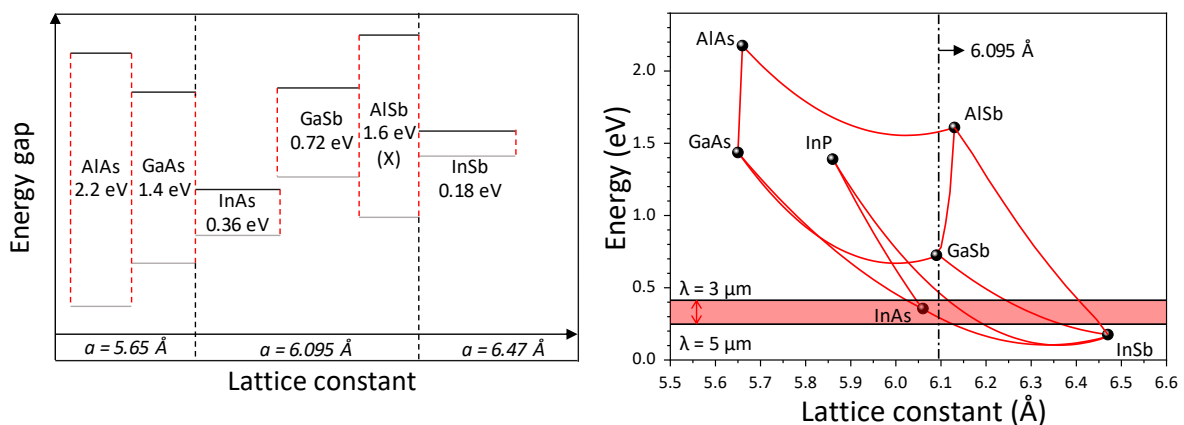


Figure I-9 - a) Different semiconductor band offset b) Energy gap as a function of lattice parameter

The first Sb-based QW laser was developed at NTT. The active zone was made with lattice matched type-I GaSb QWs within AlGaSb barrier. The laser was grown by MBE and operated in pulsed mode at room temperature (RT) with an emission at 1.65 μm [43].

Then, to increase the wavelength and reduce the threshold currents the MIT and the Sarnoff Corporation increased In and As contents within the QWs [44], allowing type-I QWs with higher compressive strain. With active region containing GaInAsSb Type-I QWs in AlGaAsSb barriers, they achieved RT operation in CW at 2.05 μm [45] and 2.7 μm [46].

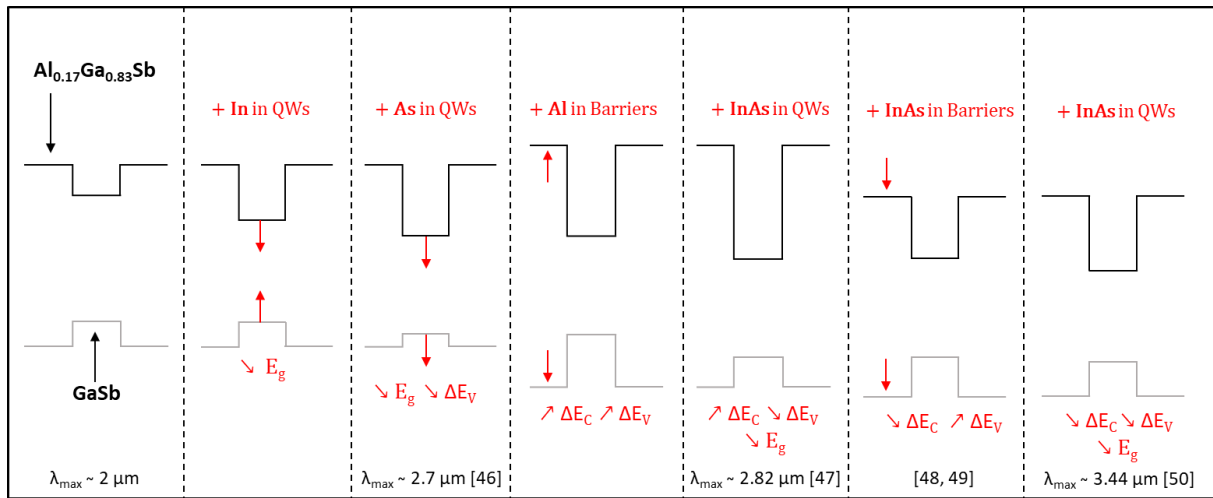


Figure I-10 - Illustration of a typical approach to extending the laser emission wavelength in GaSb-based type-I QW diode lasers

The reduction of the energy gap by increasing In and As compositions in the QWs progressively shifts the conduction and valence bands of GaInAsSb QW towards lower energies as described in Figure I-10. The valence band offset decreases ~ 50 meV, leading to a weak hole confinement, which degrades the laser performances because of the thermal hole escape. To overcome this issue, the Al-content in the barriers was increased while varying the incorporation of InAs into the QWs, but this design reached its limits at $\lambda = 2.82 \mu\text{m}$ [47] because of the remaining poor hole confinement. In 2005, the Walter Schottky Institute (WSI) in Germany proposed the use of quinary AlGaInAsSb alloys in barriers [48] improving greatly the hole confinement. With this new material, one can tailor independently both the conduction and valence band offset [49]. This approach allowed to demonstrate laser emission at RT at 3.44 μm [50] in CW operation and 3.73 μm in pulsed mode [51]. Beyond these wavelengths, the hole confinement becomes again inefficient thus limiting the application of Sb-based type-I QWs for MIR lasers.

I.2.2 Auger effect

The Auger effect is the most important mechanism of non-radiative recombinations which limits performances of long wavelengths semiconductor lasers. In this process, the energy released by an electron that recombines with a hole is absorbed by another carrier. This carrier finally dissipates its energy through a phonon emission heating the material as a consequence. This mechanism is a three-carrier process with rate which scales as the cube of carrier density $\propto n^3$ (with $n = p$). Within the Boltzmann approximation [52], one can calculate the Auger recombination coefficient, C as follows:

$$C = C_0 \cdot e^{-\frac{E_a}{k_B T}} \quad (1.11)$$

Where C_0 depends on the material, k_B is the Boltzmann constant, T is the temperature and E_a is the activation energy needed for the process. There are two main Auger recombination processes occurring in QWs, CHSH and CHCC, which are illustrated in Figure I-11 and detailed thereafter.

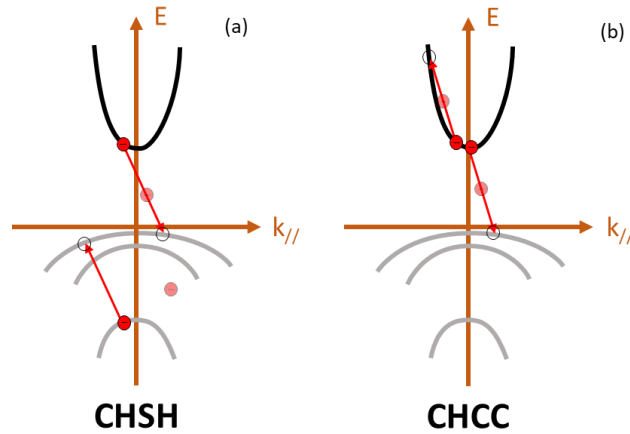


Figure I-11 - The two main Auger recombination processes in QWs

I.2.2.1 CHSH process

In the CHSH process, an electron in the conduction band (C) recombines with a heavy hole (H), while an electron in the spin orbit (S) band is excited to the heavy hole (H) band. This process is explained in Figure I-11(a). The activation energy for this process is:

$$E_a (\text{CHSH}) = \frac{m_s}{2m_h + m_c - m_s} \cdot (E_g - \Delta_{SO}) \quad , \quad E_g > \Delta_{SO} \quad (1.12)$$

$$E_a (\text{CHSH}) = \Delta_{SO} - E_g \quad , \quad E_g < \Delta_{SO} \quad (1.13)$$

Where E_g is the energy gap of the material, m_c , m_h and m_s are the in plane effective carrier masses for the electron, heavy hole and spin orbit bands and Δ_{SO} is the spin orbit splitting. According to Anikeev et al. [53], the proximity of the electron-hole recombination energy and the energy separation of the spin orbit valence band enhances CHSH auger recombination. For bulk material as GaSb and InAs, the energy gap is close to the split-off separation as shown in Table 1, which increases the probability of non-radiative recombination by CHSH Auger effect. This resonance can be easily avoided by the strained GaInAsSb QW and then the CHSH resonance decreases

Material	E_g (eV) Energy gap	Δ_{SO} (eV) Split-off
GaSb	0.72	0.76
InAs	0.3	0.39
InSb	0.17	0.81

Table 1 - Energy gap and split-off of several II-V semiconductors

I.2.2.2 CHCC process:

In the CHCC auger process, the energy released by the electron-hole recombination excites another electron in the conduction band to a higher energy level as depicted in Figure I-11(b). Assuming parabolic bands under the simplified Kane model, the activation energy during this mechanism is [54]:

$$E_a (\text{CHCC}) = \frac{m_c}{m_c + m_h} \cdot E_g \quad (1.14)$$

where E_g is the energy gap of the material and m_c and m_h are the effective carrier masses for the electron and heavy hole bands.

Figure I-12 shows the CHCC activation energy and its Auger coefficient as a function of the wavelength for GaInAsSb material strained at 1.5 % [55]. One can observe that the CHCC auger coefficient grows exponentially whilst the activation energy decreases in the narrow gap materials required to obtain long wavelength emissions. The activation energy at 3.3 μm is only 0.126 meV leading to a high Auger coefficient around $2.8 \cdot 10^{-27} \text{ cm}^6\text{s}^{-1}$.

This is due to the fact that to reach long wavelength emissions one has to use narrow gap materials with small electron effective mass, which leads to a small activation energy (equation 1.14) and thus, to a high Auger coefficient rate.

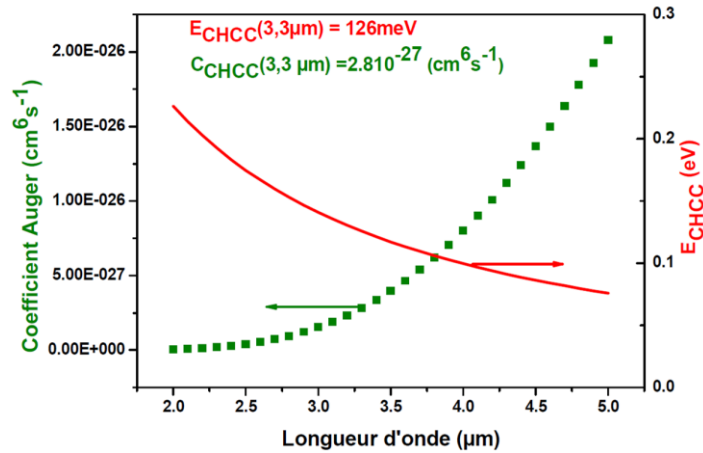


Figure I-12- the CHCC activation energy and its Auger coefficient as a function of the wavelength for GaInAsSb material strained at 1.5% at RT [55]

The situation is different in type-II QWs when small transition energies can be obtained using wide bandgap materials with large electron effective mass [56]. The spatial separation between electron and holes in type-II QWs makes more difficult conservation of momentum during the Auger process, which further reduces its efficiency [57]. The possibility to suppress Auger effect in type-II structures has been proved experimentally.

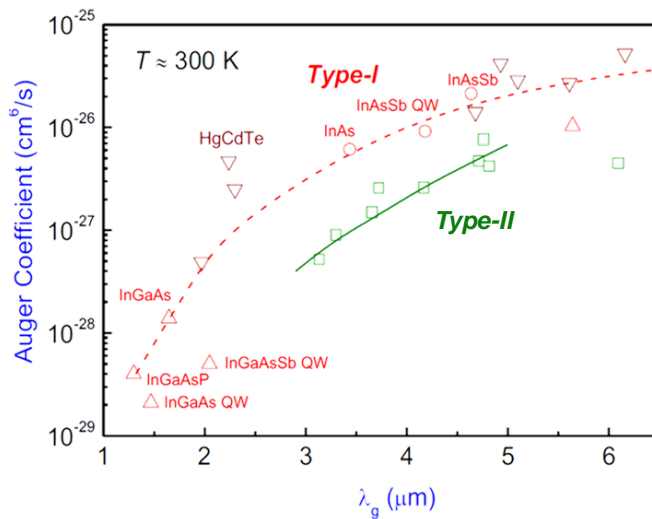


Figure I-13 - Auger coefficient versus emission wavelength at 300 for type-I and Type-II structures [58].

Figure I-13 presents Auger coefficients as a function of wavelength for several III-V bulk materials and QWs of different types. The Auger coefficient C was found to be one order of magnitude lower in type-II QWs compared with type-I emitting at the same wavelengths [58]–[62]. These results demonstrated advantages of type-II structures for the development of long wavelength emitters.

I.2.3 Sb-based type-II QWs active regions

The use of type-II structures for light emission was theoretically identified in 1983 as a possible laser structure [63]. Afterwards, such laser was demonstrated by A. Baranov et al. at the Ioffe Institute with a type-II InGaAsSb/GaSb heterojunction grown by LPE and emitting at 1.86 μm [64]. Later, laser emissions in CW at RT in the 2 – 3 μm wavelength range was achieved using type-II GaInAsSb/GaSb. [65]–[70] As regards of longer wavelengths, several efforts were made since then, achieving type-II heterojunction lasers at wavelengths of 3.2 μm at cryogenic temperatures [71]. In 1998, MBE started to be used at the Ioffe and allowed to grow type-II QWs, demonstrating electroluminescences in the 3 – 4 μm spectral range at 77K [72].

The main drawback of the type-II design is the weak wavefunction overlap of the electron and holes due to their spatial separation.

To increase the gain, the idea, previously proposed in 1987 for Infrared detectors [73], was to assemble several type-II QWs adjacent to each other. Following this way, type-II superlattice lasers appeared. Its mechanism forces the wavefunctions to overflow and increase their electron-hole overlap forming a mini-band while maintaining the same energy gap. The University of Montpellier has made progress using InAs/GaSb and InAsSb/InAs superlattice lasers achieving, at cryogenic temperatures, emissions at wavelengths of 2.85 [74] and 3.5 μm [75], respectively. These heterostructures alleviated the main issue of type-II design. Nonetheless, they suffer from three-dimension (3D) electron and hole population, which demonstrated inferior performances than QWs with their quasi-2D carrier population [76].

To overcome this issue, in 1995 Meyer et al., developed the type-II “W” QWs [77]. The W design, presented in figure I-14, is composed of a GaInSb hole QW surrounded by two InAs electron QWs. This structure provides high electron hole overlap despite the type-II band alignment. Besides, the transition energy in the W-QW can be easily tuned by adjusting the thickness of the InAs wells with only a few monolayers. This “W” concept enhances differential gain and maintains the strong Auger effect suppression of the regular type-II structures leading to lower threshold and higher operating temperature.

In 1996, the Naval Research Laboratories (NRL) and the University of Houston demonstrated the first laser emission using such W-QWs. This optically pumped laser emitted between 3.9 and 4.1 μm in pulsed regime at temperatures up to 285 K [78]. Room temperature

operation was then achieved the same year by the same research group at of 3.2 μm [59] and then optically pumped VCSEL operating at 2.9 μm was also reported in pulsed mode up to 280 K.

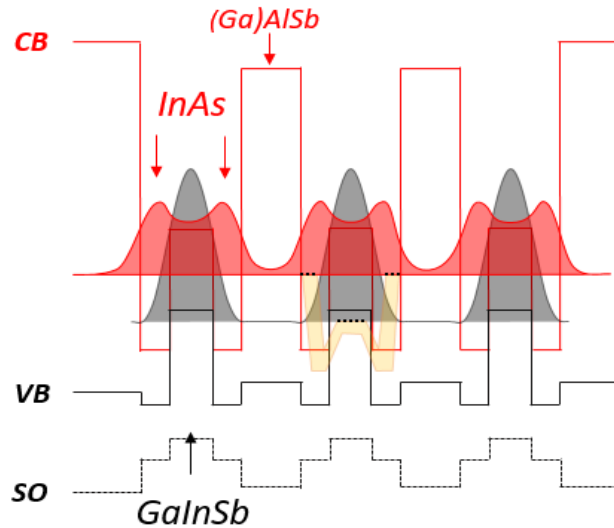


Figure I-14 - Band structure of a Type II - W multi quantum well design. Conduction band in red line and valence and split off bands in solid and dash black lines respectively. Electron and hole wavefunctions are depicted by the red and black transparent curves.

In 1999, the NRL demonstrated the first RT operation of an electrically pumped laser beyond 3 μm using this type-II W MQWs. They reached an emission wavelength of 3.3 μm at 310 K in pulsed mode mode [79] with 10 W-QWs in the active region. One year later, they achieved continuous wave (CW) regime up to 195 K with only 5 W-QWs in a broad area laser. This device exhibited a threshold current density of 1.4 kA/cm^2 and a CW output power of 3.5 mW at the maximal operation temperature [80]. Further improvements of type-II lasers have been achieved using cascade structures initially proposed by R. Q. Yang in 1994.

1.2.4 GaSb-based Interband Cascade active zone

Interband Cascade active zones are composed of several QWs connected in a series configuration within a cascade scheme allowing an interband transition. It is a hybrid structure between conventional laser diodes in which the photon emission is produced by an electron-hole recombination and the cascade design where electrons are recycled as in QCLs (Figure I-15).

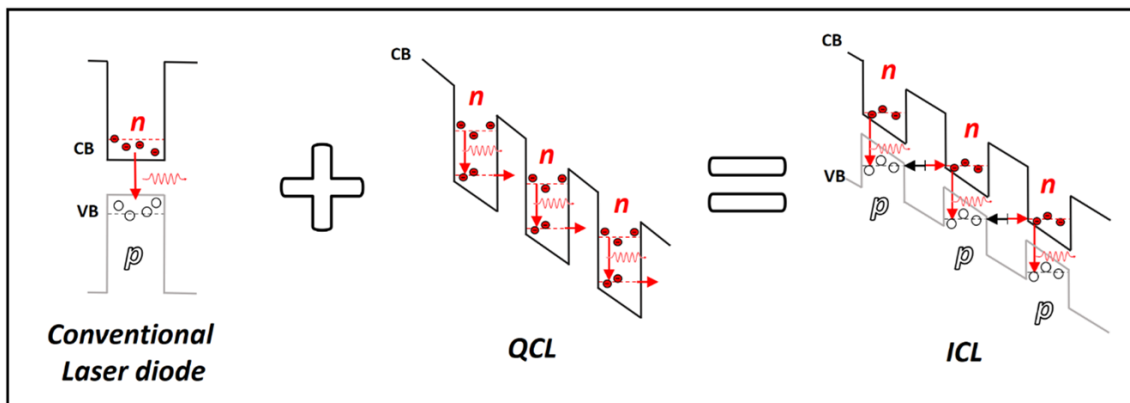


Figure I-15 - Operating principle of Interband Cascade Laser

Based on the idea of multi-heterojunctions made by Esaki et al. in 1981 [81], interband cascade lasers (ICLs) were firstly proposed by R. Q. Yang et al. in 1994 at the University of Toronto in Canada [82]. This structure consisted of the union of two InAs-GaSb QWs, forming a broken band gap alignment, into a cascade arrangement as depicted in Figure I-16.

In this design, the conduction band of the InAs QW is lower than the valence band of the GaSb QW. Besides, the broken band-gap alignment, carrier confinement is obtained with two thin AlSb barriers on each side. Therefore, the electron energy state and the hole energy state, can be tailored from a few meV to 700 meV by varying the InAs and GaSb QW layers thickness. Thus, it is possible to cover a wide spectral range from 3 to 12 μm .

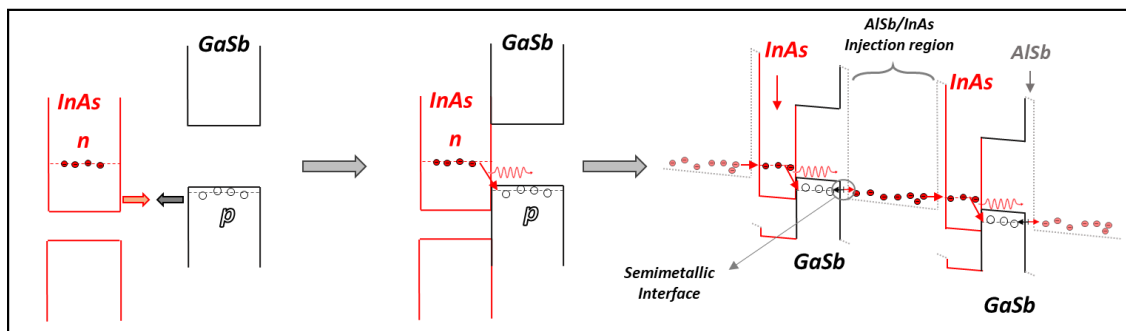


Figure I-16 - First Sb-based type-II laser proposed by Rui Q. Yang et al. in 1994 [82]

In ICLs, carriers recycling occurs at the semimetallic interface [83]. This interface is composed of a GaSb/InAs junction. Indeed, for a wide range of Fermi energies, the GaSb/InAs interface can act as a carrier source for electrons and holes on either side of the junction. As presented in Figure I-16, at the semimetallic interface, an AlSb layer is inserted between the InAs and the GaSb layers to reduce the overlap wavefunction and therefore to reduce the optical losses due to parasitic interband absorption at the semimetallic interface [84]. Under forward bias, electrons are generated at the semimetallic interface and pass through an

electron injector formed by an InAs/AlSb superlattice, to reach the next period of active QW. On the other side, after their generation at the junction, holes swept into the active region to recombine with electrons to generate a photon. They are supposed to be blocked into the GaSb QW and cannot flow to the electron injector. This process recycles injected electrons enhancing

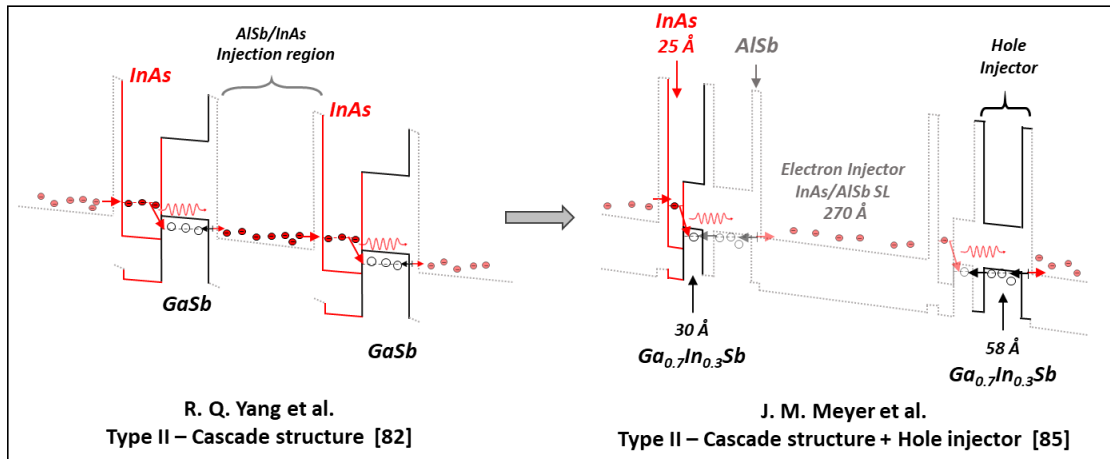


Figure I-17 - Addition of hole injector made with GaInSb

the efficiency.

In 1996, the NRL proposed to use a strained GaInSb hole quantum well to increase the emission wavelength. For better carrier confinement in the active QWs they inserted a second GaInSb layer right after the AlSb layer adjacent to the main active wells [85], as shown in Figure I-17. This part, named hole injector, prevents tunneling leakage from the InAs electron active well directly into the injection region.

In 1997 the University of Houston and Sandia National laboratories, demonstrated the first Interband cascade laser using 20 stages for the active zone [86]. This laser emitted near to 3.8 μm in pulsed operation up to 170 K with a threshold current density of 4.2 kA/cm^2 at 80 K and a differential quantum efficiency lower than 100 %. Quantum efficiency of 130% was then demonstrated the same year with conventional type-II [87] and type-II-W [88] QWs at wavelengths of 3.8 and 2.8 μm , respectively. Both designs operated only under pulsed mode with threshold current density of 0.8 kA/cm^2 at 165K. It is important to notice, that the operation temperature of the ICL with W-QWs was able to reached 220 K, i.e. 55 K higher than for the ICL with conventional type-II design.

A design with type II-W QWs containing a second GaInSb hole injector allowed the NRL to increase the maximum operating temperature of ICLs to 286 K [89]. This ICL operated in the

pulsed regime with an emission wavelength around 3.6 μm and a threshold current density of 7.5 kA/cm^2 with higher threshold current densities (2.2 kA/cm^2 at 92K) compared with the previous type-II-W ICL [88]. In 2000, the ARL reported the first ICLs operating in CW mode. They demonstrated CW operation up to 70 K with 23 stages of type-II QWs [90]. Then in 2002, a collaboration between Maxion Technologies and the Jet Propulsion Laboratory (JPL) led to the demonstration of RT operation from a type-II ICL lasing near 3.5 μm with threshold current densities of 6.5 kA/cm^2 at 300K [91].

The ICL performances were then continuously improved. The threshold current density was reduced to 1.04 kA/cm^2 at 300 K [92] with 15 cascade stages, 3.8 A/cm^2 at 78 K and 590 A/cm^2 at 300 K with 20 periods [93]. The maximum operating temperatures in CW regime were increased to 264 [94], 269 [95] and 288 K at the end of 2007 [93].

Intensive efforts in epitaxy and device technology, along with careful design optimizations (as the implementation of SL transition regions before and after the active zone to smooth the band profile, the donor density in different sections of the active zone, etc.) [96] resulted in the operation temperatures in CW mode. An important step towards this goal was the implementation of separate confinement layers (SCLs), made of GaSb, surrounding the active zone. SCLs was mainly used to increase the optical mode confinement in the active region, avoiding its overlap with the cladding layers and thus reduce optical losses [97]. Due to the higher refractive index of GaSb (~ 3.8) compared with the active region (~ 3.5), these layers increase the average refractive index contrast between the cladding and the core regions and thus improve the optical confinement. Consequently, lasers with the structures using SCLs were expected to have better performances in CW operation. However, CW operation of such ICLs was still limited to temperatures of 260 and 266 K, at 3.7 and 3.43 μm , respectively [98].

Finally, in 2008, Kim et al. from NRL reported a five stage type-II W QWs ICL, operating in CW mode up to 319 K at $\lambda = 3.75 \mu\text{m}$ using low doped ($1.5 - 2 \times 10^{17} \text{cm}^{-3}$) GaSb SCLs [99]. At 300 K, the threshold current density was 588 A/cm^2 with a maximum CW output power of 10 mW under 0.5 A of driven current.

In 2010 the University of Wurzburg in Germany proposed to shorten the electron injector in order to increase the gain. By using nine InAs/AlSb [100] QWs instead of ten [78], the intensity of the optical mode overlap throughout the complete active region was increased by

about 15% [100]. Although the performance of the laser was not as good as the state of the art, the comparison of the two different designs demonstrated a reduction of the threshold current density by approximately a factor 2. Moreover, the turn-on voltage decreased from 5 to 4 V with the shortened design and the maximum operating temperature increased from 15 to 20°C.

Therefore, it was clearly shown that besides the choice of the active QWs each element constituting the active stage has to be refined carefully to improve the performance. Indeed, in 2011 NRL developed a new generation of ICLs [101], based on empirical tests. They demonstrated that the hole-injector QWs states must be located below the upper active-hole energy level, while the electron states of the first electron-injector QW next to the semi-metallic interface must be lower than the active electron QW state. These energy conditions imply that the electron population remains localized in the injector rather than in the W-QWs region (wine-colored line in Figure I-18.(a), whereas in the case of holes, most of them reach the GaInSb active hole QW through the double QWs hole injector design (green-colored line in Figure I-18(a) [101].

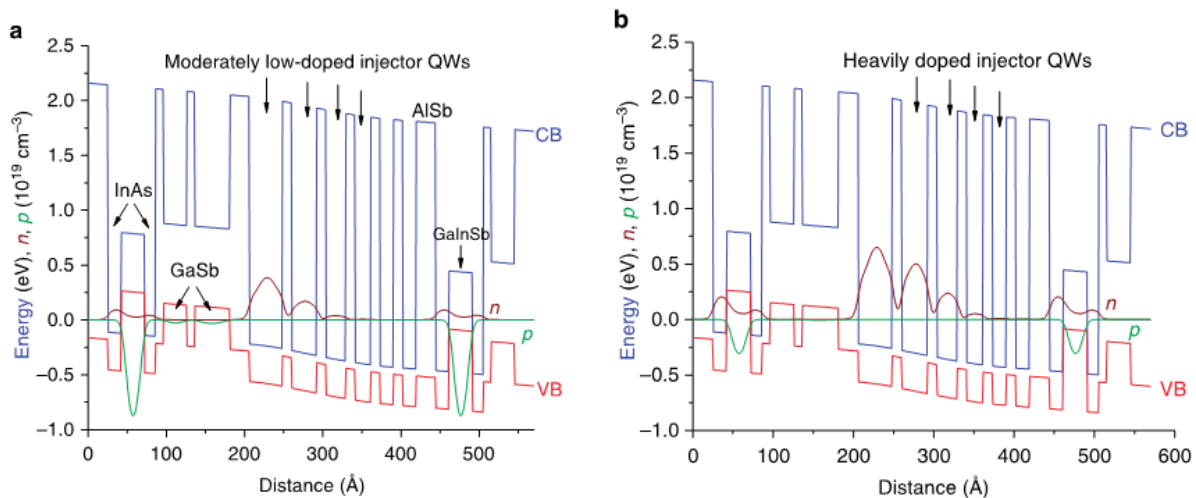


Figure I-18 - The electron (wine-colored) and hole (green) density distributions are shown for: (a) a conventional ICL design with four InAs electron injector QWs doped moderately with Si to $4 \times 10^{17} \text{ cm}^{-3}$, and (b) a rebalanced design in which four injector QWs are doped much more heavily to $5 \times 10^{18} \text{ cm}^{-3}$. The blue and red lines indicate the conduction- and valence-band bulk band edges, respectively. Positions of the doped QWs in each structure are indicated by the arrows. [101]

This situation generates an electron-hole population disparity in the W-QWs region at lasing threshold ($p_{th} \gg n_{th}$) depicted in Figure I-18(a) reducing the gain per unit current density. To prevent this constraint and equilibrate the carrier population ratio, they reduced the number of electron injector QWs to 6, and highly n-doped QW from the 2nd to the 5th. Figure I-18(a) and (b) shows the hole and electron density distribution when the InAs QWs

within the electron injectors are moderately doped ($\sim 4 \cdot 10^{17} \text{ cm}^{-3}$) and highly doped ($\sim 5 \cdot 10^{18} \text{ cm}^{-3}$), respectively. For the high doping level, the extrinsic electrons rebalance excessive holes in the active region readjusting carrier populations at lasing threshold. This new generation of ICL operated in the CW regime at temperature up to 109°C with emission wavelength ranging between 3.57 and $3.92 \mu\text{m}$. The threshold current densities were as low as 167 A/cm^2 at 300 K for an emission at $3.67 \mu\text{m}$ [101]. The power consumption required to reach the laser threshold was approximately 0.029 W at 25°C , is far lower than the best MIR QCL in which the input power varies between 0.8 W at $4.5 \mu\text{m}$ [102] and 6.4 W at $3 \mu\text{m}$ [103]. Applying the rebalanced carrier density approach has extended the high performance operation of ICLs to longer wavelengths, beyond $4.2 \mu\text{m}$ [104]. Moreover, it was the starting point of fast progress of ICL performances. An output power as high as 592 mW with 7 active stages under CW operation at RT was demonstrated [105] and threshold current density as low as 90 A/cm^2 at 10°C was obtained with 10 active stages under pulsed operation [106]. In 2015, the NRL demonstrated that when the cavity length is reduced to 1 mm , both 10-stages and 7 stages ICLs can reach 18% wallplug efficiency in CW at 25°C [107].

Finally, Figure I-19, shows the wavelength dependence of RT threshold current densities for broad area ICLs with different number stages [15]. These results represented the state of the art of ICLs in 2015. These data show clearly that type-II W ICL can cover the full range between 3 to $4 \mu\text{m}$ with threshold current density lower than 200 A/cm^2 at RT.

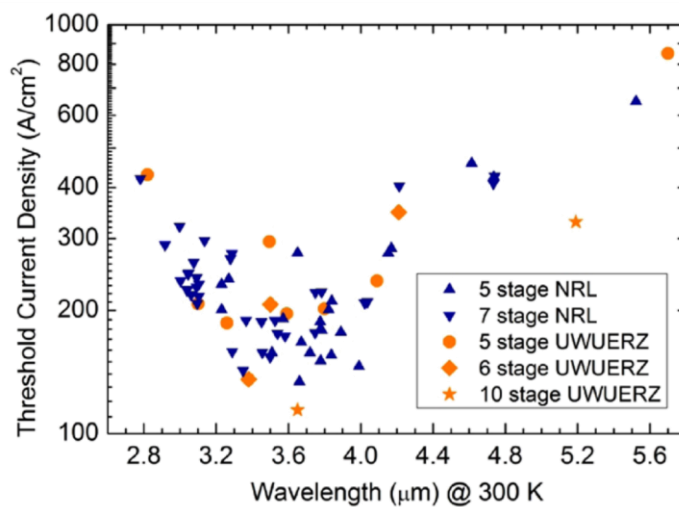


Figure I-19 - Pulsed threshold current densities for broad area ICLs with various stage numbers at 300 K

The main application area of mid-IR laser is the spectroscopy, which requires light sources producing a single narrow emission line with power of a few mWs.

I.3 VCSELS

I.3.1 Single mode lasers: DFB & VCSELS

As presented in paragraph I.1.2, the convolution of the gain curve and the Fabry Perot modes gives a multi-frequency emission spectra. For the applications targeted, single mode lasers are required. The single mode emission can be realized mainly with two different technologies, the distributed feedback lasers (DFB) and vertical cavity surface emitting lasers (VCSELS).

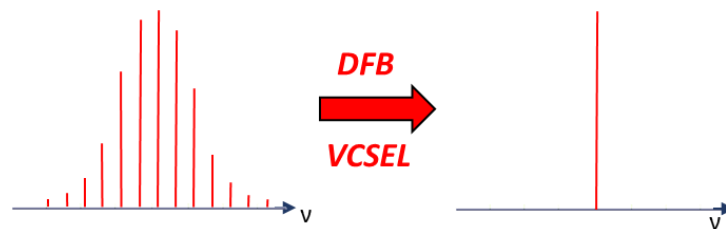


Figure I-20 - Process to realize single-mode laser with a multimode longitudinal spectrum on the left and a single mode one on the right.

The term single-mode operation, applied to lasers, is ambiguous, as it is used with different meanings:

- It can be single-longitudinal-mode operation, where the linewidth of the laser radiation can then be very small (often only a few kilohertz) and the coherence length accordingly long. It is defined by the free spectral range already explained.
- It can mean single-transverse-mode operation, where a laser operates on a single kind of transverse or spatial mode which is almost always a gaussian mode. However, laser oscillation may then still occur on multiple longitudinal (or axial) modes, which have essentially the same transverse shape but differing optical frequencies, separated by the free spectral range.

In most cases DFB lasers are used to provide single mode emission. Operation of such devices is based on the optical feedback distributed along the laser ridge created by periodic modulation of the complex refractive index of the waveguide. The optical mode that can be

amplified in such devices in one for which its wavelength λ_B can be coupled with the waveguide periodicity Λ following the equation:

$$\Lambda = \frac{m \lambda_B}{2n_{\text{eff}}} \quad (1.15)$$

where n_{eff} is the effective refractive index.

Another technology providing single frequency emission is the vertical cavity surface emitting lasers (VCSELs). They are semiconductor laser diodes in which the light emission is vertical, parallel to the growth axis. In VCSELs the mode selection is provided by short optical cavity.

As seen in the section I.1.2, the FSR is given by:

$$\Delta\nu_{\text{FSR}} = \frac{c}{2n_g L} \quad (1.16)$$

For VCSELs, the physical thickness of the cavity L is in the range of a micrometer, leading to a large FSR which favors an intrinsic single longitudinal emission as depicted in .

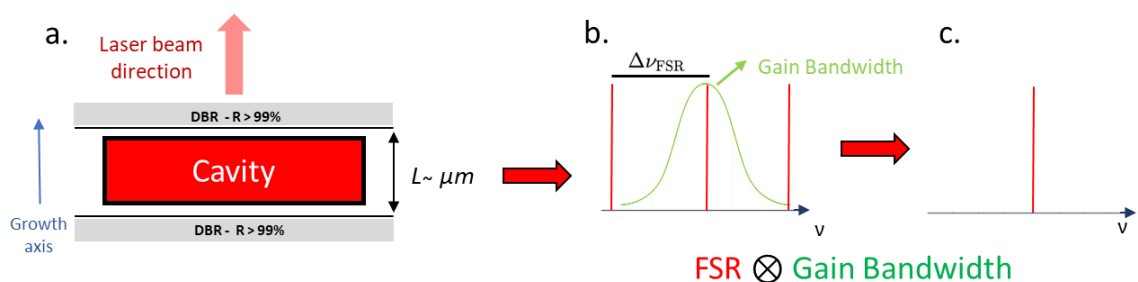


Figure I-21 - VCSEL cavity on a micrometric scale (a) leading to a spacious FSR which in convolution with the gain bandwidth (b) concludes in a single longitudinal mode spectrum (c).

One of the important requirements for the operation of a VCSEL is to compensate the small amount of gain media due to the geometry. In order to compensate the small gain and reach lasing threshold, metallic or multilayer mirrors, as distributed Bragg mirror (DBR), with reflectivity values exceeding 99.5% should be used below and above the active cavity. The principle of DBR operation will be described in the chapter III.

The first laser with emission perpendicular to the layer plane was demonstrated by I. Melngailis at MIT in 1965 [108]. An n^+pp^+ InSb structure, with a polished surface on one side and a metallic Ag/Au layer on the other side acting as mirrors. This structure emitted in the MIR

at only 10 K. The term VCSEL was proposed by Prof. Kenichi Iga from Tokyo Institute of Technology (TIT) in 1979 [109]. A vertical laser with two metallic mirrors sandwiching a DH made of GaInAsP which emitted at 1.2 μm in pulsed mode at 77 K. Later, in the early 1980s, several laboratories, including the Bell Labs and the Optical Science Center at the University of Arizona, began studying the use of lasers and nonlinear optical phenomena in microcavities for potential applications in optical switching, signal processing and optical computing. Afterwards, the first report on RT CW operation of GaAlAs/GaAs VCSEL was made at the TIT in Japan [110].

For VCSELS, to reach single-mode operation it is necessary that the output aperture of the laser beam is small in the order of 5 - 10 μm for the IR [111], [112]. Based on mesas technology VCSELS were able to achieve single mode emission obtaining new results. A monolithic structure grown by metal organic chemical vapour deposition (MOCVD) operated in a single transverse longitudinal mode at 0.9 μm with I_{th} of 32 mA at 22.5 °C. Since then, the InGaP, AlGaInAs and GaAsSb material platforms based on GaAs substrates offered emission range from 0.65 to 1.3 μm [113]–[119] exploiting AlGaAs alloys for DBR mirrors.

Moreover, the current injection by an anode of annular geometry leads to a non-negligible radial inhomogeneity. In this case, VCSELS cannot lase in their center when their diameter exceeds a few tens of microns because the peripheric injection of the anode electrode combined with self-heating problems are fatal for uniform emission [120].

For this reason, designing the best and most adapted electro-optical confinement technique is essential to achieve a circular and low divergent laser beam and obtain low threshold currents.

1.3.2 Electro-optical confinement in VCSELS

The first method of electrical confinement in VCSELS was proposed in the late 1990s. It was based on the ions implantation into the top of the structure forming a ring of which the center was protected from the ion flux [121] [115] (Figure I-22.a.). In this structure the lateral confinement is gain guided and the size of the pumped part of the active region depends on the current. For this reason, high order transvers modes can appear at high currents.

Simultaneous optical and electrical transverse confinement can be obtained in GaAs/AlGaAs-based VCSELS by lateral oxidation of Al-containing layers of the top Bragg mirror

as displayed in Figure I-22.b. These layers are converted to AlOx funneling the current into the center of the cavity. This oxide has a smaller refractive index than the AIAs inducing a transverse confinement of the photons. This approach introduced by Huffaker et al. in 1994 [122] is to date the most widely used technique for electro-optical confinement in GaAs-based VCSELS [123].

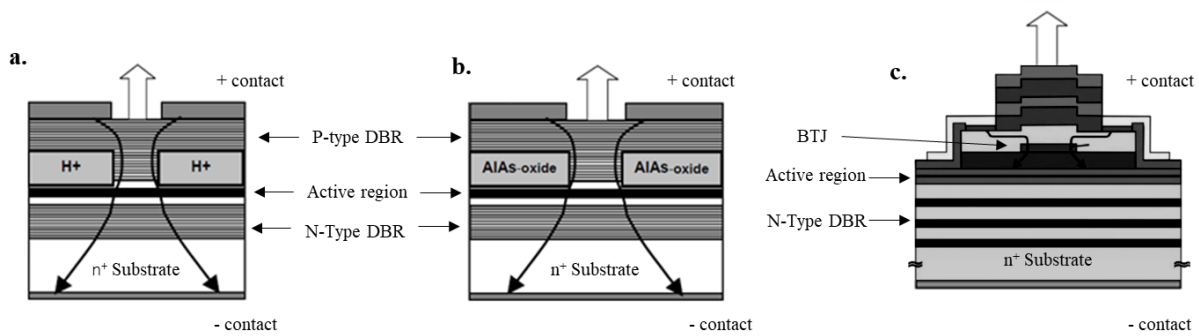


Figure I-22 – Schematics of some common VCSELS structures. (a) Proton implanted, current confined by semi-insulating region of implant; (b) AIAs layer oxidized generating confinement for the current and the optical beam; (c) BTJ structure for the electro optical confinement.

Extending the wavelength beyond 1300 nm have required new materials. The InP technology with InGaAsP QWs for emission wavelengths at 1300 and 1500 nm is suited for interconnections in telecommunication applications. With these materials, obtaining sufficient reflectivity is challenging because of the small available refractive index contrast in InGaAsP/InP DBRs [124]. Then, GaAs/AlGaAs DBRs wafer-bonded to InP lattice-matched QWs was exploited to take advantage of the great maturity and high refractive index difference of As-based DBRs [125]. To reach electro-optical confinement, InP-based VCSELS commonly employs the buried-tunnel junction (BTJ) technology [126] depicted in Figure I-22.c. In this approach, the growth is done in two steps. The first growth is finished after the active zone by an InGaAlAs(p++)/InGaAs(n++) TJ layer. Afterwards, circular mesas are etched down to the TJ interface. Subsequently, the overgrowth starts with a n-InP layer forming a blocking pn-junction outside of the mesa. Therefore, the carriers will pass only through the InGaAlAs(p++)/InGaAs(n++)/InP(n) junction, focusing the current only in the center of the device and pumping a reduced volume of the active zone. The current is injected via a highly doped InGaAs contact layer placed on top of the p-InP layer and through the n-doped bottom mirror. With this technology, the WSI with VERTILAS GmbH company demonstrated the first single-mode InP-based VCSEL operating in CW mode at temperatures up to 40°C at 2.3 μm using InGaAs QWs. A threshold current of 12.5 mA and a maximum output power of 1.5 mW at 0°C were observed

[127]. Further efforts in this technology allowed extending the wavelength to 2.5 μm [128] in CW with a maximal operating temperature of 10°C.

As mentioned before, antimonide materials are well suited for laser diodes operating in the MIR spectral range. Optically pumped VCSELs were first developed for GaSb-based lasers using Type-II - W QWs. CW operation up to 160 K was achieved at $\lambda = 2.9 \mu\text{m}$ [129]–[131].

1.3.3 MIR Sb-based VCSEL

The first electrically pumped GaSb based VCSEL was demonstrated in 1998 by Baranov et al. at the University of Montpellier [132]. It was a monolithic p-i-n structure with six type-II GaInAsSb/GaSb strained QWs grown by MBE, using top and bottom GaSb/AlAsSb quarter-wavelength DBRs. Vertical emission at 2.2 μm was observed at RT with J_{th} of 2 kA/cm² and a peak optical power of 20 mW. The main limitation of this design preventing CW operation came from the upper p-AlAsSb/GaSb DBR. Indeed, this semiconductor DBR presents low electrical conductivity and high free carrier absorption losses [133]. The problem has been alleviated by the same research group using an InAsSb (n++)/GaSb (p++) tunnel junction above the active region. This layer allowed carriers to flow from the GaSb valence band directly to the InAsSb conduction band giving the possibility to use n-type for both top and bottom DBRs [134]. In 2009, monolithic structures demonstrated transverse multimode laser emission at 20°C in CW at 2.3 μm and in pulsed regime up to 2.63 μm using type-I GaInAsSb/AlGaAsSb QWs [135].

Further extending the emission wavelengths have been obstructed by the lack of an efficient lateral confinement method compatible with the GaSb material. Indeed, for this material family the proposal based on the Al-rich layer oxidation technique used for AlGaAs/GaAs structures [136] [137] is not suitable because a wet oxidation of AlAsSb layer forms metallic antimony aggregates [138]. This not only causes an increase in the volume of the layer leading to the destruction of the device, but also creates undesirable current channels. [138]. An original suggestion to circumvent the problem was to exploit metamorphic structures with Sb free AlAs oxidation layer. This metamorphic concept successfully tested on InP VCSELs [139] still remains challenging for GaSb-based devices with only one attempt at 2.3 μm . This VCSEL operated in CW mode up to -5°C and the low performance was attributed to the large wavelength misalignment between the gain peak and the microcavity mode [140].

Today, for mid-IR VCSELS, two major technologies to circumvent this problem are reported: The Buried-Tunnel Junction (BTJ) and the under etched TJ aperture.

In the first approach, the BTJ which comes from InP-based VCSELS [126], the growth is done in two steps. The first growth step is finished after the active zone by a GaSb(p++)/InAsSb(n++) TJ layer. Afterwards, circular mesas are etched down to the TJ interface. Subsequently, the overgrowth starts with a n-GaSb layer forming a blocking pn-junction on the outside of the mesa. Therefore, the carriers will pass only through the GaSb(p++)/InAsSn(n++)/GaSb(n) junction, focusing the current only in the center of the device and pumping a reduced volume of the active zone. The current is injected via a highly Te-doped InAsSb contact layer placed on top of the p-GaSb layer and through the n-doped bottom mirror. Using this technology, the first single-mode GaSb VCSEL operating in CW mode at RT at 2.3 μm was demonstrated by the WSI in 2008 with type-I GaInAsSb/GaSb QWs. The laser exhibited a threshold current of 3.3 mA with a maximum output power of 87 μW at RT [141]. One year later, several efforts invested in this technology allowed increasing the maximum temperature operation up to 75°C [142] and the optical power up to 0.8 mW at 0° C [143] at 2.3 μm and to extend the wavelength of cw operation at RT up to 2.6 μm [144].

However, injecting the current through the n-doped DBR increases the self-heating of the device and limits the achievement of maximum reflectivity due to free carrier absorption [144]. This problem has been solved by using an intracavity approach with an InAsSb layer placed between the bottom DBR and the active zone allowing reflectivities close to 100 %. Taking into account this design and using quaternary barriers in QWs, a single mode emission at 2.97 μm in CW was achieved at temperatures up to 5°C [145].

The second technology was proposed by the University of Montpellier in 2012. In this monolithic structure, the electro-optical confinement was provided by lateral InAs/GaSb TJ under-etching [146] [147] as depicted in Figure I-23(a).

The gap created by under-etching, ensures both electrical and optical confinement. This device exhibited single mode emission at 2.3 μm up to 70°C in CW operation with a threshold current of 1.9 mA at RT [147]. In this technology the output power was improved by using a cascade scheme connecting several active zones which was initially demonstrated on GaAs [148] and InP [149] VCSELS. A VCSEL with two stacks of type-I GaInAsSb/AlGaAsSb active zones

separated by an InAs/GaAs tunnel junction enhanced the maximum output power by more than five times compared with one single active zone stage.

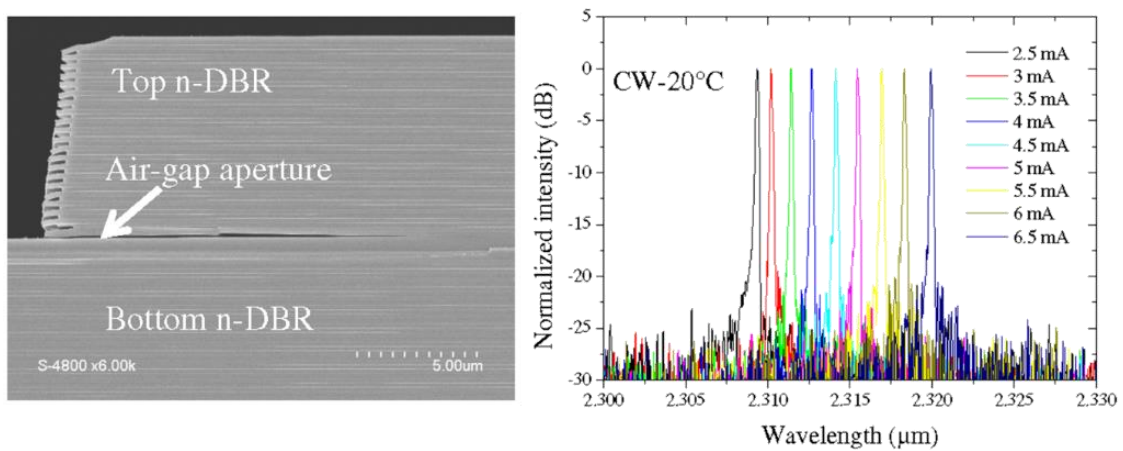


Figure I-23 – a. Cross-section SEM picture of selectively etched InAs/GaSb tunnel-junction in a monolithic GaSb VCSEL; b. Laser emission spectra taken at 20 °C under different CW drive currents for an under etched GaSb-VCSEL. [147].

It reached 1 mW of emission at 30 °C with a 5% of wall-plug efficiency [150]. Despite these very encouraging results, the under etching technique is not reliable due to its low reproducibility caused by the poor mechanical stability making this technique difficult to industrialize.

In 2016 The NRL demonstrated the first GaSb-based VCSEL emitting beyond 3 μm. They used a cascade design with 3 X 5 IC active zone stages and a top dielectric DBR. This concept achieved single mode laser emission at 3.4 μm in pulsed regime without any electrical or optical confinement [151]. Later, in 2017, the WSI extended the laser emission wavelength to 4 μm at a maximum temperature of -7°C in CW operation using type-II - W QWs and a BTJ design [152]. Nonetheless, processing BTJ technology is complex and implies epitaxial overgrowth.

I.4 Conclusion

Technology	Edge emitting lasers (EELs no DFB)			VCSELs		
	QCL	GaSb Type-I	ICL	GaSb Type-I	BTJ - Type-II-W	Hybrid - IC
Wavelength	$\lambda > 3.5 \mu\text{m}$	$\lambda < 3.3 \mu\text{m}$	$3 < \lambda < 6 \mu\text{m}$	$\lambda < 2.6 \mu\text{m}$	$\lambda = 4 \mu\text{m}$	$\lambda = 3.4 \mu\text{m}$
CW RT	✓	✓	✓	✓	-7°C max	x
Threshold current at 20°C	~ 500 mA	20mA	20mA	~ 2 mA	~ 15 mA (pulsed)	~ 10 mA (pulsed)
Power consumption (RT)	~ 700 mW	50mW	50mW	8 mW	~ 12 mW (pulsed)	~ 75 mW (pulsed)
Emission	Multimode	Multimode	Multimode	Single mode	Single mode	Single mode
Output power	~ 1 W	100 mW	100 mW	0,1 mW	0,15 mW (pulsed)	0,52 mW (pulsed)
Beam divergence	Elliptic 20°x40°	Elliptic 20°x40°	Elliptic 20° x 40°	Circular - 15°	Circular - 15°	Circular - 15°

Table 2 - laser parameters for several technologies in the MIR.

Table 2 compiles different laser parameters of the different technology for emission in the MIR. With regard to the present performance of both MIR edge-emitting lasers and VCSELs, it appears clearly that the low-cost potential together with lower power consumption development of VCSELs above $3 \mu\text{m}$ can be considered as a key component to definitively open TDLAS to a much broader market. ICLs can serve as sources for photonic sensing because of their low power consumption in the range of 50 mW in comparison of QCL (~ 700 mW), but they require DFB process to give single mode emission. However, the development of Sb-based VCSELs at wavelength higher than $3 \mu\text{m}$ requires new paradigm and approaches for both active region and device processing. Indeed, as presented before, GaSb type-I QWs laser evidences a severe efficiency drop above $2.8 \mu\text{m}$ and the selection rules of QCL are incompatible with surface emission without resorting to complex, dedicated processing [153]. The only active zone compatible with vertical emission and having demonstrated high laser performance in the $3 - 6 \mu\text{m}$ wavelength range till now is the type-II 'W' active region in an ICL scheme. Although, at the beginning of this work, IC-VCSELs have been already demonstrated in pulsed regime at RT and VCSELs with type-II W QWs in CW at -7°C , there was not VCSEL operating in CW above RT emitting between 3 and $4 \mu\text{m}$.

Furthermore, the VCSEL design, and therefore its technology, has to be modified for emissions at such a wavelength. In fact, a fully monolithic approach is not viable since the thickness of the DBR scales with the wavelength. As an example, a 22 pairs AlAsSb/GaSb pairs DBR ($R > 99.8\%$) for $3.6 \mu\text{m}$ is $11.5 \mu\text{m}$ -thick which leads to a monolithic structure thicker than $20 \mu\text{m}$. Oxidation of an Al(Ga)As metamorphic layer for the realization of an efficient electrical confinement has been successfully tested on GaSb-VCSEL emitting at $2.3 \mu\text{m}$ by the consortium of the MIMIC-SEL project [140]. Moreover, oxidation of Al(Ga)As for electrical confinement is

now well established in the VCSEL technology, it will address the stabilization of the technological flow for a simplified applicability of MIR-VCSELs.

Figure I-24 shows the final VCSEL, it will be based on ICL design for the active zone, a metamorphic oxide lateral confinement scheme and on an hybrid-mirror technology with performances suited for spectroscopy applications.

The next chapters will detail the development of the interband cascade active stage, the semiconductors and dielectric DBRs, the metamorphic III-As confinement layers and finally vertical devices.

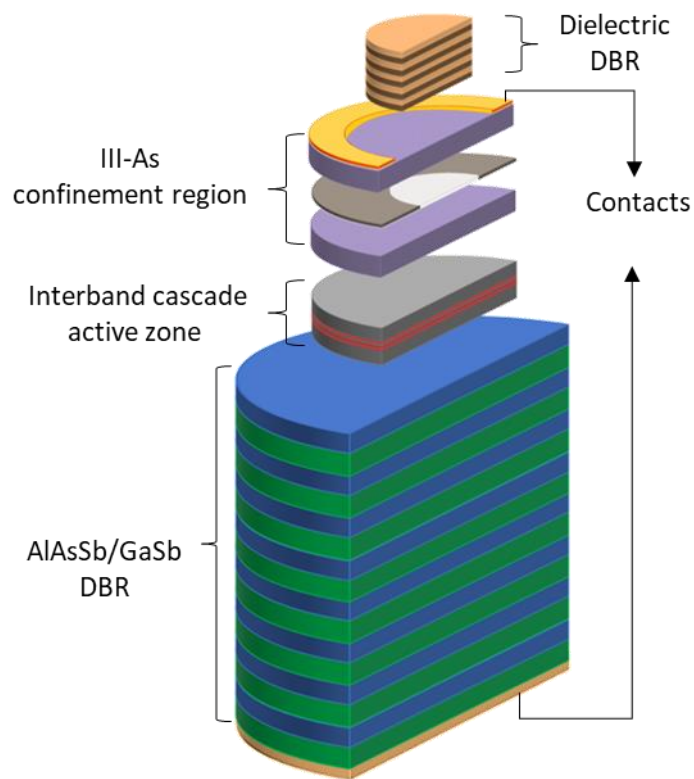


Figure I-24 - Hybrid & metamorphic IC - VCSEL proposal

Chapter II: Interband Cascade Active Region

II.1 Introduction

The active zone that provides optical gain is one of the mainstay parts of a VCSEL. As presented in the previous chapter, type-II-W IC active region can cover efficiently the full spectral range between 3 and 4 μm . To evaluate its performance before its adaptation into a VCSEL, we studied the type II-W IC active zone in edge emitting lasers (EELs). Interband cascade lasers (ICL) allow simple and short technological process and will assess the performances of the active zone.

II.2 Design of the active region

The study of a laser structure is performed in a 4-steps cycle: modelling, growth, technological process, and characterization. In the course of this work, the modelling of the active zone's band structure was carried out with Nextnano software [154]. It allows to calculate the band dispersion via the k·p method to obtain the band structure of the active zone taking into account that the electron wave function satisfies the time-independent Schrodinger equation in a periodic semiconductor crystal. First simulations reproduced the NRL design in order to position ourselves in the state of the art. Figure II-1 represents the band structure of one stage of the IC active zone designed by the NRL [101] for an emission at 3.3 μm under an electric field of 80 kV/cm. The cascade structure is divided into 4 parts: the type-II W active QWs, the hole injector, the semi-metallic interface, and the electron injector. The type-II W active QWs, where the electron-hole recombination takes place, are composed of two coupled InAs electron-QWs sandwiching a single GaInSb hole-QW. They are followed by an AlSb barrier layer. Its function is to reduce the wave-function overlap between the electrons and holes within the W-QWs and the subsequent layers. The hole injector controls the hole population reaching the active QWs and acts as a barrier for electrons increasing their confinement within the W region. Then, a semimetallic interface (SMIF), made of a GaSb/InAs junction, generates electrons and holes on each side. This junction is separated by an AlSb layer to prevent optical losses, indeed optical absorption can occur in the diagonal transition between the holes and electron states.

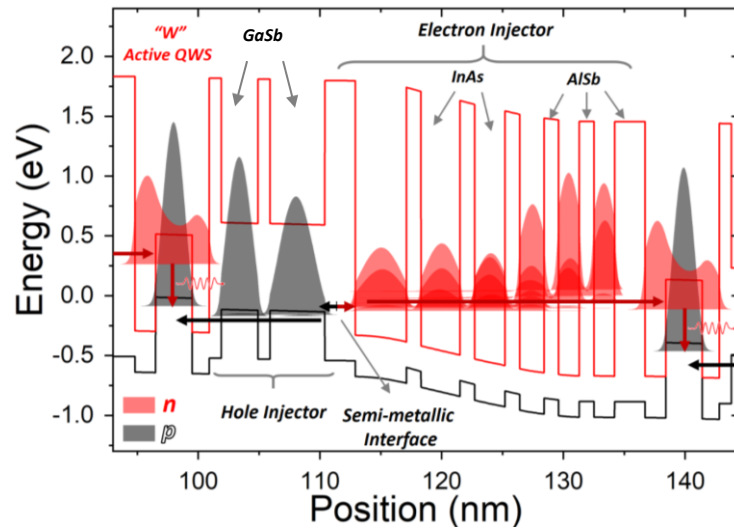


Figure II-1 - Simulated band diagram of one stage of the ICL active core for an emission at 3.3 μm at an average applied electric field of 90k V/cm.

Finally, the electron injector composed of a gradual InAs/AlSb superlattice is located after the junction and allows the electrons to reach the next active QWs. The four inner InAs-QWs are highly N-doped ($5 \cdot 10^{18} \text{ cm}^{-3}$) to rebalance the carriers in the active QWs. The electrons then pass through the injector and end up in the conduction band of the next W-zone featuring the cascade configuration.

The layer thicknesses of this active stage are presented in Table 3, where the W active QW is highlighted in red.

	Layer	Thickness (\AA)		Layer	Thickness (\AA)
1.	AlSb	25	11.	AlSb	12
2.	InAs	17	12.	InAs	32
3.	Ga _{0.65} In _{0.35} Sb	30	13.	AlSb	12
4.	InAs	14	14.	InAs	25
5.	AlSb	10	15.	AlSb	12
6.	GaSb	30	16.	InAs	20
7.	AlSb	10	17.	AlSb	12
8.	GaSb	45	18.	InAs	17
9.	AlSb	25	19.	AlSb	12
10.	InAs	42	20.	InAs	17

Table 3 - Thicknesses of one period of IC active zone for emission at 3.3 μm .

II.3 Design, epitaxy and structural characterization of ICL structures

II.3.1 Design of ICL for active stage studies

Figure II-2 displays the scheme of the ICL structure designed to carry out the studies on the IC-active stage. The active region is made of seven IC active stages and sandwiched between two GaSb SCHs to increase the refractive index difference between the active zone and the cladding layers. It allows obtaining a better optical confinement (see section I.2.4 of the Chapter I on page 23). To confine the optical mode within the active region, we used AlGaAsSb bulk material as top and bottom claddings [155] instead of the usual AlSb/InAs cladding layers [15]. Indeed, the epitaxial growth of AlGaAsSb cladding layers by MBE is well controlled by the Nanomir group and is commonly used for GaSb-based diode lasers emitting between 1.55 μm and 3.7 μm [51], [55], [156]–[159]. These layers, depicted in Figure II-2 in yellow, have a high Al-content (85%) and leads to a refractive index of $n = 3.3$ [97] at 3.3 μm . This increases the overlap between the optical mode and the active zone [160]. The thicknesses are 2.5 and 2 μm for the bottom and the top claddings, respectively. Furthermore, the thermal conductivity of this material is higher (7 W/m.K) compared to InAs/AlSb SL (3 W/mK) [161]–[163]. Thus, the AlGaAsSb bulk material will promote better heat dissipation and should result in better laser performance.

Between the claddings and the active zone, the orange layers represent n-type transition layers. They are inserted at each interface between the different regions of the structure. They lower the parasitic voltage drops at band discontinuities. Finally, the top contact layer is composed of 300 nm thick GaSb followed by 20-nm thick InAs layer.

II.3.1 Growth temperature of the Type-II W QWs

Quantum structures such as W-QWs and injectors require growth accuracies of the order of 0.1 \AA , which are usually accessible by molecular beam epitaxy (MBE). Its precise control of atomic and/or molecular beams vaporized from high temperature sources onto a heated substrate in ultra-high vacuum (UHV) chamber makes it the most suitable technique for the growth of QW lasers.

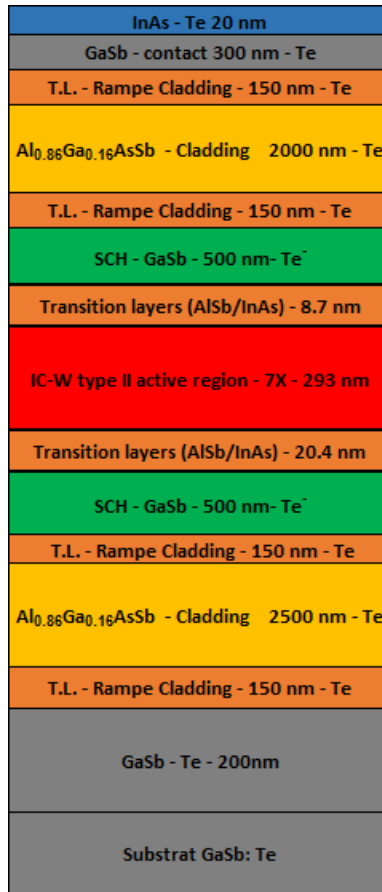


Figure II-2 - Complete design of ICL

As the first step in the fabrication process, the material growth is fundamental to the laser performance. Hence, before starting the epitaxy of the whole structure, it is necessary to evaluate the growth conditions in terms of temperature. Indeed, this growth parameter was found as one of the most relevant for obtaining a high emission efficiency [164]. For this reason, four W-QWs samples were grown between 425 to 465°C for assessment by photoluminescence. The structures were grown by solid source MBE equipped with As- and Sb-valved cracker cells.

The band structure of these samples is presented in Figure II-3. It is composed of five “W” QWs designed for emission around 3.3 μm (see Table 3) separated by GaSb barriers. A 20nm AlSb is inserted on each side to prevent the escape of photo-pumped carriers.

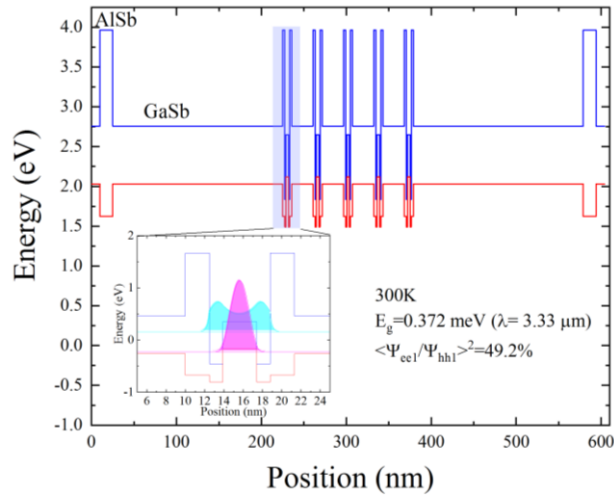


Figure II-3 - Band structure of the W-QWs samples used for photoluminescence.

The structures were studied by photoluminescence (PL) at room temperature (RT) and excited with a 780 nm GaAs diode. The spectra were measured with a Fourier transform Infrared (FTIR) spectrometer equipped with a cooled InSb detector. The PL spectra are depicted in Figure II-4(a). The PL peak intensity presented in Figure II-4(b) for the different samples clearly evidences that 435°C is the growth temperature that provides the best PL performance. The degradation of the PL at low growth temperature can be attributed to the formation of In clustering within the W-QW, while at high temperature the deterioration is related to atoms inter-diffusion at the QW interfaces [164]. This result allowed determining the growth temperature for the IC-active region of all the structures presented throughout this work.

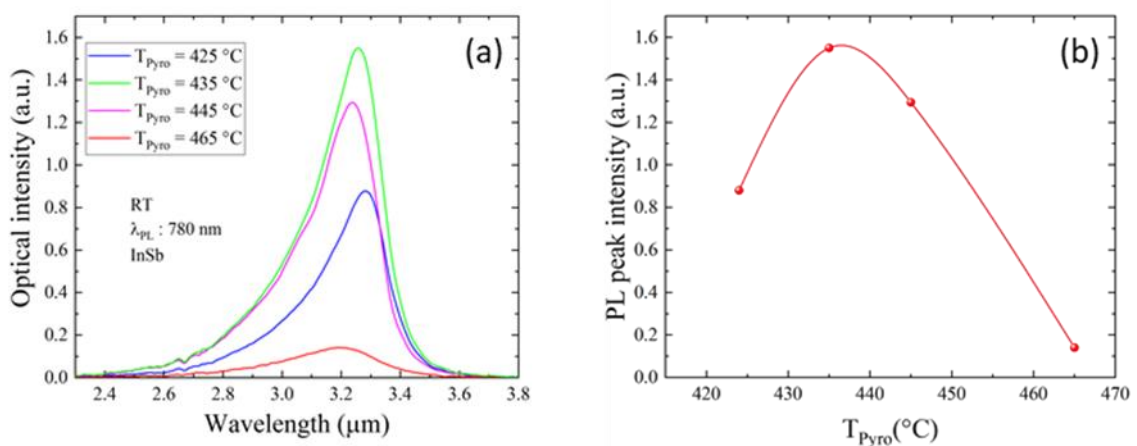


Figure II-4 - PL at RT for W-QWs grown at different temperatures. a) spectra. b) PL peak intensity

II.3.2 Epitaxy and structural characterization of ICL

The growths of ICL structures were performed on 2-inch (100)-oriented n-type GaSb substrates. After thermal de-oxidation at 550°C under Sb flux, the temperature was ramped down to 500°C to grow the n-doped GaSb buffer and the lower cladding layer. During the growth of the bottom-SCH the substrate temperature was ramped down to 435°C for the growth of the active region. Next, during the growth of the 400-nm-thick n-type GaSb upper-SCH, the temperature was ramped up to 490°C for the top cladding and contact layers. The claddings were n-doped with Te. The doping concentration was $1 \cdot 10^{17} \text{ cm}^{-3}$ close to the SCH, to reduce the optical losses [133] and was gradually increased to $2 \cdot 10^{18} \text{ cm}^{-3}$. The SCHs were low-n-doped ($5 \cdot 10^{16} \text{ cm}^{-3}$) also with Te.

The crystalline quality of the structures was evaluated by high-resolution X-ray diffraction (HR-XRD) using a PANalytical X'Pert3 MRD equipped with a PIXcel1D linear detector, an X-ray tube delivering the CuK α 1 radiation and a four-bounce asymmetric Ge (2 2 0) monochromator.

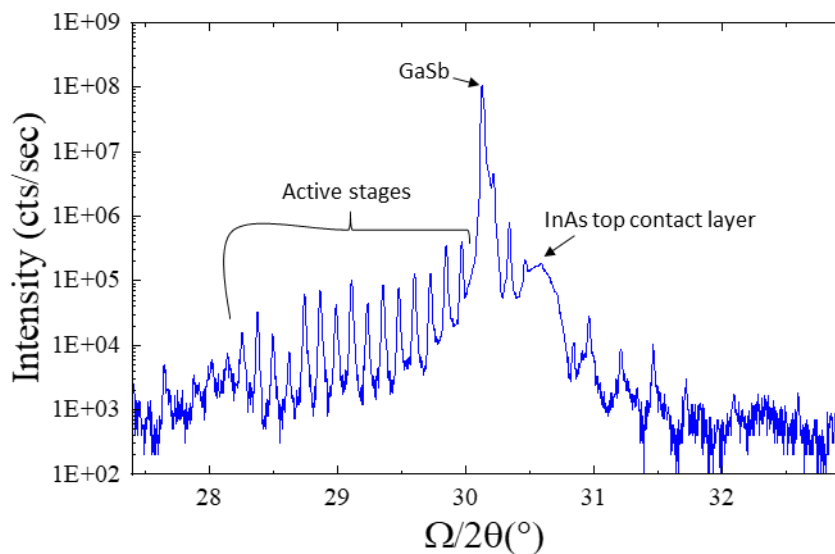


Figure II-5 - ω - 2θ HRXRD scans at the (0 0 4) reflection for a typical ICL structure.

The typical ω - 2θ patterns of a full ICL structure is shown in Figure II-5. The diffractogram depicts a peak at 30.36° corresponding to the GaSb substrate. A series of satellite peaks up to the 16th order is also shown arising from the periodicity of the stages of the IC active zone. The thickness of the IC active region extracted from the angle separation between the satellite peaks is 41.2 nm, in good agreement with the target value of 41.5 nm.

II.4 Technological process

Table 4 represents the synoptic of the technological process developed for the ICLs:

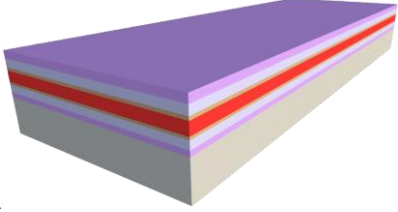
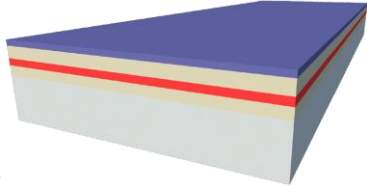
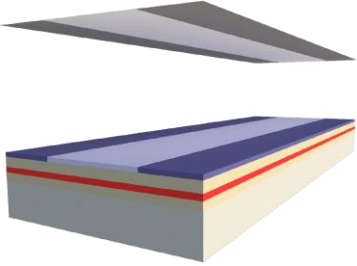
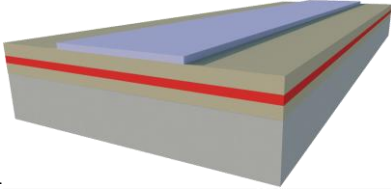
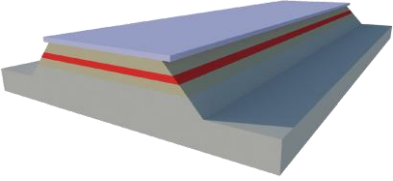
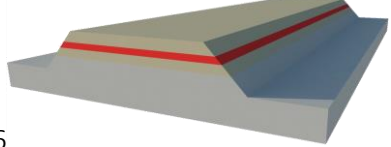
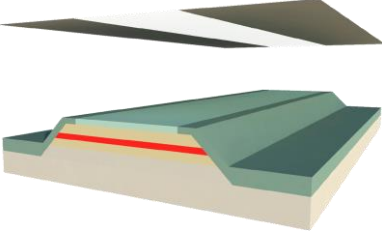
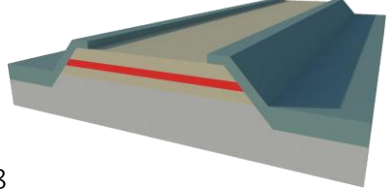
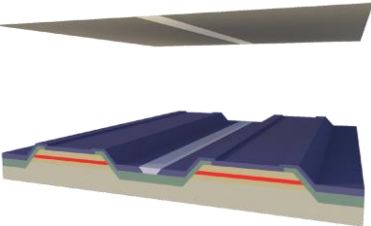
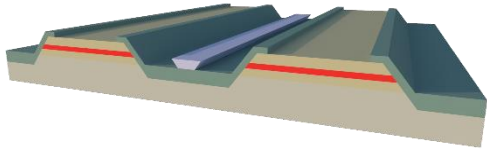
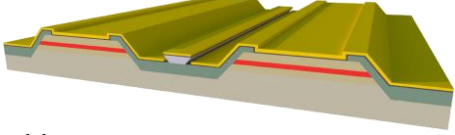
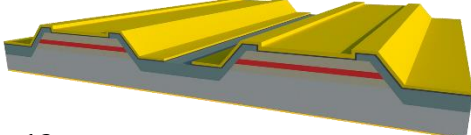
 <p>1</p>	<p>1 – Epitaxied ICL structure 2- Negative resist on the structure</p>	 <p>2</p>
 <p>3</p>	<p>3- Photolithography – etching mask 4 – Developing</p>	 <p>4</p>
 <p>5</p>	<p>5 – Etching for mesas ridges 6 – Resist removal</p>	 <p>6</p>
 <p>7</p>	<p>7 - Photolithography – isolation using photoresist 8 – Developing + baked @200°C – 2h</p>	 <p>8</p>
 <p>9</p>	<p>9- Photolithography – Metallization mask with 1 simple photoresist 10- Developing</p>	 <p>10</p>
 <p>11</p>	<p>11- Structure after metallization 12- Final devices</p>	 <p>12</p>

Table 4 - Complete technological process for the ICLs.

The descriptions and the optimizations of each step are detailed in the next paragraph.

II.4.1 Cleaning

After the growth, the 2-inch wafer is cleaved into pieces of approximately 1 cm x 1.5 cm. Then, the samples are cleaned with acetone, methanol, isopropanol and deionized water. If impurities persist on the sample, a second cleaning using reacting ion etching (RIE) with argon and oxygen is carried out with low RF power (50 W) to prevent damaging of the InAs cap layer. The cleaning step is followed by baking the sample at 120°C for 5 min. This bake is important to dehydrate the sample surface and facilitate the photoresist adhesion in the next steps.

II.4.2 Etching

Before the etching process, the ridge area is defined by UV photolithography. This technique is based on the exposition of a photo-sensible polymer (a photoresist) deposited on the sample. The UV insolation is realized through a mask which is partially metalized with chrome forming a pattern. The polymer molecules reached by the UV-light are altered to be more or less soluble in a developer. It depends whether the photoresist is positive (dissolve away the exposed regions) or negative (dissolve away the non-exposed regions). In our process, we used the AZ1518 positive photoresist. It was spin coated on the sample at 3000 rpm creating a ~2 μm thick photoresist film. Then, the sample was exposed to the UV light for 23 s with a MJB4 mask aligner. The ridge pattern consisted of eight periodic ridges of different widths: 15, 19, 23, and 27 μm. Then the UV-insulated parts of the resist were removed with AZ726MIF developer. After the ridge pattern development, we etched the sample using either wet (chemical) or dry (physical-chemical) etching.

II.4.2.1 Wet etching

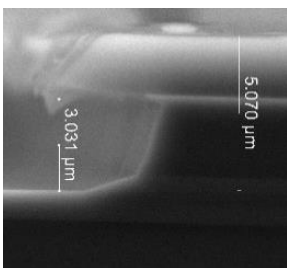


Figure II-6 - MESA ridge after wet etching process.

The wet-based etching process employs liquid etchants. The sample is immersed in a bath of the etchant, which reacts with the semiconductor by gradually removing the layers from the exposed surface. For the ICLs structures, we used two etchant solutions. The first one, a citric acid solution ($C_6H_8O_7:H_2O_2$ (1 : 1)) diluted 2:1 in deionized water, allows etching Indium-based materials. Indeed, citric-based solution is highly selective between InAs and GaSb [165]. The

kinetics of Sb-based material etching is so slow that the etching is stopped at the GaSb layer.

With the citric based solution, we removed the InAs cap layer in 13 seconds. The second etchant is based on chromic acid (CrO₃) and hydrofluoric acid (HF) solution. The concentration is HF(1):Cr₂O₃(1):H₂O(3) diluted 1:4 in deionized water. This solution, originally used to reveal dislocations in GaAs [166], has been adapted for the etching of Sb-based structures [167]. It etches mainly aluminum or gallium-based materials, but does not etch indium-based compounds. Table 5 shows the etching rates of these two solutions for the different materials of interest. Figure II-6 shows smooth and almost vertical walls in the upper cladding. When entering the SCH the etching rate decreases until it stops in the first layers of the active zone containing indium. The presence of AlSb/InAs chirped SL within the active region lies to a high in plane electrical conductivity, and therefore the lateral current spreading in ICLs is significant [15] [168], increasing the threshold current. Thus, an etching that allows to etch completely the active zone is mandatory, to constrain the current injection only on the laser ridge and reduce the laser threshold. In the laboratory, we do not have a solution which can etch with similar etching rates In-based and Al-based materials. For this reason, we have to use another etching technique to fabricate our lasers.

SOLUTION / MATERIAL	ETCHING RATE (nm/min)			
	InAs	InAsSb	GaSb	AlAsSb
Citric-based solution [169]	92.8 ± 2.8	88.9 ± 3.0	0.84 ± 0.04	-
Cr & HF-based solution [170]	125 ± 3	142 ± 4	3900 ± 100	12700 ± 700

Table 5 - Etch rates for the various materials and etchants.

II.4.2.2 Dry etching:

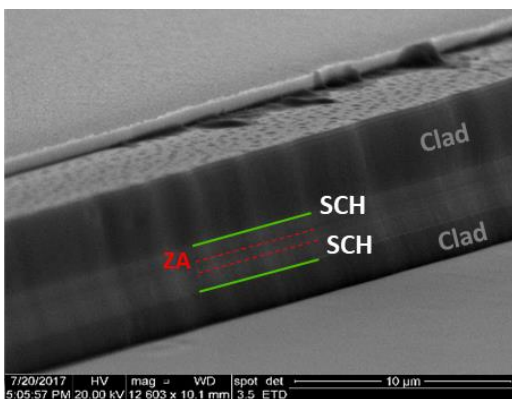


Figure II-7 - SEM picture of an ICL ridge performed by dry etching.

The whole etching could be performed in a single run through the active zone down to the bottom cladding by dry etching using AZ1518 photoresist mask. We studied the chlorine-based inductively coupled plasma reactive ion etching (ICP-RIE). This technique uses BCl₃ and Cl₂ chemistry combined with ion bombardment and physical desorption of Ar plasma as a key factor to control the etching characteristics of GaSb and/or relative

semiconductors [171]. In this process we used Ar: 6.5 sccm, Cl₂: 2 sccm and BCl₃: 4 sccm. The

pressure was 2 mTorr, the temperature was 10°C and the RF and ICP powers were 60 W and 300 W, respectively. The sample is adhered to the holder with thermal oil for efficient thermal contact. After 15 min of etching time, we get a 5.3 μm deep trench. Figure II-7 depicts a laser ridge fabricated with these dry etching conditions. The sidewalls and the etching surface are smooth with low roughness.

II.4.3 Passivation

After the etching, the ICLs are insulated with a dielectric material deposited by plasma enhanced chemical vapor deposition (PECVD). The deposition is achieved by introducing reactive gases between parallel electrodes, a grounded and a biased electrode. The capacitive coupling between the electrodes ignites a plasma, which induces a chemical reaction and results in the reaction product to be deposited on the substrate.

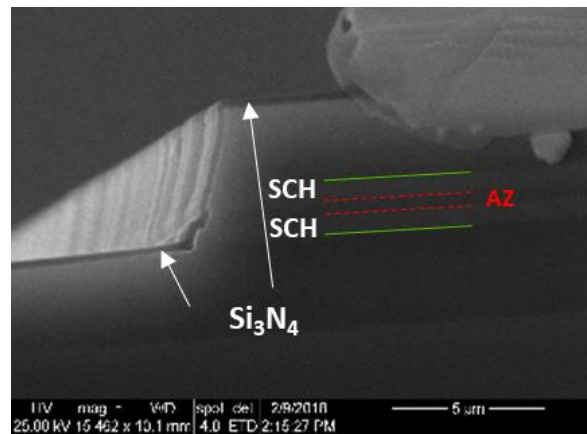


Figure II-8 - SEM picture of an ICL ridge formed by dry etching after Si₃N₄ deposition by PECVD

For the ICL, a 300 nm-thick Si₃N₄ layer is deposited at a temperature between 200°C and 280°C. The choice of Si₃N₄ over SiO₂ (also used for isolation) relies on the use of oxygen plasma which would strongly oxidize the walls surface. This oxidation would cause appearance of metallic antimony which will migrate to the surface resulting in short circuits or lateral leakage. Figure II-8 shows an ICL after deposition at 280°C of a conformal Si₃N₄ at a rate of 144 nm/min. The Si₃N₄ film outline perfectly the ridge structure even with under-etched side walls as depicted in Figure II-8. After the Si₃N₄ deposition, we carried out the second photolithography to perform the dielectric opening for the current injection contact. The patterning design was performed using the AZ1518 positive resist which was spin coated at 3000 rpm during 30s. The openings were narrower than the ridge width to prevent electrical short circuit and corresponds to 11, 15, 19 and 23 μm ridge widths from the narrowest to the largest ridge,

respectively. After the developing, CHF_3 based RIE process (pressure 13 mTorr, RF 40 W, CHF_3 100 sccm, and O_2 35 sccm) was carried out to etch the dielectric on the ridge. It is important to notice that during this work the PECVD found several problems. Thus, an optional way for the ridge passivation was to use directly the AZ1518 resist as displayed in Table 4 - Figure 7 and 8. This was baked in a furnace at 200°C for two hours after the developing.

II.4.4 Metallization

The next step is the metal deposition on the top of the ridge to ensure ohmic contact. Before the deposition of the contact the samples are de-oxidized in a 10 % diluted HCl solution. This step removes the native oxide formed on the semiconductor on the top of the ridge. Afterwards, we performed a second photolithography and then, a metal film was deposited over the entire surface of the sample. The unwanted parts were removed by eliminating the resist with a solvent. The resist removed the metal that have been deposited on its surface, leaving behind the desired metallic patterns on the ridge. This process is commonly called Lift-Off. When a photosensitive resist is used for the metallization mask, the polarity of the resist will have a significant influence on the efficiency of this process. Indeed, a negative resist will result in a profile with a negative slope reached by underexposing the photoresist (Figure II-9, exposition time t_1). This slope will be convenient for the lift-off creating a discontinuity of the deposited metal film as depicts Figure II-9, time t_1 . This discontinuity allows the solvent (usually acetone) to be in contact with the resist and dissolve it.

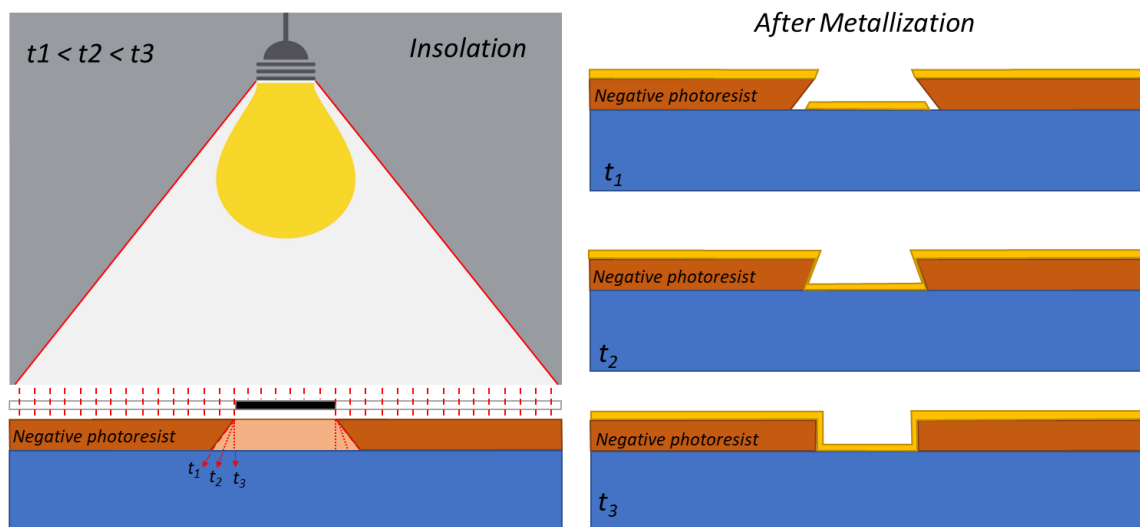


Figure II-9 - Photolithography with a single negative resist and profile after metallization as a function of insulation time.

Another factor to consider for a successful lift-off process is the metal deposition technique. In the laboratory, at the beginning of my thesis, we had only a sputtering available for metallization. This technique is a plasma-based coating method. Positively charged energetic ions from a magnetically confined plasma collide with a negatively charged target material. The material is then ejected (or “sputtered”) in atoms from the target (metal) and are deposited onto a sample. This technique is isotropic and allow to deposit metal in all directions making the lift-off more difficult.

A study of several types of photoresist-mask was carried out in order to choose the most suitable for the lift-off. Five samples were processed using five different resist masks and the same chromic mask design.

The first two samples were treated using single layers of AZ2020 and AZ2070 photoresists. The other three samples employed bilayer resists with different sensitivities to obtain a more inclined profile mask. For the bilayers, the first spun resist was always the LOR5A which is sensitive only to the contact with a developer. The second layers were negative photosensitive resists for each sample: AZ2020, AZ2070 and AZ5214 respectively. All resists were spin coated at 4000 rpm during 30 s with the photolithography parameters shown in Table 6.

The SEM pictures **a.** and **b.** in the Table 6 depict the mask profiles with a single photoresist layer, AZ2020 and AZ2070 respectively. In those two cases, there is no metal discontinuity even with a thinner metal thickness on the side walls resulting in an unreliable lift-off.

When we used a bilayer resist mask as presented in Figures **c.**, **d.**, and **e.** in Table 6, the width of the dissolved resist after the developing was different for each layer resulting in a cap-shaped mask profile. Since the shape is mainly driven by the difference in the development of each resist, it is better to overexpose the sample during the photolithography as explained in Figure II-10 time t_3 . Even if Figure c. in Table 6 shows a very thin metal film on the profile wall on the bilayer with AZ2020 photoresist, we obtained a successful lift-off for all three bilayer masks. Thanks to the cap-shaped geometry, the metal film deposited was more discontinuous as the photoresist thickness increased as shown in the Figures c., d., and e. in the Table 6. However, a thick photoresist reduces the resolution of the deposited metal as in the case for the bilayer using AZ2070 photoresist.

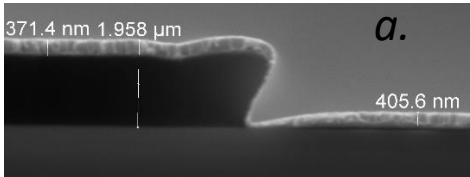
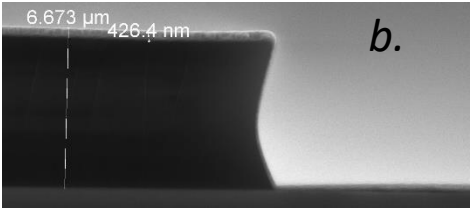
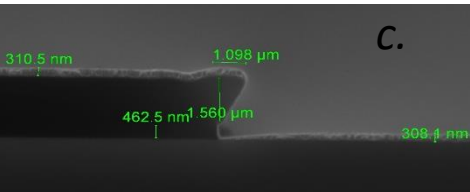
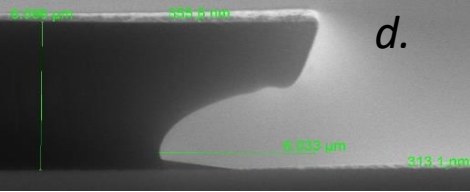
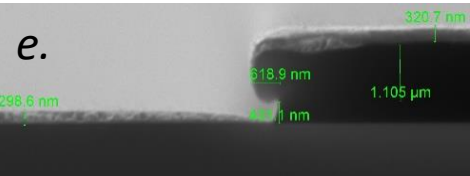
Resist	Bake	UV time	Developing time	Profile
AZ2020	1 min @110°C Before and after insolation.	6 s	1 min 45 s	
AZ2070	1 min @ 110°C Before and after insolation.	9 s	1 min 30 s	
LOR 5A + AZ2020	2 min @ 180°C - LOR5A. 1 min @110°C AZ2020 + 1 min @110°C AZ2020 after insolation	8 s	2 min 15 s	
LOR 5A + AZ2070	2 min @ 180°C - LOR5A 1 min @ 110°C AZ2070 + 1 min @ 110°C AZ2070 after insolation	10	2 min 30 s	
LOR 5A + AZ5214	2 min @ 180°C - LOR5A 1 min @ 110°C AZ5214 Insolation 1 min @ 110°C Insolation flood exposure	8 s + 1 min flood exposure	1 min 5 s	

Table 6 – Metallization masks

The choice then rested between the bilayers using AZ2020 or AZ5414 on the mask that provides the best resolution. As in the method using AZ5214 photoresist there is an extra step with flood exposure, our choice for the mask for the metallization was the bilayer LOR5A and AZ2020 displayed in Figure C in Table 6. The top contact layer is made of n-type InAs. Thus, after the lift-off process, the deposition of 20 nm of Ti for adhesion layer, followed by 300-nm-thick Au leads to a very low ohmic contact resistance [172].

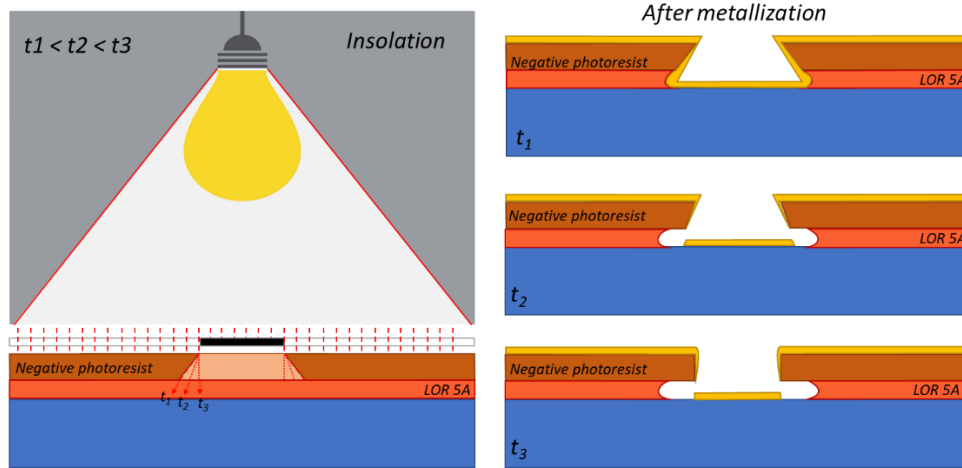


Figure II-10 - Photolithography with a bilayer LOR5A and a negative resist and mask profile after metallization (sputtering) as a function of insulation time.

II.4.5 Polishing and bottom contact

The top contact deposition is then followed by the thinning of the substrate and the deposition of the bottom contact. The substrate is thinned to ease the cleavage along [011] crystalline axis and to form the mirror facets on each side of the ridge. Initially the substrate is 550 μm thick and is polished down to 150 μm . Then the GaSb substrate is de-oxidized with HCl before the bottom contact metallization. In this case, the junction between the metal and the n-GaSb forms a Schottky barrier as depicted in Figure II-11(a). This increases the voltage required to reach current flowing. The influence of this barrier can be reduced by heavily doping the semiconductor improving the carrier flow by electron tunneling. Unfortunately, the doping of GaSb with Te, is limited to $2 \cdot 10^{18} \text{ cm}^{-3}$ [173]. To get an ohmic contact, it is necessary to anneal the sample after metallization. The annealing allows the metal diffusion into the semiconductor, creating an overdoped layer on the surface which reduces the potential barrier at the metal-semiconductor interface as shown in Figure II-11(b). Previous studies have established that Pd/AuGeNi allows an ohmic contact with a resistivity as low as $5 \cdot 10^{-6} \Omega \text{ cm}^2$ [111] on N-type GaSb. Thus, the substrate was coated with 5 nm of Pd and 200 nm of AuGeNi alloy. Then the sample was annealed at $\sim 200^\circ\text{C}$ during 30-60 s. The annealing completion can be directly observed under the microscope with the tarnishing of the metal color.

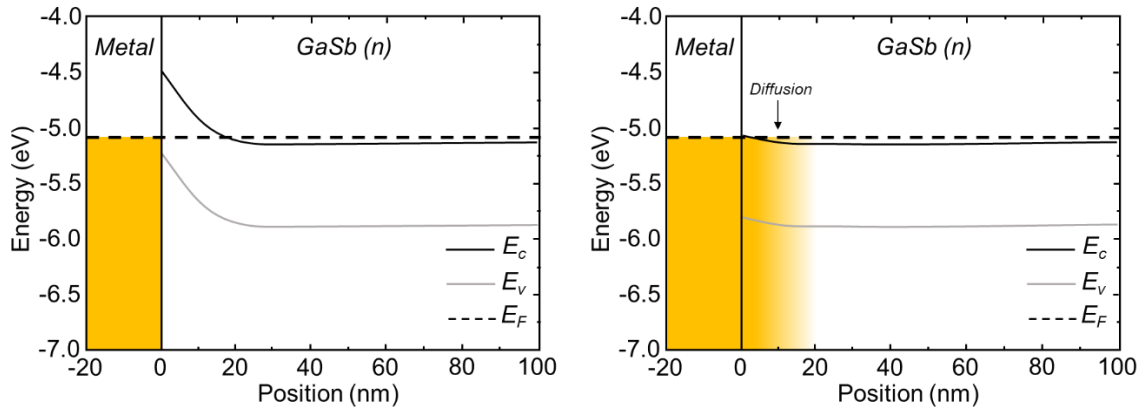


Figure II-11 – Scheme of the band structure of the metal- GaSb(n) interface a) before and b) after annealing.

II.4.6 Mounting and top contacting

Finally, the structures are cleaved forming the laser facets perpendicular to the mesas with different length ranging from 1 to 4 mm. Afterwards, the devices are separated for mounting. They are then soldered epi-side "down" with indium on a copper plate to promote the heat dissipation from the ICL [174]. A pad of gold-plated alumina is placed on the copper plate to connect the other contact. Then, 50 μm diameter gold wires were bonded between the bottom contact of the device and the alumina pad. Pictures of an ICL mounted is depicted in Figure II-12.

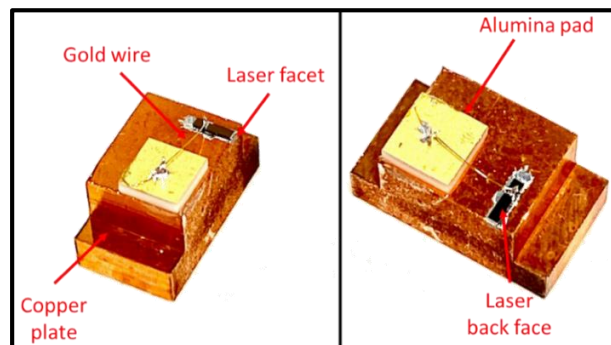


Figure II-12 - Epi-side down ICL mounted in a copper plate.

II.5 Characterizations of ICLs

Until now, we have detailed the key elements of the design and process of ICLs for emission at 3.3 μm at RT. In this section, we will present the electro-optical characterizations of ICLs, such as threshold current density, threshold voltage, characteristic temperature (T_0), emission wavelength, internal losses (α_i) and internal quantum efficiency (η_i). The first measurements are carried out in pulsed regime on broad area (100 μm wide-ridges) ICLs to avoid thermal issue

and determine the real properties of the devices. Pulse widths between 100 ns and 1 μ s at frequencies between 10 and 100 kHz were used. No change in threshold or quantum efficiency was observed over these pulse ranges. Various structures and designs will be studied and simulated using Nextnano software in order to improve the ICL performances.

II.5.1 Studies and improvement of the IC active region

II.5.1.1 First ICL structure (ICL A)

The design and the HRXRD of this structure were given in the paragraph II.3.

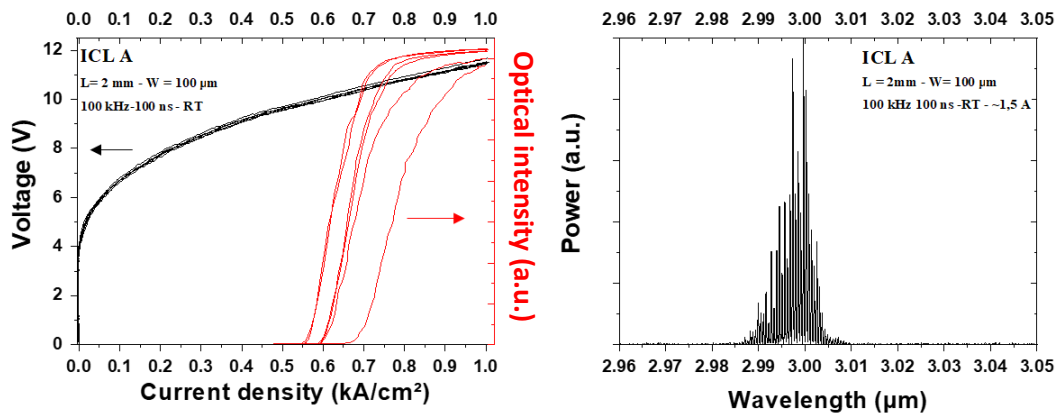


Figure II-13 - (a) Pulsed (300 ns/100 KHz) light-current-voltage characteristic of a 2-mm-long ICL and (b) Laser emission spectra both from ICL A.

The ICL A was processed in broad-area 100- μ m-wide ridges and cleaved into 2 mm long cavity. The ICLs were characterized in pulsed mode (100 ns pulses, 100 kHz repetition rate) at RT. The optical intensity was measured with a cooled InAs-based photodetector. Figure II-13(a) shows light-current-voltage (L-I-V) characteristics of a set of six ICLs, whereas Figure II-13(b) displays the emission spectrum. The average threshold current density was around 0.6 kA/cm² with a minimum of 0.55 kA/cm², a value 3 times higher than the state of the art [15]. The threshold voltage is $V_{th} = 9$ V which is 3.1 times higher than the theoretical value at 3 μ m ($V_{th} = \hbar\omega \times 7 \sim 2.89$ V). This value corresponds to a voltage efficiency of 32 %, well lower than 80 % usually obtained in ICLs [101]. The series resistances is around 4.3 Ω which is higher than the typical value for GaSb laser with AlGaAsSb cladding layer (1.8 Ω) [160]. The saturation of the optical intensity observed in Figure II-13 is due to the measuring InAs photodetector device. The emission wavelength is $\lambda = 3$ μ m which is 10% shorter than the targeted wavelength. Despite the higher threshold current and voltage and the blue-shifted wavelength, these results were a very encouraging starting point for the comprehension of ICL design. The next

paragraphs will be dedicated to the analysis of the obtained results and the consequent optimization of the design.

II.5.1.2 Voltage drop issue

In ICLs structures, the majority of the potential drop occurs in the active region and is proportional to the energy of the emitted photon and the number of QW stages. Thus, to better understand the operation of our devices, we used Kelvin Probe Force Microscopy (KPFM) technique to visualize the special profile of the voltage drop across the structure. In this technique, an AFM tip, performs two scans on the cleaved facet of the sample. During the first pass, a topographic measurement is performed. Once the topography has been recorded, the sample is placed at a given distance. The surface is scanned at this height, reproducing the topography acquired during the first pass. In this way, only the variations due to applied potential are measured.

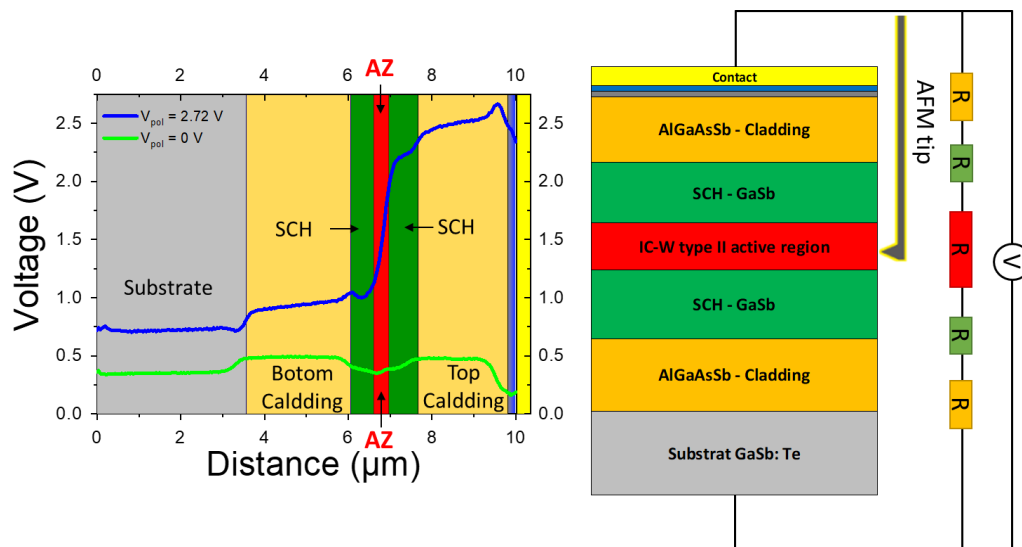


Figure II-14 - KPFM voltage characterization performed in a facet of the ICL.

Figure II-14 depicts both a schematic diagram of the measurement and the obtained results for the ICL with and without bias below the threshold voltage ($V = 2.72$ V). When the laser structure is biased, the bands bend modifying their work function. We can thus measure the potential difference at each layer composing our structure. Although, the applied voltage was below the threshold voltage (2.7 V) the voltage drop found is 1.5 V. The results obtained are therefore purely qualitative since the surface states modify the measurement of what really happens in the volume. However, these results clearly show that most of the potential drop occurs in the active zone as displayed in Figure II-14.

For better understanding, it is interesting to explore the band structure diagram of the whole active region. It is divided in 3 parts: the input transition region, the active stage and the output transition region. In our ICL, the input transition region connecting the GaSb SCH and the first cascade is composed of InAs/AlSb layers where the AlSb is 12 Å thick and the InAs (Si doped to $5.10^{18} \text{ cm}^{-3}$ to rebalance carriers on the first stage of the AZ) thickness is increased from 10 Å to 17 Å with a step of 1 Å in order to shift the electronic level down to the W-QW. The output transition region is made with the same design that the electron injector and three InAs layers with thickness of 16 Å, 13 Å and 10 Å separated with 12 Å of AlSb layers. The active region and the calculated module square of the wave-function of the structure under an average applied voltage of 90 kV/cm ($\hbar\omega / 41.85 \text{ nm}$) are shown in Figure II-15. It represents three active stages instead of seven for sake of clarity.

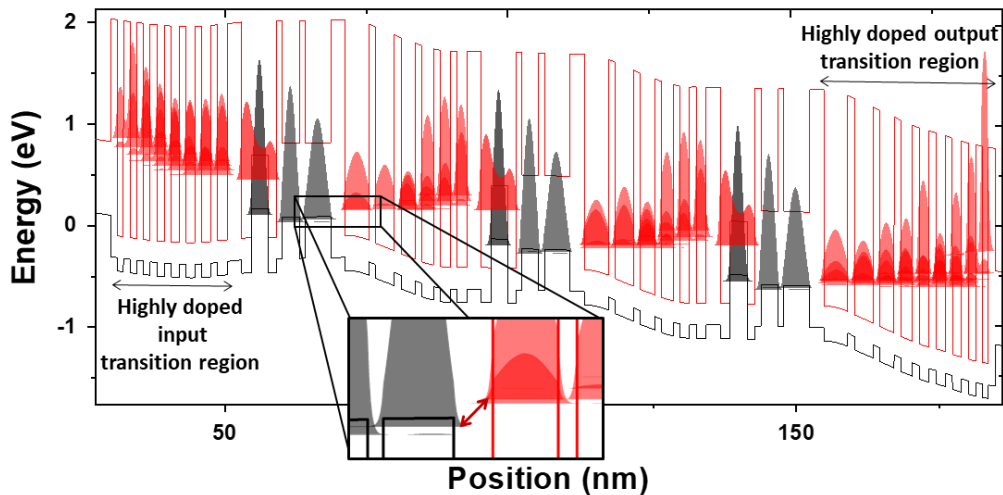


Figure II-15 - Band structure simulation of an extended active zone design of the ICL A. The simulation was done with an electric field of 90 kV/cm and the transition region has been doped at $5.10^{18} \text{ cm}^{-3}$

The simulation revealed a defect of this design as illustrated in Figure II-15. Due to the heavy doping within the input transition region ($5.10^{18} \text{ cm}^{-3}$). The bands are significantly bended in this zone and the semimetallic interface is misadjusted as illustrated in the inset in Figure II-15. Indeed, the electron level of the semi-metallic interface is above the hole level just before. This misalignment prevents the electron-hole generation and consequently the carrier transport. For this reason, an additional bias is required to align the semi-metallic interface, which occurs at the average electric field of 238 kV/cm corresponding to 7 V applied to the entire structure. The real threshold voltage is even larger (9 V) due to the high series resistance of the device as depicted in Figure II-13.

II.5.1.1 ICL with improved voltage drop

To verify this hypothesis, a simulation of a new structure without doping of the InAs layers within the transitions region is presented in Figure II-16. For an average electric field of 90 kV/cm, the electron and hole levels next to the semi-metallic interface are aligned which should allow a correct carrier generation.

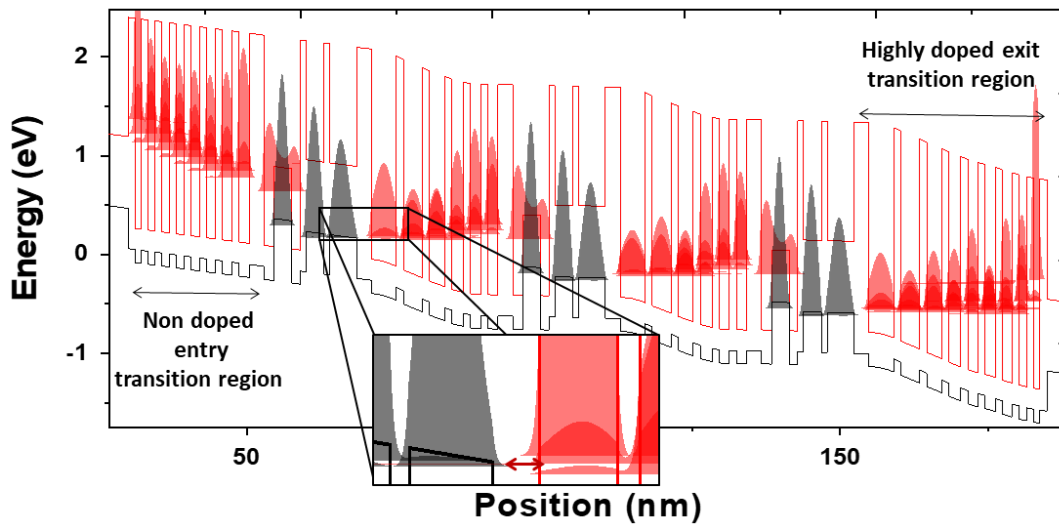


Figure II-16 - Band structure simulation of a new extended active zone design of the ICL A. The simulation was done with an average electric field of 90k V/cm and the input transition region without doping.

This new ICL structure, the ICL B, is similar to the ICL A except that the input transition region was undoped. The L-I-V performances of broad area laser in pulsed regime at RT are reported in Figure II-17(a). The threshold current density is 700 A/cm². However, the threshold voltage is 5 V, a value well lower than obtained with ICL A. Following this optimization, all the consequent ICL structures presented in this work will have undoped input transitions region.

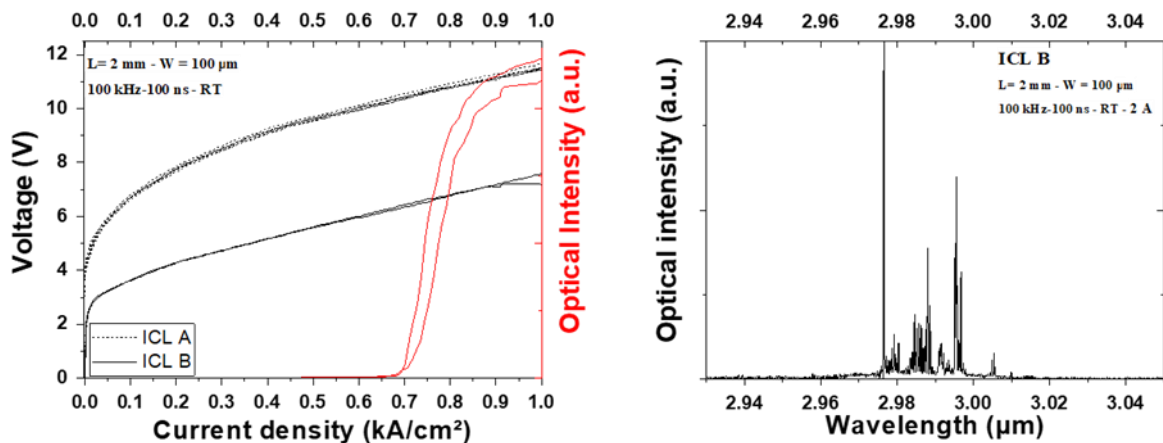


Figure II-17 - (a) Pulsed (300 ns/100 KHz) current-voltage comparison between ICL A and B. (b) Pulsed Light-current characteristic of a 2-mm-long ICL from ICL B and its (b) laser emission spectra.

Despite the electrical improvement, this structure still emitted at 3 μm as presented in Figure II-17(b).

II.5.1.2 Emission wavelength shift

This section is devoted to investigate the origin of the blue shift wavelength. First, it was necessary to ensure that the transition between spontaneous and stimulated emission remained consistent. For this purpose, emission spectra of the ICL A were measured from currents below threshold to above. The electro-luminescence peak was observed around 3 μm as shown in Figure II-18 and the intensity increases with the current. A slight redshift related to the band gap variation with temperature generated by the current increase is also observed. No electroluminescence around 3.3 μm was observed. This demonstrate that recombination occurs at the same position but with no evidence of the emission from the active QWs.

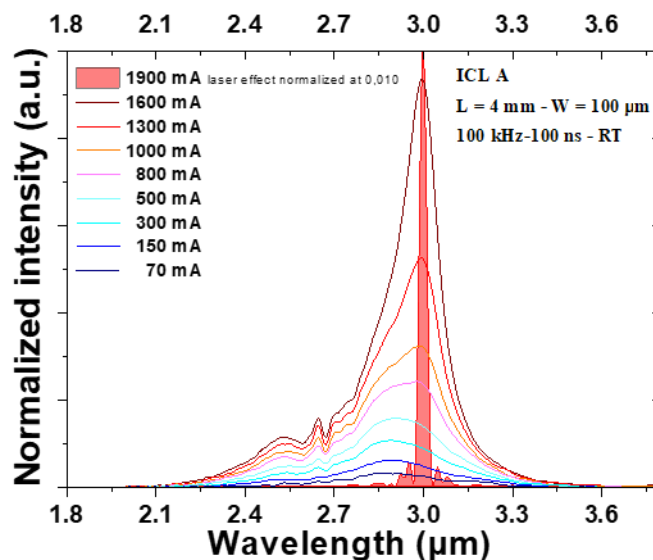


Figure II-18 - Spontaneous emission and laser emission spectra from ICL A.

To clarify whether the laser emission occurred from the W-QWs, a third structure was grown similar to the ICL B, except for the thickness of the InAs within the W-QWs. In this structure, named ICL C, the thicknesses of these InAs layers were increased to 19 and 16 \AA . The calculation of the transition with these thickness gives an emission at 3.7 μm .

Figure II-19 shows the emission spectra of ICLs B and C. As we can see, the ICL C, with thicker InAs electron-QWs, emitted at 3.21 μm which is longer than for the ICL B ($\lambda = 2.99 \mu\text{m}$), but still less than the expected value.

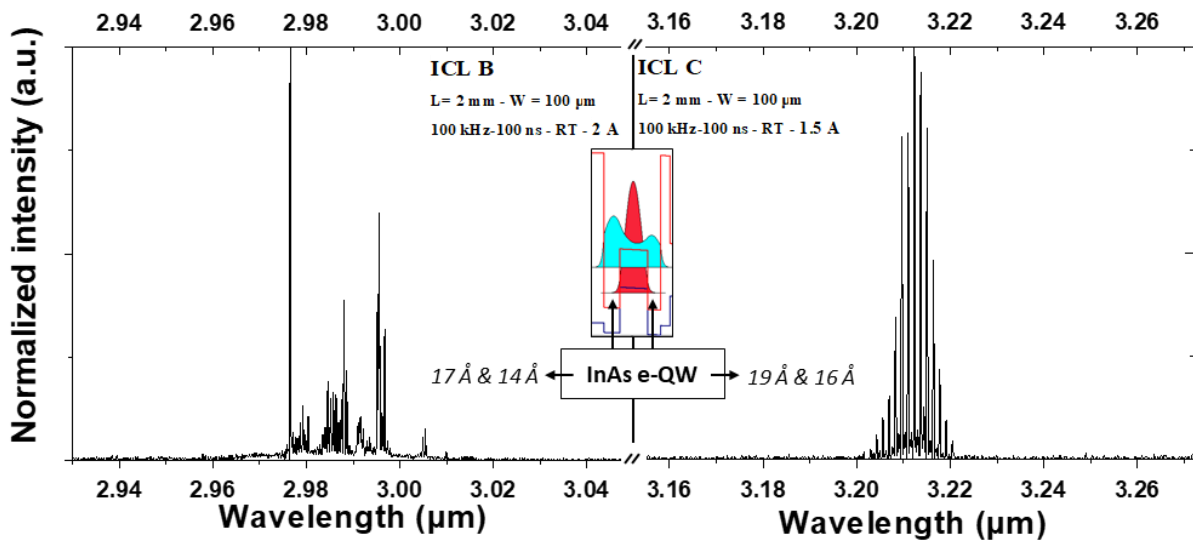


Figure II-19 - Emission spectra of (a) ICL B with InAs electron-QW thicknesses of 17 & 14 Å and (b) ICL C with InAs electron-QW thicknesses of 19 & 16 Å

Since the only variation between the two structures was the InAs electron QW thicknesses within the “W” region, we can conclude that the recombination occurs well within the W-QWs. Although the wavelength was increased, the origin of the blue shift was still unclear.

Since the problem is not from the W-QWs, we studied the electron injectors. As it was discussed previously, the doping level in the electron injector is a key parameter for the ICL performance. Following the rebalancing concept, the electron injectors of the ICLs A, B and C were highly doped ($5 \cdot 10^{18} \text{ cm}^{-3}$). To verify the influence of this doping on the ICL performance a new structure, the ICL D, was grown with a lower doping concentration ($5 \cdot 10^{17} \text{ cm}^{-3}$) within the electron injectors. The W-QWs thickness remained the same as A and B ICLs.

Figure II-20 shows the HR-XRD of the four structures. It is interesting to see that the full width half maximum (FWHM) of the satellite peak related to the periodicity of the active region presents a larger value (~ 81 arcsec) for A, B and C structures than the ICL D (~ 61 arcsec). This could be attributed to a higher roughness at the numerous interfaces within the active stage when high doping concentration is used in electron injectors.

After the processing, electro-optical measurements were performed in pulsed mode. The Figure II-21 shows a comparison between B and D structures. Despite the fact that the W-zone had exactly the same thickness, the wavelength emission of the ICL D was 3.3 μm.

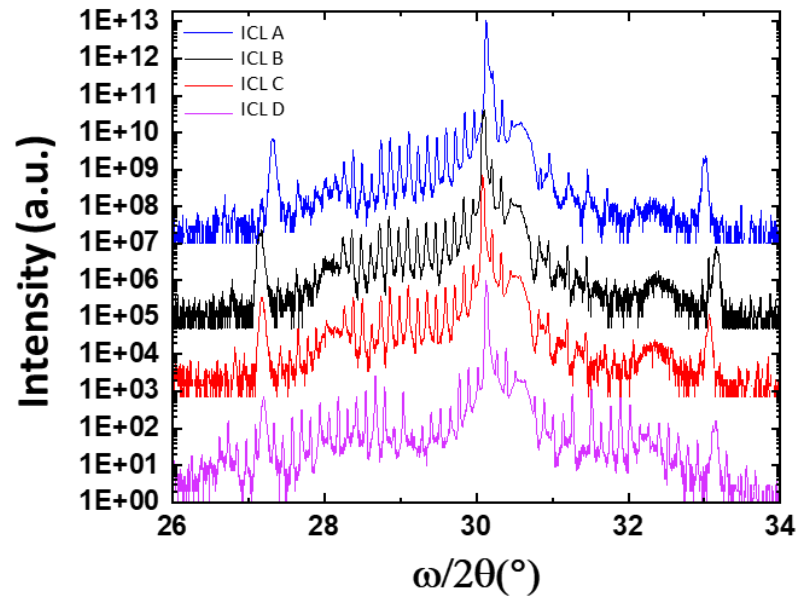


Figure II-20 - ω - 2θ HRXRD scans at the (0 0 4) reflection for the ICLs A, B, C and the most important D

Nevertheless, this structure exhibited higher threshold current densities and voltage thresholds, which can be attributed to the lower doping level and the efficiency of the rebalancing carrier concept.

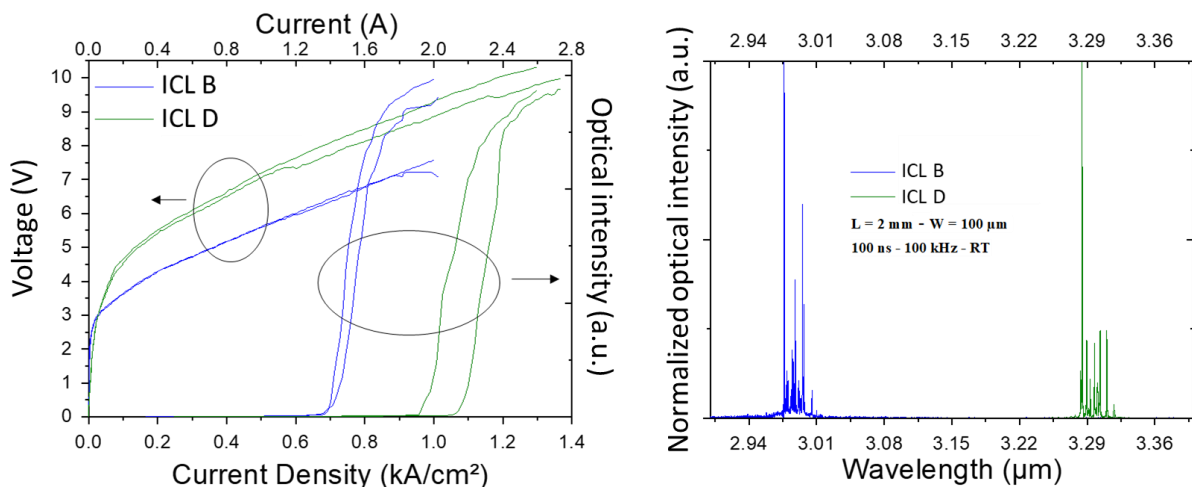


Figure II-21 - (a) Pulsed (300 ns/100 kHz) Light-current-voltage comparison between ICL B and D and (b) their laser emission spectra.

We can observe that the structure with high doped electron injectors provides better performances, however the origin of the shift of the wavelength emission with the doping level is still unclear. For these reasons, we studied the effect of the growth conditions on the laser performances.

II.5.1.3 Influence of the top cladding temperature.

The large difference between the optimal growth temperature of the cladding layer material (490°C) and the underlying active region (435°C) along with the high doping concentration in the second case can affect the electro-optical behavior of the ICLs. To investigate this point, four different structures (E, F, G and H) were grown with substrate growth temperatures of the top cladding layers respectively at 490°C, 475°C, 460°C and 435°C. In these four structures, the four inner InAs QWs within the electron injectors were highly doped ($5 \cdot 10^{18} \text{ cm}^{-3}$) with Si.

The ω -2 θ HRXRD patterns for these four structures are shown in Figure II-22 together with the simulated curve. The cladding layers are lattice matched except for the one grown at the lower temperature due to a lower As incorporation. A slight shift of the satellite peaks toward tensile strain when the top cladding layer temperature increases was observed. This can indicate an intermixing of the InSb bonds with respect of the AlAs bonds that exists at AlSb/InAs interfaces. The inset displays the FWHM averaged of the 10 satellite peaks closest to the substrate. The narrower satellite peaks are achieved for the samples grown at the lowest temperature which indicates more homogeneous interfaces within the IC-active region.

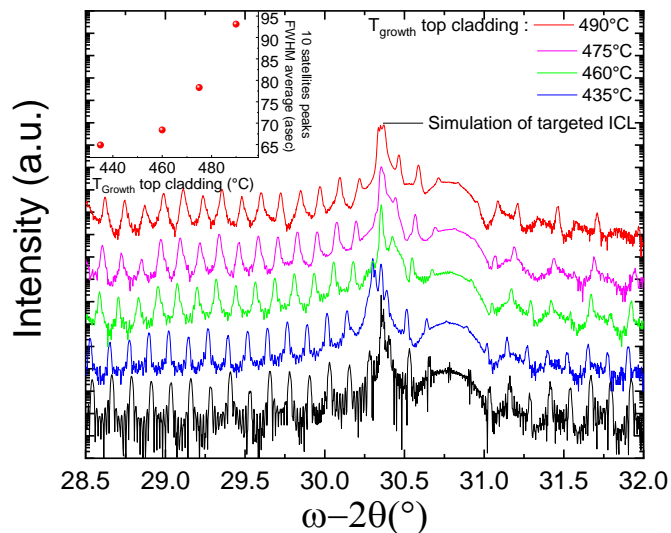


Figure II-22 – ω -2 θ HRXRD scans at the (0 0 4) reflection for the ICL structures with top cladding layers grown at different temperatures and simulation of the targeted ICL. Inset: Evolution of the average FWHM value of the satellite peaks versus the substrate growth temperature of the top cladding layers.

Pulsed P-I and optical characteristics (Figure II-23) of broad area ICLs (100 μm x 2 mm) displayed a typical threshold current density of 690 A/cm² and a laser emission around 2.98 μm (as the ICL A and B) for the laser whose top cladding layer was grown at 490°C (Structure E).

We then observed a clear redshift of the emission wavelength and an improvement in the performance of the lasers as the upper cladding layer growth temperature decreases. When the latter is 435°C, the threshold current density decreases down to 220 A/cm² while the emission wavelength shifts up to 3.3 μm, the target wavelength. This performance is comparable to the best threshold current densities obtained with state-of-the-art ICLs with a similar emission wavelength but based on AlSb/InAs cladding layers (150-200 A/cm²) [175].

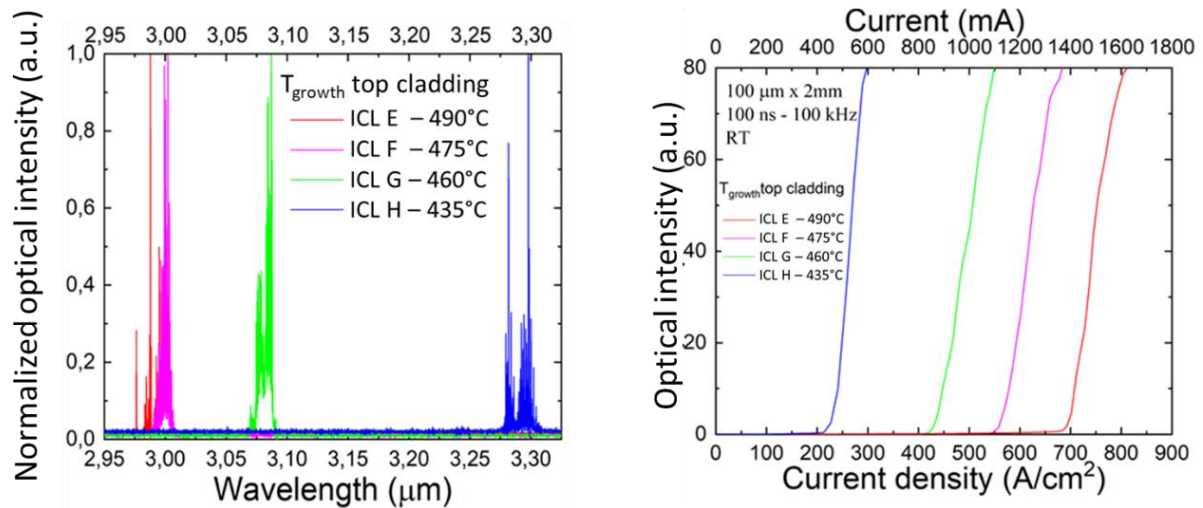


Figure II-23 - Electro-optical properties of 100 μm x 2 mm ICLs with top cladding layers respectively grown at 490°C (red), 475°C (purple), 460°C (green) and 435°C (blue). (a) Laser emission spectra. (b) Light-current characteristics in pulsed injection regime.

Figure II-24(a) summarizes the evolution of the threshold current density and emission wavelength with the growth temperature of the top cladding layer. The threshold current density increases linearly with the growth temperature. The latter observation along with the interface non-homogeneity seen by HRXRD could be explained by atom intermixing at the numerous InAs/AlSb and InAs/GaInSb interfaces of the active region. Such behavior has already been reported for “W” QWs active zones grown at different temperatures [176].

We show in Figure II-24(b) the band diagram and the energy position of electron and hole levels of the “W” QWs without (b1), with 0.5 nm (b2) and with 1 nm (b3) broad intermixing at the interfaces. For this simulation, we assumed a linearly gradual composition of AlInAsSb between AlSb and InAs and GaInAsSb between InAs and Ga_{0.65}InSb. In the structure with sharp interfaces, the transition energy corresponds to the emission wavelength of 3.3 μm.

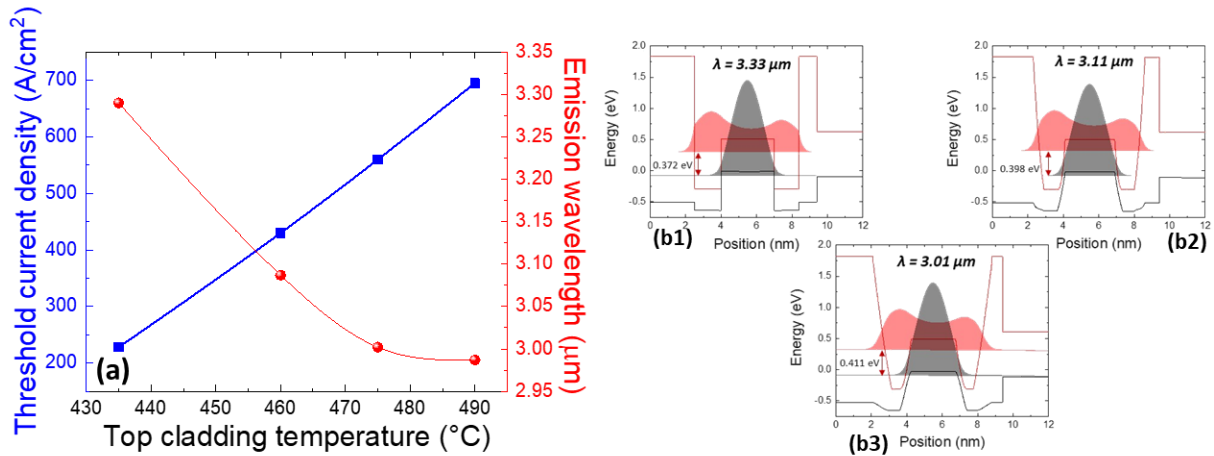


Figure II-24 - (a) Evolution of the threshold current density and emission wavelength with the growth temperature of the top cladding layer. (b) Calculated band alignment and wavefunction of the type-II "W" AlSb/InAs/GaSb/InAs/AlSb QW used in the ICL, without (b1), with 0.5 nm (b2) and 1 nm (b3) broad intermixing at the interfaces

Assuming a 0.5 and 1-nm broadening of the interfaces [177] due to the intermixing leads to a shift of the quantum levels within the QWs that results in an emission wavelength of 3.11 and 3 μm, respectively. We believe that intermixing also affects the injector regions thus modifying their band structure, which results in decreasing injection efficiency and high threshold current density. These simulations are consistent with the data measured but do not explain the involvement of doping in the wavelength blue shift compared in ICLs B and D. It could be that the dopant may segregate or diffuse at high temperatures (> 435 °C) activating or somehow increasing the atom intermixing at the interfaces. Therefore, this effect would only occur at high growing temperatures. Having reached value close of the state of the art for threshold current density the state of the art of ICLs by the proper choice of the growth temperature, we have then extracted the characteristic parameters of the best ICL.

II.5.1.4 Properties of broad area ICLs with optimized growth temperature.

The epitaxial structure with the top cladding grown at a substrate temperature of 435 °C (ICL H) was cleaved to form 2, 3 and 4-mm-long cavities to determine internal losses (α_i) and internal quantum efficiency (η_i).

The measurements were performed in pulsed regime (300 ns/100 kHz) at 25 °C. The optical power was measured with a power meter placed in front of the ICL.

Figure II-25(a) presents typical L-I-V characteristics of the 2-mm-long lasers. The I-V curve shows a threshold voltage of 3.8 V which exceeds the theoretical value by only 1.2 V corresponding to a voltage efficiency of 68%. The series resistance is in the range of 1-2 Ω , comparable with published results on ICLs emitting in the same wavelength range.

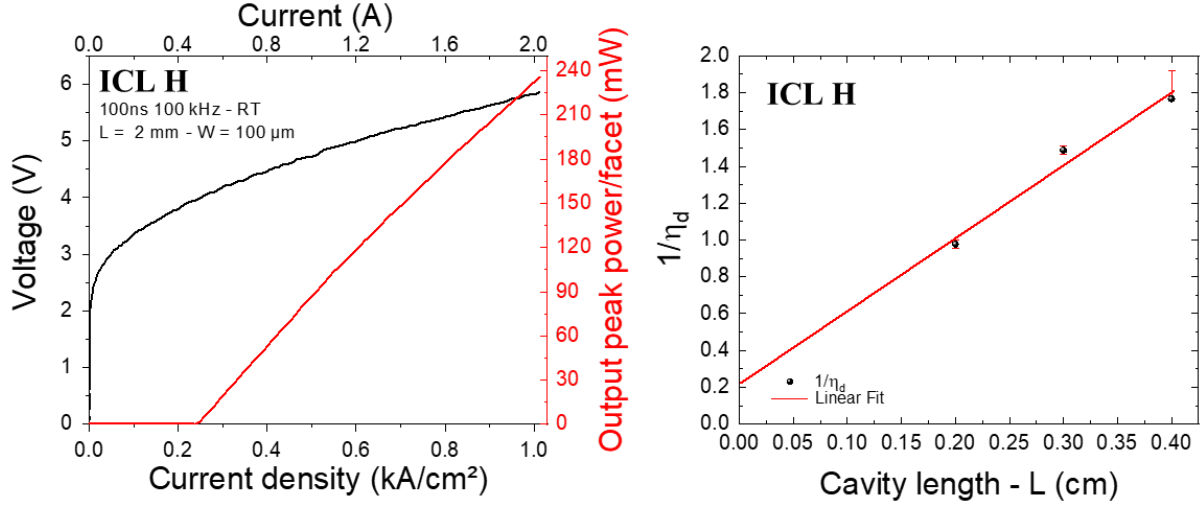


Figure II-25 - (a) Pulsed (300 ns/100 kHz) light-current-voltage characteristic of a 2-mm-long 100- μm -wide laser at 25°C. (b) Reciprocal differential quantum efficiency versus the cavity length in pulsed regime (300 ns/100 kHz) at 25°C. Each datapoint represents averaged measurements from several devices (4-5) except for the 4 mm cavity length which only features the 2 best results

The reciprocal differential external quantum efficiency ($1/\eta_d$) is shown in Figure II-25(b) as a function of the laser length (L). From the well-known relation:

$$\frac{1}{\eta_d} = \frac{1}{\eta_i} + \frac{1}{\eta_i \cdot \ln\left(\frac{1}{R}\right)} \alpha_i L \quad (2.1)$$

where L is the cavity length and R is the facet reflectivity ($R = 0.31$), the value of η_i and α_i are extracted to be 65% per stage and 15 cm^{-1} , respectively.

The η_i value is close to those reported for ICLs with AlSb/InAs claddings whereas α_i is higher than the values typically measured on ICLs [101], [178]. The origin of those high internal losses is not well understood and could be due to a stronger absorption in the n-type $\text{Al}_{0.85}\text{Ga}_{0.15}\text{As}_{0.06}\text{Sb}_{0.94}$ cladding layers compared with superlattice claddings material typically used for ICLs. Indeed, the Te-doped AlSb presents a strong absorption between 3 and 4 μm since Te is considered to act as a shallow donor [179], [180]. A thicker GaSb SCH layer could be employed to reduce the overlap between the optical mode and the cladding layers and thus to decrease the waveguide loss [106], [107].

II.5.1.5 Performances of narrow ridge ICL with optimized growth temperature.

The ICL H was also processed in narrow ridge. Figure II-26(a) shows the electro-optical characteristics of a 19 μm wide-ridge and 3 mm long cavity ICL soldered epi-side down. CW operation was achieved up to 55°C with a maximum output power of 10 mW/facet at 17°C. The threshold voltage was 4.9 V and the series resistance was 5.3 Ω . Figure II-26(b) shows emission spectra the lasing wavelength measured at various temperatures and current. The ICL was multimode and emitted between 3.25 and 3.42 μm at temperatures ranging from -3 to 55°C, respectively.

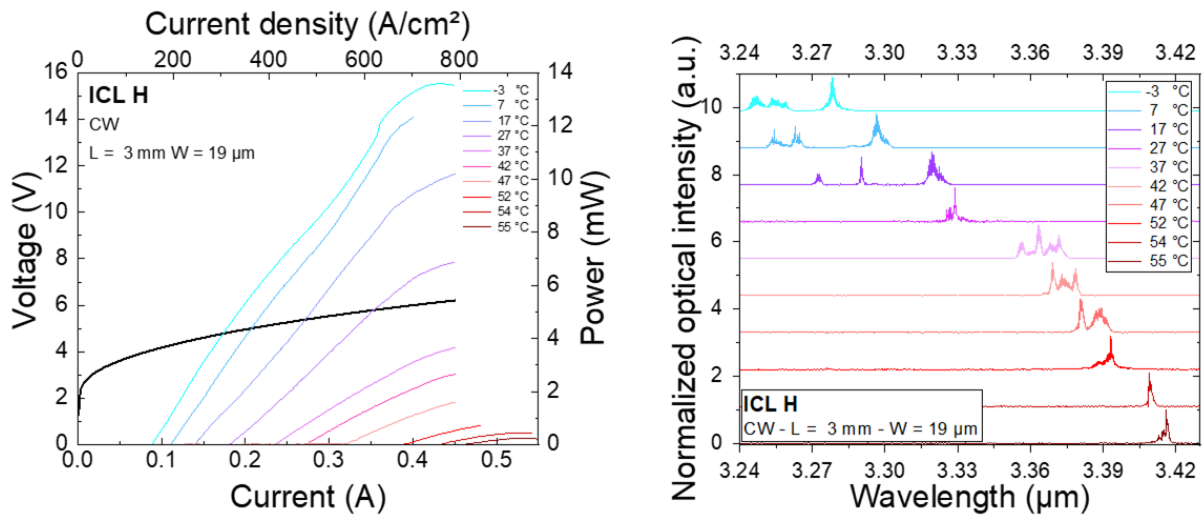


Figure II-26 - (a) CW light-current-voltage curves at different temperatures between -3°C and 55°C from a 19 μm ridge width and 3 mm long cavity of the ICL H with AlGaAsSb cladding layers and (b) their associated spectra.

Within the framework of the MIMIC-SEL project a piece of this structure was processed at LAAS. The process was similar to that developed during this work; except they can get narrower ridge width. Figure II-27 presents a SEM micrograph of the ICL after processing. The different layers can be clearly identified. A magnification on the active region shows the seven active stages.

Figure II-28(a) shows the L-I-V curve of a 7 μm x 2 mm ridge laser mounted epi-side down. The ICL operated up to a heat sink temperature as high as 80°C limited by the used set up. The maximum output power could not be measured for mount temperatures above than 60°C because of the limitation of the power supply to 8V, but it exceeded 12 mW/uncoated facet and 10 mW at 20°C and 40°C, respectively. About 1 mW/uncoated facet was still measured at 80 °C. The I-V curve exhibits a threshold voltage of 4.5 V and a serial resistance of 20 Ω .

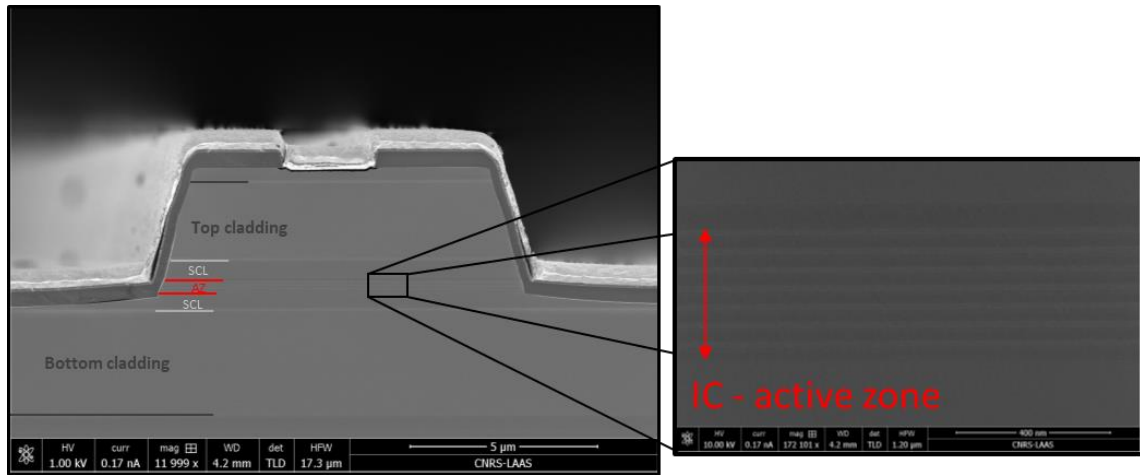


Figure II-27 - SEM picture of an ICL ridge processed at LAAS. Magnification on the active regions shows the 7 different stages.

In comparison with the above-reported broad area ICLs and the 19 μm wide-ridge this poor electrical performance is attributed to the etching of the InAs top contact layer during the process as you can observe in Figure II-27 and the fact that Ti:Au contacts on n-doped GaSb tend to lead to Schottky contacts [181] which, in turn, increase the turn-on voltage and series resistance.

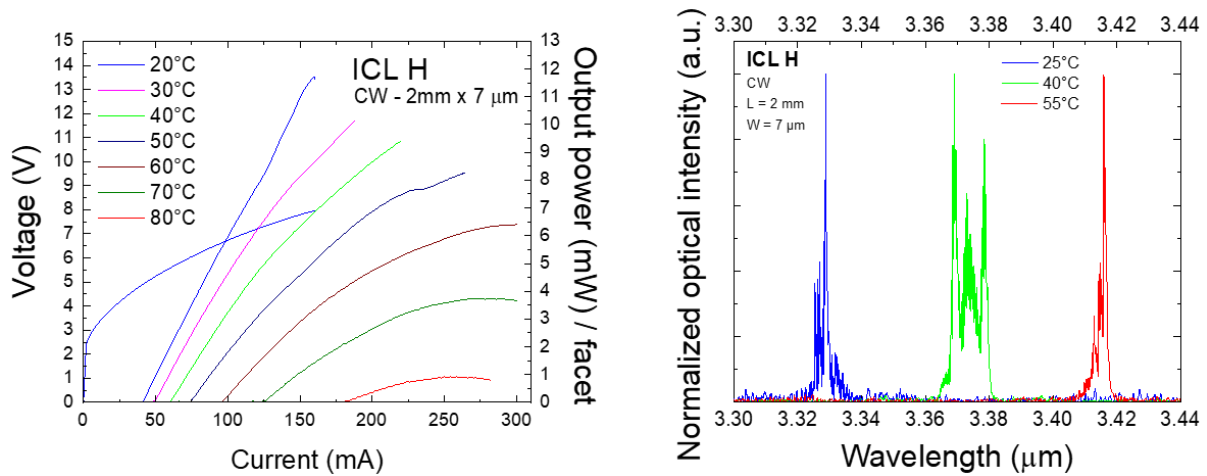


Figure II-28 - (a) CW light-current-voltage curves at different temperatures between 20°C and 80°C from a 7 μm ridge width and 2 mm long cavity of an ICL H device with AlGaAsSb cladding layers. (b) CW laser emission spectra taken at 150 mA at different temperatures (25°C, 40°C and 55°C)

Nevertheless, the threshold current was as low as 40 mA at 20°C, equivalent to 286 A/cm^2 , slightly higher than the pulsed value measured for the broad-area lasers, an expected degradation imposed by the excess ridge-wall related losses and the increased thermal load. Between 20°C and 80°C, the temperature dependence of the threshold current gives a characteristic temperature $T_0 = 50$ K up to 65°C and 25 K between 65°C and 80°C. This value is comparable to that of ICLs with AlSb/InAs cladding layers [106]. The emission spectra of this laser measured at 25°C, 40°C and 55°C are shown in Figure II-28(b). The spectra reveal

multimode operation and a peak emission wavelength increasing from 3.33 μm at 25°C to 3.41 μm at 55°C with a rate of about 2.6 nm/K.

II.5.1.6 ICL with InAs/AlSb superlattice cladding layers emitting at 3.6 μm

As presented in the section II.5.1.3, the ICL with AlGaAsSb claddings presents high internal losses. For comparison, we fabricated an ICL with superlattice cladding. For this structure, the top and the bottom n-doped cladding layers were 24.3 Å InAs/23 Å AlSb superlattice which present an average lattice constant matched to the GaSb substrate.

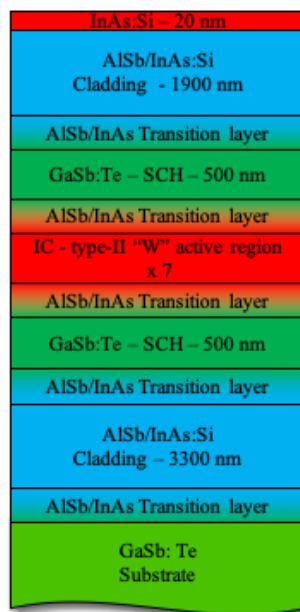


Figure II-29 - Complete design of ICL II. Structure with InAs/AlSb superlattice cladding layers. W structure is designed to emit at 3.6 μm .

The thickness of the cladding is increased to compensate the higher optical index in comparison to AlGaAsSb layers and to prevent mode interaction with both top metallization and GaSb substrate [182]. The bottom and top claddings are made of 700 periods (3.3 μm) and 400 periods (1.9 μm), respectively. For this structure we have targeted a wavelength of 3.6 μm , which is the second wavelength aimed in the MIMIC-SEL project. To achieve this wavelength, the thicknesses of the InAs layers in the “W”-QWs were increased to 18 Å and 16 Å. The scheme of the structure, named ICL I, is depicted in Figure II-29.

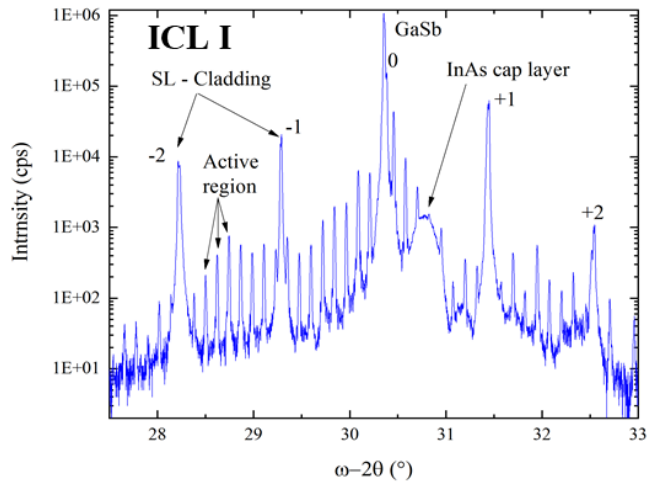


Figure II-30 - ω - 2θ HRXRD scans at the (0 0 4) reflection for the ICL I.

The HRXRD of the ICL I is presented in Figure II-30 and it can be clearly seen the peaks related to the periodicity of the cladding superlattice. The central peak of the cladding is almost coincident with the substrate peak, indicating nearly perfect lattice matching.

After structural characterization, the wafer was processed into 100 μm broad area laser and characterized in pulsed regime (1 μs /10 kHz) at RT.

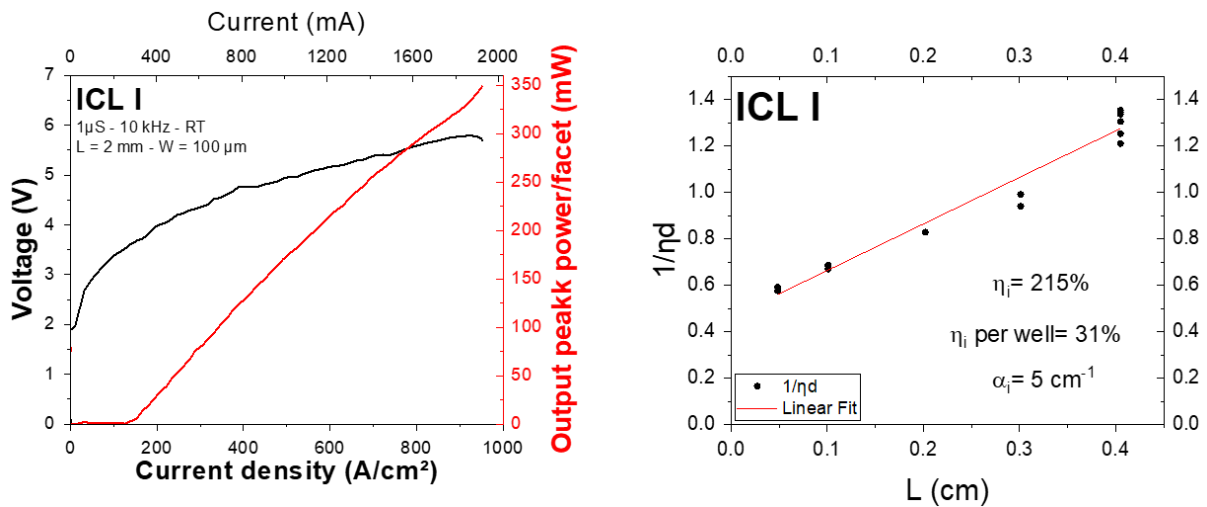


Figure II-31 - (a) Pulsed (1 μs /10 kHz) light-current-voltage characteristic of a 2-mm-long 100- μm -wide laser at RT and (b) Reciprocal differential quantum efficiency versus the cavity length in pulsed regime (1 μs /10 kHz) at 25°C

Pulsed electro-optical characteristics of the 2 mm long cavity are shown in Figure II-31(a). The threshold current density was found as low as 147 A/cm^2 , similar to the state of the art at 3.6 μm [6]. The V_{th} was around 3.5 V, which represents a voltage efficiency of 70%. The series resistance was 1.2 Ω , a value consistent with ICL using SL cladding layers [101]. The peak output power was 345 mW per facet at RT at 2 A. Figure II-31(b) shows the inverse slope efficiency versus the cavity length for five different laser lengths measured at RT. The extracted internal

quantum efficiency and optical losses were $\eta_i = 31\%$ per stage and $\alpha_i = 5 \text{ cm}^{-1}$, respectively. In comparison to ICL with AlGaAsSb cladding layers the optical losses were greatly improved, corroborating the strong absorption in AlGaAsSb.

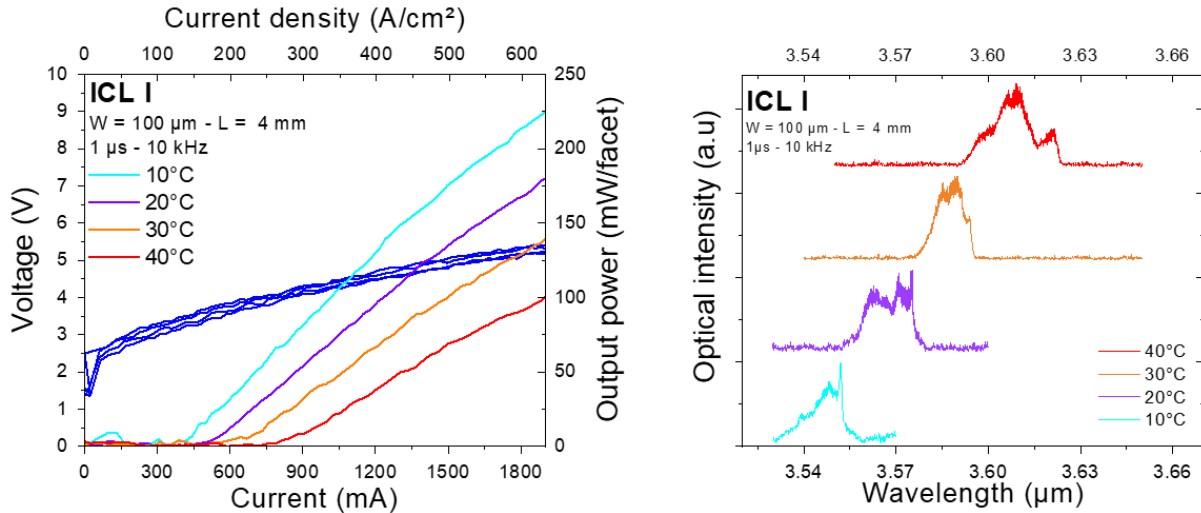


Figure II-32 - (a) Pulsed (1 μs /10 kHz) light-current-voltage characteristic of a 2-mm-long 100- μm -wide laser at RT and (b) Temperature dependent (normalized) laser emission wavelength of the ICL I

Figure II-32(a) shows electrical and optical characteristics of a 4 mm long device between 10°C and 40°C. Due to the temperature induced change in the bandgaps and the resulting redshift of the emission, the voltage for the same current values decreases at higher temperatures. The characteristic temperature was determined to be $T_0 = 45 \text{ K}$. Figure II-32(b) presents lasing spectra for this device at different temperatures. The emission peak is located between 3.55 and 3.62 μm as expected with this design.

To summarize, we obtained performances close to the state of the art, which demonstrate that we control each step of this structure from the modelling to the fabrication. To go further, we designed new active regions in attempt to improve the performances.

II.5.2 ICL with new electron-injector design.

In NRL's design, the electronic levels of the electron injector raised up to 151 meV higher of the electron level in the "W" region. The 4 inner InAs QWs of the electron injector were heavily doped in order to rebalance carriers and obtain enough electrons arriving in the "W" zone. Nevertheless, this high doping should increase optical losses and could decrease the optical performance. For these reasons, we conceived a new design in which we can avoid the

high doping concentration and ensure an efficient electron transport within the electron injector.

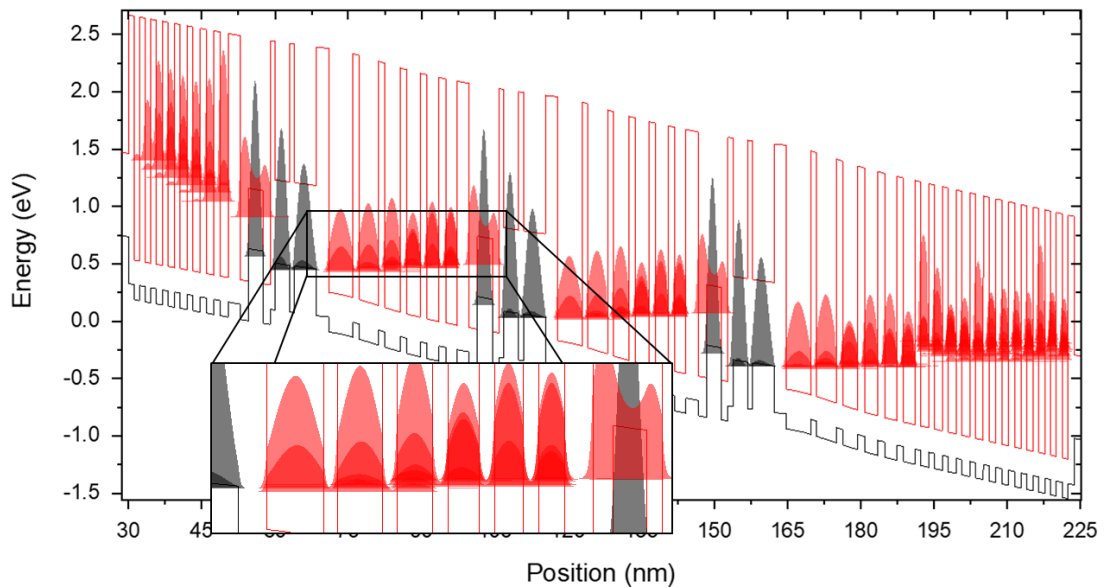


Figure II-33 – Band structure simulation of the active zone design of the ICL J. The simulation was done with an average electric field of 90k V/cm.

This new design (ICL J) consists of changing the InAs-QWs thicknesses (50 Å, 40 Å, 31 Å, 27 Å, 25 Å, 23 Å) in the electron injector to linearly align the electron levels from the semi-metallic interface to the W as depicted in the inset of Figure II-33. In this design, the transport through a flat band allows to reduce the doping concentration in the four inner InAs QWs within the electron injector to $5 \cdot 10^{17} \text{ cm}^{-3}$.

This structure was similar to the ICL H. It was constituted of AlGaAsSb cladding layers and the second cladding was grown at low temperature. The ICL J was manufactured into 100 μm x 2mm broad area laser and characterized in pulsed regime (100 ns x 100 kHz).

The Figure II-34 shows the power-current-voltage characteristics of this device. The threshold current density was 470 A/cm², twofold higher than the ICL H. The voltage threshold was 4.5 V, i.e. 0.7 V higher than the ICL J. This first design does not demonstrate better performances on the NRL's structure, but refinements on the band structure modelling coupled with ICLs fabrication should improve the performances of this design to outperform the state of the art.

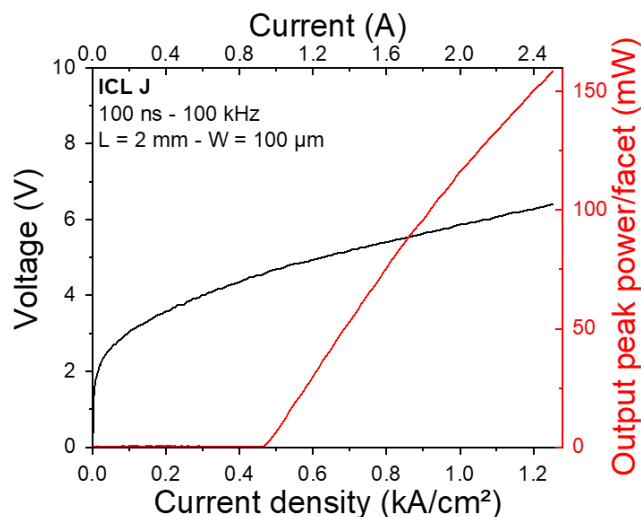


Figure II-34 - Power-current-voltage characteristics of the ICL J measured at 20°C in pulsed regime (100 ns/100 kHz) for a 100 μm broad area ICLs with 2 mm long cavity

II.6 Conclusion

In this chapter, we discussed the design, fabrication and characterization of several type-II W ICLs to study the properties of the IC active stage. The ICLs were fabricated by Cl-based ICP-RIE. This dry etching technique allow to etch during the same step the top cladding and the active region. A series of ICLs with active region based on the design of the NRL and AlGaAsSb cladding layers were fabricated. We demonstrated the importance of each part of the active stage. Thus, we showed the influence of the doping within the transition layer as well the growth temperature after the epitaxy of the active region. These investigations have brought down the threshold current densities of our ICLs. Thus, for optimized ICL a threshold current density as low as 220 A/cm^2 was obtained for broad area lasers in pulsed regime at 3.3 μm and CW operation has been achieved for narrow-stripe wide lasers up to 80°C. We have also observed high internal losses related to the absorption in Te-doped AlGaAsSb layer between 3 and 4 μm which can be overcome with the use of AlSb/InAs SL cladding layers. An ICL at 3.5 μm fabricated with optimized design and SL cladding demonstrated current density threshold as low as 150 A/cm^2 , a value similar to the state of the art.

Finally, we have designed an innovative IC-active stage with electron injector flat band and low doping concentration. Unfortunately, the electro-optical characterization showed threshold current density twofold higher than ICL designed from the NRL. Nevertheless, this first result is encouraging and there is ample room for design improvement.

To summarize, we have understood the mechanism of type-II W IC active stage and demonstrated state of the art ICL. This understanding is required for the realization of complex vertical structure such as VCSEL emitting between 3 and 4 μm .

Chapter III: Distributed Bragg Mirrors and III-As metamorphic layer.

In this chapter, we will describe the design of the DBRs that we have developed to fabricate IC-VCSELS. We will also present our investigation on the metamorphic interface used for the electro-optical confinement in our VCSEL.

III.1 Distributed Bragg Reflectors (DBRs)

As presented in Chapter I, one of the important requirements to ensure low threshold operation in VCSEL is to compensate the weak gain due to the small volume of active material. In order to reach the lasing threshold, mirrors with reflectivity exceeding 99.9% should be used in both sides of the active region. Distributed Bragg reflectors (DBRs) can be used for this purpose.

DBR consists of a periodic multilayer structure, composed of dielectric or semiconductor materials with different optical index and quarter-wave optical thickness given by the relation 3.1.

$$n \times d = \frac{\lambda_b}{4} \quad (3.1)$$

with n the refractive index of the material and d , its layer thickness and λ_b the working wavelength.

A DBR is usually formed by N pairs of high and low refractive indices noted n_H , n_L , respectively, and can be expressed by $(n_S | (n_H n_L)^N | n_0)$, with n_S and n_0 the refractive index of the substrate and the cavity index, respectively.

The Bragg's mirror operation, depicted in Figure III-1, is based on the phase shift of the incident beam. The phase changes by $\pi / 2$ when the beam passes through a quarter-wave layer. Moreover, at each interface the partial reflection introduces a π phase change when the wave goes from a medium with a low optical index to a high optical index. The quarter wave stacking layer then engenders constructive and destructive interferences in reflection and transmission, respectively.

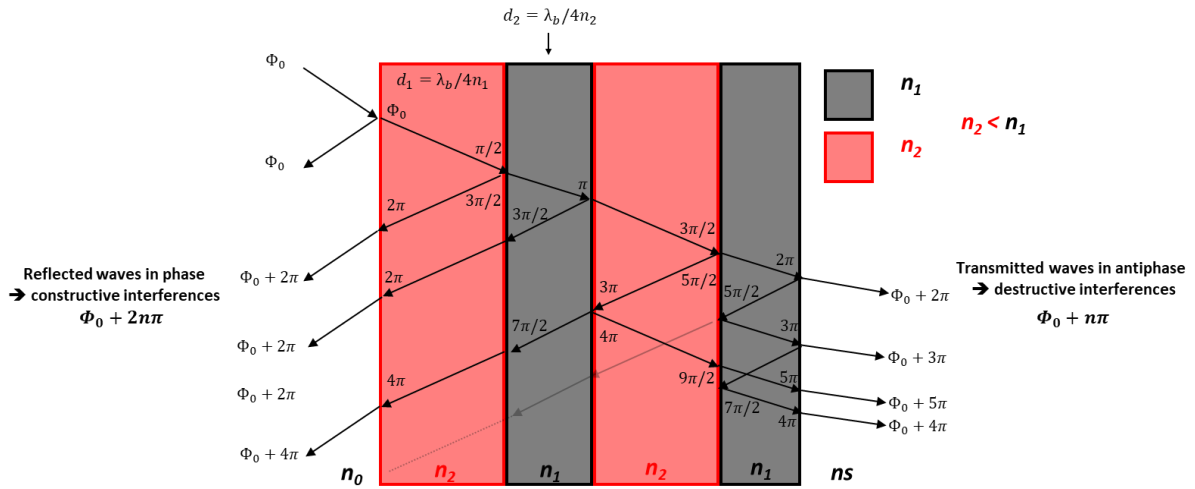


Figure III-1 - DBR operation principle

Among the advantages of DBRs over metal mirrors are their selectivity in wavelengths, the lower optical losses, and possibility to reach higher reflectivities. Thus, DBRs are very attractive for applications in optoelectronic devices, for their ability to select emissions and detections at specific wavelengths.

III.1.1 Bragg Mirror design parameters

The characteristic parameters of the DBR, in normal incidence condition, are the maximum of reflectivity and the stop-band width [183].

Both parameters depend on the contrast of refractive index between the two materials,

$$\Delta n = n_H - n_L \quad (3.2)$$

where n_H and n_L are the high and the low optical refractive index material, respectively and the number of periods, N . They increase the reflectivity value in such a way that if Δn is high, N can take a moderate value, while maintaining high values of reflectivity. For the structure defined above, the expression of reflectivity is:

$$R = \frac{\left(1 - g^{2N} \cdot \frac{n_S}{n_0}\right)^2}{\left(1 + g^{2N} \cdot \frac{n_S}{n_0}\right)^2} \quad (3.3)$$

where $g = n_L/n_H$.

Some of these applications require not only high reflectivity values at a certain wavelength, but also a wide stop-band $\Delta\lambda_b$ defined as the spectral band with the highest reflectivity

(equation 3.4). This last increases with the difference between the refractive indexes, this width is given by the expression: [184]

$$\Delta\lambda_b = \frac{2\lambda_b \Delta n}{\pi n_{eff}} \quad (3.4) \quad \text{with} \quad n_{eff} = 2 \cdot \left(\frac{1}{n_H} + \frac{1}{n_L} \right)^{-1} \quad (3.5)$$

Since the reflectivity and the stop band are defined by the index contrast between the DBR components, it is important to know the optical properties of the materials that will be used in our VCSEL for an emission in the MIR spectral range.

We will first establish the properties of semiconductor materials lattice matched to GaSb that can be used to design the bottom DBR. The optical losses related to doping concentration will be evaluated. Then we will study the case of dielectric materials to be used as a top DBR.

III.1.2 Semiconductor AlAsSb\GaSb DBR

It is convenient to use materials with high reflective index contrast which gives the possibility to reduce the total thickness of the DBR keeping high reflectivities and a large stop band. Among the III-Sb materials, the AlSb/GaSb couple has a refractive index difference large enough to achieve reflectivities of 98% with 10 pairs [185] but is not perfectly matched on GaSb. Therefore, it is preferable to use the ternary AlAs_{0.08}Sb which is lattice matched to GaSb [186].

The index contrast between the AlAsSb and GaSb is around 0.6 over a wide wavelength range from 2 to 5 μm ($n_{GaSb} = 3.8 - n_{AlAsSb} = 3.2$) [97], [133]. The corresponding quarter wave thicknesses at 3.3 μm are 217 and 257 nm for the GaSb and the AlAsSb, respectively. Figure III-2 depicts simulated reflectivity spectra of an AlAsSb/GaSb DBRs, calculated with the transfer matrix method, with the number of periods ranging between 10 and 24 pairs. The reflectivities are centered at 3.3 μm and the maximum of reflectivity increases with the number of periods. For instance, with 10 pairs the maximum is 97.34 % and for 24 pairs it is 99.98 %. The calculated stop band for this Bragg mirror is 362 nm.

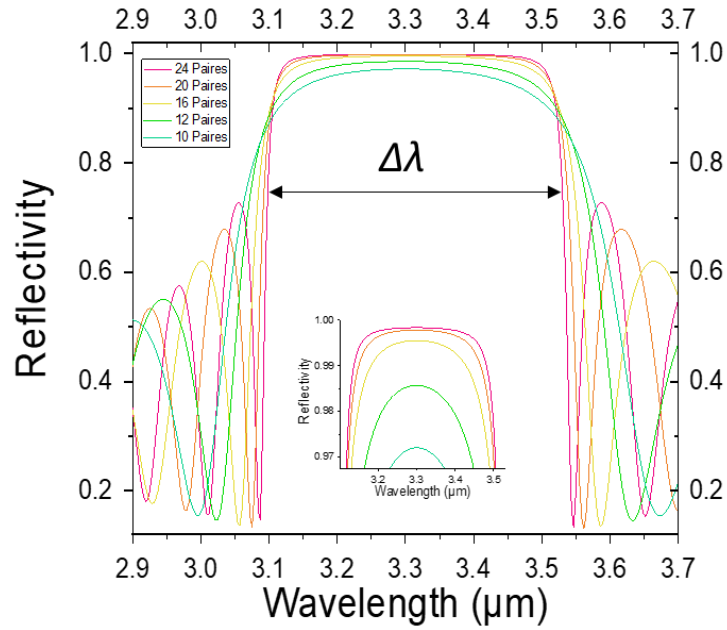


Figure III-2 - Simulated reflectivity of an AlAsSb/GaSb Bragg mirror centered at 3.3 μm for different period number.

III.1.2.1 Doping

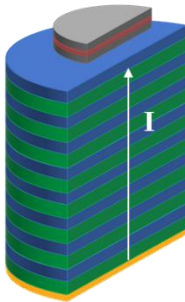


Figure III-3 - Current injection scheme through the bottom DBR

The VCSEL is designed with a current flowing through the semiconductor DBR as depicted in Figure III-2. Thus, to reduce the electrical resistance across the mirror, it is necessary to dope the GaSb/AlAsSb. However, doping will induce free carrier absorption losses that decrease the maximum reflectivity of the DBR. We will now discuss and study the impact of the doping on the optical losses since this last reduces the maximum optical reflectivity.

Figure III - 4 (a) presents the absorption spectra of n-type and p-type GaSb. [187], [188]. The data in Figure III - 4(a) were measured with a FTIR on bulk layer while the data in Figure III - 4(b) were measured through a GaSb waveguide at 4 μm . The structure was a GaSb and an $\text{Al}_{0.8}\text{GaAsSb}$ layers epitaxied onto a GaSb substrate and then the first layer was etched forming a ridge waveguide. The optical losses of p-type GaSb with a doping level of 10^{18} cm^{-3} at 3.3 μm are higher than 100 cm^{-1} which prevents its use in Sb-based VCSEL [133]. Whereas n-GaSb presents much lower absorption [97], [133], [187].

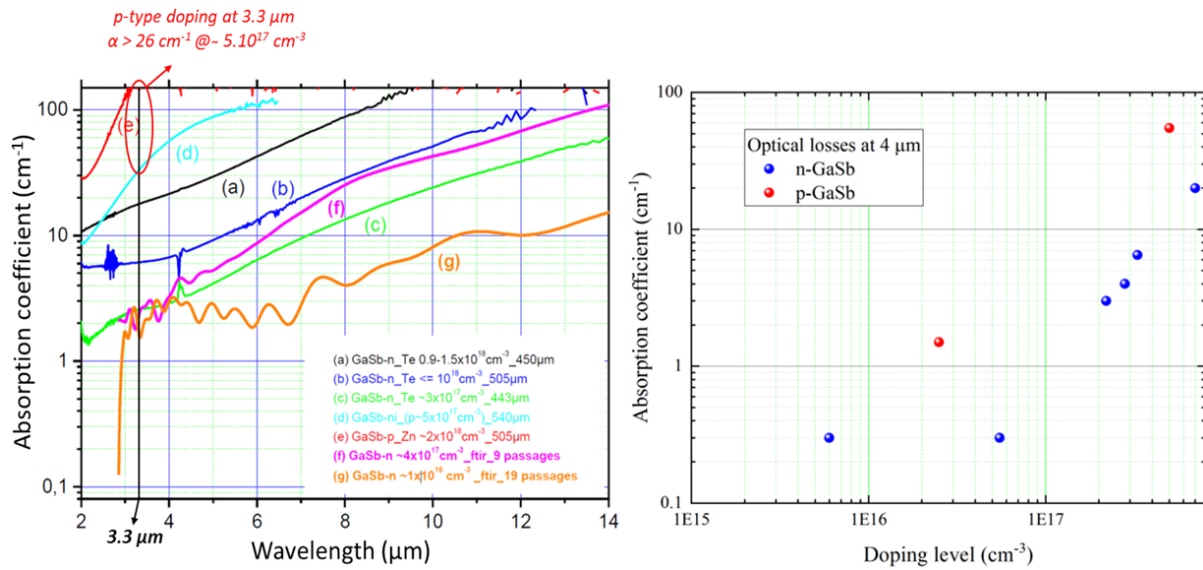


Figure III - 4 - (a) Measurements on epitaxied layers using the multi-pass FTIR device and measurements on GaSb substrates with various types of doping [187]. (b) Free carrier absorption based on the density of holes and electrons obtained by FTIR measurements and loss measurement in a waveguide; dotted lines: trend curve

As depicted in Figure III - 4(b), n-doping decreases optical losses down to ~20 cm⁻¹ for a concentration of $N_d \sim 1.10^{18}$ cm⁻³. Figure III-5 shows the reflectivities calculated for DBR with various optical losses. As it can be seen from this figure, for 24 pairs a maximum of reflectivity of 99.91 % can be reached for a DBR with optical losses of 20 cm⁻¹. However, to reach a reflectivity higher than 99.95%, optical losses must be lower than 10 cm⁻¹.

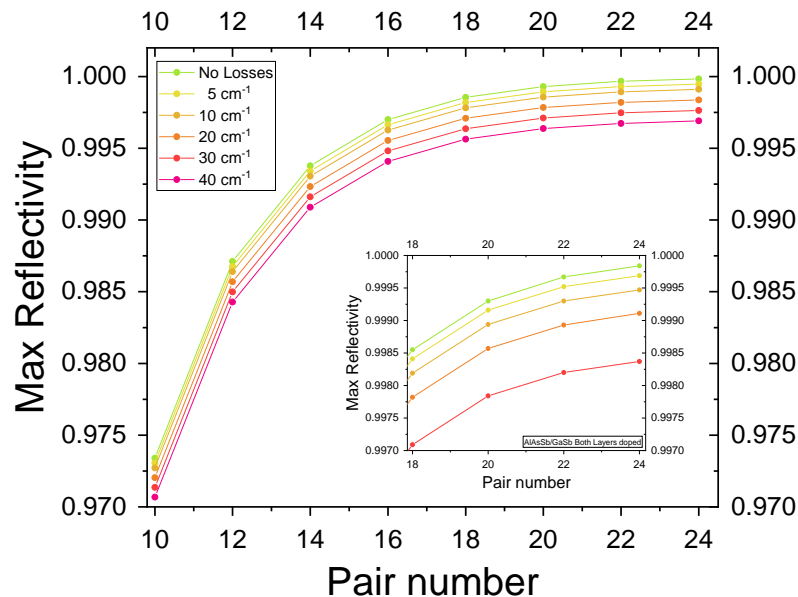


Figure III-5 – Maximum DBR reflectivity as a function the pair number for various values of optical losses .

We studied the electro-optical behavior of this type of DBR, a structure made of 24 pairs of AlAsSb/GaSb was epitaxied onto a n-GaSb substrate. The DBR was n-type doped with Te at

$1.5 \times 10^{18} \text{ cm}^{-3}$. The reflectivity spectrum of this DBR is shown in Figure III-6(a) along with a simulated curve. For the simulation we used thicknesses of 215.6 nm and 254.71 nm with optical index of 3.79 and 3.2 for the GaSb and the AlAsSb, respectively. The fabricated DBR with a total thickness of $\sim 15 \mu\text{m}$ presents a wide stop band of 353 nm and is well centered at $3.27 \mu\text{m}$.

The structure was then processed by standard photolithography and chlorine-based dry etching to form mesa with diameter ranging between 20 to $200 \mu\text{m}$ and metallized with Pd/AuGeNi to create full disc contacts. The substrate was thinned down to $300 \mu\text{m}$ and coated with Pd/AuGeNi. Electrical measurements were carried out in several DBR mesa samples. The I(V) characteristics of the DBR are presented in Figure III-6(b).

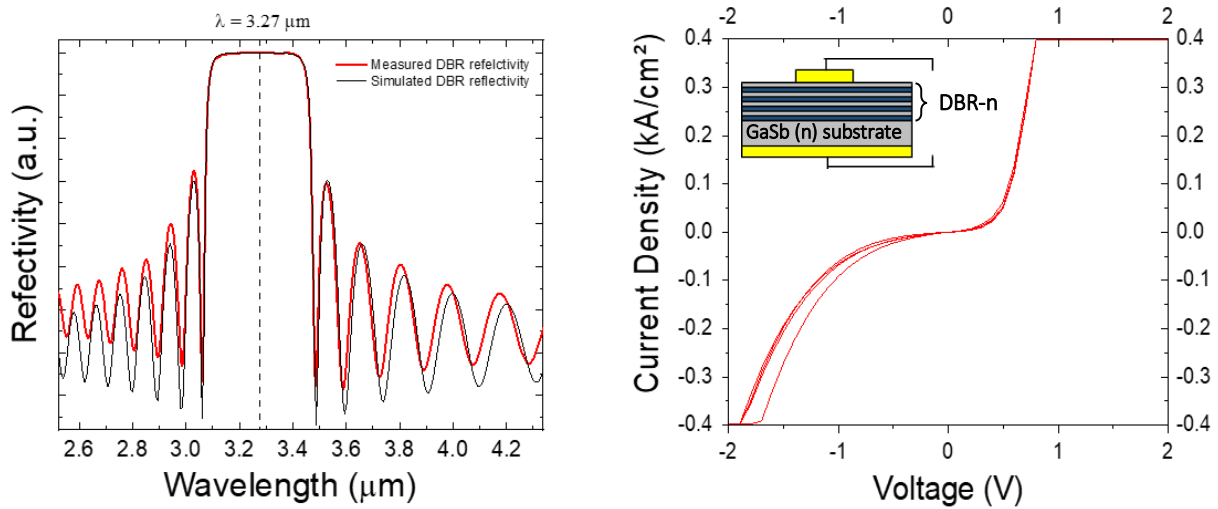


Figure III-6 - (a) Experimental and simulated reflectivity of 24 pairs of n-doped AlAsSb/GaSb DBR centered at $3.27 \mu\text{m}$. (b) I(V) curves of mesas with $210 \mu\text{m}$ diameter from the DBR.

The DBR exhibited nonlinear and asymmetrical I(V) curves. The Schottky behavior, already observed in $2.3 \mu\text{m}$ GaSb/AsAsSb DBR [133], [189] is attributed to the high conduction band offset between AlAsSb and GaSb (0.46 eV). The voltage drop is around 0.6 V , meaning a voltage drop per pair of 25 mV consistent with previous studies [133], [189]. This extra voltage will be added to the voltage of the IC-VCSEL structure, which should increase the thermal budget of the device reducing the performances.

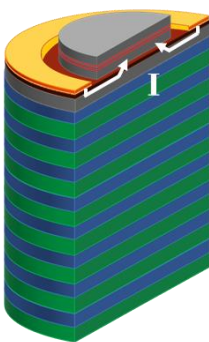


Figure III-7 - Intracavity design with its current injection scheme through the InAsSb contact layer.

To avoid optical losses due to the doping of the bottom DBR and reduce the self-heating of the final VCSEL, we propose a VCSEL with an intracavity design. In this configuration, displayed in Figure III-7.

a bottom contact layer is placed between the bottom DBR and the active zone. This layer can be made of a thin (~ 20 nm) lattice matched $n^{++}\text{-InAs}_{0.08}\text{Sb}_{0.92}$ layer with a high electrical conductivity [190]. This design offers a possibility of avoiding doped layers within the DBR.

Nevertheless, the MBE grown GaSb is intrinsically p-type doped ($\sim 3 \cdot 10^{16} \text{ cm}^{-3}$). Absorption of the intrinsic p-GaSb at $3.3 \mu\text{m}$ is still high with a value around $26 - 33 \text{ cm}^{-1}$ as depicted in the blue curve in the Figure III - 4(a). To compensate the optical losses generated by this residual doping, the GaSb should be slightly n-doped ($N_d \sim 10^{17} \text{ cm}^{-3}$). According to Figure III - 4(b), with this n-doping concentration, optical losses are reduced down to 2 cm^{-1} allowing a theoretical maximum reflectivity of 99.97% with 24 pairs.

III.1.3 Dielectric DBR

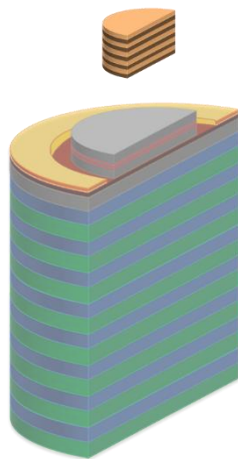


Figure III-8 - Top DBR implementation

Within the framework of the MIMIC-SEL project, the VCSEL is a hybrid structure with a dielectric top Bragg mirror. This part of the work was made in collaboration with FOTON Institute in Rennes.

In this paragraph, we summarize the main investigations developed by this group and the optical characterization done at IES on such DBR.

III.1.3.1 a-Si/SiN_x dielectric DBR

FOTON is well known for their research field in the telecom wavelength range and particularly for their fabrication of high optical quality dielectric DBR [191], [192] using the couple Si/SiN_x.

At $3.5 \mu\text{m}$ this set of material has a refractive index difference of $\Delta n \sim 1.87$. They sputtered 5 pairs of a-Si/SiN_x to assess their reflectivity around the target wavelength. The deposition thickness corresponded to $d_{\text{a-Si}} = 224 \text{ nm}$ and $d_{\text{SiN}_x} = 458 \text{ nm}$.

Figure III-9(b) shows the reflectivity of the DBR as a function of wavelength. The reflectivity is well centered at $3.3 \mu\text{m}$ and matches perfectly the simulated curve. However, one can notice an absorption peak between 3 and $3.2 \mu\text{m}$ decreasing the maximum of DBR reflectivity to $95 - 98\%$.

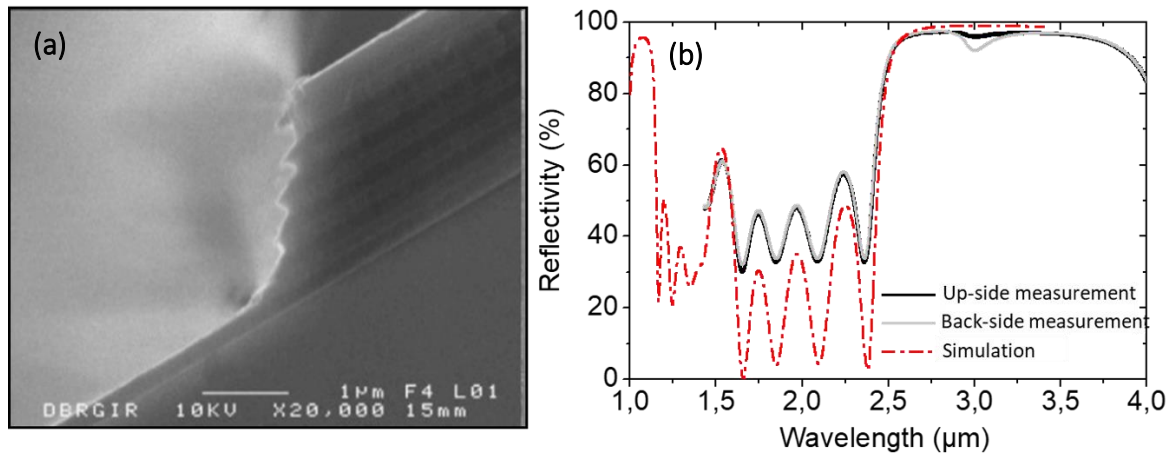


Figure III-9 - Dielectric DBR composed of 5 pairs of a-Si/SiN_x (a) SEM picture and (b) Reflectivity.

As depicted in the in Figure III-10, this absorption is related to N-H bonds [193]–[196] which shows the absorption spectra of a SiN layer measured with a FTIR. In our case, the SiN layers are deposited in a reactive plasma atmosphere containing hydrogen species and it leads to a strong absorption in the DBR at wavelength greater than 3 μm.

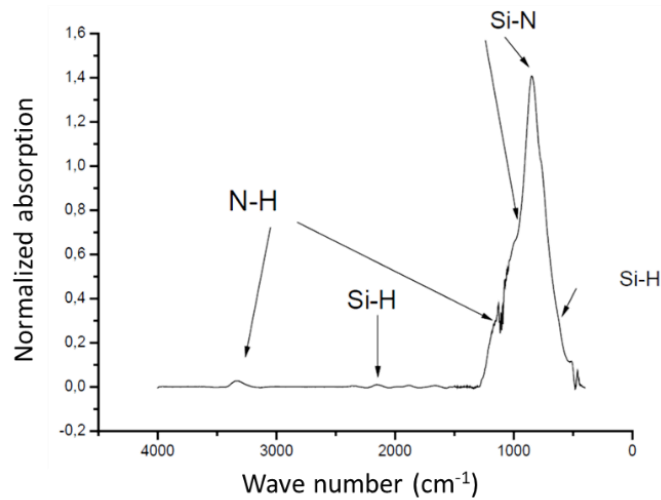


Figure III-10 – Absorption spectra measured with a FTIR of a SiN_x layer [197, p. 4].

Because of this strong absorption in the SiN, it was decided to use another couple of dielectric material. Among the dielectric materials used to fabricate DBRs, there are Ge and Si as high refractive index materials with $n_{Ge}=4.2$ $n_{Si}=3.67$ at 3.5 μm [198]. For low refractive index materials, there are ZnS with $n_{ZnS}=2.23$, SiN_x with $n_{SiN_x}=1.8$, MgF₂, SrF₂, CaF₂, BaF₂ with n_{MgF_2} , SrF_2 , CaF_2 , BaF_2 = (1.35–1.46) and the air [199].

III.1.4 Ge/ZnS dielectric DBR

We have made our choice on the couple of Ge/ZnS. Indeed, a hybrid GaSb based VCSEL using such a dielectric DBR was successfully demonstrated at 3 and 4 μm [145]. It presents a large refractive index contrast of $\Delta n = 2$, allowing a theoretical maximum of reflectivity of 99.5% with only 5 pairs.

The shows the experimental and theoretical reflectivity spectra of a 5 pairs Ge/ZnS DBR deposited by sputtering. The reflectivity shows a large stop band, centered at 3.4 μm , with a theoretical stop band where the reflectivity is higher than 99% of around 1000 nm. The whole thickness is only 2.9 μm .

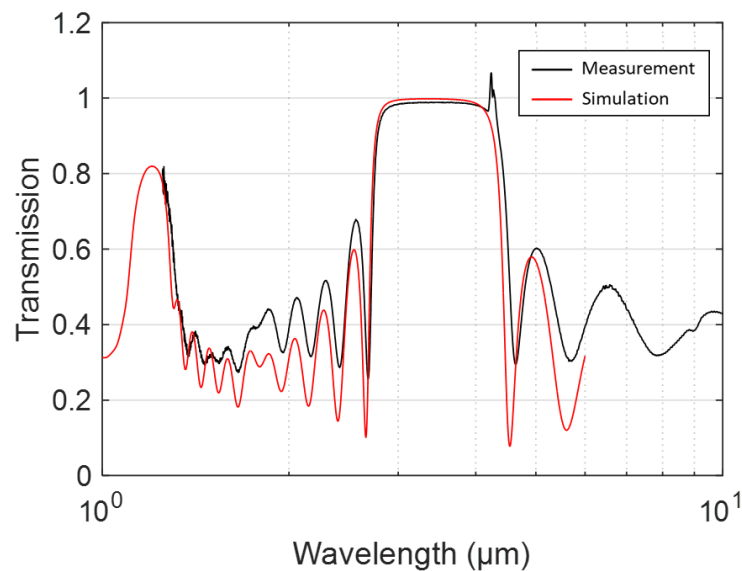


Figure III-11 - Experimental and simulated reflectivity of 5 periods of Ge/ZnS centered at 3.4 μm .

To go further, a hybrid microcavity structure was made with ten pairs of semiconductor AlAsSb/GaSb DBR, a $\lambda/2$ Ge cavity and two pairs of a dielectric Ge/ZnS DBR. Figure III-12 shows the scheme of such a structure and the reflectivity spectra of the semiconductor DBR and the whole structure. The stop band of semiconductor DBR is centered at 3.4 μm and it can be seen clearly the micro-cavity mode of the whole structure also at 3.4 μm , demonstrating the very accurate control of the dielectric thickness deposition.

In order to make circular patterns it was necessary to establish a technological process. A dry etching based on $\text{SF}_6/\text{CH}_4/\text{H}_2$ plasma, was used to form the patterns, but it was impossible to remove the photoresist after that without delamination of the ZnS layer.

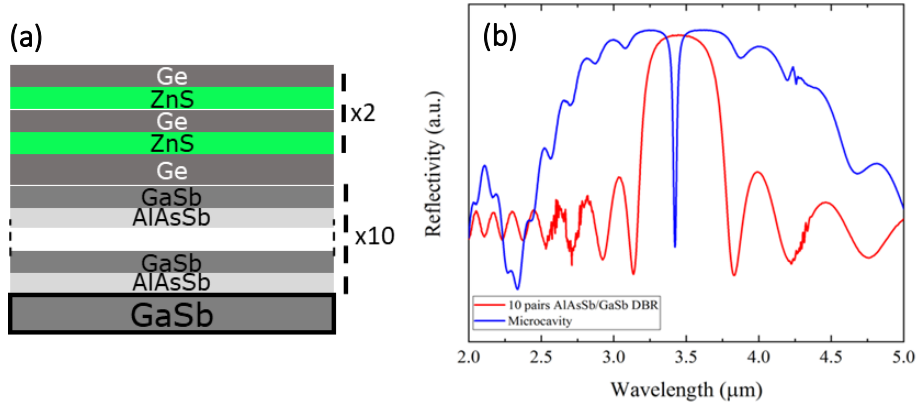


Figure III-12 - (a) Structure scheme of the hybrid microcavity and (b) the reflectivity of the semiconductor DBR (red) and the microcavity (blue).

The use of an Al hard mask did not solve the problem as presented in the SEM picture in Figure III-13

To overcome this issue, LAAS proposed to use a lift-off process employing a thick (7 μm) photoresist (nLOF) before the DBR deposition as depicted in Figure III-14. Then this resist can be removed easily with acetone.

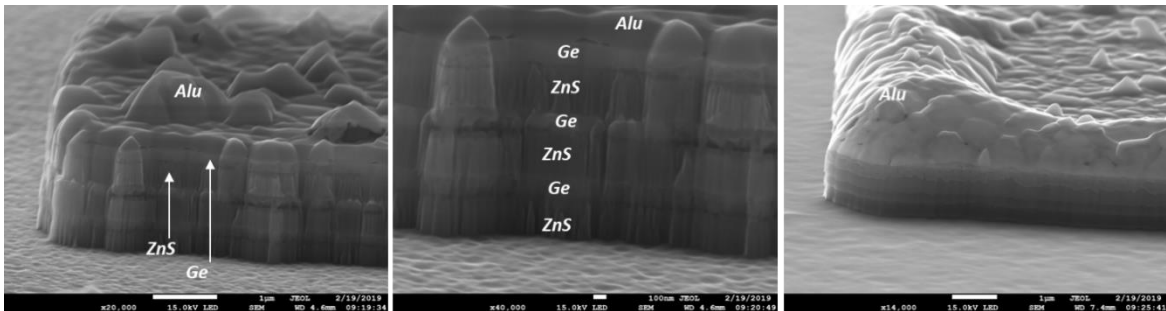


Figure III-13 - SEM picture of after a dry etching of a Ge/ZnS Bragg mirror.

The Figure III-14 presents the SEM picture after deposition of the a 5 pairs dielectric DBR and lift-off on 100 μm aperture square with circular mesa with a diameter of 80 μm. Although there is still some material on the edge, the lift-off does not damage the DBR.

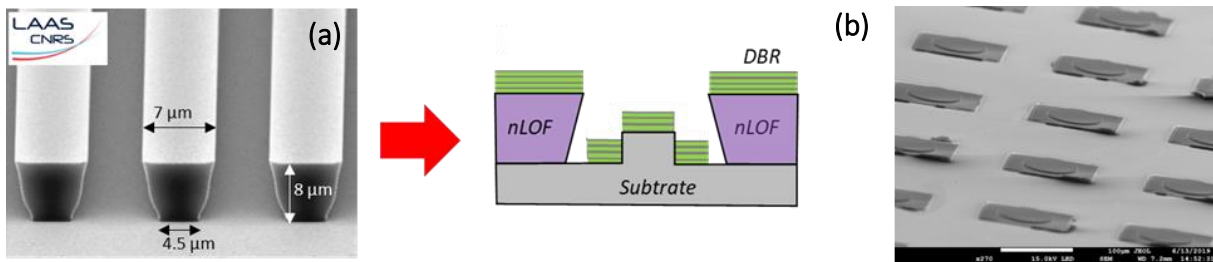


Figure III-14 – (a) Lift - Off technique for the Dielectric DBR deposition b) SEM pictures of a ZnS/Ge DBR array after lift-off

III.2 Electro-optical confinement using metamorphic III-As material

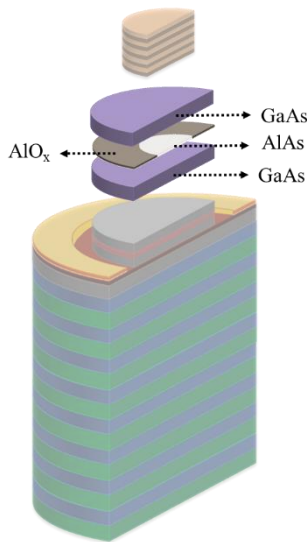


Figure III-15 - Scheme of the III-As section on the final device.

The lateral wet oxidation of aluminum-based III-V semiconductor materials is well suited in the field of electronic and optoelectronic devices, as it allows, in a similar way in microelectronics with the Si/SiO₂ couple.

Whereas lateral confinement is highly desirable to improve VCSEL performance and achieve single mode laser emission, in the case of GaSb-based VCSELs, lateral confinement is difficult to obtain mainly due to material issues. In our VCSEL, we selected the lateral oxidation of an Al(Ga)As layer to benefit from the well-known AlO_x technology for electro-optical confinement [140]. This material exhibits insulating properties and a low refractive index which can be exploited as confinement diaphragms in VCSELs. This technique implies the use of III-As materials which have a smaller lattice parameter (~5.65 Å) than antimonides (~6.1 Å). As depicted in Figure III-15, for the final device, the AlGaAs layer is sandwiched between two GaAs spacers on top of a GaSb layer building a metamorphic structure.

In this section, we will first detail the growth of III-As materials on the top of the VCSEL active region. Then, we will study the electrical behavior of the metamorphic interface between GaSb and GaAs. And finally, we will present a comparison between an IC-light emitting diode (LED) with and without metamorphic layer and the performance of an ICL using GaAs as top cladding layer.

III.2.1 Doping of GaAs at optimized growth temperature

Typically, the growth temperature of the GaAs is about 600°C, but as we concluded in chapter II, the growth temperature after the active zone should remain at 435°C to avoid degradation of the IC active zone caused by atomic intermixing at the interfaces [155]. For this reason, we have first studied the material properties of the GaAs grown at 435°C. To ensure a correct current spreading through this material, we studied the doping of the GaAs at such a low temperature. We first epitaxied two structures, GaAs and GaSb onto semi-insulating GaAs

substrates with two different doping concentrations with Te. The growth temperature was 435°C. The GaSb growth rate was 0.63 ML/sec which corresponds to the same Ga cell temperature at a growth rate of 0.54 ML/sec. In Figure III-16(a), we can observe that for the same Te cell temperature the carrier concentration is higher for the GaAs which can be explained in part by its lower growth rate and also maybe by a better dopant activation in GaAs material grown at low temperature [200]. We can see that the saturation level is in the range of 10^{19} cm^{-3} in GaAs and one order of magnitude less for GaSb [173], [201].

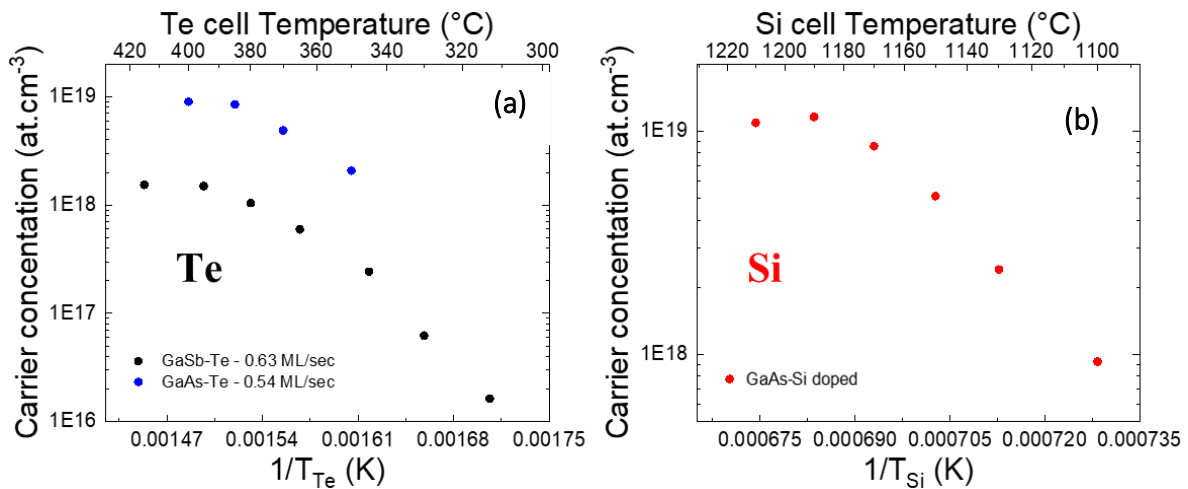
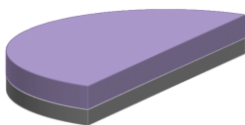


Figure III-16 - (a) Te-doping incorporation into GaAs and GaSb grown at 435°C. (b) Si-doping incorporation into GaAs grown at 435°C.

On the other hand, we repeated the same study with Si as dopant. We have to keep in mind that Si is an amphoteric atom which is a p-dopant in GaSb and n-dopant in GaAs. Figure III-16(b) shows the Si doping incorporation into GaAs grown at 435°C. We observe that even at this low growth temperature we can achieve doping concentration as high as 10^{19} cm^{-3} in GaAs with both Te or Si.

The electrical behavior of the metamorphic GaSb/GaAs interface grown at low temperature was then analyzed.

III.2.2 Electrical study of the GaAs/GaSb interface



The lattice mismatch between GaSb and GaAs is $\Delta a/a \sim 8\%$. This large value leads to relaxation after few monolayers generating a high density of dislocations [202], which can contribute to performance degradations.

To study the electrical properties of such structures, a set of four metamorphic samples (MS) were grown. Each structure was grown onto a n-GaSb substrate and consisted of a 300 nm

GaSb buffer layer followed by 1 μm of GaAs. The growth was done at 435°C with different doping concentrations and doping atoms as described in Figure III-17.

Highly doped		Low doped	
MS 1 (Te)	MS 2 (Si)	MS 3 (Te)	MS 4 (Si)
N-GaAs – 1 μm Te @ $8.10^{18} \text{ cm}^{-3}$	N-GaAs – 1 μm Si @ $8.10^{18} \text{ cm}^{-3}$	N-GaAs – 1 μm Te @ $2.10^{18} \text{ cm}^{-3}$	N-GaAs – 1 μm Si @ $9.10^{17} \text{ cm}^{-3}$
N-GaSb – 300 nm Te @ $1.3.10^{18} \text{ cm}^{-3}$	N-GaSb – 300 nm Te @ $1.3.10^{18} \text{ cm}^{-3}$	N-GaSb – 300 nm Te @ $5.10^{17} \text{ cm}^{-3}$	N-GaSb – 300 nm Te @ $1.3.10^{18} \text{ cm}^{-3}$
N-GaSb – Substrate Te @ $8.10^{17} \text{ cm}^{-3}$			

Figure III-17 - Doping concentration of 4 different Metamorphic Structures (MS)

The crystalline quality of the MS structures was assessed by HR-XRD. The typical ω -2 θ pattern is shown on Figure III-18.(a). We can observe a narrow peak corresponding to the GaSb substrate and a broad peak related to the relaxed GaAs. The morphology of the surface was studied by atomic force microscopy (AFM). The Figure III-18(b) presents a flat surface with a RMS roughness as low as 0.47 nm. The four structures present the same surface and crystalline characteristics.

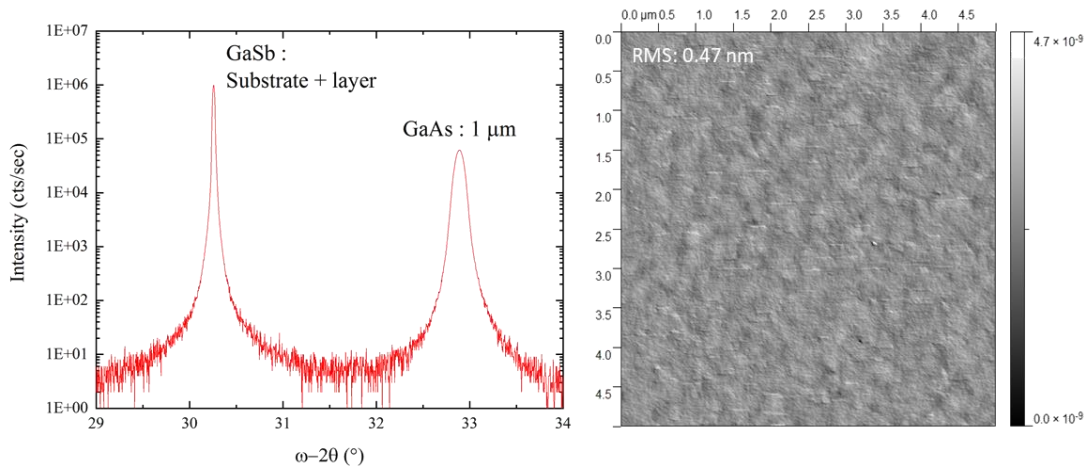


Figure III-18 – (a) ω -2 θ HRXRD scans at the (0 0 4) reflection of one metamorphic structure and (b) its surface observed by AFM.

Afterwards, the four MS were processed by standard photolithography and chlorine-based dry etching to form 200 μm mesa diameter and metallized with Pd/AuGeNi on the top of the mesas and the back-side of the substrate. Then, the samples were baked at $\sim 200^\circ\text{C}$ to create an ohmic interface between the metal and the semiconductor by diffusing the metal into the semiconductor. Figure III-19 presents the I(V) characteristics carried out on several mesas. This shows different behaviors as depicted in the I(V) characteristics.

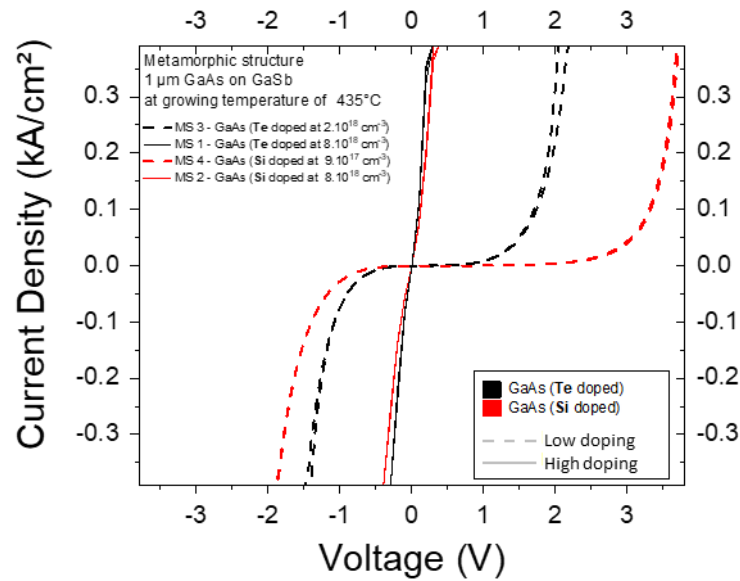


Figure III-19 – I(V) characteristics of different metamorphic structures with 4 different GaAs doping concentrations

The I(V) curves presents a Schottky behavior for the GaAs doped with both Si and Te doped at 9.10^{17} and $2.10^{18} \text{ cm}^{-3}$, respectively. For the structures with doping level at $8.10^{18} \text{ cm}^{-3}$ we can observe an ohmic behavior with a resistivity as low as $9.98 \cdot 10^{-4}$ and $7.44 \cdot 10^{-4} \Omega \cdot \text{cm}^2$ for the GaAs doped with Si and Te, respectively.

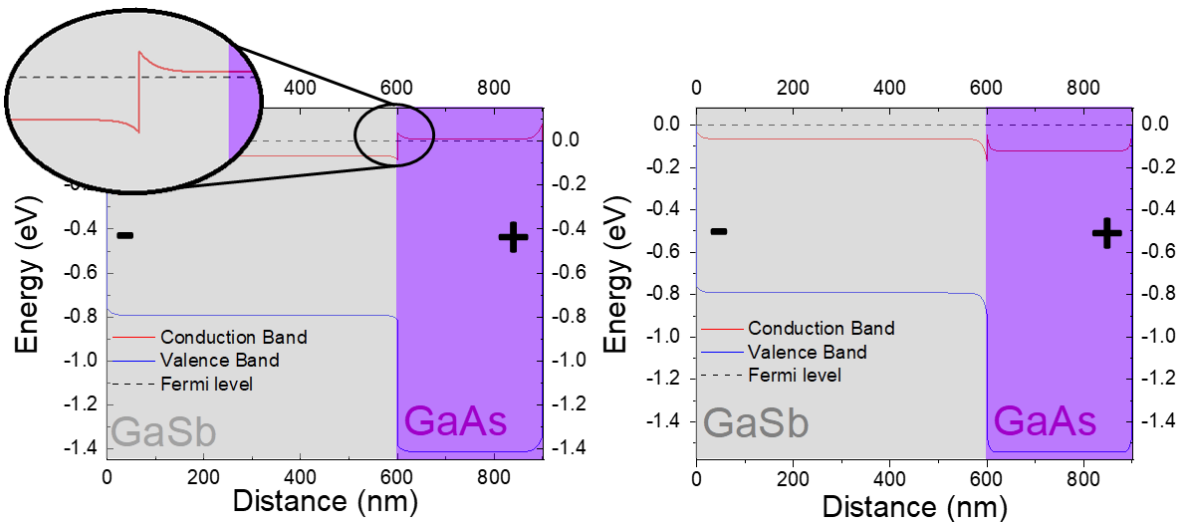


Figure III-20 - Band diagram of the GaSb/GaAs hetero-interface for different GaAs n-type doping level. The GaSb is N-doped at 10^{18} cm^{-3} (a) GaAs doped at 10^{18} cm^{-3} (b) GaAs doped at $8.10^{18} \text{ cm}^{-3}$

AuGeNi metal alloy contact on n-GaAs presents an ohmic behavior for a doping concentration around $1 \times 10^{18} \text{ cm}^{-3}$ [203]. It shows resistivities around $4 \times 10^{-6} \Omega \cdot \text{cm}^2$, a value comparable to that on n-GaSb ($6 \times 10^{-5} \Omega \cdot \text{cm}^2$) [147] using the same contact. Since our doping in the GaAs layers is of the order of $1 \times 10^{18} \text{ cm}^{-3}$ we can suppose that the Schottky barrier arises from the hetero-interface between the GaAs and the GaSb. The Figure III-20 shows the

simulation carried out with Nextnano software of the GaSb/GaAs interface for the different doping level. The Figure III-20(a) presents the metamorphic structure with both GaAs and GaSb doped at $1 \cdot 10^{18} \text{ cm}^{-3}$ and Figure III-20(b) with GaAs doped at $8 \cdot 10^{18} \text{ cm}^{-3}$. For the lower doping, the conduction band of the GaAs is at higher energy than the Fermi level leading to a potential barrier for the electrons. Therefore, an extra voltage is required to achieve a correct carrier flow in this structure. On the other hand, when the doping in GaAs is increased up to $\sim 8 \cdot 10^{18} \text{ cm}^{-3}$ the energy of the conduction band of the GaAs decreases removing the barrier for electrons. These results are in good agreement with the experimental data shown previously in Figure III-19.

To summarize, to reach a high conductive metamorphic interface it is needed to have a high doping level in GaAs. Finally, it was decided to use Te as a dopant because it is an n-dopant for both GaAs and GaSb and can ease the growth conditions because any change in the temperature of the cell is not required.

III.2.3 VCSEL design for the metamorphic interface and the oxidation layer

III.2.3.1 Position of the GaSb/GaAs metamorphic interface

We have demonstrated the importance of the doping level to achieve a GaSb/GaAs hetero-interface with a low resistivity. Nevertheless, this high doping in both GaSb and GaAs leads to increase optical losses by free carrier absorption. Indeed, we have seen in the section III.1.2.1 that 10^{18} cm^{-3} n-doped GaSb induces optical losses of 20 cm^{-1} at $3.3 \mu\text{m}$. Similarly, increase the doping concentration in GaAs will increase the optical absorption. Although few data are available on the infrared absorption between 3 and $4 \mu\text{m}$ as a function of the carrier concentration for the n-type GaAs [204]–[206], it is possible to figure out a tendency. Most of the results are given for a doping level lower than 10^{18} cm^{-3} which give a maximal optical losses of 5 cm^{-1} . For n type doping level of $5.4 \cdot 10^{18} \text{ cm}^{-3}$ optical absorption of 40 cm^{-1} was measured [204]. Thus, for higher doping concentration, the optical losses should be higher. Obviously, the position of the GaSb/GaAs hetero-interface in the VCSEL structure is crucial to avoid high optical losses. It should be placed at a node of the electrical optical field.

III.2.3.2 Position of the AIAs oxidation layer in the structure

Another important point comes from the position of the electro-optical confinement layer. Indeed, the position of the AIAs layer is defined by the position of the GaSb/GaAs metamorphic interface. We simulated the current distribution in the active zone when we placed the metamorphic interface at the three first nodes after the active region. Figure III-21, presents the optical field standing wave around the active region for a VCSEL designed at $3.3\ \mu\text{m}$ for the three configurations when the metamorphic interface is located at the first, the second and the third minima.

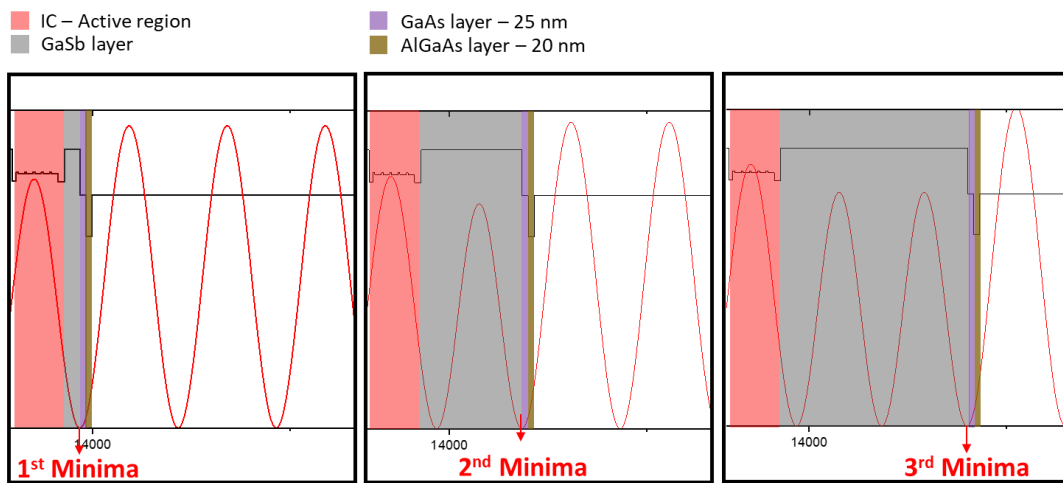


Figure III-21 - Scheme of the structure around the active region with the refractive index profile (black) and the EM intensity distribution (red) for the interface placed at the first, the second and the third minima.

The electrical simulations were done with COMSOL software which is based on the finite element method (FEM). For the electrical study it used the resolution of the Maxwell equations. The simulation was performed for a mesa diameter of $30\ \mu\text{m}$ and an Al(Ga)As diaphragm diameter of $6\ \mu\text{m}$. Table 7. shows the electrical conductivity values for the different materials used for these electrical simulations. The values for GaSb, InAs and the Au contact were taken from the Thesis of D. Sanchez [111] while the GaAs and AlGaAs were directly given by COMSOL. For the active zone mainly composed of a superlattice InAs/AlSb, we considered a value lower than the InAsSb in which the lateral conduction is higher than the longitudinal one. This difference in electrical conductivity was the main reason why ICLs required deep etching crossing the active zone (Chapter II).

	Electrical conductivity (S/m)	
	Lateral	Longitudinal
Au – contacts	$45.6 \cdot 10^6$	$45.6 \cdot 10^6$
GaAs (n)	32000	32000
AlGaAs	30	30
AlO _x	0	0
IC – Active region	100000	70000
GaSb(n)	28600	28600
n++ InAsSb	500000	500000

Table 7 - Electrical conductivity of different materials used in the electrical simulation of the electrical confinement.

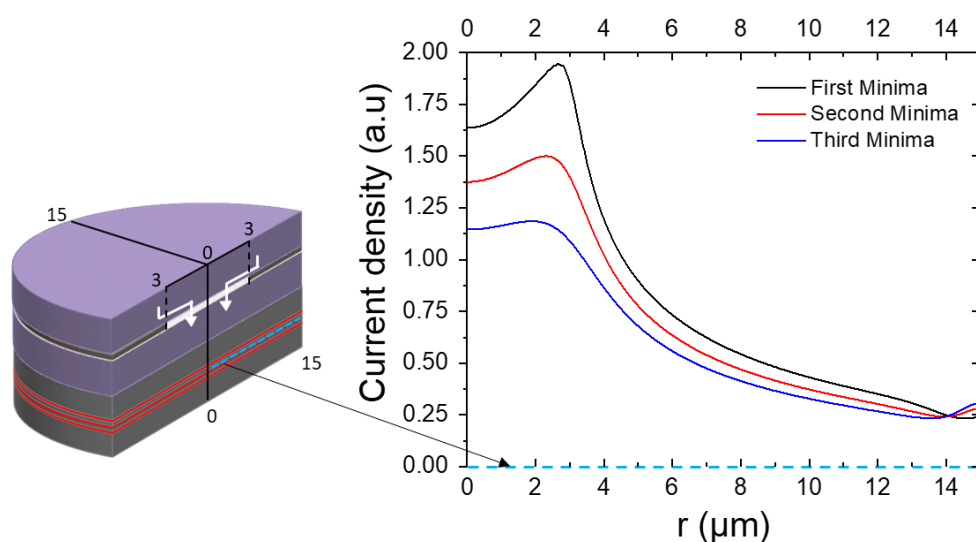


Figure III-22 - Scheme of the active zone and III-As region and the simulation of the current density profile in the active zone placing the metamorphic interface at three first nodes of the optical mode above the active zone.

Figure III-22 shows the scheme of the simulated structure and the radial electrical profile within the active area for a fixed current injection. When the confinement layer is placed close to the first minima, we can observe a stronger current crowding in comparison with two other configurations. However, the current density in the active region is higher when the metamorphic interface is placed at the first node of the internal optical mode.

Figure III-23 depicts a schematic diagram of the complete IC-VCSEL structure designed following the conclusions of this study and the intrinsic optical field standing wave intensity distribution at $3.3 \mu\text{m}$. The IC-AR is placed at the anti-node of the internal optical field, the bottom n++-InAsSb contact layer is located at the node to reduce the optical losses and the

GaSb/GaAs metamorphic interface followed by the AlAs layer for the electro-optical confinement is placed at the first node above the active region to ensure an efficient current confinement.

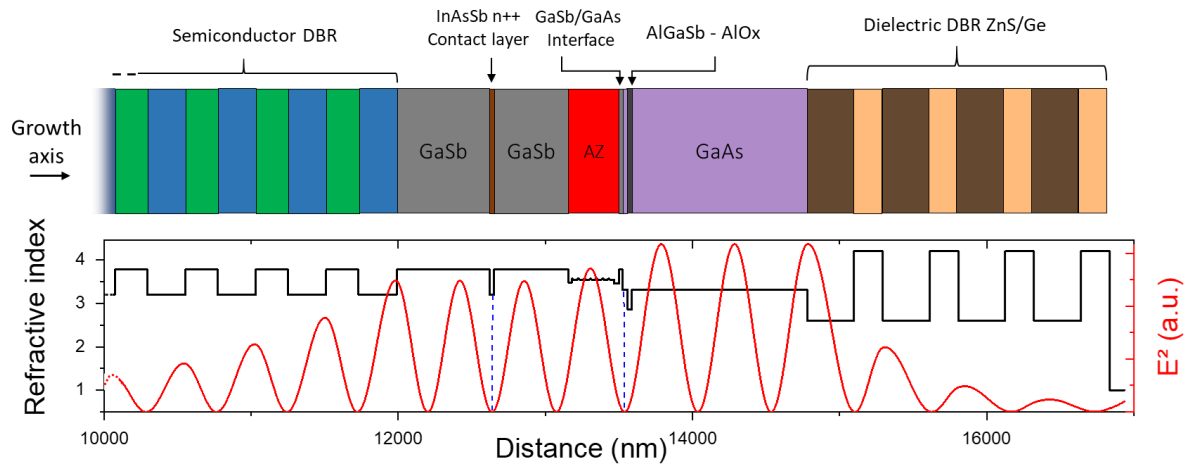


Figure III-23 - Scheme of the IC-VCSEL structure with the refractive index profile (black) and the EM intensity distribution (red)

III.2.4 Study of IC-Light Emitted Diode with metamorphic GaAs top layer

We fabricated and studied an IC-LED with a metamorphic GaAs layer on top of the active region (IC-LED 1). For comparison a conventional Sb-based IC-LED was also fabricated (IC-LED 2) as depicted in Figure III-24.

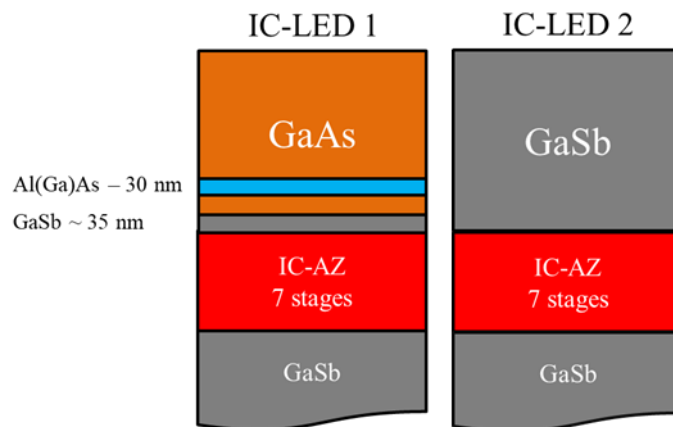


Figure III-24 - Design of IC-LEDs structures. IC-LED1, with metamorphic III-As layers and IC-LED2 with GaSb top layer

The growth of both structures was performed on a $\frac{1}{4}$ of 2-inch (100)-oriented N-doped GaSb substrates. The growth was started by 1 μm thick N-doped GaSb layer ($1 \cdot 10^{18} \text{ cm}^{-3}$) and

followed by a 7-stages IC active zone designed for emission around 3.3 μm . Then for the IC-LED 2, a 1 μm thick N-doped GaSb layer ($1.10^{18} \text{ cm}^{-3}$) was epitaxied on top. In the case of the IC-LED 1, the IC active region was followed by 35-nm-thick N-doped GaSb layer doped with Te at $1.10^{18} \text{ cm}^{-3}$. Next, a 25 nm thick Te-doped GaAs layer with a doping concentration of $8.10^{18} \text{ cm}^{-3}$ was grown to ensure the ohmic behavior of the metamorphic interface. Then, a 30 nm-thick $\text{Al}_{0.98}\text{GaAs}$ layer was grown next to this interface. This layer was capped by a 1- μm -thick N-doped ($1.10^{18} \text{ cm}^{-3}$) GaAs terminated by a 20 nm thick heavily doped ($8.10^{18} \text{ cm}^{-3}$) GaAs contact layer, to ensure ohmic contact. The entire metamorphic part of the structure was grown at 435°C.

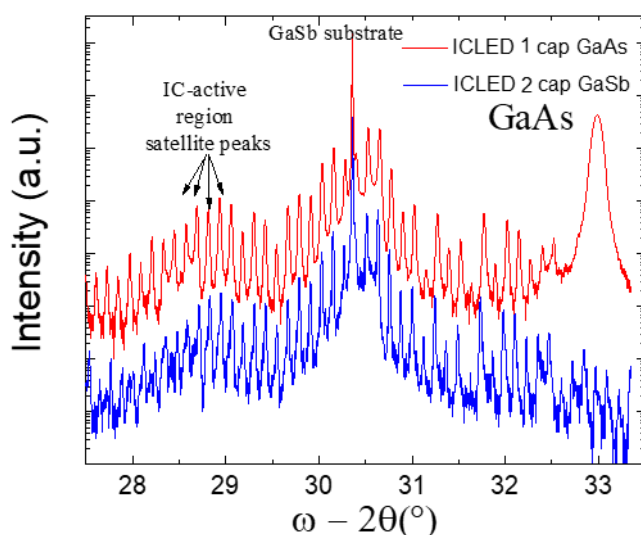


Figure III-25 - (a) ω - 2θ HRXRD scans at the (0 0 4) reflection of IC-LED 1 (metamorphic LED) in red and IC-LED 2 (antimonide LED) in blue.

The crystalline quality of the grown structures was characterized by HR-XRD. The ω - 2θ patterns are shown on Figure III-25. The diffractogram depicts, for both structures a series of satellite peaks up to the 16th order arising from the periodicity of the stages of the IC active zone. For the metamorphic structure, a larger peak appears at higher angles corresponding to the fully relaxed GaAs. The thickness of the IC active region extracted from the angle separation between the satellite peaks is 41.5 nm for the IC-LED 1 and 42.3 nm for the IC – LED 2.

The satellite peaks for the IC-LED 1 are however observed to be larger than those of the conventional IC-LED 2, because of the high density of dislocations coming from the GaAs-based region. To confirm this hypothesis, the top GaAs was dry etched using inductively coupled plasma reactive ion etching (ICP-RIE) on a part of the sample. Four etching steps of 250 nm

were performed and HRXRD was carried out between each stage. Figure III-26(b), displays the evolution of the full width half maximum (FWHM) averaged over the 10 satellite peaks closest to the substrate peak. Upon removal of the GaAs section, the FWHM of the satellite peaks from the IC-LED 1 approaches the value of the IC-LED 2, which confirms our hypothesis. We can also observe in Figure III-26(a), that the intensity of the peak corresponding to the fully relaxed GaAs decreased with the etching.

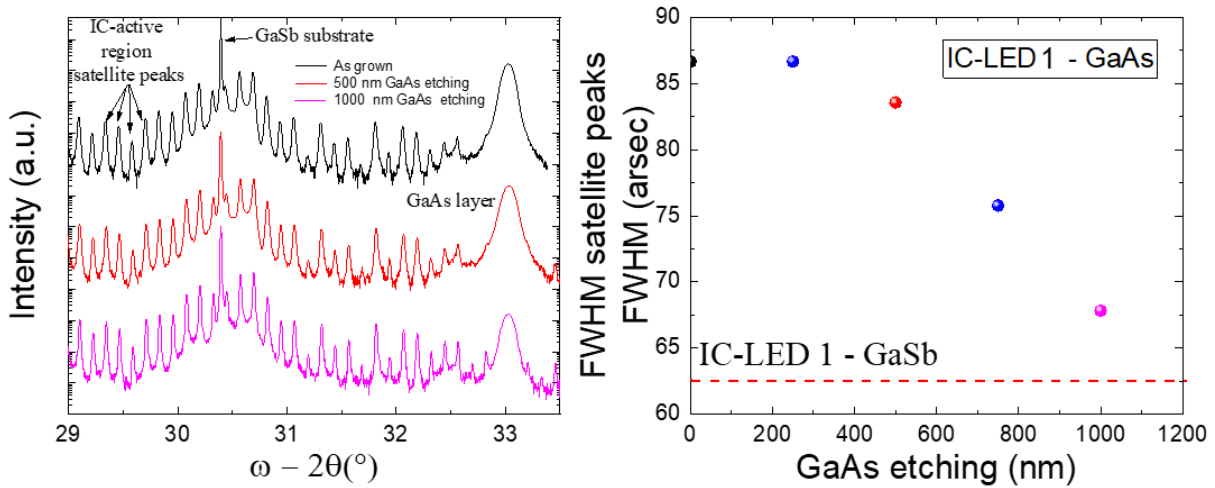


Figure III-26 - (a) $\omega - 2\theta$ HRXRD scans at the (0 0 4) reflection for the IC LED 2 after growing, after 500 nm etching and 1000 nm etching – b) Evolution of the FWHM of the satellite peaks of the RCLLED with etched GaAs

Both structures were patterned with circular mesas with diameters ranging from 20 μm to 200 μm using standard optical photolithography and chlorine-based dry etching. The mesas were etched down to the GaSb layer below the AZ. This step was followed by surface passivation of the structures using a Si_3N_4 ICP-PECVD coating and then Pd/AuGeNi and Ti/Au metallization for the top contacts of the IC-LED 1 and IC-LED 2, respectively. The structures were thinned down to 200 μm and the substrates were coated with Pd/AuGeNi for the bottom contacts. To form ohmic contacts the structure was baked during 1 min at 200 °C.

Electro-optical measurements of the fabricated devices were performed under CW operation. Figure III-27(a) shows the CW-I(V) characteristics of both IC-LEDs at RT for an aperture diameter of 180 μm . The turn-on voltage for the IC-LEDs is around 3.4 V and the differential series resistance is 4.9 and 2.7 Ω , for IC-LED 1 and 2 respectively. This disparity may be attributed to the GaSb/GaAs junction, to a low performance of the contact on the GaAs layer or the Al(Ga)As layer which add a potential barrier in the conduction band. Figure III-27(b) shows typical emission spectra of both structures.

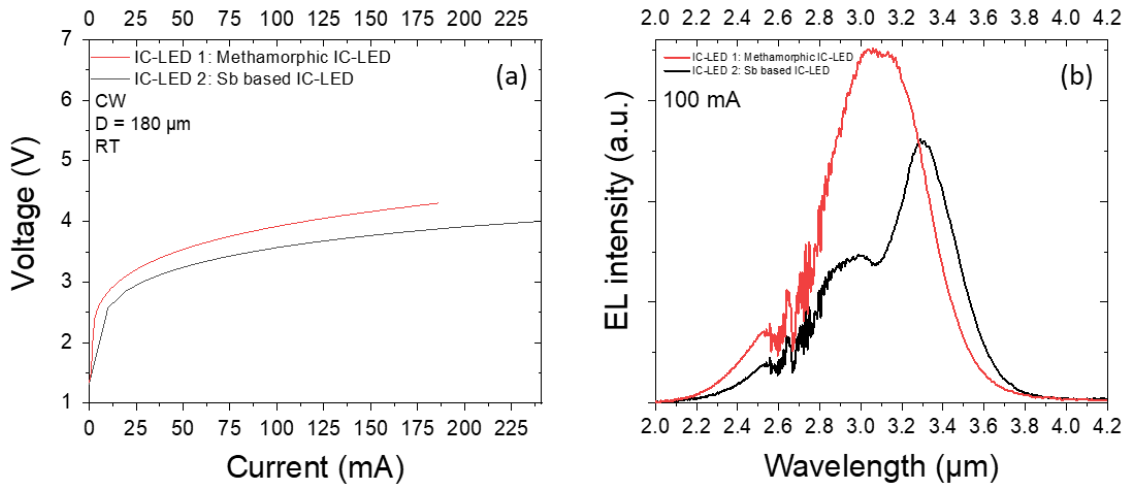


Figure III-27 - (a) CW I(V) characteristics of IC-LED 1 and 2 and (b) their corresponding spectrum.

The emission intensity is in the same order which tend to demonstrate that the IC active region is not impacted by the growth of the metamorphic layer. The emission peak of the IC-LED 2 is at 3.3 μm and presents a shoulder at shorter wavelengths that was not well understood but which has been already observed in IC-LED [207]. The emission peak of the IC-LED 1 is around 3.1 μm, 200 nm shorter than the IC-LED 1, and seems to be broader. The shorter emission wavelength can be attributed to the smaller period thickness of the active region (8 Å).

III.2.5 ICLs with metamorphic GaAs top cladding

The good performance of the IC-LED with the top GaAs layer can open the way for novel devices with new functionalities. Indeed, type-I GaSb diode laser emitting at 2.3 μm [208] and 2.7 μm [209] with a GaAs top cladding have been successfully demonstrated. For instance in ICL, the GaAs can offer a lower refractive index at 3.3 μm ($n=3.3$) than the InAs/AlSb SL ($n=3.39$), a higher thermal conductivity ($k=55$ W/m.K) and can facilitate the growth in comparison to the AlSb/InAs SL. Figure III-28 shows a comparison of the optical mode for a conventional ICL and ICL with a GaAs metamorphic top cladding calculated using an online 1D mode solver for waveguide [210]. The structure is composed of a 3.5-μm-thick bottom AlSb/InAs cladding, two 400-nm-thick GaSb SCH, the IC active region, and 1.7 μm top cladding made either with an AlSb/InAs SL or a GaAs layer. The optical mode overlap with the active zone for the metamorphic ICL is slightly higher than in the conventional ICL, with a value $\Gamma = 28.3\%$ and 27.6% , respectively

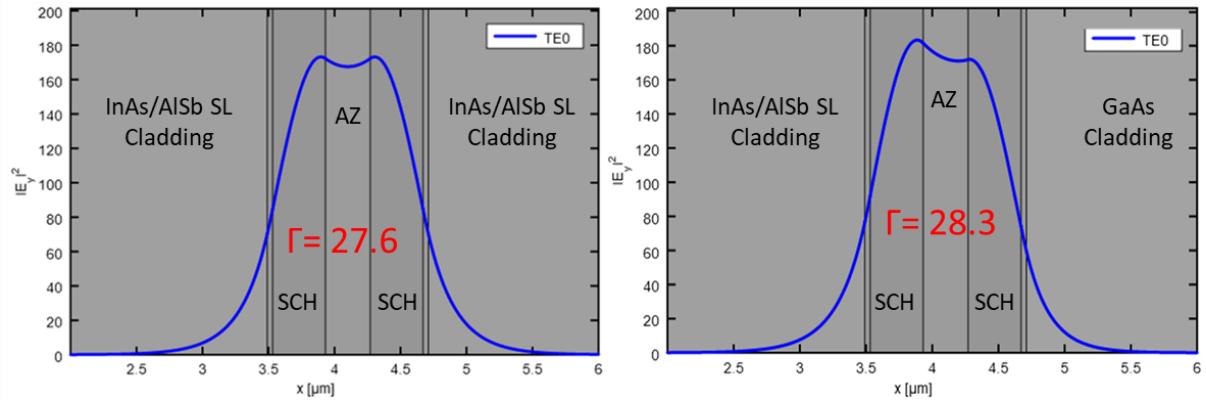


Figure III-28 – Optical mode simulation through (a) ICL with InAs/AlSb SL and (b) GaAs top claddings.

A new ICL structure, named ICL K, was epitaxied, following the scheme represented in Figure III-29.

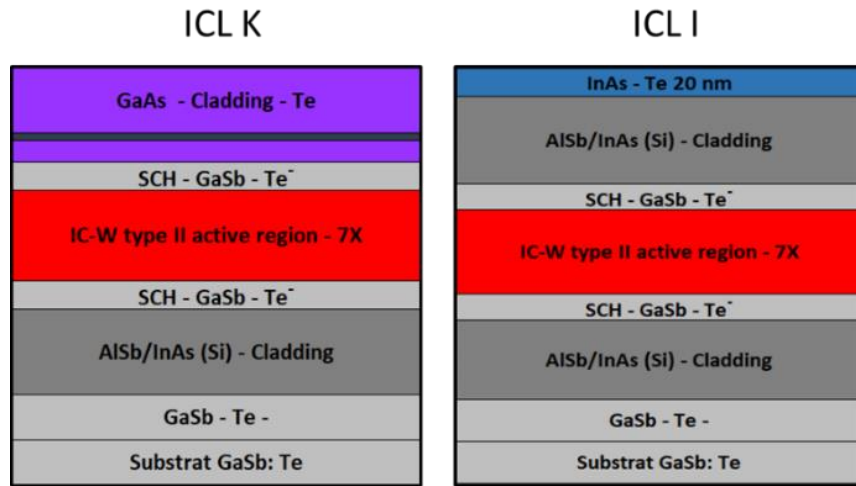


Figure III-29 - Scheme of the ICL K. This structure is the same as the ICL I shown at right and described in section II.5.1.6 except the top cladding which is made with a metamorphic GaAs layer.

The growth conditions for the ICL K was the same as for the ICL I. The GaAs metamorphic layer was grown above the top 400 nm thick GaSb SCH. After 25 nm of GaAs, a 20-nm-thick $Al_{0.98}GaAs$ layer was grown to form, after oxidation “narrow ridge” lasers in order to favor single spatial mode operation. The ICL K was processed into 100 μm wide ridges and cleaved to form 1, 2, 3 and 4-mm-long cavities following the process described in chapter II.

Figure III-30 shows the inverse slope efficiency versus the cavity length for four different laser lengths measured at RT.

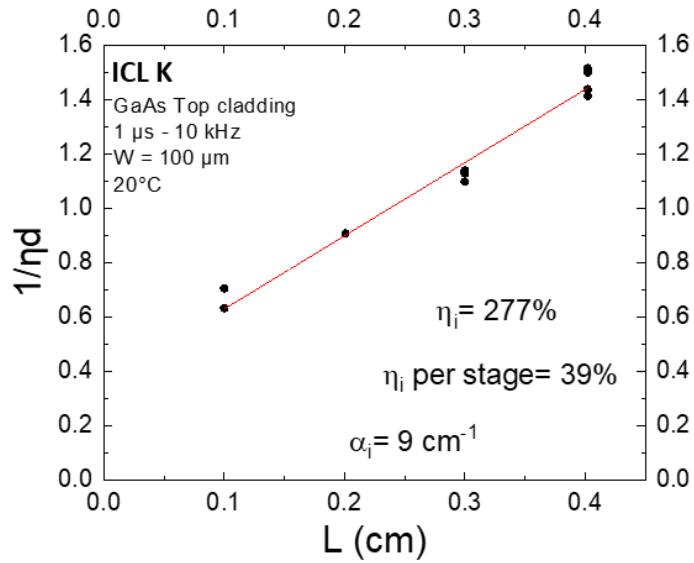


Figure III-30 - Reciprocal differential quantum efficiency versus the cavity length in pulsed regime (1 μ s/10 kHz) of the ICL K.

The extracted internal optical losses and quantum efficiency were $\alpha_i = 8 \text{ cm}^{-1}$ and $\eta_i = 277\%$, respectively.

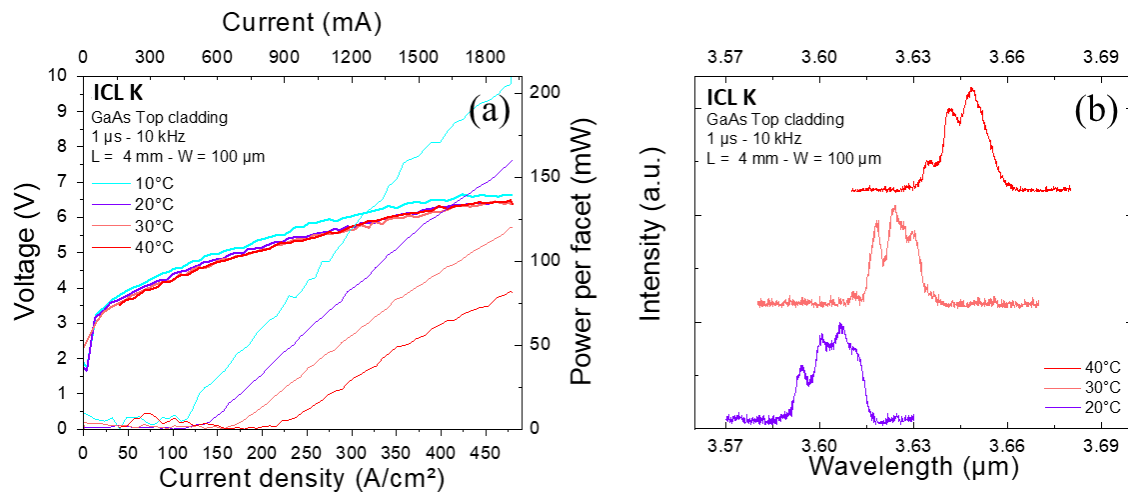


Figure III-31 - 100 μ m x 4 mm long cavity ICL with GaAs top cladding layers characteristics in pulsed regime (1 μ s/10 kHz) and at different temperature (a) P-I-V (b) Laser spectra

Figure III-31 shows the P-I-V characteristics of a 4 mm long cavity characterized in pulsed mode (1 μ s/10 kHz) at different temperatures ranging from 10°C to 40°C and their corresponding spectra. The threshold current density varied from 100 A/cm² to 220 A/cm² at 10°C and 40°C, respectively, and we can deduce a $T_0 = 38\text{K}$. The threshold current density was 127 A/cm² at 20°C and the peak output power was 155 mW per facet at RT at 1.9 A. The V_{th} was 4.6 V, which represents a voltage efficiency of 52% and the series resistance measured was

1.3 Ω . The Figure III-31(b) displays the spectra of the laser at 1 A for different temperature. The wavelength shifts from 3.61 to 3.64 μm between 20 and 40°C.

The table 2 lists the performances of 100- μm -wide laser from the ICLs I and K.

	pulsed at 20°C		100 μm x 4 mm – 20°C			
ICL	α_i	η_i	J_{th}	V_{th}	R_s	$P_{\text{peak @ 1.9 A}}$
I (conventional ICL)	5 cm^{-1}	251%	150 $\text{A}\cdot\text{cm}^{-2}$	3.6 V	1.3 Ω	180 mW
K (Top GaAs cladding)	9 cm^{-1}	277%	127 $\text{A}\cdot\text{cm}^{-2}$	4.6 V	1.3 Ω	155 mW

Table 2 – Performance comparison for 100 μm broad area ICL in pulsed regime (1 μs /10kHz) at 20°C the ICL with AlSb/InAs top cladding (ICL I) and GaAs top cladding (ICL K)

All the characteristics of both lasers are comparable, which demonstrates the potential of using GaAs as top cladding layer in ICL without degradation of the performances.

The ICL is now under process at LAAS to study narrow ridge ICL with oxidation of the Al(Ga)As layer

III.3 Summary and conclusions of the metamorphic electro-optical confinement

In this chapter we studied the different parts composing our VCSEL. We showed that low n-doped AlAsSb/GaSb DBR is required to reach reflectivity as high as 99.95%. An intracavity contact is however required to reach this performance. The couple ZnS/Ge have been chosen for the top dielectric DBR because of its large optical index contrast. Then, we have demonstrated that low resistivity GaAs/GaSb interface requests high doping level which leads to high optical losses. Thus, the interface must be located at a node of the electric field. The Al(Ga)As layer should be placed close to this interface and at the first node above the IC-active region to ensure an efficient electrical confinement. Finally, we have showed that IC-LEDs and ICLs using GaAs metamorphic layer exhibited performances similar to the conventional structures, demonstrating the possibility to use such layer in more complex structures like VCSELs.

Chapter IV: IC- Vertical Cavity Surface Emitting devices

In the previous chapters, we have presented the developed IC active region and the GaSb/GaAs metamorphic interface for electrical confinement. In this chapter, we will describe vertical cavity surface emitting devices combining both technologies.

IV.1 Simple IC-resonant cavity light emitting diodes

On the first step to VCSELS, we studied resonant cavity LEDs (RCLEDs). These devices are attractive for the development of low-cost systems for gas analysis [211] Due to their narrower emission linewidth [212] such sources can offer a better spectral overlap with absorption features of the analyzed gas molecule and thus improved sensitivity compared with the conventional LEDs [213]. Since their first demonstration in 1992 [214], only a few mid-IR RCLEDs, based on arsenide [215], phosphide [216] and antimonide compounds have been reported [217], [218], with only one IC-RCLED operating at RT [219].

IV.1.1 Design of the RCLED-A

The first IC-RCLED (named RCLED-A) was conceived for emission at 3.3 μm . For the initial evaluation of this RCLED, we decided to inject the current through the bottom DBR. The bottom DBR was composed of 14 pairs of n-GaSb and n- $\text{AlAs}_{0.08}\text{Sb}_{0.92}$ quarter wavelength layers doped with Te at $2 \cdot 10^{18} \text{ cm}^{-3}$, with calculated reflectivity of 99.3%. The DBR was followed by 945- μm -thick GaSb layer. On top, seven periods of IC- active stage were grown and placed at the anti-node of the internal optical field. The active region was followed by 25 nm of GaSb and 35nm of GaAs, Te-doped at 2 and $9 \cdot 10^{18} \text{ cm}^{-3}$, respectively. Then a 30-nm-thick $\text{Al}_{0.98}\text{Ga}_{0.02}\text{As}$ layer used for the electro optical confinement was grown and covered with 1.2 μm thick-GaAs spreading layer Te-doped at 10^{18} cm^{-3} to ensure an efficient current injection. The metamorphic interface and the AlGaAs layer were placed at the first node of the internal optical field above the active region. At the end, the optical cavity thickness of the whole device (RCLED-A), presented in Figure IV-1 was 3λ .

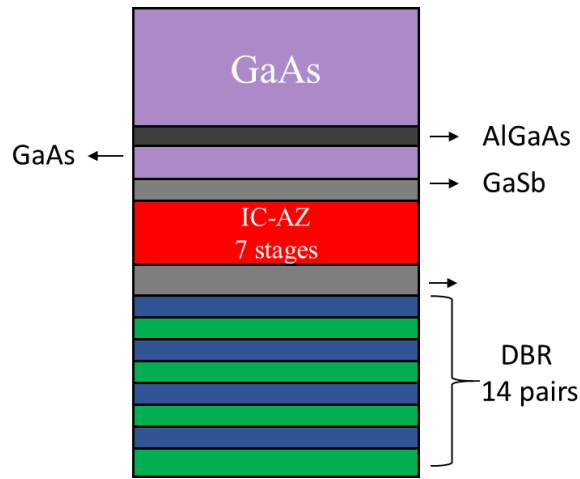


Figure IV-1 - Complete scheme of the structure L, a half metamorphic RC-LED A

IV.1.2 Optical characterization of the RCLED-A

The top optical reflectance spectrum of the RCLED-A is shown in Figure IV-2. The measurement was performed with a Bruker FTIR spectrometer under a quasi-normal incidence.

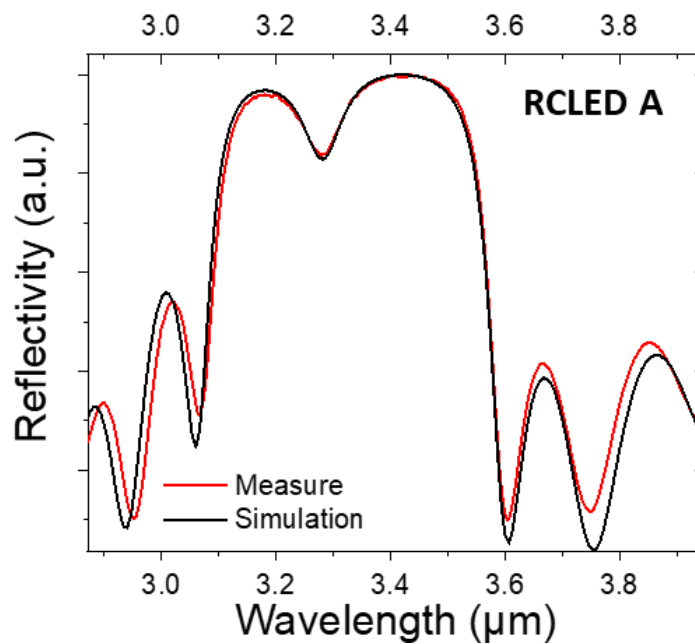


Figure IV-2 - Measured and simulated top reflectivity spectrum of the RCLED-A epitaxial structure without the top dielectric DBR

The simulated spectra show a stop-band centered at 3.32 μm with a dip related to the cavity mode at 3.28 μm. This wavelength detuning from 3.3 μm is attributed, based on reflectivity calculation, to a cavity thickness of about 2% smaller than the target value and could be explained by a variation of the Ga flux during the growth.

IV.1.3 RCLED-A processing and electro-optical characterizations

Electrically-pumped RCLEDs were then fabricated from this wafer. First, the structure was dry etched by Cl-based ICP-RIE down to the GaSb layer below the active region using photolithography to define mesas with diameters of 70, 90, 130 and 210 μm . Then, 300 nm of Si_3N_4 were deposited by PECVD on the whole structure to electrically isolate the mesas. ICP-RIE was then employed to open the contact and RCLED emission zones. Then, 10/400 nm of Pd/AuGeNi were sputtered to make the metal contacts rings around the emission surface of the devices. The substrate was thinned down to 100 μm and the same metallization was made for the bottom contact. The samples were then baked at 200°C to form the contacts. The metal ring width was 25 μm , so the final aperture surfaces of the RCLED were 20, 40, 80 and 160 μm .

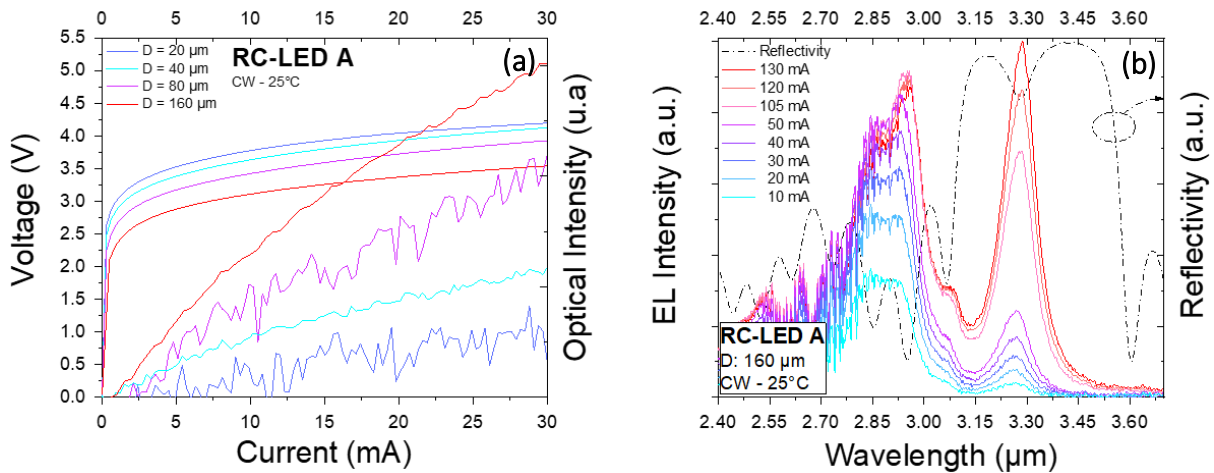


Figure IV-3 - (a) CW - light-current-voltage characteristic and (b) optical emission spectra of the RC LED A

Figure IV-3(a) depicts the light-current-voltage characteristics of the RCLEDs in CW at 25°C. We observe an increase in the light intensity with increasing aperture diameter. The turn on voltage varies from 2.6 V to 3.5 V for the 160 and the 20 μm , respectively. The series resistance is almost the same, 10 Ω , for all measured devices. Figure IV-3(b) displays the top reflectivity of the structure and the CW electroluminescence spectra at different currents injections on a 160- μm -aperture diameter device. For currents below 100 mA, the emission occurs mainly between 2.7 and 2.8 μm with a weak but narrow emission band at 3.28 μm . For currents higher than 100 mA, the emission intensity at 3.28 μm increases whilst the intensity at shorter wavelength remains constant. The spectra depict a blue-shift of the maximum of the electroluminescence. This can be observed with the increase of the optical intensity coming from the microcavity mode. We can estimate that the maximum of the emission of the active

region is blue-shifted of 300 nm compared to the cavity mode. The FWHM of the emission enhanced by the resonant cavity at 3.28 μm is 110 nm significantly narrower with respect to the 570 nm measured with the IC-LED-1.

The vertical devices containing together the DBR, the IC-active region and the III-As metamorphic layers is a starting point towards a VCSEL.

IV.2 IC-RCLED with AlOx confinement layer and top Ge/ZnS DBR

IV.2.1 Design of the RCLED-B

A more complicated RCLED-B was fabricated as the next step towards the VCSEL. This new structure was conceived to emit at 3.3 μm . We have presented in the section III.1.2.1 of the Chapter III, the interest to decrease the doping concentration in the AlAsSb/GaSb DBR to reduce the optical losses. Nevertheless, such approach requires the insertion of a special layer to provide an intracavity contact. The RCLED-B was based on the same design of the IC-RCLED-A with Te-concentration within the bottom DBR decreased to $1.10^{17} \text{ cm}^{-3}$ and with a 30 nm-thick $\text{InAs}_{0.92}\text{Sb}_{0.08} \text{ n}^{++}$ (10^{19} cm^{-3}) layer located at a node of the internal optical field below the active region. Figure IV-4 depicts a schematic diagram of the RCLED-B structure and the optical field standing wave intensity distribution at 3.3 μm . The semiconductor part is capped with 2 pairs of ZnS/Ge dielectric DBR.

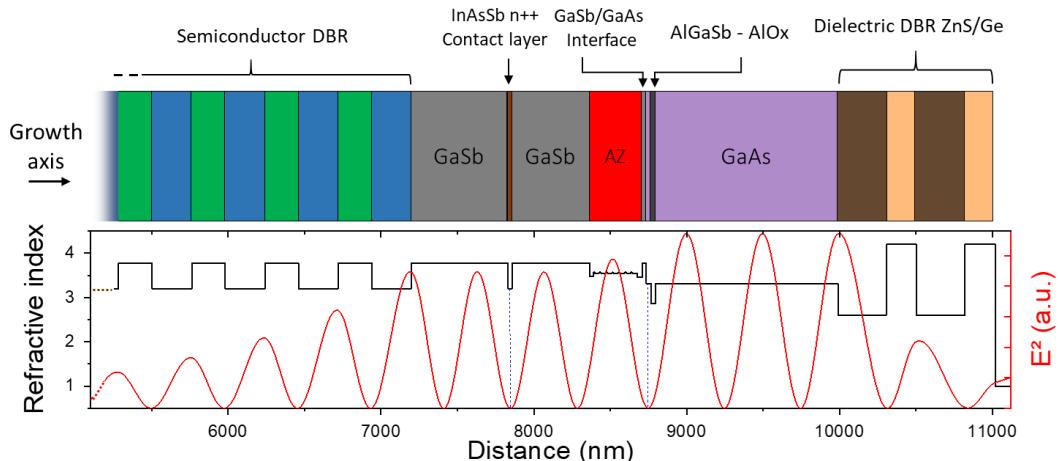


Figure IV-4 - Scheme of the RCLED-B structure with the refractive index profile (black) and the EM intensity distribution (red).

IV.2.2 Structural and optical properties

IV.2.2.1 TEM characterizations

The structural properties of the RCLED-B were investigated using transmission electronic microscopy (TEM) at the Center for Nanoscience and Nanotechnology (C2N) in Palaiseau by the team of Dr. Gilles Patriarche. The Figure IV-5 shows the TEM cross section of the RCLED. We can observe clearly the AlAsSb/GaSb DBR, the n++ InAs bottom contact layer, the seven active stages, the metamorphic interface and the Al(Ga)As layer.

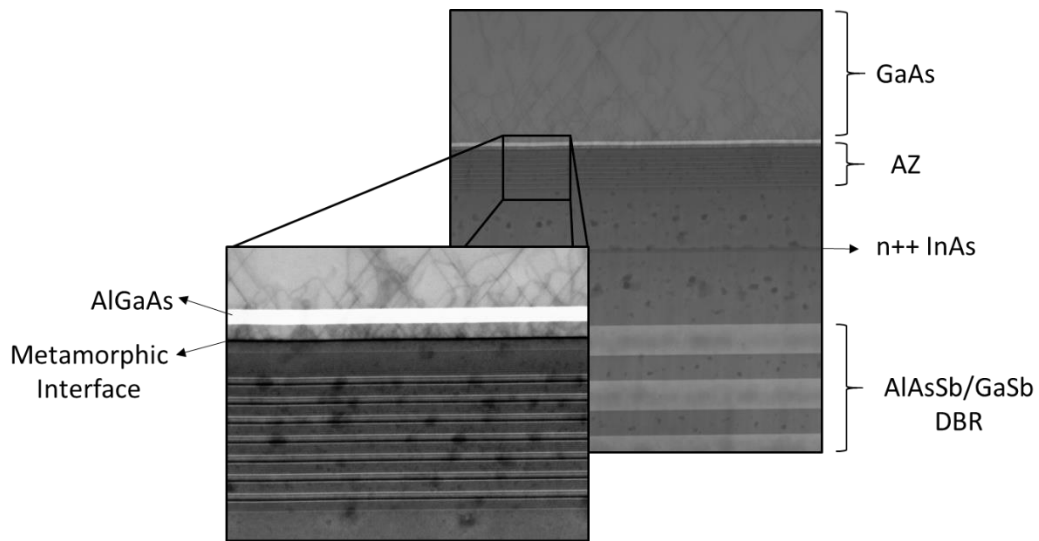


Figure IV-5 - Transmission electron microscopy (TEM) cross-section view of the RCLED showing the different parts of the epitaxied structure

Figure IV-6 clearly demonstrates that the misfit dislocations do not extend from the GaAs/GaSb interface to the active region, as it was observed in metamorphic GaAs/InP structures [220], and remain confined to the arsenide layers.

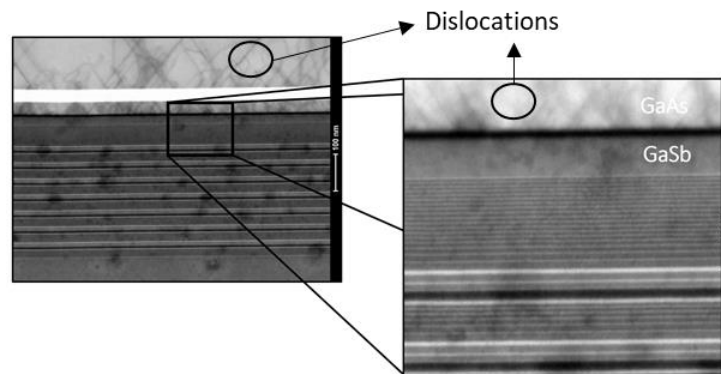


Figure IV-6 - TEM cross-section views of the RCLED showing dislocations propagating above the GaSb/GaAs metamorphic interface

Figure IV-7 shows a TEM picture focused on one stage of the active zone. We can clearly distinguish the different layers within one stage. In this TEM mode, the AlSb barriers are bright whilst the InAs QWs and the GaSb layer are darker. Unfortunately, the W QWs is not clearly visible and the GaInSb layer appears mixed with the InAs layers. The layer thicknesses were compared to the band diagram for emission at $3.3 \mu\text{m}$. The TEM picture displayed in Figure IV-7 shows good agreement between the real structure and the targeted thicknesses.

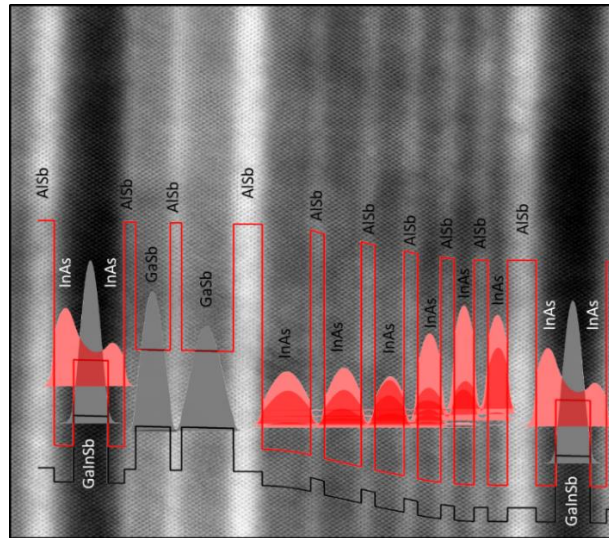


Figure IV-7 - Calculated band structure and squared wave functions of active region overlaid on top of one active stage TEM image from the RCLED-B

IV.2.2.2 Reflectivity

Figure IV-8 shows the measured and calculated reflectivity spectrum of the RCLED-B. The reflectivity spectrum exhibits a DBR centered at $3.32 \mu\text{m}$ with a resonant dip at $3.26 \mu\text{m}$. This detuning between the DBR and the cavity mode implies a reduction on the cavity thickness of around 3%.

IV.2.1 RCLED-B Processing

The RCLED-B contains all the components of a VCSEL including two DBRs. Thus, the process described in this section is the same that will be employed for VCSEL structures.

The process was carried out at LAAS, in collaboration with the Dr. Oleksandr Stepanenko, post-doc in the framework of the MIMIC-SEL project. I was involved directly in the devices manufacture during my stay at LAAS.

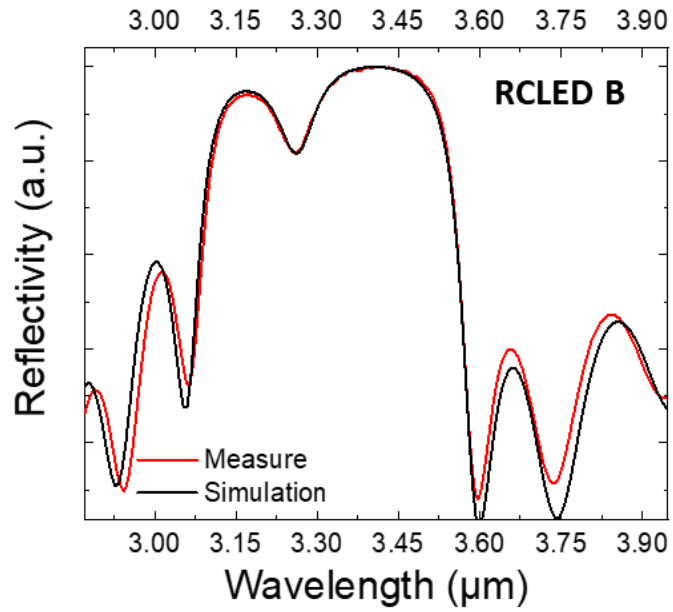


Figure IV-8 - Experimental and simulated top reflectivity spectrum of the RCLED-B epitaxial structure without the top dielectric DBR.

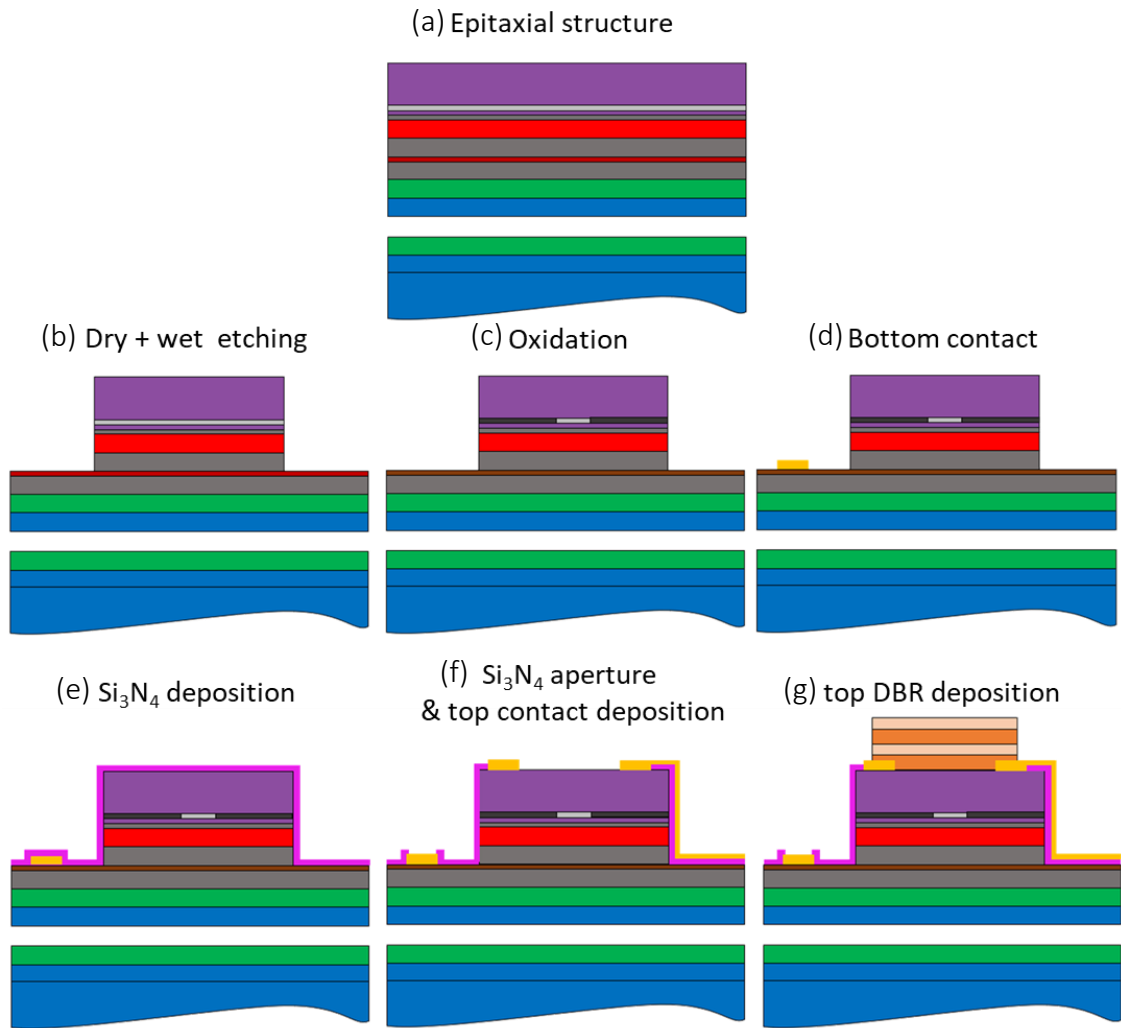


Figure IV-9 - Technological steps of vertical cavity surface emitting devices (RCLED or VCSEL) processed at LAAS

First, the epitaxial structure was cleaned following the same steps described in section II.4.1 of the Chapter II. Then, circular mesas were defined by UV photolithography using SPR700 positive photoresist. It was spin coated on the sample at 1500 rpm creating a $\sim 2 \mu\text{m}$ thick photoresist. The sample was exposed to the UV light using $190 \text{ mJ}/\text{cm}^2$ with a MA6 4th generation mask aligner. The pattern consisted of 16 circles placed in a square region 4 by 4 with dimensions ranging from 25 to 55 μm diameter at a 2 μm pitch. Then the UV-insulated parts of the resist were removed with MFCD 26 developer.

After the pattern development, the uncovered region was etched down to the GaSb layer below the active zone. For this, we used chlorine-based inductively coupled plasma reactive ion etching (ICP-RIE) providing an etching depth of 1.6 μm in 5 minutes ((b)).

After dry etching, we used the MFCD 26 developer which is a tetramethylammonium hydroxide (TMAH) based solution diluted 2.5% with water. To etch the last part of the GaSb layer the etching was stopped at the n^{++} InAsSb layer as this solution doesn't react with In-based materials, which can be controlled by the surface color change.

After this step, a thermal selective lateral oxidation process of the Al-rich AlGaAs layer was performed as displayed in (c). This oxidation provides the electrical confinement necessary for the lateral control of the current. It also suppresses the surface recombination on mesa edges, which is usually high on GaSb [136], [140], [221], [222]

The oxidation consists to expose the sidewall of the mesa, specifically the AlGaAs layer, to a flow of water vapor at a temperature of 400°C [136], [137]. The wet oxidation chemical reaction is very selective regarding to the Al composition of the layer. This allows deeply oxidizing a very thin layer of the order of a few tens of nanometers thick. This makes it possible to deeply oxidize (a few tens to a few hundred micrometers) a very thin layer of the order of a few tens of nanometers thick. This oxidation is carried out using a furnace in which hydrogenated nitrogen charged with water circulates in the chamber to cause the diffusion and reaction of the water molecules through the layer [223] [224].

Figure IV-10 shows near-infrared microscopic images of mesas with circular and rectangle shape before and after the oxidation process that can be recorded with a real-time in-situ monitoring optical system [225]. The two pictures are separated in time by 2 h and we can estimate an oxidation front progression of $\sim 0.17 \mu\text{m}/\text{min}$. The visible aperture allows us to

follow the evolution of the oxidation front shape during the whole process. After oxidation, the aperture diameters for the RCLED-B spanned from 5 to 35 μm incremented by a step of 2 μm .

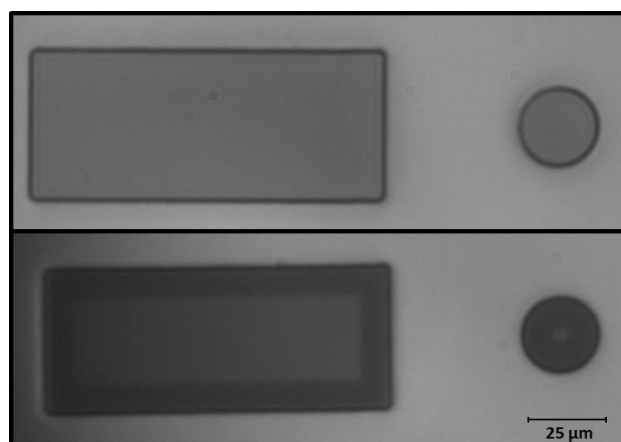


Figure IV-10 - Optical image of a 25 μm diameter and 50 μm x 150 μm rectangle RCLED mesas before and after the oxidation process.

Then, we carried out another photolithography to deposit 20/400 nm of Ti/Au for the bottom contact ((d)). As explained in Chapter I, this photolithography should be suited to the metal deposition technique. At LAAS, we used evaporation technique which allow a directional deposition of the metal. Thus, we employed the nLOF negative photoresist as metallization mask.

After the metallization, we deposited 300 nm-thick Si_3N_4 by PECVD to passivate and protect the mesas ((e)). Subsequently, we performed another photolithography to open the dielectric on the circular part of the top metal contacts as well as the top part of the mesas as depicted in (f). The photolithography for this opening was performed using the AZ4562 positive photoresist. After the developing, CF_4 based RIE (pressure 5 mTorr, RF 40 W, CF_4 40 sccm) was carried out to etch the dielectric. Later, contact pads for top metallic contacts were deposited. The metal pattern was deposited at the angle of 90° to the bottom contact to avoid any short circuit between top and bottom contacts ((f)). Finally, photolithography with the nLOF negative resist was performed to define a mask for the top DBR deposition and its subsequently lift-off. The aperture diameters were 150 μm for all devices. Afterwards the sample was separated into two pieces; one was sent to FOTON for deposition of 2 pairs of ZnS/Ge top DBR by sputtering ((g)) and another part of the wafer was kept for electro-optical measurements.

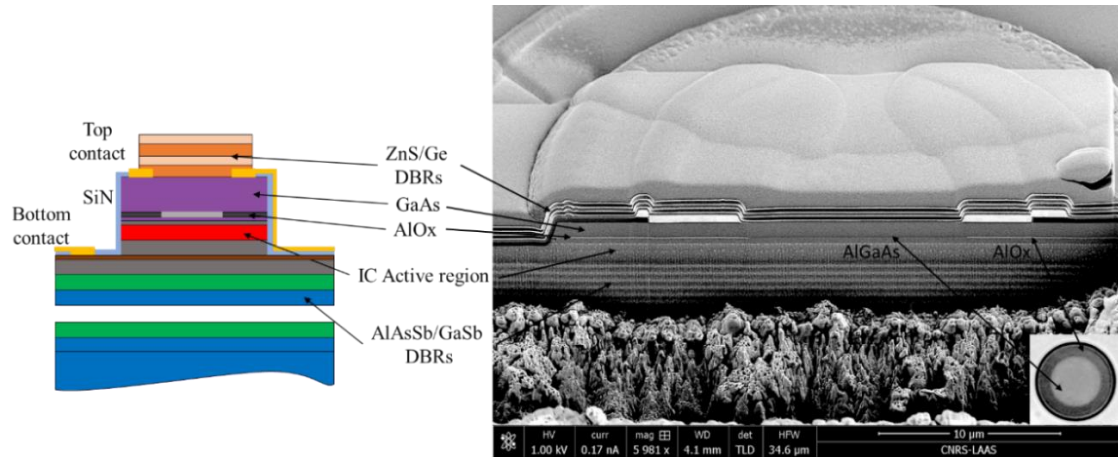


Figure IV-11 - Schematic and Scanning Electron Microscopy (SEM) picture of a cross section of the RCLED-B after processing - Inset: Top optical picture of a 55 μm mesa after oxidation.

Figure IV-11 shows a SEM picture of a cross section of the whole RCLED-B structure after processing. The inset depicts an optical picture of a 55 μm mesa after oxidation. In both pictures, the oxidation front is clearly visible and goes beyond the contact ring to ensure an efficient current confinement.

Afterwards, the samples were sent back to the IES for electro-optical measurements.

IV.2.1 Electro-optical characterizations of RCLED-B

The measurements were performed under CW operation using a thermoelectrically-controlled stage. Figure IV-12(a) shows the CW P-I-V characteristics at 20°C for different oxide aperture diameters. The turn-on voltage for all IC-RCLEDs at 20°C is around 4.5 - 5 V, which is higher than the expected value for the IC active region ($N \times E_g$) and may be attributed to the GaSb/GaAs junction or to a low performance of the contact on the metamorphic GaAs layer. The optical power increases with the device oxide aperture. It varies between 9 μW at 9 mA to 60 μW at 36 mA, respectively for 5 and 35 μm oxide aperture diameter. As presented in Figure IV-12(b), when the aperture diameter increases from 5 to 35 μm , the differential series resistances decreases from 115 to 10 Ω , similar to the values obtained for oxide-apertured GaAs VCSELs [226]–[228] and mid-IR-emitting implanted InP VCSELs [229] demonstrating efficient lateral electrical confinement. This parameter was fitted using the relationship 4.1:

$$R_S = R_L + R_V \quad (4.1)$$

where R_L is lateral resistance, given by the equation 4.2:

$$R_L = \rho_L / \pi D_a \quad (4.2)$$

and the vertical resistance

$$R_V = \rho_V / \pi D_a^2 \quad (4.3)$$

with D_a the aperture diameter, where $\rho_L \sim 1200 \Omega \cdot \mu\text{m}$ and $\rho_V \sim 1000 \Omega \cdot \mu\text{m}^2$

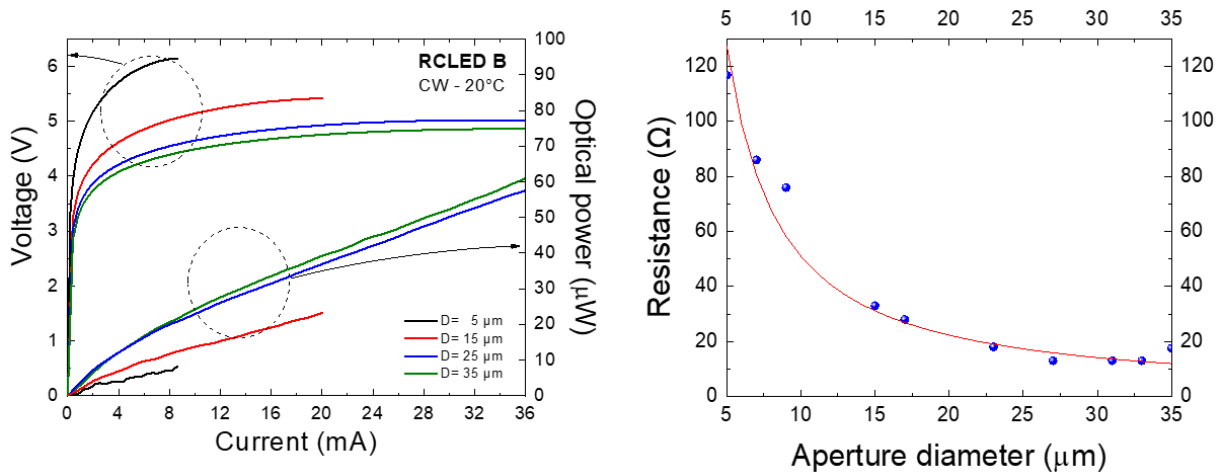


Figure IV-12 - CW L – I – V characteristics, and (b) series resistance for RCLEDs as a function of the aperture diameter ranging from 5 μm to 35 μm.

For comparison, the RCLED B without top Bragg mirror was also characterized. The power measured from RC-LEDs with the top DBR is two times higher than the half structures as depicted in Figure IV-13. This behavior demonstrates the effectiveness of light amplification by the microcavity formed by the 2 DBRs this time (semiconductor bottom and Ge/ZnS top DBRs).

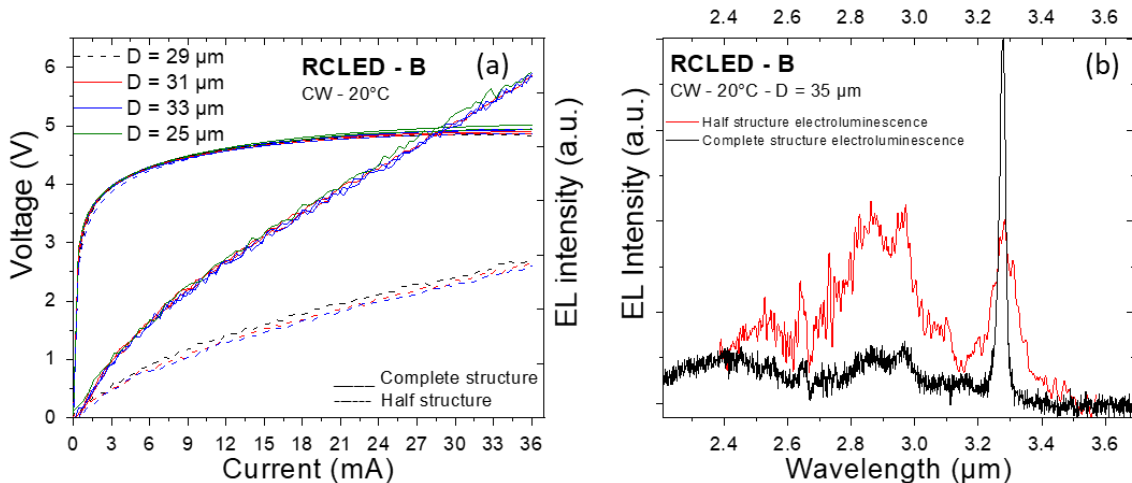


Figure IV-13 - (a) CW L – I – V characteristics of the RCLED. Dash curves show the devices characteristics without top DBR and bold curves the complete RCLED structure. (b) Spectra of two 35 μm aperture oxide RCLED device with (black) and without (red) top DBR.

Figure IV-13, shows the electroluminescence spectra (EL) of an RCLED-B with and without top DBR. We can notice that the optical emission at shorter wavelengths between 2.6 – 3.1 μm is modulated by the top DBR and enhanced at 3.28 μm .

The RCLED-B EL spectrum presents a narrow peak at 3.28 μm that matches perfectly with the microcavity resonant mode of the simulated reflectivity shown in Figure IV-14.

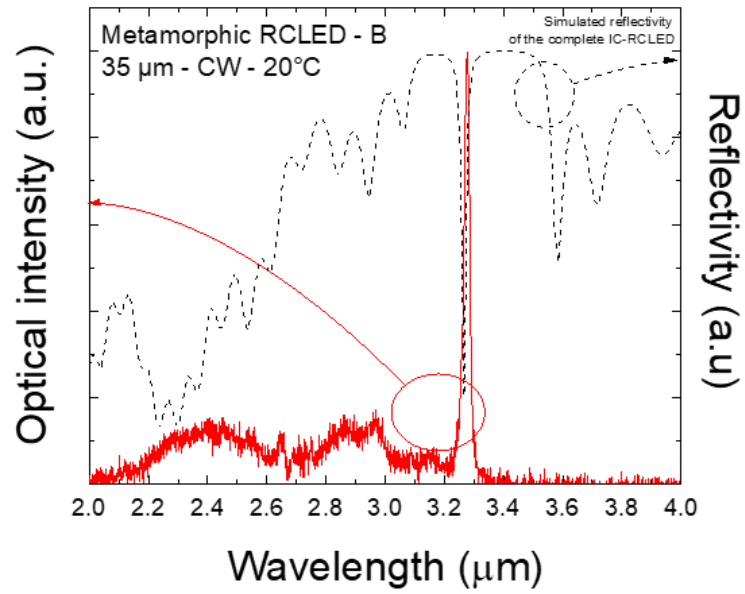


Figure IV-14 - Emission spectra of a 35 μm oxide aperture RCLED-B at 20°C in CW and simulated reflectivity of the whole RCLED-B

Figure IV-15 shows the P-I-V and the electroluminescence (EL) spectra at different temperatures between 20°C and 80°C for the RCLED-B.

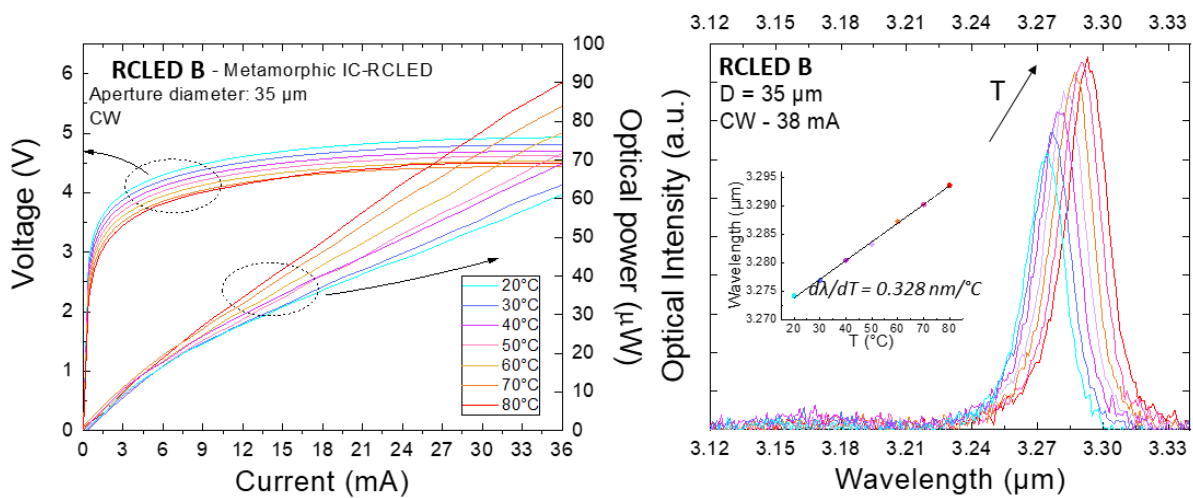


Figure IV-15 - CW P – I – V characteristic (a) and electroluminescence spectra (b) for an RCLED of the structure M with a 35 μm diameter aperture given at different temperatures. Inset shows the temperature dependence of the wavelength. Solid line represents a linear fit to the data

In the temperature range (20 – 80°C), the turn-on voltage varied between 4.1 V and 3.5 V, due to the band gap temperature variation, whereas the series resistance remains essentially constant at ~10 Ω. It is interesting to note that the EL intensity increases with temperature, which can be attributed to a better alignment of the peak of the spontaneous emission in the IC active region with the microcavity resonance. The intensity of the RCLED emission increased with the temperature in the studied range by a factor of ~ 1.35 while maintaining the same FWHM of ~ 20 nm. The measured emission linewidth is about 20 times smaller as compared to the conventional IC-LED in the whole studied temperature range. Another advantage of this RCLED is a better temperature stability of the emission wavelength. Indeed, as it is shown on the inset of the Figure IV-15(b), the emission peak wavelength linearly increases with a rate of ~ 0.32 nm/°C, which is considerably lower than the temperature shift those measured for IC-LED [207] and very similarly than other Sb-based VCSELs [5] [6]. Contrary to the IC-LED where the tunability of about 1.37 nm/°C [207], that is related to the band gap variation with temperature, in RCLEDs the low tuning rate is due to the slow temperature dependence of the refractive indices of the materials forming the optical cavity.

The electro-optical performances of the RCLED demonstrate the relevance of our developments and the next step is the application of the design and the process developed for RCLED on VCSEL structure.

IV.3 First IC-VCSEL structures

IV.3.1 Design

The first VCSEL (named VCSEL-A) structure was similar to the RCLED-B, except it was composed of 24 pairs of $1 \times 10^{17} \text{ cm}^{-3}$ N-doped $\lambda/4$ GaSb and $\text{AlAs}_{0.08}\text{Sb}_{0.92}$ layers and a $11\lambda/4$ -thick anti-resonant optical cavity. As already mentioned, this doping concentration in the DBR leads to low optical losses [133] providing a theoretical maximum reflectivity seen from the cavity as high as 99.97 %. The cavity consisted of a 1 μm-thick GaSb layer Te-doped with a concentration of 10^{17} cm^{-3} increased at 10^{18} cm^{-3} at the nodes of the electric field to minimize the free carrier absorption. A 30 nm-thick InAsSb layer with a doping concentration of 10^{19} cm^{-3} is placed at the second node to act as bottom contact layer. The active region consists of seven IC-active stages designed for an emission at 3.3 μm. On the upper side of the cavity, the metamorphic GaAs layer (25 nm) was grown, with the GaSb/GaAs interface placed at the first

node of the electrical field. Then a 20-nm-thick $\text{Al}_{0.98}\text{GaAs}$ layer is grown next to this interface to realize the electrical confinement layer. Finally, the antiresonant cavity is closed with a 950 nm-thick GaAs layer to ensure an efficient lateral current spreading. This layer is modulation doped, to obtain good electrical and optical performance. The GaAs is doped with a concentration of $9 \cdot 10^{18} \text{ cm}^{-3}$ at the nodes of the electric field, whilst it is doped at 10^{18} cm^{-3} elsewhere. In this anti-resonant structure, the surface was also at a node which allowed us to highly dope the contact layer. The total thickness of this half VCSEL structure is of $13.5 \mu\text{m}$.

IV.3.2 Optical properties

Figure IV-16 shows the measured reflectivity spectrum of the half-VCSEL A. The DBR stop band is well centered at $3.3 \mu\text{m}$. The simulated reflectivity spectrum is inserted in the same figure. The antiresonant cavity dips should be placed on each side of the stop band, but they are slightly shifted to higher wavelengths. Following the simulations, this wavelength shift is due to the increase of the cavity thickness of about 7% compared with the target value.

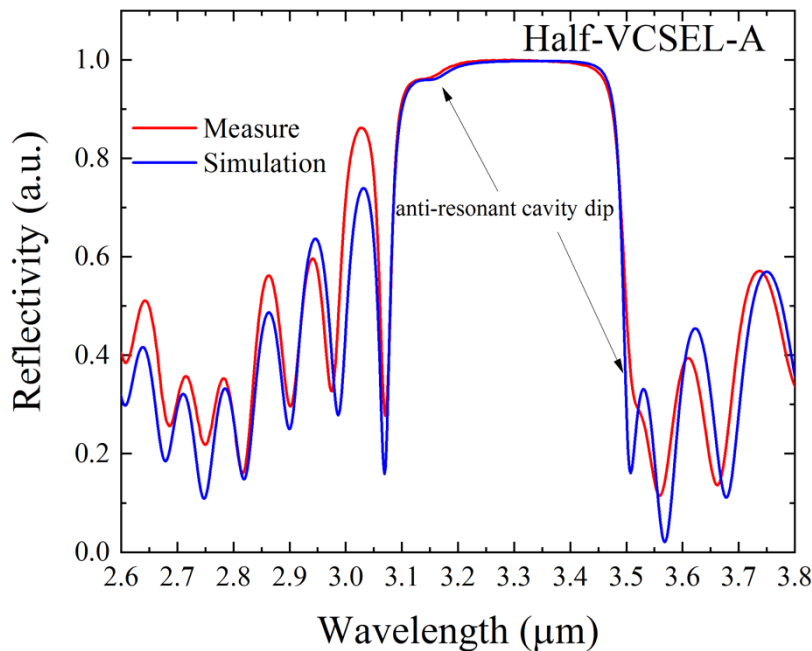


Figure IV-16 - Experimental and simulated top reflectivity of the semiconductor part of the VCSEL-A

In this case the cavity mode can be adjusted with an additional dielectric compensation layer deposited before the top Bragg mirror.

Afterwards, this VCSEL structure was processed at LAAS and FOTON following the technological steps described for the RCLED-B (see paragraph IV.2.3). For this structure, it is

important to notice that the growth of the active zone was similar to this of the RCLED-A and -B. However, we have observed for these structures a peak emission wavelength well shorter than $3.3 \mu\text{m}$. Thus, the compensation layer and the top DBR was designed for $3.2 \mu\text{m}$, and was composed of 40 nm of Ge following by four pairs of ZnS/Ge DBR.

Figure IV-17 displays the experimental and the simulated reflectivity spectrum of the VCSEL-A after the whole process along with the reflectivity of the as-grown wafer. The microcavity is well positioned at $3.2 \mu\text{m}$. The simulation of the reflectivity of the whole structure performed by FOTON before the deposition of the dielectric fits perfectly with the reflectivity of the processed VCSEL.

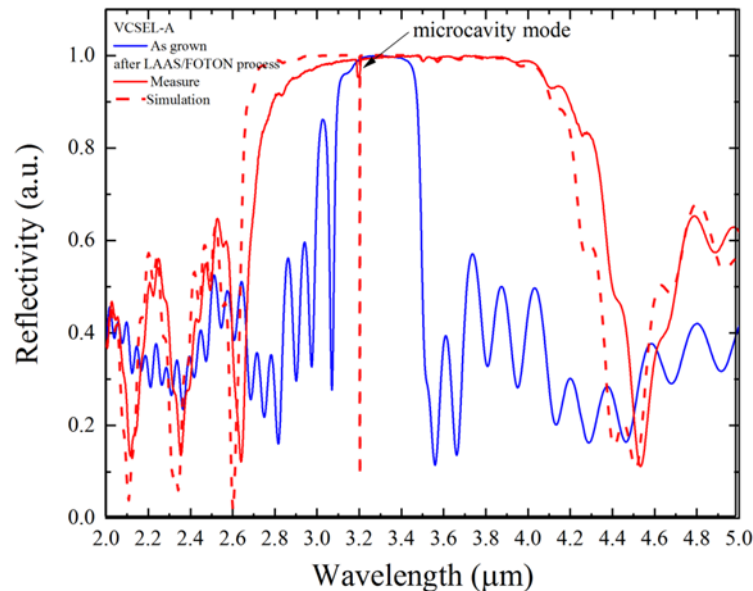


Figure IV-17 - Experimental and simulated reflectivity of the VCSEL-A after process at LAAS and FOTON together with the as grown structure.

IV.3.3 Electro-optical properties

Figure IV-18 shows the CW L – I – V at 20°C of several VCSEL devices with a mesa diameter of $55 \mu\text{m}$ and an oxide diameter aperture of $35 \mu\text{m}$. The I -V presents a turn-on voltage at 4 V , but it appears after an injection current of 9 mA . The I(V) curve shows current leakage before the turn-on. Moreover, a very weak and noisy EL signal was measured. The same behaviors were observed for smaller devices.

The Figure IV-19 shows that the emission occurs mainly between 2.1-3.1 μm and only a very weak emission takes place at 3.2 μm .

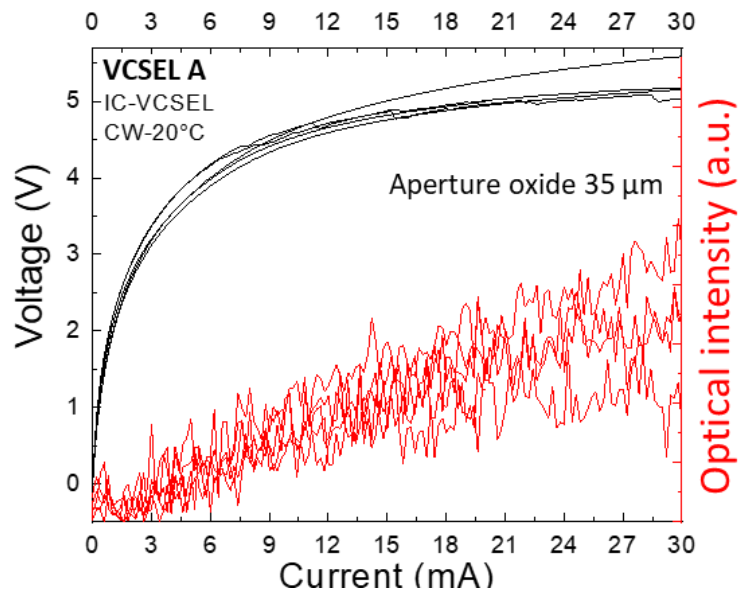


Figure IV-18 - L-I-V characteristics of a 35 μm device with 35 μm aperture oxide of the VCSEL A.

This demonstrates a clear misalignment between the optical gain from the active zone and the cavity design.

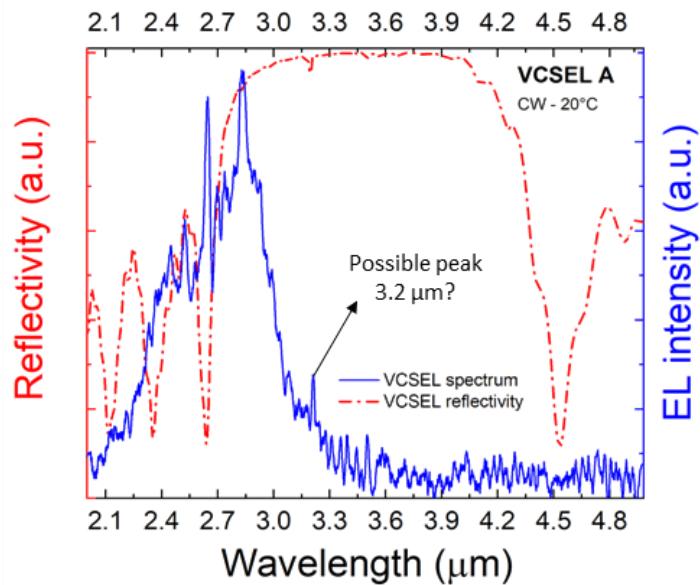


Figure IV-19 - Emission spectra of a 35 μm oxide aperture VCSEL-A at 20°C in CW and reflectivity of the whole VCSEL-A.

IV.3.4 Discussions on VCSEL-A issues

IV.3.4.1 Current leakage

While we have observed a usual electrical behavior on the RCLED-B, the similar VCSEL-A exhibited poor electrical properties. The only difference between the two structures was on the first dielectric layer deposited on top of the semiconductor part. Indeed, it was ZnS for the RCLED-B and Ge for the VCSEL-A. In the Figure IV-20 displaying a SEM cross section picture of the final VCSEL-A.

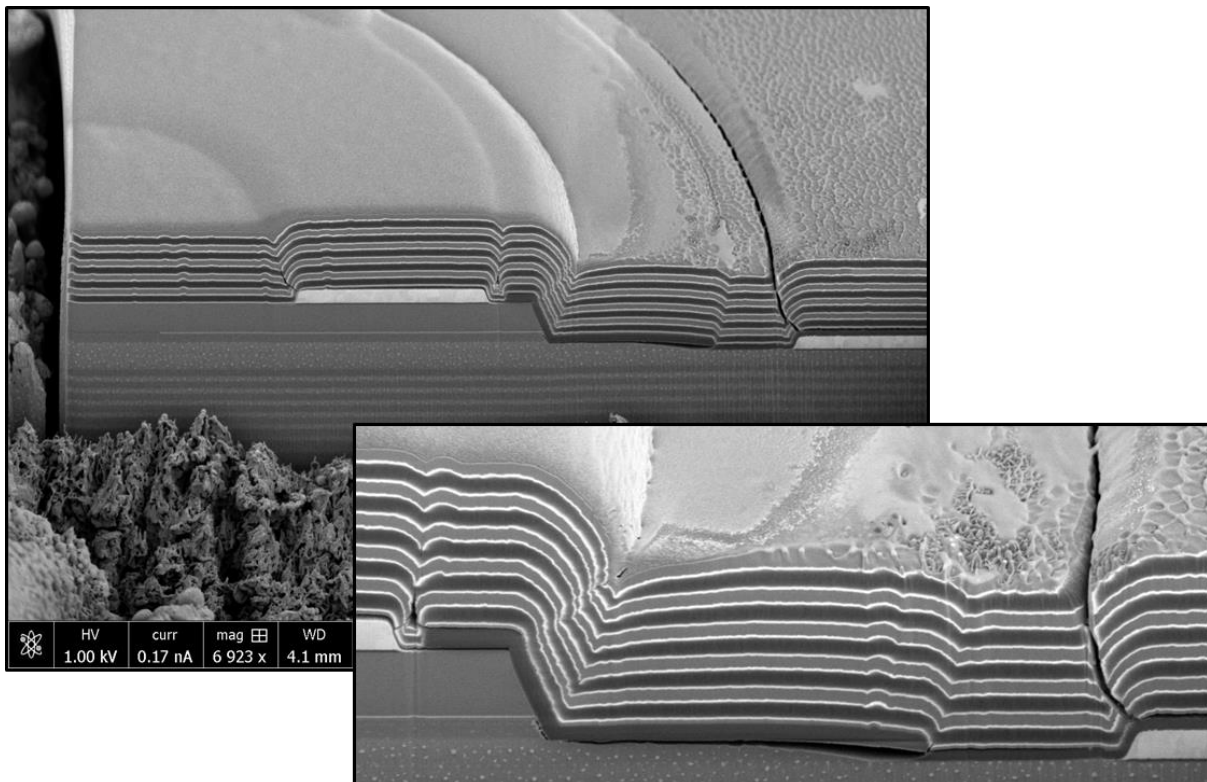


Figure IV-20 - SEM cross section of VCSEL A - High relief due to the top DBR diameter

We can observe that the high relief due to the mesa can cause discontinuities in the Si_3N_4 insulating layer. Then the first layer of the DBR or compensation layer can overlap both top and bottom contact. If this layer is conductive, it could generate current leakage and even short circuits. For that reason, FOTON carried out I-V measurements to extract the electrical resistivity of a Ge and a ZnS layers. On a Si substrate a Ti/Au metal layer was deposited by sputtering. Then, a $\lambda/4$ -layer thick of Ge or ZnS were sputtered. Then, circular Ti/Au contact with different surface were evaporated on the surface of the dielectric.

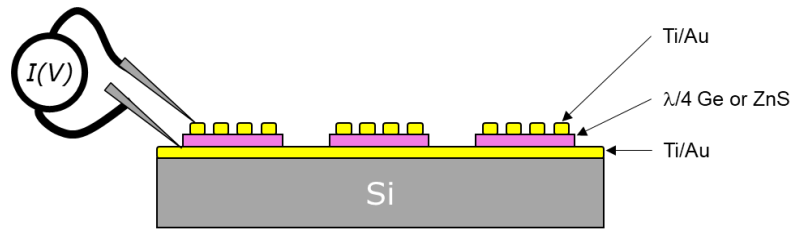


Figure IV-21 – Scheme of the I(V) measurement of a $\lambda/4$ thick dielectric layer.

Figure IV-21 illustrates the measurement set-up.

The measurements demonstrate that ZnS is completely insulating with an electrical breakdown between 40 and 60 V which means a breakdown electric field of 1 ~1.5 MV/cm. On the other hand, it was possible to measure an electrical resistivity for the Ge. The Figure IV-22 displays the evolution of the electrical resistance as a function of inverse of the surface. The experimental data can be fitted with a resistivity of 190 Ω .cm.

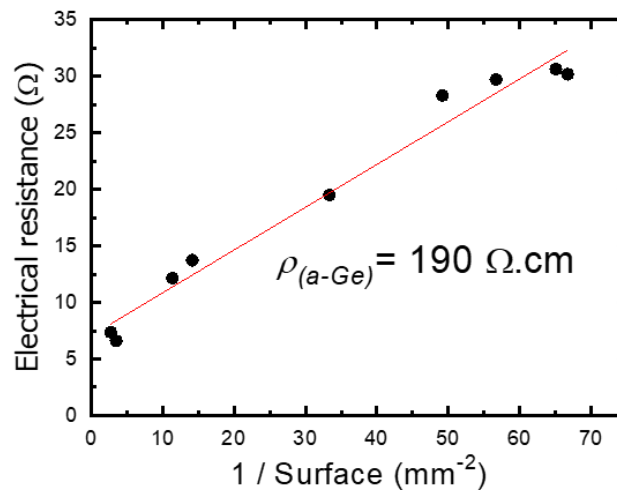


Figure IV-22 – Electrical resistance of a $\lambda/4$ thick Ge layer

This value is far lower compared to the typical dielectric materials as Si_3N_4 and SiO_2 with resistivities around 10^{14} and 10^{16} Ω .cm. [230]. These results could explain the leakage current observed in the I-V characteristics of the VCSEL-A.

To overcome the electrical issue, it is mandatory to avoid the overlap of the Ge layer with the bottom and the top contacts. The deposition of the dielectric DBR must be constrain on the top of the mesa. Thus, the aperture on the photoresist before the DBR dielectric deposition have to be adapted to the diameter of the mesa.

IV.3.4.2 Cavity-gain offset

The relative position of the cavity gain peaks is very important in VCSELs. If the former depends on the cavity optical length the latter depends on the QWs thickness. Therefore, both are dependent of the MBE growth rate variations. Thus, it is very difficult to match the gain peak with the cavity mode when the whole epitaxial structure is grown in a single sequence especially when the growth of the semiconductor DBR takes more than 15 hours. In order to prevent this problem of mismatch, it is possible to divide the growth in two steps [231]. The semiconductor DBR is grown first and then the DBR central wavelength is determined by reflectivity. The flux of the different elements in the MBE are adjusted to perform the adequate regrowth of the cavity and the IC-active stage activates. Besides, it is possible to grow an active region containing only the W-QWs to do PL measurement and refine the thickness of the W-QWs.

IV.4 Optimized VCSEL structure

A new VCSEL structure, named VCSEL-B, was fabricated considering the results obtained on the VCSEL – A structure.

IV.4.1 Bragg mirror and W-MQW PL structure

For the VCSEL-B, the DBR was grown first for optical characterization. The measured reflectivity is shown in Figure IV-23 along with the simulated curve.

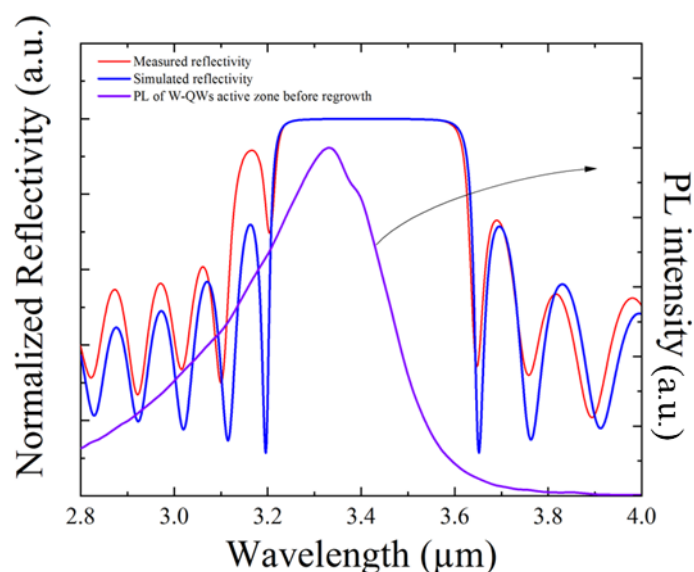


Figure IV-23 - Experimental and simulated top reflectivity of the bottom DBR with the PL of a W-QW active region at RT

The DBR is centered at 3.4 μm , slightly shifted compared with the expected value. The experimental curve could be well fitted with a 2.6 % of thickness increase on both materials of the DBR. (Figure IV-23)

Afterwards, an active region containing five W QWs designed for a peak emission at 3.35 μm was grown. The PL emission of this active region is presented in together with the reflectivity of the DBR. A strong and well-defined PL peak around 3.33 μm can be observed, with a shoulder at 3.39 μm . It was demonstrated that the optimum gain-offset to reach the minimum threshold at RT in CW for GaSb-based VCSEL emitting at 2.6 μm is 60 nm [232], [233]. The tuning rate is due to the temperature dependence of the refractive indices of the materials forming the optical cavity. The maximum is shifted from the center of the DBR by 70 nm which is optimal for VCSEL operation at RT considering the red-shift of the EL peak with the heating.

IV.4.2 Characterization of the half VCSEL

The cavity of the VCSEL-B is similar to that of the VCSEL-A. It was an anti-resonant cavity centered at 3.4 μm . The active zone was exactly the same as the structure characterized by PL. With an anti-resonant cavity, the EL cannot be characterized on the as-grown structure. To verify that the IC-active region emitted at the right wavelength, we grew the similar structure on a GaSb substrate right after the previously regrowth supposed to emit at the same wavelength.

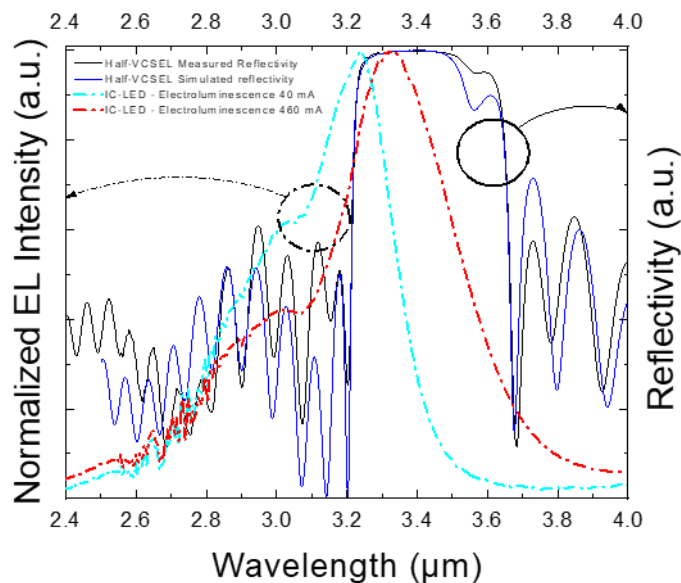


Figure IV-24 - Experimental and simulated top reflectivity of Half-VCSEL as well as the electroluminescence of the IC-LED at 40 and 460 mA.

The reflectivity of the half VCSEL-B is presented in Figure IV-24. It can be seen a dip at $3.55 \mu\text{m}$ related to the antiresonant cavity mode can be seen. The fit of the reflectivity required a reduction of the cavity thickness. The IC-LED was cleaved in a square piece of $5 \text{ mm} \times 5 \text{ mm}$ and directly soldered epi side up with In. A pad of gold-plated alumina was placed on the copper plate to connect the top of the IC-LED. Then, $50 \mu\text{m}$ diameter gold wires were bonded with In on the surface of IC-LED and the alumina pad. The EL at RT in CW of this unprocessed IC-LED is displayed in Figure IV-24. The EL peak emission wavelength shifts from 3.23 to $3.33 \mu\text{m}$ with current increasing from 40 to 460 mA . At any current the EL peak is blue-shifted from the center of the stop band, which is favorable

IV.4.3 Process of the VCSEL-B

The VCSEL-B was processed as the VCSEL-A except for the last photolithography step. The aperture diameter for the deposition of the dielectric DBR was reduced to only overlap the mesa. The lithography was performed by direct laser writing.

Because of the 70 nm offset between the peak EL and the DBR center, the top dielectric was designed to position the microcavity mode at $3.35 \mu\text{m}$. This allows to reduce the gain-cavity offset in operation and place the microcavity close to the maximum of reflectivity of the semiconductor DBR. The dielectric deposition started with a 32 nm thick Ge compensation layer followed by a 4.5 pairs Ge/ZnS providing a maximal theoretical reflectivity of 99.5%.

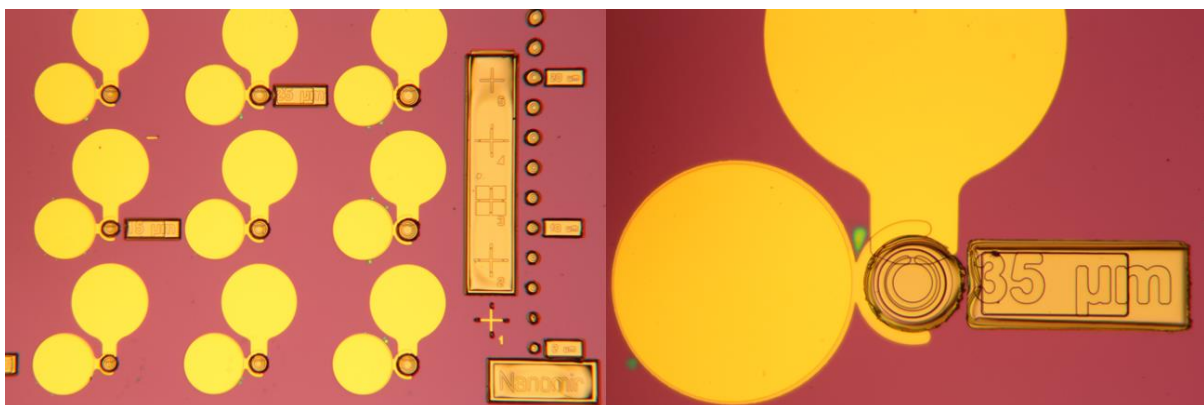


Figure IV-25 – Top optical picture of several VCSEL-B (left) and a $35 \mu\text{m}$ oxide aperture (right) after the whole process.

Figure IV-25 shows optical pictures of the final VCSEL-B devices. As we can see in Figure IV-25(b) the top DBR covers only the mesa surface.

IV.4.4 Electro-optical properties of the VCSEL-B

The Figure IV-26(a) shows the CW L-I-V characteristics of VCSEL-B at 10°C for several mesas with oxide aperture diameters ranging from 7 to 35 μm.

Unfortunately, no lasing was achieved on these devices. However, the I-V shows diode characteristic without any current leakage. This result validates the deposition process of the top DBR. The turn on voltage varies from 4.5 to 6 V when the aperture diameter decreases from 35 down to 7 μm, respectively. Those relatively high values may be attributed to the quality of the Ti/Au contact on GaAs.

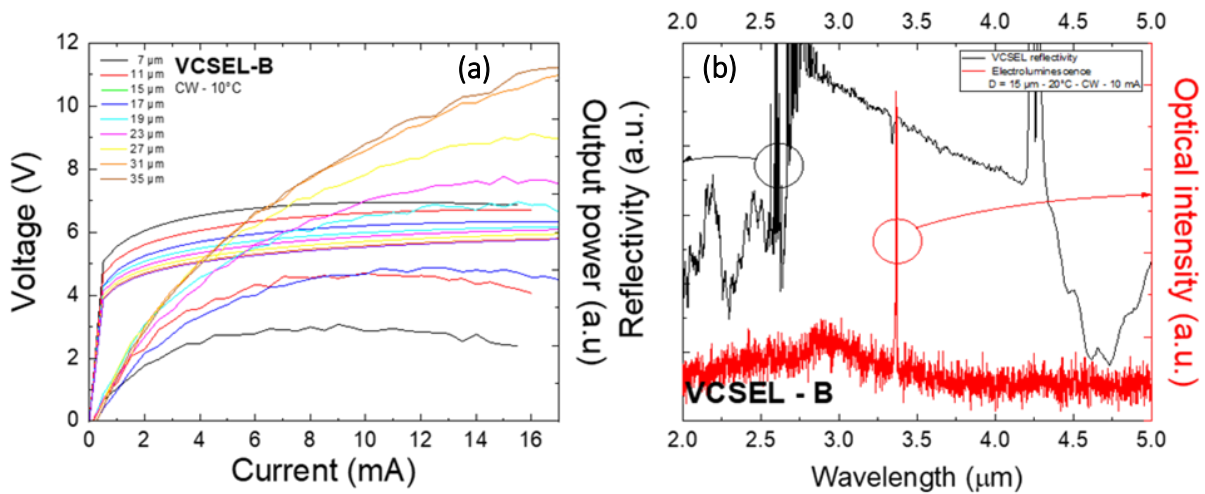


Figure IV-26 – (a) CW L – I – V characteristic for different devices with oxide aperture diameters from 7 to 35 μm and (b) EL spectra of the VCSEL-B devices with a 15 μm diameter aperture together with the top reflectivity.

Figure IV-26(b) shows an emission spectrum of a 15 μm aperture diameter device. It presents a very narrow and intense emission at 3.37 μm. The FWHM of the emitted peak is 4 nm, 5 times smaller as compared to the RCLED-B. The reflectivity is shown in Figure IV-26(b).

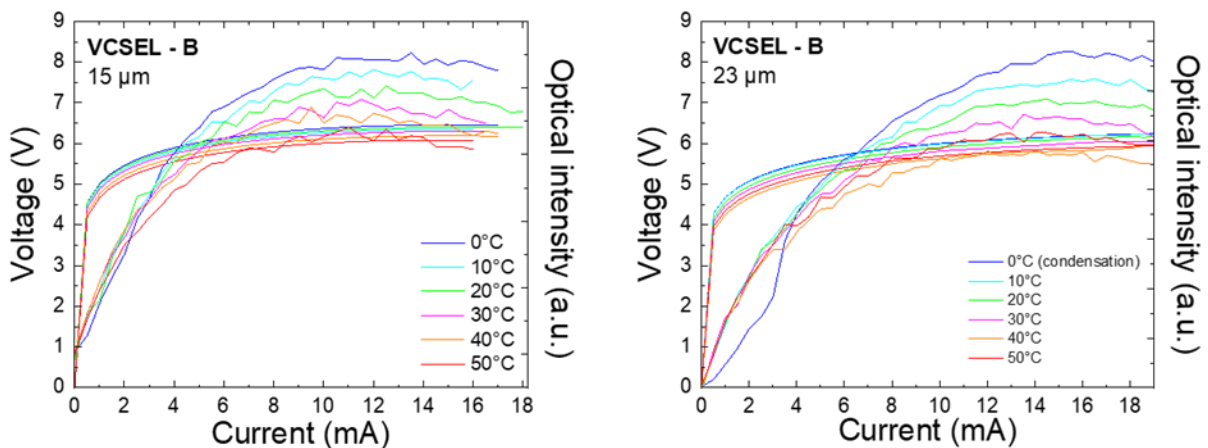


Figure IV-27 - L-I-V characteristics taken at various temperatures in CW for VCSEL-B devices with a 15 μm (left) and 23 μm (right) oxide aperture diameter.

We can notice the microcavity mode located at 3.34 μm . This is 20 nm lower than the emitted wavelength because of the temperature wavelength shift under CW operation

Figure IV-27 reports the CW L-I-V characteristics of two devices at different temperatures.

Figure IV-28 depicts the emission spectra of these two devices. For both structures, it was measured a wavelength shift at constant current of 0.33 nm/K, the same value than the RCLED-B. As observed on the L-I curves from Figure IV-27 and the spectra from Figure IV-28, the EL

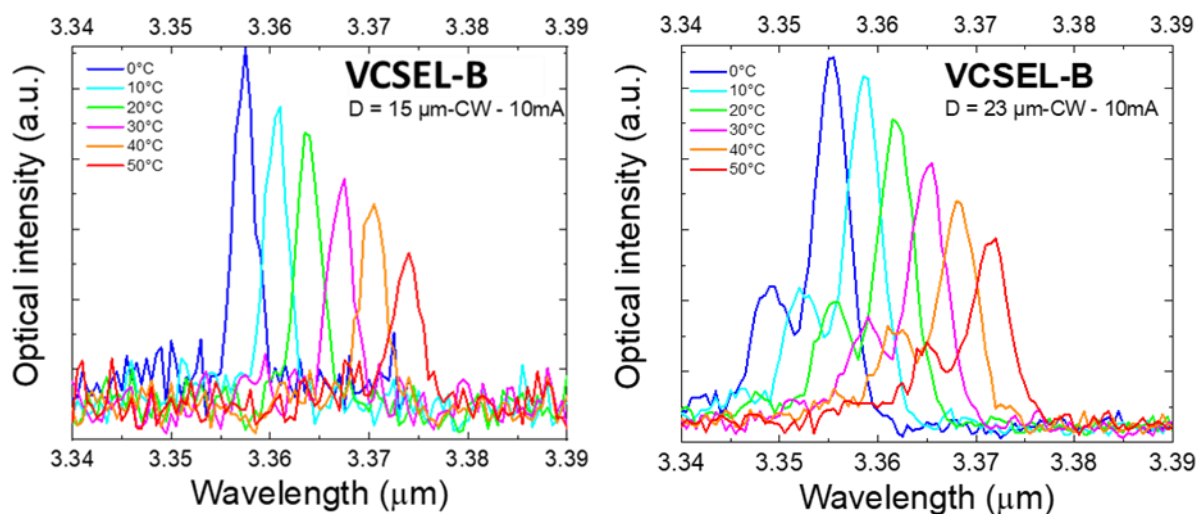


Figure IV-28 - Optical spectra of a 15 and 23 μm oxide aperture diameters devices.

intensity of the emission peak decreases when the temperature increases, which is attributed to the peak emission at longer wavelength than the microcavity resonance. In order to approach the gain peak of the cavity mode we performed measurements in pulsed mode (500 ns/1 kHz) and at low temperature (-15°C), but we did not reach laser threshold.

The presence of a second peak in larger devices can be due to the appearance of high order transverse modes.

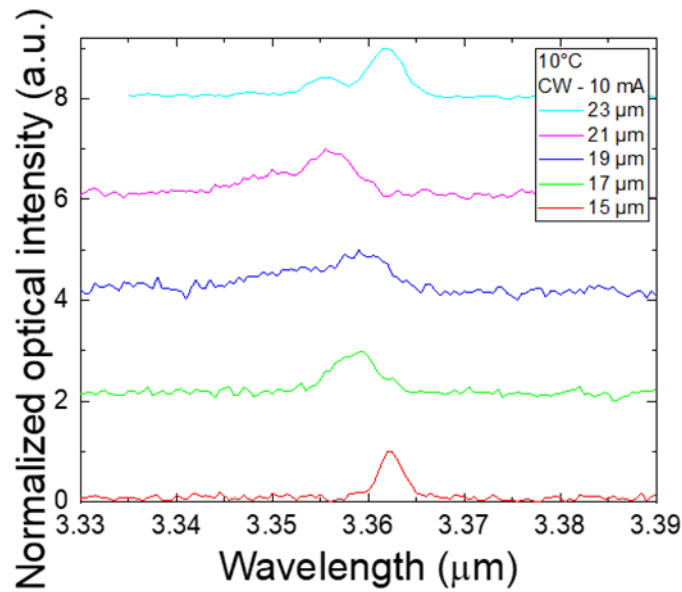


Figure IV-29 - Optical spectrum in CW at 10°C of VCSEL-B devices for various aperture oxide diameters.

To verify this hypothesis, we measured the emission spectra of the devices with oxide aperture ranging between 15 and 23 μm (Figure IV-29). As the diameter increases, the spectrum broadens until the appearance of the second peak for the devices of 23 μm .

IV.5 Conclusions

In summary, we have demonstrated a mid-IR IC-RCLD combining the benefits of both antimonide and arsenide materials and of their processing technologies. The device emitting near 3.3 μm was grown on a GaSb substrate by MBE and operated in CW regime up to 80°C (setup-limited). An electro-optical lateral confinement was applied within the device structure by wet thermal oxidation of an AlGaAs layer metamorphically grown after the active region. It was demonstrated that this metamorphic layer did not affect the crystal quality of the active region of the device. Thanks to this optimal IC-RCLD configuration combining intracavity electrical injection and lateral confinement, the emission spectral width could be reduced to 20 nm, either a factor of 20 smaller compared to a conventional IC-LED. The narrow emission line and its weak shift with temperature make this device attractive for low-cost systems for gas analysis. Afterwards a first antiresonant-VCSEL structure was grown, processed and characterized. This first VCSEL structure presented leakage currents and the emission peak was blue-shifted in comparison to the cavity mode. Compared with IC-RCLD, the only difference was the resonance of the half semiconductor structure. For a resonant structure the first layer of the DBR is ZnS whereas for an anti-resonant it is Ge. We have studied the resistivity of each

material finding a resistivity for the Ge of $\rho_{Ge} = 190 \Omega \cdot \text{cm}$. The possibility to have current leakage increased if the Ge layer overlap the bottom contact. Thus, it was necessary to constrain the DBR deposition only on the top of the mesa device. Thus, a second antiresonant VCSEL structure was designed applying the reduced top DBR diameter. The wavelength emission was supervised with the growth of the structure divided in two steps. The bottom DBR was firstly characterized and then we performed the regrowth of the cavity. An ICL-LED was subsequently grown with the same QWs as the VCSEL structure. After electro-optical characterizations we could approve the reduced top DBR diameters approach but we did not reach the laser threshold. This could be attributed to a redshift misalignment between the peak emission and the microcavity-mode and the reflectivity of the top DBR maybe not sufficient.

Conclusion and outlook

The work presented in this thesis describes the development towards an interband cascade VCSELs for emission at 3.3 and 3.6 μm operating in CW above RT. The VCSELs should exhibit low threshold single-mode operation to be integrated in low cost and low consumption power TDLAS based-photonics sensors. At the beginning of this study, no demonstration of VCSEL operating in CW at RT beyond 3 μm has been reported.

In Chapter 1, different types of semiconductor lasers have been described. Then, in the second part, we focused on the state of the art of semiconductor lasers for emission above 3 μm . We presented the limits of the type-I QWs, mainly due to the Auger effect, and the advantages of type-II QWs lasers, in particular those based on the design called "W". The use of the interband cascade configuration with such "W" QWs provides high performances ICL emitting between 2.8 and 5 μm in CW above RT. Thanks to the nature of the interband transition of the IC active zone, vertical emission is allowed in such devices. Afterwards, a state of the art of mid-IR VCSELs is detailed and different technological challenges for an emission within the chosen spectral range are exposed. At the end we presented the optimal VCSEL structure. It will be based on IC the active region for the active zone with metamorphic oxide lateral confinement scheme and a hybrid DBRs.

Chapter 2 describes the study of the IC active region. A complete technological process of Type-II "W" ICL was developed. ICP-RIE dry etching was used allowing the laser ridges to be etched all down to the bottom cladding and suppressing leakage current. Studies of several ICLs allowed us to identify key parameters of the design and the MBE growth, and to demonstrate ICLs close to the state-of-the-art. However, these devices exhibited high internal losses $\alpha_i \sim 15 \text{ cm}^{-1}$ attributed to the absorption in Te-doped AlGaAsSb cladding layer, ICLs with a threshold current density as low as 220 A/cm^2 was obtained for broad area lasers in pulsed mode at 3.3 μm and CW operation has been achieved for narrow-stripe wide lasers up to 80°C . Better performances were then demonstrated with new ICLs structures using AlSb/InAs cladding layers and threshold current densities reduced to 150 A/cm^2 at 3.6 μm

In chapter 3 we studied and characterized semiconductor and dielectric DBR. We demonstrated that using n-doped AlAsSb/GaSb DBR, a theoretical reflectivity as high as 99.95% can be achieved. For this purpose, an n^{++} -doped InAsSb contact layer has to be integrated within

the VCSEL. To reduce both structure thickness and growth time, it was chosen to employ a top dielectric top DBR made of ZnS/Ge. Then, we developed the technology dedicated for the electro-optical confinement using metamorphic III-As/III-Sb heterostructures. We obtained low resistivity of the metamorphic interface using heavy Te-doping. We have showed that IC-LEDs and ICLs using GaAs metamorphic layer exhibited performances similar to the conventional structures, validating the use of such approach in more complex structures like VCSELs. Once the active zone, the DBRs and the metamorphic interface with the Al(Ga)As layers had been studied separately, we designed the complete vertical structure. In the optimal structure the Al(Ga)As oxidation layer is located at the first node of the electric field above the active region to ensure an efficient electrical confinement.

The chapter 4 is dedicated to the fabrication and the studies of IC-vertical cavity surface emitting devices. We validated the full technological process with the realization of an IC-RLED. The device emitted near 3.3 μm with a linewidth 20 times smaller than that of a conventional IC-LED (20 nm) and operated in CW regime up to 80°C (setup-limited). The good properties of this RLED demonstrated that the metamorphic layer did not degrade the quality of the active region of the device. Subsequently, the first VCSEL structure was grown, processed and characterized. This structure presented high current leakage and an emission blue-shifted in comparison to the cavity mode. The current leakage was attributed to the electrical conductivity of the first Ge layer deposited on the top of the half-VCSEL overlapped with the bottom contact. Another VCSEL was realized with a two steps growth to match the cavity-mode and the IC-active region emission. Finally, the top DBR was sputtered on aperture avoiding deposition of the first Ge layer on the bottom DBR thus preventing the current leakage. However, we did not reach the laser operation. This could be attributed to a misalignment between the emission peak and the microcavity-mode and maybe to an insufficient reflectivity of the top DBR.

In 2019, the University of Santa Barbara, Praevium research Incorporation and Thorlabs Quantum Electronics laboratories realized a VCSEL illustrated in Figure 0-1(a). The structure employed a 33 pairs GaAs/AlGaAs bottom DBR [234]. They demonstrated the first RT CW electrically pumped 3.3 μm IC-VCSEL. It showed a single frequency emission at 3.34 μm in CW regime up to 26°C as presented in Figure 0-1(b) [235].

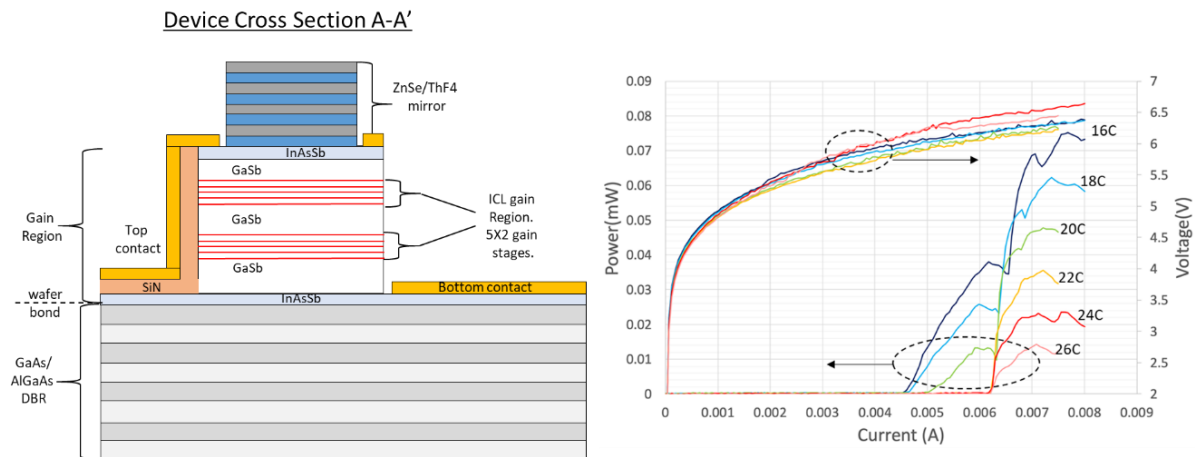


Figure 0-1 - (a) Device cross section of the RT-CW electrically pumped VCSEL emitting at 3.3 μm and fabricated by the university of Santa Barbara, THORLABS and Praeivum incorporation (b) L-I-V in CW regime at various temperature.

This complicated technology required a wafer bonding and the GaSb substrate removal. Despite this very encouraging result, it is still far to spread this technology at industrial level.

Although different advancements have been made, there is ample room for improvement. Practically, it is impossible to exhaust all the design possibilities, but there are several ideas for the future work on our VCSEL.

First, is necessary to add at least one ZnS/Ge couple to the top DBR to increase its reflectivity. On the other hand, since the technology used by the University of Santa Barbara employed 33 pairs for the bottom DBR leading to a maximum of reflectivity of 99.98%, we can also increase the reflectivity of the bottom DBR to reach the value obtained by the University of Santa Barbara to further reduce optical losses.

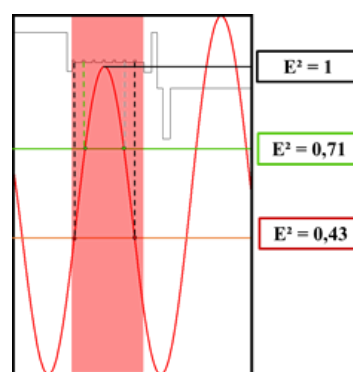


Figure 0-2 - Optical field intensity distribution in the active zone and overlap with the QWs

The second improvement concerns an increase of the optical gain within the VCSEL. As we can see in Figure 0-2, the overlap of the internal optical field intensity with the QWs decreases to 43% on both sides of the IC-active region for the external QWs. We designed a new ICL

structure in which we shortened the electron injector from 6 to 5 InAs/AlSb stacks and the AlSb semimetallic layer thickness in the active zone. The whole thickness reduction is 3.4 nm per period which allowed us to increase the overlap of the active region with the optical field to 52% for the external QWs. The simulated band diagram of one period of the active zone is depicted in (a). This structure was investigated very recently. Figure 0-3(b) shows the L-I-V characteristics in pulsed regime of broad area 100 μm x 2 mm ICL containing seven stages of this active region. The average threshold current density was around 124 A/cm^2 , a value comparable with the state of the art [15]. These results are really promising to be implemented in a new optimized VCSEL.

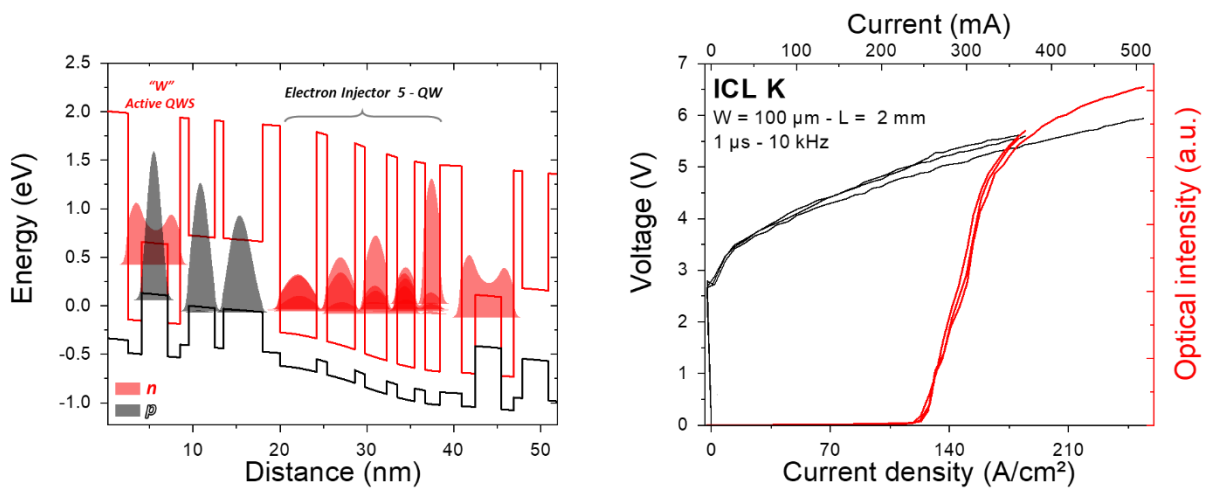


Figure 0-3 - (a) Simulated band diagram of one stage of the ICL K with reduced electron injector and SMIF thickness. (b) Light-current-voltage characteristics of the ICL K measured at RT in pulsed regime (1 $\mu\text{s}/10$ kHz) for a 100 μm broad area ICLs with 2 mm long cavity.

This thesis work resulting in better understanding of the ICL operation and the development of promising technological approaches. The proposed metamorphic structure opens a door to a novel devices concept and functionalities thanks to the mature GaAs technology.

List of publications

Journal papers

1. Z. Loghmari, M. Bahriz, **D. Díaz Thomas**, A. Meguekam, H. Nguyen Van, R. Teissier and A.N. Baranov, "Room temperature continuous wave operation of InAs/AlSb-based quantum cascade laser at $\lambda \sim 11 \mu\text{m}$," Electronics Letters, vol. 54, no. 17, pp. 1045–1047, 2018, doi: 10.1049/el.2018.5258.
2. **D. A. Díaz-Thomas**, O. Stepanenko, M. Bahriz, S. Calvez, E. Tournié, A. N. Baranov, G. Almuneau, and L. Cerutti, "Interband cascade Lasers with AlGaAsSb cladding layers emitting at $3.3 \mu\text{m}$," Optics Express, vol. 27, no. 22, p. 31425, Oct. 2019, doi: 10.1364/OE.27.031425.
3. L. Monge-Bartolomé, T. Cerba, **D. A. Díaz-Thomas**, M. Bahriz, M. Rio Calvo, G. Boissier, T. Baron, J. B. Rodriguez, L. Cerutti, and E. Tournié, "Etched-cavity GaSb laser diodes on a MOVPE GaSb-on-Si template," Optics Express, vol. 28, no. 14, pp. 20785–20793, 2020, doi: 10.1364/OE.397164.

D.A. Díaz-Thomas, O. Stepanenko, M. Bahriz, S. Calvez, T. Batte, C. Paranthoen, G. Patriarche, E. Tournié, A.N. Baranov, G. Almuneau, C. Levallois, and L. Cerutti, "3.3 μm interband-cascade resonant-cavity light-emitting diode with narrow spectral emission linewidth", Semiconductor Science and Technology, vol. 35, no 12, p. 125029, 2020, doi: 10.1088/1361-6641/abbebc.

Communications at conferences

1. **D. A. Díaz Thomas**, J. A. Meguekam Sado, M. Bahriz, E. Tournié, A. N. Baranov and L. Cerutti, "Study of Sb-based Interband cascade active region for mid-IR VCSELs" (poster) 16ème journée de la Nano, Micro et Optoélectronique (poster) (June 2018, France).

2. **D. A. Díaz Thomas**, J. A. Meguekam Sado, M. Bahriz, E. Tournié, A. N. Baranov and L. Cerutti, “Study of Sb-based Interband cascade active region for mid-IR VCSELs” (poster) 34th International Conference on the Physics of Semiconductors (July 2018, France).
3. L. Cerutti, **D. A. Díaz Thomas**, J. A. Meguekam Sado, M. Bahriz, E. Tournié and A. N. Baranov, “Influence of the top AlGaAsSb cladding growth temperatures on the performances of Interband Cascade Lasers grown on GaSb substrate” (poster) 20th International Conference MBE 2016 (September 2018, Shanghai-Chine).
4. **D. A. Díaz Thomas**, J. A. Meguekam Sado, M. Bahriz, E. Tournié, A. N. Baranov and L. Cerutti, “Study of interband cascade lasers for MIR-VCSELs” (poster) 14th International Conference on Mid-IR Optoelectronics: Materials and Devices MIOMD-XIV (October, USA).
5. **D. A. Díaz Thomas**, O. Stepanenko, M. Bahriz, S. Calvez, T. Batte, C. Paranthoen, E. Tournié, A. Baranov, G. Almuneau, C. Levallois and L. Cerutti, “Towards MIR VCSELs operating in CW at RT” (Talk) Compound Semiconductor Week 2019 (May 2019, Japan).
6. Stéphane Calvez, Oleksandr Stepanenko, **Daniel Andres Diaz Thomas**, Thomas Batte, Michael Bahriz, Cyril Paranthoen, Eric Tournié, Christophe Levallois, Alexei Baranov, Guilhem Almuneau, and Laurent Cerutti, “Progress in Interband Cascade Lasers: From Edge Emitting Lasers to VCSELs,” 2020 22nd International Conference on Transparent Optical Networks (ICTON) (July 2020, Bari-Italy)

Bibliography

- [1] I. E. Gordon *et al.*, “The HITRAN 2016 molecular spectroscopic database,” *Journal of Quantitative Spectroscopy and Radiative Transfer*, vol. 203, pp. 3–69, Dec. 2017, doi: 10.1016/j.jqsrt.2017.06.038.
- [2] P. Werle, F. Slemr, K. Maurer, R. Kormann, R. Mücke, and B. Jänker, “Near- and mid-infrared laser-optical sensors for gas analysis,” *Optics and Lasers in Engineering*, vol. 37, no. 2–3, pp. 101–114, Feb. 2002, doi: 10.1016/S0143-8166(01)00092-6.
- [3] U. Willer, M. Saraji, A. Khorsandi, P. Geiser, and W. Schade, “Near- and mid-infrared laser monitoring of industrial processes, environment and security applications,” *Optics and Lasers in Engineering*, vol. 44, no. 7, pp. 699–710, Jul. 2006, doi: 10.1016/j.optlaseng.2005.04.015.
- [4] Q. Peng *et al.*, “Lasers in medicine,” *Rep. Prog. Phys.*, vol. 71, no. 5, p. 056701, May 2008, doi: 10.1088/0034-4885/71/5/056701.
- [5] S.-S. Kim, C. Young, B. Vidakovic, S. G. A. Gabram-Mendola, C. W. Bayer, and B. Mizaikoff, “Potential and Challenges for Mid-Infrared Sensors in Breath Diagnostics,” *IEEE Sensors J.*, vol. 10, no. 1, pp. 145–158, Jan. 2010, doi: 10.1109/JSEN.2009.2033940.
- [6] B. Bird and M. J. Baker, “Quantum Cascade Lasers in Biomedical Infrared Imaging,” *Trends in Biotechnology*, vol. 33, no. 10, pp. 557–558, Oct. 2015, doi: 10.1016/j.tibtech.2015.07.003.
- [7] Á. I. López-Lorente and B. Mizaikoff, “Mid-infrared spectroscopy for protein analysis: potential and challenges,” *Anal Bioanal Chem*, vol. 408, no. 11, pp. 2875–2889, Apr. 2016, doi: 10.1007/s00216-016-9375-5.
- [8] P. Skolik, M. R. McAinsh, and F. L. Martin, “Biospectroscopy for Plant and Crop Science,” in *Comprehensive Analytical Chemistry*, vol. 80, Elsevier, 2018, pp. 15–49.
- [9] S. Wallin, A. Pettersson, H. Östmark, and A. Hobro, “Laser-based standoff detection of explosives: a critical review,” *Anal Bioanal Chem*, vol. 395, no. 2, pp. 259–274, Sep. 2009, doi: 10.1007/s00216-009-2844-3.
- [10] M. B. Pushkarsky, I. G. Dunayevskiy, M. Prasanna, A. G. Tsekoun, R. Go, and C. K. N. Patel, “High-sensitivity detection of TNT,” *Proceedings of the National Academy of Sciences*, vol. 103, no. 52, pp. 19630–19634, Dec. 2006, doi: 10.1073/pnas.0609789104.
- [11] C. Bauer *et al.*, “A Mid-infrared QEPAS sensor device for TATP detection,” *J. Phys.: Conf. Ser.*, vol. 157, p. 012002, Mar. 2009, doi: 10.1088/1742-6596/157/1/012002.
- [12] N. S. Prasad, “Optical communications in the mid-wave IR spectral band,” p. 45.
- [13] L. S. Rothman *et al.*, “The HITRAN2012 molecular spectroscopic database,” *Journal of Quantitative Spectroscopy and Radiative Transfer*, vol. 130, pp. 4–50, 2013.
- [14] A. Vicet, D. A. Yarekha, A. Pérona, Y. Rouillard, S. Gaillard, and A. N. Baranov, “Trace gas detection with antimonide-based quantum-well diode lasers,” *Spectrochimica Acta Part A: Molecular and Biomolecular Spectroscopy*, vol. 58, no. 11, pp. 2405–2412, Sep. 2002, doi: 10.1016/S1386-1425(02)00055-0.
- [15] I. Vurgaftman *et al.*, “Interband cascade lasers,” *J. Phys. D: Appl. Phys.*, vol. 48, no. 12, p. 123001, Apr. 2015, doi: 10.1088/0022-3727/48/12/123001.
- [16] D. G. Revin, J. P. Commin, S. Y. Zhang, A. B. Krysa, K. Kennedy, and J. W. Cockburn, “InP-based midinfrared quantum cascade lasers for wavelengths below 4 μm ,” *IEEE Journal of*

- Selected Topics in Quantum Electronics*, vol. 17, no. 5, pp. 1417–1425, 2011, doi: 10.1109/JSTQE.2011.2128858.
- [17] H. Hora, “Charles Townes, How the Laser Happened: Adventures of a Scientist,” *Laser Part. Beams*, vol. 18, no. 1, pp. 151–152, 1999, doi: 10.1017/S026303460000118X.
- [18] M. A. Shampo, R. A. Kyle, and D. P. Steensma, “Charles Townes—Nobel Laureate for Maser-Laser Work,” *Mayo Clinic Proceedings*, vol. 86, no. 9, p. e48, Sep. 2011, doi: 10.4065/mcp.2011.0496.
- [19] N. Basov and A. Prokhorov, “Theory of the molecular generator and molecular power amplifier,” *Sov. Phys. JETP*, vol. 3, no. 3, pp. 426–429, 1956.
- [20] N. V. Karlov, O. N. Krokhin, and S. G. Lukishova, “History of quantum electronics at the Moscow Lebedev and General Physics Institutes: Nikolaj Basov and Alexander Prokhorov,” *Appl. Opt.*, vol. 49, no. 25, p. F32, Sep. 2010, doi: 10.1364/AO.49.000F32.
- [21] A. L. Schawlow and C. H. Townes, “Infrared and Optical Masers,” *Phys. Rev.*, vol. 112, no. 6, pp. 1940–1949, Dec. 1958, doi: 10.1103/PhysRev.112.1940.
- [22] T. H. Maiman, “Stimulated optical radiation in ruby,” *nature*, vol. 187, no. 4736, pp. 493–494, 1960.
- [23] R. N. Hall, G. E. Fenner, J. D. Kingsley, T. J. Soltys, and R. O. Carlson, “Coherent Light Emission From GaAs Junctions,” *Phys. Rev. Lett.*, vol. 9, no. 9, pp. 366–368, Nov. 1962, doi: 10.1103/PhysRevLett.9.366.
- [24] N. Holonyak Jr and S. Bevacqua, “Coherent (visible) light emission from Ga (As_{1-x}P_x) junctions,” *Applied Physics Letters*, vol. 1, no. 4, pp. 82–83, 1962.
- [25] M. I. Nathan, W. P. Dumke, G. Burns, F. H. Dill, and G. Lasher, “STIMULATED EMISSION OF RADIATION FROM GaAs *p-n* JUNCTIONS,” *Appl. Phys. Lett.*, vol. 1, no. 3, pp. 62–64, Nov. 1962, doi: 10.1063/1.1777371.
- [26] T. M. Quist *et al.*, “SEMICONDUCTOR MASER OF GaAs,” *Appl. Phys. Lett.*, vol. 1, no. 4, pp. 91–92, Dec. 1962, doi: 10.1063/1.1753710.
- [27] M. Ishikawa, Y. Ohba, H. Sugawara, M. Yamamoto, and T. Nakanisi, “Room - temperature cw operation of InGaP/InGaAlP visible light laser diodes on GaAs substrates grown by metalorganic chemical vapor deposition,” *Appl. Phys. Lett.*, vol. 48, no. 3, pp. 207–208, Jan. 1986, doi: 10.1063/1.96796.
- [28] H. Sugawara, M. Ishikawa, and G. Hatakoshi, “High - efficiency InGaAlP/GaAs visible light - emitting diodes,” *Appl. Phys. Lett.*, vol. 58, no. 10, pp. 1010–1012, Mar. 1991, doi: 10.1063/1.104407.
- [29] M. Müller and C. Grasse, “InP-based 1.3 μm and 1.55 μm Short-Cavity VCSELs Suitable for Telecom- and Datacom-Applications,” p. 4, 2012.
- [30] M. Benyoucef, M. Yacob, J. P. Reithmaier, J. Kettler, and P. Michler, “Telecom-wavelength (1.5 μm) single-photon emission from InP-based quantum dots,” *Appl. Phys. Lett.*, vol. 103, no. 16, p. 162101, Oct. 2013, doi: 10.1063/1.4825106.
- [31] S. Nakamura, “Development and Future Prospects of InGaN-based,” *Introduction to Nitride Semiconductor Blue Lasers and Light Emitting Diodes*, p. 317, 2000.
- [32] S. Nakamura *et al.*, “InGaN Multi-Quantum-Well-Structure Laser Diodes with Cleaved Mirror Cavity Facets,” *Jpn. J. Appl. Phys.*, vol. 35, no. Part 2, No. 2B, pp. L217–L220, Feb. 1996, doi: 10.1143/JJAP.35.L217.

- [33] S. Nakamura *et al.*, "Room - temperature continuous - wave operation of InGaN multi - quantum - well structure laser diodes," *Appl. Phys. Lett.*, vol. 69, no. 26, pp. 4056–4058, Dec. 1996, doi: 10.1063/1.117816.
- [34] M. Isshiki and J. Wang, "Wide-bandgap II-VI semiconductors: Growth and properties," in *Springer Handbook of Electronic and Photonic Materials*, Springer, 2017.
- [35] N. Yamada, "GROUP II-VI SEMICONDUCTOR LASER AND METHOD FOR THE MANUFACTURE THEREOF," p. 7.
- [36] M. San Miguel, Q. Feng, and J. V. Moloney, "Light-polarization dynamics in surface-emitting semiconductor lasers," *Phys. Rev. A*, vol. 52, no. 2, pp. 1728–1739, Aug. 1995, doi: 10.1103/PhysRevA.52.1728.
- [37] R. Q. Yang and S. S. Pei, "Novel type - II quantum cascade lasers," *Journal of Applied Physics*, vol. 79, no. 11, pp. 8197–8203, Jun. 1996, doi: 10.1063/1.362554.
- [38] J. Faist, F. Capasso, D. L. Sivco, C. Sirtori, A. L. Hutchinson, and A. Y. Cho, "Quantum Cascade Laser," *Science*, vol. 264, no. 5158, pp. 553–556, Apr. 1994, doi: 10.1126/science.264.5158.553.
- [39] J. Ch. Garcia *et al.*, "Epitaxially stacked lasers with Esaki junctions: A bipolar cascade laser," *Appl. Phys. Lett.*, vol. 71, no. 26, pp. 3752–3754, Dec. 1997, doi: 10.1063/1.120408.
- [40] E. Tournié and A. N. Baranov, "Mid-Infrared Semiconductor Lasers," in *Semiconductors and Semimetals*, vol. 86, Elsevier, 2012, pp. 183–226.
- [41] N. Kobayashi, Y. Horikoshi, and C. Uemura, "Room Temperature Operation of the InGaAsSb/AlGaAsSb DH Laser at 1.8 μm Wavelength," *Jpn. J. Appl. Phys.*, vol. 19, no. 1, pp. L30–L32, Jan. 1980, doi: 10.1143/JJAP.19.L30.
- [42] W. T. Tsang and N. A. Olsson, "Preparation of 1.78 - μm wavelength Al_{0.2}Ga_{0.8}Sb/GaSb double - heterostructure lasers by molecular beam epitaxy," *Appl. Phys. Lett.*, vol. 43, no. 1, pp. 8–10, Jul. 1983, doi: 10.1063/1.94132.
- [43] Y. Ohmori, S. Tarucha, Y. Horikoshi, and H. Okamoto, "Room Temperature Operation of Al_{0.17}Ga_{0.83}Sb/GaSb Multi-Quantum Well Lasers Grown by Molecular Beam Epitaxy," *Jpn. J. Appl. Phys.*, vol. 23, no. Part 2, No. 2, pp. L94–L96, Feb. 1984, doi: 10.1143/JJAP.23.L94.
- [44] S. J. Sweeney, T. D. Eales, and A. R. Adams, "The impact of strained layers on current and emerging semiconductor laser systems," *Journal of Applied Physics*, vol. 125, no. 8, p. 082538, Feb. 2019, doi: 10.1063/1.5063710.
- [45] G. W. Turner, H. K. Choi, and M. J. Manfra, "Ultralow-threshold (50 A/cm²) strained single-quantum-well GaInAsSb/AlGaAsSb lasers emitting at 2.05 μm ," *Appl. Phys. Lett.*, vol. 72, no. 8, pp. 876–878, Feb. 1998, doi: 10.1063/1.120922.
- [46] D. Z. Garbuzov, H. Lee, V. Khalfin, R. Martinelli, J. C. Connolly, and G. L. Belenky, "2.3–2.7- μm Room Temperature CW Operation of InGaAsSb–AlGaAsSb Broad Waveguide SCH-QW Diode Lasers," *IEEE PHOTONICS TECHNOLOGY LETTERS*, vol. 11, no. 7, p. 3, 1999.
- [47] L. Shterengas, G. Belenky, J. Kim, and R. Martinelli, "Design of high-power room-temperature continuous-wave GaSb-based type-I quantum-well lasers with $\lambda > 2.5 \mu\text{m}$," *Semiconductor science and technology*, vol. 19, no. 5, p. 655, 2004.
- [48] M. Grau, C. Lin, O. Dier, C. Lauer, and M.-C. Amann, "Room-temperature operation of 3.26 μm GaSb-based type-I lasers with quinary AlGaInAsSb barriers," *Appl. Phys. Lett.*, vol. 87, no. 24, p. 241104, Dec. 2005, doi: 10.1063/1.2140875.

- [49] M. P. C. M. Krijn, "Heterojunction band offsets and effective masses in III-V quaternary alloys," *Semicond. Sci. Technol.*, vol. 6, no. 1, pp. 27–31, Jan. 1991, doi: 10.1088/0268-1242/6/1/005.
- [50] T. Hosoda, G. Kipshidze, L. Shterengas, and G. Belenky, "Diode lasers emitting near 3.44 μm in continuous-wave regime at 300K," *Electronics letters*, vol. 46, no. 21, pp. 1455–1457, doi: 10.1049/el.2010.2564.
- [51] K. Vizbaras and M.-C. Amann, "Room-temperature 3.73 μm GaSb-based type-I quantum-well lasers with quinary barriers," *Semiconductor Science and Technology*, vol. 27, no. 3, p. 032001, 2012.
- [52] R. I. Taylor, R. A. Abram, C. Smith, and M. G. Burt, "Auger recombination in a quantum-well-heterostructure laser," *IEE Proc. J Optoelectron. UK*, vol. 132, no. 6, p. 364, 1985, doi: 10.1049/ip-j.1985.0069.
- [53] S. Anikeev *et al.*, "Measurement of the Auger recombination rate in p-type 0.54 eV GaInAsSb by time-resolved photoluminescence," p. 4, 2014.
- [54] H. K. Choi and G. W. Turner, "Antimonide-based strained quantum-well diode lasers," *Phys. Scr.*, vol. T69, pp. 17–25, Jan. 1997, doi: 10.1088/0031-8949/1997/T69/003.
- [55] S. Belahsene, "Lasers moyen infrarouge innovants pour analyse des hydrocarbures," 2011.
- [56] G. G. Zegrya and A. D. Andreev, "Mechanism of suppression of Auger recombination processes in type-II heterostructures," *Appl. Phys. Lett.*, vol. 67, no. 18, pp. 2681–2683, Oct. 1995, doi: 10.1063/1.114291.
- [57] C. Grein, P. Young, and H. Ehrenreich, "Theoretical performance of InAs/In_xGa_{1-x}Sb superlattice-based midwave infrared lasers," *Journal of Applied Physics*, vol. 76, no. 3, pp. 1940–1942, 1994.
- [58] J. R. Meyer *et al.*, "Auger coefficients in type-II InAs/Ga_{1-x}In_xSb quantum wells," *Appl. Phys. Lett.*, vol. 73, no. 20, pp. 2857–2859, Nov. 1998, doi: 10.1063/1.122609.
- [59] J. L. Malin *et al.*, "Type II mid-IR lasers operating above room temperature," *Electronics Letters*, vol. 32, no. 17, pp. 1593–1595, 1996, doi: 10.1049/el:19961057.
- [60] C. Felix *et al.*, "High-temperature 4.5- μm type-II quantum-well laser with Auger suppression," *IEEE Photonics Technology Letters*, vol. 9, no. 6, pp. 734–736, 1997, doi: 10.1109/68.584973.
- [61] W. W. Bewley *et al.*, "Above-room-temperature optically pumped midinfrared W lasers," *Appl. Phys. Lett.*, vol. 73, no. 26, pp. 3833–3835, Dec. 1998, doi: 10.1063/1.122909.
- [62] D. Stokes *et al.*, "Type-II quantum-well 'W' lasers emitting at $\lambda = 5.4\text{--}7.3 \mu\text{m}$," *Journal of applied physics*, vol. 86, no. 9, pp. 4729–4733, 1999, doi: 10.1063/1.371436.
- [63] H. Kroemer and G. Griffiths, "Staggered-lineup heterojunctions as sources of tunable below-gap radiation: operating principle and semiconductor selection," *IEEE Electron Device Letters*, vol. 4, no. 1, pp. 20–22, 1983, doi: 10.1109/EDL.1983.25631.
- [64] A. Baranov, B. Dzhurtanov, A. Imenkov, A. Rogachev, Y. M. Shernyakov, and Y. P. Yakovlev, "GENERATION OF COHERENT RADIATION IN A QUANTUM-WELL STRUCTURE WITH ONE HETEROJUNCTION," *SOVIET PHYSICS SEMICONDUCTORS-USSR*, vol. 20, no. 12, pp. 1385–1387, 1986.
- [65] A. Baranov, Y. Cuminal, G. Boissier, C. Alibert, and A. Joullié, "Low-threshold laser diodes based on type-II GaInAsSb/GaSb quantum-wells operating at 2.36 μm at room temperature," *Electronics Letters*, vol. 32, no. 24, pp. 2279–2280, 1996, doi: 10.1049/el:19961496.

- [66] A. N. Baranov, Y. Cuminal, N. Bertru, C. L. Alibert, and A. F. Joullie, "Strained multiple-quantum-well lasers grown on GaSb emitting between 2 and 2.4 μm ," San Jose, CA, Jan. 1997, pp. 2–13, doi: 10.1117/12.264141.
- [67] A. N. Baranov *et al.*, "Mid-infrared GaSb-InAs-based multiple quantum well lasers," San Jose, CA, Apr. 1998, p. 247, doi: 10.1117/12.304451.
- [68] Y. Cuminal *et al.*, "Room-temperature 2.63 μm GaInAsSb/GaSb strained quantum-well laser diodes," *Semicond. Sci. Technol.*, vol. 14, no. 3, pp. 283–288, Mar. 1999, doi: 10.1088/0268-1242/14/3/013.
- [69] A. Joullie *et al.*, "Continuous-wave operation of GaInAsSb-GaSb type-II quantum-well ridge-lasers," *IEEE J. Select. Topics Quantum Electron.*, vol. 5, no. 3, pp. 711–714, Jun. 1999, doi: 10.1109/2944.788440.
- [70] D. A. Yarekha *et al.*, "High efficiency GaInSbAs/GaSb type-II quantum well continuous wave lasers," *Semicond. Sci. Technol.*, vol. 15, no. 4, pp. 390–394, Apr. 2000, doi: 10.1088/0268-1242/15/4/314.
- [71] M. Mikhailova *et al.*, "Interface-induced phenomena in type II antimonide–arsenide heterostructures," *IEE Proceedings-Optoelectronics*, vol. 145, no. 5, pp. 268–274, 1998, doi: 10.1049/ip-opt:19982305.
- [72] K. D. Moiseev *et al.*, "Electroluminescence of quantum-well structures on type-II InAs/GaSb heterojunctions," *Tech. Phys. Lett.*, vol. 24, no. 6, pp. 477–479, Jun. 1998, doi: 10.1134/1.1262152.
- [73] D. Smith and C. Mailhot, "Proposal for strained type II superlattice infrared detectors," *Journal of Applied Physics*, vol. 62, no. 6, pp. 2545–2548, 1987.
- [74] A. N. Baranov, N. Bertru, Y. Cuminal, G. Boissier, C. Alibert, and A. Joullie, "Observation of room-temperature laser emission from type III InAs/GaSb multiple quantum well structures," *Appl. Phys. Lett.*, vol. 71, no. 6, pp. 735–737, Aug. 1997, doi: 10.1063/1.119629.
- [75] A. Wilk *et al.*, "Type-II InAsSb/InAs strained quantum-well laser diodes emitting at 3.5 μm ," *Appl. Phys. Lett.*, vol. 77, no. 15, pp. 2298–2300, Oct. 2000, doi: 10.1063/1.1317537.
- [76] W. T. Tsang, "Extremely low threshold (AlGa)As modified multiquantum well heterostructure lasers grown by molecular - beam epitaxy," *Appl. Phys. Lett.*, vol. 39, no. 10, pp. 786–788, Nov. 1981, doi: 10.1063/1.92583.
- [77] J. R. Meyer, C. A. Hoffman, F. J. Bartoli, and L. R. Ram - Mohan, "Type - II quantum - well lasers for the mid - wavelength infrared," *Appl. Phys. Lett.*, vol. 67, no. 6, pp. 757–759, Aug. 1995, doi: 10.1063/1.115216.
- [78] J. I. Malin *et al.*, "Type II mid - infrared quantum well lasers," *Appl. Phys. Lett.*, vol. 68, no. 21, pp. 2976–2978, May 1996, doi: 10.1063/1.116374.
- [79] H. Lee *et al.*, "Room-temperature type-II W quantum well diode laser with broadened waveguide emitting at $\lambda = 3.30 \mu\text{m}$," *Electronics Letters*, vol. 35, no. 20, pp. 1743–1745, 1999.
- [80] W. Bewley *et al.*, "Continuous-wave operation of $\lambda = 3.25 \mu\text{m}$ broadened-waveguide W quantum-well diode lasers up to $T = 195 \text{ K}$," *Applied Physics Letters*, vol. 76, no. 3, pp. 256–258, 2000.
- [81] L. Esaki, L. Chang, and E. Mendez, "Polytype superlattices and multi-heterojunctions," *Japanese Journal of Applied Physics*, vol. 20, no. 7, p. L529, 1981.

- [82] R. Q. Yang, "Infrared laser based on intersubband transitions in quantum wells," *Superlattices and Microstructures*, vol. 17, no. 1, pp. 77–83, 1995.
- [83] A. A. Allerman, R. M. Biefeld, and S. R. Kurtz, "InAsSb - based mid - infrared lasers (3.8–3.9 μm) and light - emitting diodes with AlAsSb claddings and semimetal electron injection, grown by metalorganic chemical vapor deposition," *Appl. Phys. Lett.*, vol. 69, no. 4, pp. 465–467, Jul. 1996, doi: 10.1063/1.118141.
- [84] I. Vurgaftman *et al.*, "Mid-IR Type-II Interband Cascade Lasers," *IEEE J. Select. Topics Quantum Electron.*, vol. 17, no. 5, pp. 1435–1444, Sep. 2011, doi: 10.1109/JSTQE.2011.2114331.
- [85] J. Meyer, I. Vurgaftman, R. Yang, and L. Ram-Mohan, "Type-II and type-I interband cascade lasers," *Electronics Letters*, vol. 32, no. 1, pp. 45–46, 1996.
- [86] C.-H. Lin *et al.*, "Type-II interband quantum cascade laser at 3.8 μm ," *Electronics Letters*, vol. 33, no. 7, pp. 598–599, 1997, doi: 10.1049/el:19970421.
- [87] R. Q. Yang *et al.*, "High power mid-infrared interband cascade lasers based on type-II quantum wells," *Appl. Phys. Lett.*, vol. 71, no. 17, pp. 2409–2411, Oct. 1997, doi: 10.1063/1.120076.
- [88] C. L. Felix *et al.*, "Interband cascade laser emitting >1 photon per injected electron," *IEEE Photon. Technol. Lett.*, vol. 9, no. 11, pp. 1433–1435, Nov. 1997, doi: 10.1109/68.634699.
- [89] L. J. Olafsen *et al.*, "Near-room-temperature mid-infrared interband cascade laser," *Appl. Phys. Lett.*, vol. 72, no. 19, pp. 2370–2372, May 1998, doi: 10.1063/1.121359.
- [90] J. L. Bradshaw, J. D. Bruno, J. T. Pham, D. E. Wortman, and R. Q. Yang, "Continuous wave operation of type II interband cascade lasers," p. 4.
- [91] R. Q. Yang, "Mid-Infrared Type-II Interband Cascade Lasers," *IEEE JOURNAL OF QUANTUM ELECTRONICS*, vol. 38, no. 6, pp. 559–568, 2002, doi: 10.1109/JQE.2002.1005406.
- [92] C. J. Hill, B. Yang, and R. Q. Yang, "Low-threshold interband cascade lasers operating above room temperature," *Physica E: Low-dimensional Systems and Nanostructures*, vol. 20, no. 3–4, pp. 486–490, Jan. 2004, doi: 10.1016/j.physe.2003.08.064.
- [93] C. L. Canedy *et al.*, "High-power, narrow-ridge, mid-infrared interband cascade lasers," *Journal of Vacuum Science & Technology B: Microelectronics and Nanometer Structures Processing, Measurement, and Phenomena*, vol. 26, no. 3, pp. 1160–1162, 2008, doi: 10.1116/1.2884733.
- [94] K. Mansour, Y. Qiu, C. J. Hill, A. Soibel, and R. Q. Yang, "Mid-infrared interband cascade lasers at thermoelectric cooler temperatures," *Electron. Lett.*, vol. 42, no. 18, p. 1034, 2006, doi: 10.1049/el:20062442.
- [95] W. W. Bewley *et al.*, "Interband cascade laser operating to 269 K at =4.05 [micro sign]m," *Electron. Lett.*, vol. 43, no. 5, p. 283, 2007, doi: 10.1049/el:20073759.
- [96] C. Canedy *et al.*, "Molecular beam epitaxy growth and characterization of mid-IR type-II 'W' diode lasers," *Journal of Vacuum Science & Technology B: Microelectronics and Nanometer Structures Processing, Measurement, and Phenomena*, vol. 23, no. 3, pp. 1119–1124, 2005, doi: 10.1116/1.1861933.
- [97] S. Roux *et al.*, "Mid-infrared characterization of refractive indices and propagation losses in GaSb/Al_xGa_{1-x}AsSb waveguides," *Appl. Phys. Lett.*, vol. 107, no. 17, p. 171901, Oct. 2015, doi: 10.1063/1.4934702.
- [98] R. Q. Yang *et al.*, "Recent progress in interband cascade lasers with separate confinement layers," San Jose, CA, Feb. 2009, p. 72300S, doi: 10.1117/12.807595.

- [99] M. Kim *et al.*, "Interband cascade laser emitting at $\lambda = 3.75 \mu\text{m}$ in continuous wave above room temperature," *Appl. Phys. Lett.*, vol. 92, no. 19, p. 191110, 2008, doi: 10.1063/1.2930685.
- [100] A. Bauer, "Shortened injector interband cascade lasers for 3.3- to 3.6- μm emission," *Opt. Eng.*, vol. 49, no. 11, p. 111117, Nov. 2010, doi: 10.1117/1.3505831.
- [101] I. Vurgaftman *et al.*, "Rebalancing of internally generated carriers for mid-infrared interband cascade lasers with very low power consumption," *Nat Commun*, vol. 2, no. 1, p. 585, Sep. 2011, doi: 10.1038/ncomms1595.
- [102] Y. Bai, S. R. Darvish, N. Bandyopadhyay, S. Slivken, and M. Razeghi, "Optimizing facet coating of quantum cascade lasers for low power consumption," *Journal of Applied Physics*, vol. 109, no. 5, p. 053103, Mar. 2011, doi: 10.1063/1.3553863.
- [103] N. Bandyopadhyay, Y. Bai, S. Tsao, S. Nida, S. Slivken, and M. Razeghi, "Room temperature continuous wave operation of $\lambda \sim 3\text{--}3.2 \mu\text{m}$ quantum cascade lasers," *Applied Physics Letters*, vol. 101, no. 24, p. 241110, 2012, doi: 10.1063/1.4769038.
- [104] W. W. Bewley *et al.*, "High-power room-temperature continuous-wave mid-infrared interband cascade lasers," *Opt. Express*, vol. 20, no. 19, p. 20894, Sep. 2012, doi: 10.1364/OE.20.020894.
- [105] C. L. Canedy *et al.*, "Pulsed and CW performance of 7-stage interband cascade lasers," *Opt. Express*, vol. 22, no. 7, p. 7702, Apr. 2014, doi: 10.1364/OE.22.007702.
- [106] R. Weih, M. Kamp, and S. Höfling, "Interband cascade lasers with room temperature threshold current densities below 100 A/cm^2 ," *Appl. Phys. Lett.*, vol. 102, no. 23, p. 231123, Jun. 2013, doi: 10.1063/1.4811133.
- [107] M. Kim *et al.*, "High-power continuous-wave interband cascade lasers with 10 active stages," *Opt. Express*, vol. 23, no. 8, p. 9664, Apr. 2015, doi: 10.1364/OE.23.009664.
- [108] I. Melngailis, "LONGITUDINAL INJECTION - PLASMA LASER OF InSb," *Appl. Phys. Lett.*, vol. 6, no. 3, pp. 59–60, Feb. 1965, doi: 10.1063/1.1754164.
- [109] H. Soda, K. Iga, C. Kitahara, and Y. Suematsu, "GaInAsP/InP surface emitting injection lasers," *Japanese Journal of Applied Physics*, vol. 18, no. 12, p. 2329, 1979, doi: 10.1143/JJAP.18.2329.
- [110] F. Koyama, S. KINOSHITA, and K. IGA, "Room temperature cw operation of GaAs vertical cavity surface emitting laser," *IEICE TRANSACTIONS (1976-1990)*, vol. 71, no. 11, pp. 1089–1090, 1988.
- [111] D. Sanchez, "Nouveau système de confinement pour le VCSEL GaSb," PhD Thesis, Université de Montpellier, Montpellier, 2012 (in French), University of Montpellier, 2012.
- [112] S. Arafin, "Electrically-pumped GaSb-based vertical-cavity surface-emitting lasers," 2012.
- [113] J. A. Lott, R. P. Schneider, K. D. Choquette, S. P. Kilcoyne, J. J. Figiel, and J. A. Lott, "Room temperature continuous wave operation of red vertical cavity surface emitting laser diodes," *Electron. Lett.*, vol. 29, no. 19, p. 1693, 1993, doi: 10.1049/el:19931126.
- [114] R. P. Schneider, M. Hagerott Crawford, K. D. Choquette, K. L. Lear, S. P. Kilcoyne, and J. J. Figiel, "Improved AlGaInP - based red (670–690 nm) surface - emitting lasers with novel C - doped short - cavity epitaxial design," *Appl. Phys. Lett.*, vol. 67, no. 3, pp. 329–331, Jul. 1995, doi: 10.1063/1.115434.

- [115] Y.-H. Lee, B. Tell, K. Brown-Goebeler, J. Jewell, and J. Hove, "Top-surface-emitting GaAs four-quantum-well lasers emitting at 0.85 μm ," *Electronics Letters*, vol. 26, no. 11, pp. 710–711, 1990, doi: 10.1049/el:19900463.
- [116] Y. H. Wang *et al.*, "GaAs/AlGaAs multiple quantum well GRIN-SCH vertical cavity surface emitting laser diodes," *IEEE Photon. Technol. Lett.*, vol. 2, no. 7, pp. 456–458, Jul. 1990, doi: 10.1109/68.56622.
- [117] R. S. Geels, J Thibeault, and L. A. Coldren, "Design and Characterization of In_{0.2}Ga_{0.8}As MQW Vertical-Cavity Surface-Emitting Lasers," *IEEE JOURNAL OF QUANTUM ELECTRONICS*, vol. 29, no. 12, pp. 2977–2987, 1993, doi: 10.1109/3.259415.
- [118] K. D. Choquette *et al.*, "Room temperature continuous wave InGaAsN quantum well vertical-cavity lasers emitting at 1.3 μm ," *Electronics Letters*, vol. 36, no. 16, pp. 1388–1390, 2000, doi: 10.1049/el:20000928.
- [119] M. Yamada *et al.*, "Room temperature low-threshold CW operation of 1.23 μm GaAsSb VCSELs on GaAs substrates," *Electronics Letters*, vol. 36, no. 7, p. 1, 2000, doi: 10.1049/el:20000483.
- [120] C. E. Webb and J. D. Jones, *Handbook of laser technology and applications*, vol. 2, pp. 675–675. 2004.
- [121] K. Tai, R. J. Fischer, K. W. Wang, S. N. G. Chu, and A. Y. Cho, "Use of implant isolation for fabrication of vertical cavity surface-emitting laser diodes," *Electron. Lett.*, vol. 25, no. 24, p. 1644, 1989, doi: 10.1049/el:19891102.
- [122] D. L. Huffaker, D. G. Deppe, K. Kumar, and T. J. Rogers, "Native - oxide defined ring contact for low threshold vertical - cavity lasers," *Appl. Phys. Lett.*, vol. 65, no. 1, pp. 97–99, Jul. 1994, doi: 10.1063/1.113087.
- [123] J. Cheng and N. K. Dutta, *Vertical-cavity surface-emitting lasers: technology and applications*, vol. 10. CRC Press, 2000.
- [124] T. Tadokoro, H. Okamoto, Y. Kohama, T. Kawakami, and T. Kurokawa, "Room Temperature Pulsed Operation of 1.5 μm GaInAsP/InP Vertical-Cavity Surface-Emitting Laser," *IEEE Photonics Technology Letters*, vol. 4, no. 5, pp. 409–411, 1992, doi: 10.1109/68.136468.
- [125] J. J. Dudley *et al.*, "Low threshold, wafer fused long wavelength vertical cavity lasers," *Appl. Phys. Lett.*, vol. 64, no. 12, pp. 1463–1465, Mar. 1994, doi: 10.1063/1.111913.
- [126] M. Ortsiefer, R. Shau, G. Böhm, F. Köhler, and M.-C. Amann, "Low-threshold index-guided 1.5 μm long-wavelength vertical-cavity surface-emitting laser with high efficiency," *Applied Physics Letters*, vol. 76, no. 16, pp. 2179–2181, 2000, doi: 10.1063/1.126290.
- [127] M. Ortsiefer *et al.*, "Electrically pumped room temperature CW VCSELs with 2.3 μm emission wavelength," *Electronics Letters*, vol. 42, no. 11, pp. 640–641, doi: 10.1049/el:20061096.
- [128] S. Sprengel, A. Andrejew, F. Federer, G. Veerabathran, G. Boehm, and M.-C. Amann, "Continuous wave vertical cavity surface emitting lasers at 2.5 μm with InP-based type-II quantum wells," *Applied Physics Letters*, vol. 106, no. 15, p. 151102, 2015, doi: 10.1063/1.4917282.
- [129] C. L. Felix *et al.*, "Midinfrared vertical-cavity surface-emitting laser," *Appl. Phys. Lett.*, vol. 71, no. 24, pp. 3483–3485, Dec. 1997, doi: 10.1063/1.120366.
- [130] W. W. Bewley *et al.*, "Continuous-wave mid-infrared VCSELs," *IEEE Photon. Technol. Lett.*, vol. 10, no. 5, pp. 660–662, May 1998, doi: 10.1109/68.669235.

- [131] W. W. Bewley *et al.*, "Mid-infrared vertical-cavity surface-emitting lasers for chemical sensing," *Appl. Opt.*, vol. 38, no. 9, p. 1502, Mar. 1999, doi: 10.1364/AO.38.001502.
- [132] A. N. Baranov, Y. Rouillard, G. Boissier, P. Grech, S. Gaillard, and C. Alibert, "Sb-based monolithic VCSEL operating near 2.2 μm at room temperature," *Electron. Lett.*, vol. 34, no. 3, p. 281, 1998, doi: 10.1049/el:19980142.
- [133] A. Perona *et al.*, "AlAsSb/GaSb doped distributed Bragg reflectors for electrically pumped VCSELs emitting around 2.3 μm ," *Semicond. Sci. Technol.*, vol. 22, no. 10, pp. 1140–1144, Oct. 2007, doi: 10.1088/0268-1242/22/10/010.
- [134] L. Cerutti, A. Ducanhez, P. Grech, A. Garnache, and F. Genty, "Room-temperature, monolithic, electrically-pumped type-I quantum-well Sb-based VCSELs emitting at 2.3 μm ," *Electronics Letters*, vol. 44, no. 3, pp. 203–205, 2008, doi: 10.1049/el:20083424.
- [135] A. Ducanhez, L. Cerutti, P. Grech, F. Genty, and E. Tournie, "Mid-infrared GaSb-based EP-VCSEL emitting at 2.63 μm ," *Electronics Letters*, vol. 45, no. 5, pp. 265–267, 2009, doi: 10.1049/el:20090134.
- [136] Y. Laaroussi, G. Almuneau, D. Sanchez, and L. Cerutti, "Efficient lateral confinement by an oxide aperture in a mid-infrared GaSb-based vertical light-emitting source," *J. Phys. D: Appl. Phys.*, vol. 44, no. 14, p. 142001, Apr. 2011, doi: 10.1088/0022-3727/44/14/142001.
- [137] D. G. Deppe, D. L. Huffaker, Tchang-Hun Oh, Hongyu Deng, and Qing Deng, "Low-threshold vertical-cavity surface-emitting lasers based on oxide-confinement and high contrast distributed Bragg reflectors," *IEEE J. Select. Topics Quantum Electron.*, vol. 3, no. 3, pp. 893–904, Jun. 1997, doi: 10.1109/2944.640643.
- [138] K. Meneou, H. C. Lin, K. Y. Cheng, J. G. Kim, and R. U. Martinelli, "Wet thermal oxidation of AlAsSb alloys lattice matched to GaSb," *Journal of Applied Physics*, vol. 95, no. 9, pp. 5131–5136, May 2004, doi: 10.1063/1.1687976.
- [139] Decai Sun *et al.*, "Sub-mA threshold 1.5- μm VCSELs with epitaxial and dielectric DBR mirrors," *IEEE Photon. Technol. Lett.*, vol. 15, no. 12, pp. 1677–1679, Dec. 2003, doi: 10.1109/LPT.2003.819711.
- [140] Y. Laaroussi *et al.*, "Oxide-confined mid-infrared VCSELs," *Electronics Letters*, vol. 48, no. 25, pp. 1616–1618, Dec. 2012, doi: 10.1049/el.2012.3572.
- [141] A. Bachmann, T. Lim, K. Kashani-Shirazi, O. Dier, and C. Lauer, "Continuous-wave operation of electrically pumped GaSb-based vertical cavity surface emitting laser at 2.3 μm ," *Electronics Letters*, vol. 44, no. 3, pp. 202–203, 2008.
- [142] A. Bachmann, K. Kashani-Shirazi, S. Arafin, and M.-C. Amann, "GaSb-Based VCSEL With Buried Tunnel Junction for Emission Around 2.3 μm ," *IEEE J. Select. Topics Quantum Electron.*, vol. 15, no. 3, pp. 933–940, 2009, doi: 10.1109/JSTQE.2009.2013361.
- [143] A. Bachmann, S. Arafin, K. Kashani-Shirazi, and M.-C. Amann, "Long wavelength electrically pumped GaSb-based buried tunnel junction VCSELs," *Physics Procedia*, vol. 3, no. 2, pp. 1155–1159, Jan. 2010, doi: 10.1016/j.phpro.2010.01.155.
- [144] S. Arafin, A. Bachmann, K. Kashani-Shirazi, and M.-C. Amann, "Electrically pumped continuous-wave vertical-cavity surface-emitting lasers at $\sim 2.6 \mu\text{m}$," *Appl. Phys. Lett.*, vol. 95, no. 13, p. 131120, doi: 10.1063/1.3240406.
- [145] A. Andrejew, S. Sprengel, and M.-C. Amann, "GaSb-based Vertical-Cavity Surface-Emitting Lasers with Emission Wavelength at 3 μm ," *Optics letters*, vol. 41, no. 12, pp. 2799–2802, 2016, doi: 10.1364/OL.41.002799.
- [146] D. Sanchez, L. Cerutti, and E. Tournié, "Selective lateral etching of InAs/GaSb tunnel junctions for mid-infrared photonics," *Semicond. Sci. Technol.*, vol. 27, no. 8, p. 085011, Aug. 2012, doi: 10.1088/0268-1242/27/8/085011.

- [147] D. Sanchez, L. Cerutti, and E. Tournié, "Single-Mode Monolithic GaSb Vertical-Cavity Surface-Emitting Laser," *Opt. Express*, vol. 20, no. 14, p. 15540, Jul. 2012, doi: 10.1364/OE.20.015540.
- [148] T. Knodl, M. Golling, A. Straub, R. Jager, R. Michalzik, and K. J. Ebeling, "Multistage bipolar cascade vertical-cavity surface-emitting lasers: theory and experiment," *IEEE J. Select. Topics Quantum Electron.*, vol. 9, no. 5, pp. 1406–1414, Sep. 2003, doi: 10.1109/JSTQE.2003.819484.
- [149] R. Koda, C. S. Wang, D. D. Lofgreen, and L. A. Coldren, "High-differential-quantum-efficiency, long-wavelength vertical-cavity lasers using five-stage bipolar-cascade active regions," *Appl. Phys. Lett.*, vol. 86, no. 21, p. 211104, May 2005, doi: 10.1063/1.1931060.
- [150] D. Sanchez, L. Cerutti, and E. Tournié, "Mid-IR GaSb-Based Bipolar Cascade VCSELs," *IEEE Photon. Technol. Lett.*, vol. 25, no. 9, pp. 882–884, May 2013, doi: 10.1109/LPT.2013.2254707.
- [151] W. W. Bewley *et al.*, "Room-temperature mid-infrared interband cascade vertical-cavity surface-emitting lasers," *Appl. Phys. Lett.*, vol. 109, no. 15, p. 151108, Oct. 2016, doi: 10.1063/1.4964840.
- [152] G. K. Veerabathran, S. Sprengel, A. Andrejew, and M.-C. Amann, "Room-temperature vertical-cavity surface-emitting lasers at 4 μm with GaSb-based type-II quantum wells," *Appl. Phys. Lett.*, vol. 110, no. 7, p. 071104, Feb. 2017, doi: 10.1063/1.4975813.
- [153] R. Colombelli *et al.*, "Quantum Cascade Surface-Emitting Photonic Crystal Laser," *Science*, vol. 302, no. 5649, pp. 1374–1377, Nov. 2003, doi: 10.1126/science.1090561.
- [154] "See www.nextnano.com/index.php for Nextnano GmbH - semiconductor software solutions."
- [155] D. A. Díaz-Thomas *et al.*, "Interband cascade Lasers with AlGaAsSb cladding layers emitting at 3.3 μm ," *Opt. Express*, vol. 27, no. 22, p. 31425, Oct. 2019, doi: 10.1364/OE.27.031425.
- [156] T. Hosoda, G. Kipshidze, G. Tsviid, L. Shterengas, and G. Belenky, "Type-I GaSb-Based Laser Diodes Operating in 3.1 to 3.3 μm Wavelength Range," *IEEE Photon. Technol. Lett.*, vol. 22, no. 10, pp. 718–720, May 2010, doi: 10.1109/LPT.2010.2044659.
- [157] L. Cerutti *et al.*, "GaSb-based composite quantum wells for laser diodes operating in the telecom wavelength range near 1.55 μm ," *Applied Physics Letters*, vol. 106, no. 10, p. 101102, 2015, doi: 10.1063/1.4914884.
- [158] A. Castellano, "Laser telecom à base de GaSb. Intégration sur Silicium," 2016.
- [159] Q. Gaimard, "Diodes lasers DFB à couplage par l'indice émettant entre 2 μm et 3, 3 μm sur substrat GaSb," 2014.
- [160] R. Weih, A. Bauer, M. Kamp, and S. Höfling, "Interband cascade lasers with AlGaAsSb bulk cladding layers," *Optical Materials Express*, vol. 3, no. 10, pp. 1624–1631, 2013, doi: 10.1364/OME.3.001624.
- [161] T. Borca-Tasciuc *et al.*, "Thermal conductivity of AlAs_{0.07}Sb_{0.93} and Al_{0.9}Ga_{0.1}As_{0.07}Sb_{0.93} alloys and (AlAs)₁/(AlSb)₁₁ digital-alloy superlattices," *Journal of Applied Physics*, vol. 92, no. 9, pp. 4994–4998, Nov. 2002, doi: 10.1063/1.1506194.
- [162] T. Borca-Tasciuc, D. Achimov, W. L. Li, "Thermal conductivity of InAs/AlSb superlattices," *Microscale Thermophysical Engineering*, vol. 5, no. 3, pp. 225–231, Jul. 2001, doi: 10.1080/108939501753222896.
- [163] C. Zhou *et al.*, "Thermal conductivity tensors of the cladding and active layers of interband cascade lasers," *Appl. Phys. Lett.*, vol. 105, no. 26, p. 261905, Dec. 2014, doi: 10.1063/1.4905279.

- [164] C. L. Canedy, W. W. Bewley, C. S. Kim, M. Kim, I. Vurgaftman, and J. R. Meyer, "Dependence of type II 'W' mid-infrared photoluminescence and lasing properties on growth conditions," *Journal of Applied Physics*, vol. 94, no. 3, pp. 1347–1355, Aug. 2003, doi: 10.1063/1.1586974.
- [165] DeSalvo, DeSalvo, R. Kaspi, and C. Bozada, "Citric Acid Etching of GaAs,_xSb_x, Al_{0.5}Ga_{0.5}Sb, and InAs for Heterostructure Device Fabrication," *J. Electrochem. Soc.*, vol. 141, no. 12, p. 6, 1994.
- [166] J. Weyher, "SELECTIVE ETCHING AND PHOTOETCHING OF { 100} GALLIUM ARSENIDE IN CrO₃-HF AQUEOUS SOLUTIONS I. Influence of composition on etching behaviour," *Journal of Crystal Growth*, vol. 63, no. 2, pp. 285–291, 1983, doi: 10.1016/0022-0248(83)90217-8.
- [167] A. Baranov, "Etchant for treatment of the GaSb-Based semiconductor materials," USSR patent n° 1396861, 1986.
- [168] D. A. Díaz-Thomas, "Conception, réalisation et étude de structures pour la fabrication des Lasers à cascade interbande émettant dans le moyen infrarouge," 2017.
- [169] O. Dier, C. Lin, M. Grau, and M.-C. Amann, "Selective and non-selective wet-chemical etchants for GaSb-based materials," *Semicond. Sci. Technol.*, vol. 19, no. 11, pp. 1250–1253, Nov. 2004, doi: 10.1088/0268-1242/19/11/006.
- [170] A. Ducanchez, "Etude et mise au point des procédés technologiques pour la fabrication de VCSELs moyen infrarouge pompés électriquement à base de GaSb," University of Montpellier, France, 2009.
- [171] L. Zhang, L. F. Lester, R. J. Shul, C. G. Willison, and R. P. Leavitt, "Inductively coupled plasma etching of III–V antimonides in BCl₃/Ar and Cl₂/Ar," *J. Vac. Sci. Technol. B*, vol. 17, no. 3, p. 6, 1999.
- [172] G. Stareev, H. Künzel, and G. Dortmann, "A controllable mechanism of forming extremely low - resistance nonalloyed ohmic contacts to group III - V compound semiconductors," *Journal of Applied Physics*, vol. 74, no. 12, pp. 7344–7356, Dec. 1993, doi: 10.1063/1.355002.
- [173] T. H. Chiu, J. A. Ditzenberger, H. S. Luftman, W. T. Tsang, and N. T. Ha, "Te doping study in molecular beam epitaxial growth of GaSb using Sb₂Te₃," *Appl. Phys. Lett.*, vol. 56, no. 17, pp. 1688–1690, Apr. 1990, doi: 10.1063/1.103118.
- [174] D. Barat, "Lasers monofréquences à base de GaSb émettant à 2, 6 μm pour l'analyse de gaz," University of Montpellier, 2007.
- [175] C. L. Canedy *et al.*, "Interband Cascade Lasers with Wavelengths Spanning 2.9 μm to 5.2 μm," *Journal of Elec Materi*, vol. 37, no. 12, pp. 1780–1785, Dec. 2008, doi: 10.1007/s11664-008-0444-1.
- [176] M. J. Yang *et al.*, "Optimum growth parameters for type-II infrared lasers," *Journal of Applied Physics*, vol. 86, no. 4, pp. 1796–1799, Aug. 1999, doi: 10.1063/1.370971.
- [177] W. Barvosa-Carter, M. E. Twigg, M. J. Yang, and L. J. Whitman, "Microscopic characterization of InAs/In_{0.28}GaSb_{0.72}/InAs/AlSb laser structure interfaces," *Phys. Rev. B*, vol. 63, no. 24, p. 245311, Jun. 2001, doi: 10.1103/PhysRevB.63.245311.
- [178] C. D. Merritt *et al.*, "Gain and loss as a function of current density and temperature in interband cascade lasers," *Appl. Opt.*, vol. 54, no. 31, p. F1, Nov. 2015, doi: 10.1364/AO.54.0000F1.

- [179] W. J. Turner and W. E. Reese, "Infrared Absorption in n-Type Aluminum Antimonide," *Phys. Rev.*, vol. 117, no. 4, pp. 1003–1004, Feb. 1960, doi: 10.1103/PhysRev.117.1003.
- [180] W. Jost, M. Kunzer, U. Kaufmann, and H. Bender, "Bistability of the Te donor in AlSb:Te bulk crystals," *Phys. Rev. B*, vol. 50, no. 7, pp. 4341–4344, Aug. 1994, doi: 10.1103/PhysRevB.50.4341.
- [181] A. Subekti, V. W. L. Chin, and T. L. Tansley, "Ohmic contacts to n-type and p-type GaSb," *Solid-State Electronics*, vol. 39, no. 3, pp. 329–332, Mar. 1996, doi: 10.1016/0038-1101(95)00144-1.
- [182] W. W. Bewley, C. L. Canedy, C. S. Kim, I. Vurgaftman, M. Kim, and J. R. Meyer, "Antimonide type-II 'W' lasers: growth studies and guided-mode leakage into substrate," *Physica E: Low-dimensional Systems and Nanostructures*, vol. 20, no. 3–4, pp. 466–470, Jan. 2004, doi: 10.1016/j.physe.2003.08.060.
- [183] S. S. Murtaza *et al.*, "High-reflectivity Bragg mirrors for optoelectronic applications," *IEEE J. Quantum Electron.*, vol. 31, no. 10, pp. 1819–1825, Oct. 1995, doi: 10.1109/3.466057.
- [184] H. A. Macleod, *Thin-film optical filters*. CRC press, 2017.
- [185] G. Tuttle, J. Kavanaugh, and S. McCalmont, "(Al,Ga)Sb long-wavelength distributed Bragg reflectors," *IEEE Photon. Technol. Lett.*, vol. 5, no. 12, pp. 1376–1379, Dec. 1993, doi: 10.1109/68.262546.
- [186] L. Cerutti, "Etude et mise au point des moyens et procédures d'épitaxie par jets moléculaires pour fabriquer des structures VCSEL à base d'antimoniures," 2004.
- [187] S. Roux, "Conversion de fréquence vers les grandes longueurs d'onde dans des guides d'onde en semi-conducteurs à orientation périodique," 2016.
- [188] S. Roux *et al.*, "Low-loss orientation-patterned GaSb waveguides for mid-infrared parametric conversion," *Opt. Mater. Express*, vol. 7, no. 8, p. 3011, Aug. 2017, doi: 10.1364/OME.7.003011.
- [189] O. Dier, M. Sterkel, M. Grau, C. Lin, C. Lauer, and M.-C. Amann, "Tunnel junctions for ohmic intra-device contacts on GaSb-substrates," *Appl. Phys. Lett.*, vol. 85, no. 12, pp. 2388–2389, Sep. 2004, doi: 10.1063/1.1793349.
- [190] C. Lauer, O. Dier, and M.-C. Amann, "Low-resistive metal / n+-InAsSb/n-GaSb contacts," *Semicond. Sci. Technol.*, vol. 21, no. 9, pp. 1274–1277, Sep. 2006, doi: 10.1088/0268-1242/21/9/011.
- [191] C. Levallois *et al.*, "Si wafer bonded of a - Si/ a - Si N x distributed Bragg reflectors for 1.55 - μ m-wavelength vertical cavity surface emitting lasers," *Journal of applied physics*, vol. 98, no. 4, p. 043107, 2005, doi: 10.1063/1.2009075.
- [192] C. Levallois *et al.*, "Design and Fabrication of GaInAsP/InP VCSEL with Two a-Si/a-SiNx Bragg Reflectors," *Opt Quant Electron*, vol. 38, no. 4–6, pp. 281–291, Mar. 2006, doi: 10.1007/s11082-006-0029-2.
- [193] A. J. Lowe, M. J. Powell, and S. R. Elliott, "The electronic properties of plasma - deposited films of hydrogenated amorphous SiN_x (0 < x < 1.2)," *Journal of Applied Physics*, vol. 59, no. 4, pp. 1251–1258, Feb. 1986, doi: 10.1063/1.336513.
- [194] C. W. Pearce, R. F. Fetcho, M. D. Gross, R. F. Koefer, and R. A. Pudliner, "Characteristics of silicon nitride deposited by plasma - enhanced chemical vapor deposition using a dual frequency radio - frequency source," *Journal of Applied Physics*, vol. 71, no. 4, pp. 1838–1841, Feb. 1992, doi: 10.1063/1.351396.

- [195] W.-S. Liao, "Water-Resistant Coating on Low Temperature Amorphous Silicon Nitride Films by a Thin Layer of Amorphous Silicon Hydrogen Alloy," *J. Electrochem. Soc.*, vol. 144, no. 4, p. 1477, 1997, doi: 10.1149/1.1837615.
- [196] A. J. Flewitt, A. P. Dyson, J. Robertson, and W. I. Milne, "Low temperature growth of silicon nitride by electron cyclotron resonance plasma enhanced chemical vapour deposition," *Thin Solid Films*, vol. 383, no. 1–2, pp. 172–177, Feb. 2001, doi: 10.1016/S0040-6090(00)01628-X.
- [197] S. Jeannot, "Chapitre 4 : Propriétés optiques du Nitrure de Silicium et du silicium amorphe déposés par PECVD," Institut National des Sciences Appliquées de Lyon, 2006.
- [198] E. D. Palik, *Handbook of optical constants of solids*, vol. 3. Academic press, 1998.
- [199] E. Palik, "Handbook of Optical Constants of Solids, Academic Press, San Diego 1998."
- [200] T. Hakkarainen *et al.*, "Te incorporation and activation as n-type dopant in self-catalyzed GaAs nanowires," *Physical Review Materials*, vol. 3, no. 8, p. 086001, 2019.
- [201] S. Subbanna, G. Tuttle, and H. Kroemer, "N- type doping of gallium antimonide and aluminum antimonide grown by molecular beam epitaxy using lead telluride as a tellurium dopant source," *JEM*, vol. 17, no. 4, pp. 297–303, Jul. 1988, doi: 10.1007/BF02652109.
- [202] S. H. Huang *et al.*, "Epitaxial growth and formation of interfacial misfit array for tensile GaAs on GaSb," *Appl. Phys. Lett.*, vol. 90, no. 16, p. 161902, Apr. 2007, doi: 10.1063/1.2723649.
- [203] M. Heiblum, M. I. Nathan, and C. A. Chang, "Characteristics of AuGeNi ohmic contacts to GaAs," *Solid-State Electronics*, vol. 25, no. 3, pp. 185–195, Mar. 1982, doi: 10.1016/0038-1101(82)90106-X.
- [204] W. G. Spitzer and J. M. Whelan, "Infrared Absorption and Electron Effective Mass in n - Type Gallium Arsenide," *Phys. Rev.*, vol. 114, no. 1, pp. 59–63, Apr. 1959, doi: 10.1103/PhysRev.114.59.
- [205] S.-H. Lin and Y.-C. Cheng, "Free-Carrier Absorption in n-type Gallium Arsenide," *Chinese Journal of Physics*, vol. 19, no. 2 & 3, pp. 76–86, 1981.
- [206] A. Chandola, R. Pino, and P. S. Dutta, "Below bandgap optical absorption in tellurium-doped GaSb," *Semicond. Sci. Technol.*, vol. 20, no. 8, pp. 886–893, Aug. 2005, doi: 10.1088/0268-1242/20/8/046.
- [207] C. S. Kim *et al.*, "Improved mid-infrared interband cascade light-emitting devices," *Opt. Eng.*, vol. 57, no. 01, p. 1, Aug. 2017, doi: 10.1117/1.OE.57.1.011002.
- [208] R. Hanfoug, A. Salesse, D. Yarekha, A. Baranov, and C. Alibert, "Use of AlOx in cladding layers of an antimonide laser structure emitting at 2.3 μm ," *Semiconductor science and technology*, vol. 16, no. 11, p. 936, 2001, doi: 10.1088/0268-1242/16/11/309.
- [209] T. Bate *et al.*, "GaSb-based 2.7 μm laser diode with GaAs top cladding," 2018, pp. JTu2A-27, doi: 10.1364/CLEO_AT.2018.JTu2A.27.
- [210] "<https://www.computational-photonics.eu/oms.html>."
- [211] S. Böttger, M. Köhring, U. Willer, and W. Schade, "Off-beam quartz-enhanced photoacoustic spectroscopy with LEDs," *Appl. Phys. B*, vol. 113, no. 2, pp. 227–232, Nov. 2013, doi: 10.1007/s00340-013-5462-x.
- [212] F. Sarcan, Y. Wang, T. F. Krauss, T. Erucar, and A. Erol, "Dilute nitride resonant-cavity light emitting diode," *Optics & Laser Technology*, vol. 122, p. 105888, Feb. 2020, doi: 10.1016/j.optlastec.2019.105888.
- [213] F. A. Al-Saymari, A. P. Craig, Q. Lu, A. R. Marshall, P. J. Carrington, and A. Krier, "Mid-infrared resonant cavity light emitting diodes operating at 4.5 μm ," *Optics Express*, vol. 28, no. 16, pp. 23338–23353, 2020, doi: 10.1364/OE.396928.

- [214] E. F. Schubert, Y. - H. Wang, A. Y. Cho, L. - W. Tu, and G. J. Zydzik, "Resonant cavity light - emitting diode," *Appl. Phys. Lett.*, vol. 60, no. 8, pp. 921–923, Feb. 1992, doi: 10.1063/1.106489.
- [215] A. M. Green, D. G. Gevaux, C. Roberts, and C. C. Phillips, "Resonant-cavity-enhanced photodetectors and LEDs in the mid-infrared," *Physica E: Low-dimensional Systems and Nanostructures*, vol. 20, no. 3–4, pp. 531–535, Jan. 2004, doi: 10.1016/j.physe.2003.09.004.
- [216] C. Grasse, P. Wiecha, T. Gruendl, S. Sprengel, R. Meyer, and M.-C. Amann, "InP-based 2.8–3.5 μm resonant-cavity light emitting diodes based on type-II transitions in GaInAs/GaAsSb heterostructures," *Applied Physics Letters*, vol. 101, no. 22, p. 221107, 2012.
- [217] A. Ducanhez, L. Cerutti, A. Gassenq, P. Grech, and F. Genty, "Fabrication and Characterization of GaSb-Based Monolithic Resonant-Cavity Light-Emitting Diodes Emitting Around 2.3 μm and Including a Tunnel Junction," *IEEE J. Select. Topics Quantum Electron.*, vol. 14, no. 4, pp. 1014–1021, 2008, doi: 10.1109/JSTQE.2008.922014.
- [218] F. A. Al-Saymari, A. P. Craig, Y. J. Noori, Q. Lu, A. R. J. Marshall, and A. Krier, "Electroluminescence enhancement in mid-infrared InAsSb resonant cavity light emitting diodes for CO₂ detection," *Appl. Phys. Lett.*, vol. 114, no. 17, p. 171103, Apr. 2019, doi: 10.1063/1.5090840.
- [219] J. L. Bradshaw, J. D. Bruno, K. M. Lascola, G. P. Meissner, J. T. Pham, and F. J. Towner, "Interband cascade resonant cavity surface emitting LEDs for 2D-array scene projectors," Orlando, Florida, Apr. 2010, vol. 7663, p. 76630C, doi: 10.1117/12.853111.
- [220] J. Boucart, F. Gaborit, C. Fortin, L. Goldstein, J. Jacquet, and K. Leifer, "Optimization of the metamorphic growth of GaAs for long wavelength VCSELs," *Journal of Crystal Growth*, vol. 201–202, pp. 1015–1019, May 1999, doi: 10.1016/S0022-0248(99)00032-9.
- [221] H. Gebretsadik *et al.*, "InP-based 1.5 μm vertical cavity surface emitting laser with epitaxially grown defect- free GaAs-based distributed Bragg reflectors," *ELECTRONICS LETTERS*, vol. 34, no. 13, p. 3, 1998.
- [222] A. E. Bond, P. D. Dapkus, and J. D. O'brien, "Aperture placement effects in oxide-defined vertical-cavity surface-emitting lasers," *IEEE Photon. Technol. Lett.*, vol. 10, no. 10, pp. 1362–1364, Oct. 1998, doi: 10.1109/68.720261.
- [223] S. Calvez, A. Arnoult, A. Monmayrant, H. Camon, and G. Almuneau, "Anisotropic lateral oxidation of Al-III–V semiconductors: inverse problem and circular aperture fabrication," *Semicond. Sci. Technol.*, vol. 34, no. 1, p. 015014, Jan. 2019, doi: 10.1088/1361-6641/aaf2f1.
- [224] F. Chouchane, J. Doucet, A. Arnoult, G. Lacoste, C. Fontaine, and G. Almuneau, "A new approach of planar oxidation of buried Al_xGa_{1-x}As/GaAs epitaxial structures for optical and electrical confinement applications," *physica status solidi c*, vol. 9, no. 2, pp. 338–341, 2012, doi: 10.1002/pssc.201100264.
- [225] G. Almuneau *et al.*, "Real-time in situ monitoring of wet thermal oxidation for precise confinement in VCSELs," *Semicond. Sci. Technol.*, vol. 23, no. 10, p. 105021, Oct. 2008, doi: 10.1088/0268-1242/23/10/105021.
- [226] R. Michalzik, M. Grabherr, R. Jaeger, M. Miller, and K. J. Ebeling, "Progress in high-power VCSELs and arrays," 1998, vol. 3419, p. 34190P.
- [227] M. Grabherr *et al.*, "Bottom-emitting VCSEL's for high-CW optical output power," *IEEE Photon. Technol. Lett.*, vol. 10, no. 8, pp. 1061–1063, Aug. 1998, doi: 10.1109/68.701502.

- [228] Y. Ou, J. S. Gustavsson, P. Westbergh, A. Haglund, A. Larsson, and A. Joel, "Impedance Characteristics and Parasitic Speed Limitations of High-Speed 850-nm VCSELs," *IEEE Photon. Technol. Lett.*, vol. 21, no. 24, pp. 1840–1842, Dec. 2009, doi: 10.1109/LPT.2009.2034618.
- [229] M. M. Dummer, K. Johnson, M. Hibbs-Brenner, and W. K. Hogan, "Implant confined 1850nm VCSELs," San Francisco, California, USA, Feb. 2012, vol. 8276, p. 82760Y, doi: 10.1117/12.915888.
- [230] "<https://www.eesemi.com/sio2si3n4.htm>."
- [231] L. Cerutti, A. Garnache, A. Ouvrard, and F. Genty, "High temperature continuous wave operation of Sb-based vertical external cavity surface emitting laser near 2.3 μ m," *Journal of Crystal Growth*, vol. 268, no. 1–2, pp. 128–134, Jul. 2004, doi: 10.1016/j.jcrysgro.2004.02.116.
- [232] A. B. Ikyo *et al.*, "Temperature stable mid-infrared GaInAsSb/GaSb Vertical Cavity Surface Emitting Lasers (VCSELs)," *Sci Rep*, vol. 6, no. 1, p. 19595, Apr. 2016, doi: 10.1038/srep19595.
- [233] A. Ikyo *et al.*, "Gain peak–cavity mode alignment optimisation in buried tunnel junction mid-infrared GaSb vertical cavity surface emitting lasers using hydrostatic pressure," *IET optoelectronics*, vol. 3, no. 6, pp. 305–309, 2009, doi: 10.1049/iet-opt.2009.0045.
- [234] G. D. Cole *et al.*, "High-performance near- and mid-infrared crystalline coatings," *Optica*, vol. 3, no. 6, p. 647, Jun. 2016, doi: 10.1364/OPTICA.3.000647.
- [235] V. Jayaraman *et al.*, "Room-Temperature Continuous-Wave Electrically Pumped 3.3 Micron Vertical Cavity Laser," 2019, p. cb_11_5, doi: 10.1109/CLEOE-EQEC.2019.8872766.

Abstract

The availability of electrically pumped VCSELs at wavelength longer than 3 μm operating in continuous wave above room temperature is considered as a breakthrough for laser-based optical sensing applications. Indeed, these devices have a low-cost potential, low power consumption and overall emits single frequency with mode-hop free tunability. These ideal and unmatched properties will enable widespread utilization of photonic sensor networks. Electrically-pumped mid-IR VCSELs rely on GaSb-based materials. But entering in the 3-5 μm wavelength range requires new approaches for both active zone design and device processing. Thus, the main objective of this thesis was to investigate the building blocks required to develop such VCSEL.

To provide efficient emission in the 3-4 μm range, the active region is based on a Sb-based interband cascade (IC) type-II "W" quantum wells (QWs). Principal characteristics of Sb-based QW lasers, such as the emission wavelength and current threshold, are strongly affected by the design and the fabrication. Using the optimized conditions, we succeeded to fabricate ICLs emitting at 3.3 μm and operating in the CW regime up to 80°C, which confirms the potential of the developed active region. Since the DBRs thickness scales with the wavelength, we employed a hybrid VCSEL configuration with a semiconductor AlAsSb/GaSb DBR in the bottom part of the device and a dielectric ZnS/Ge DBR on the top. Another issue in the VCSEL design is the high electrical resistance of the AlAsSb/GaSb DBR resulting in the overheating of the device. To reduce the ohmic losses we employed an intracavity injection scheme. Afterwards, to ensure an efficient lateral electro-optical confinement, we propose to use an oxide-aperture similarly as short infrared VCSELs. This approach is based on the metamorphic growth and the selective thermal oxidation of an Al(Ga)As heterostructure on top of a GaSb-based half-VCSEL. This architecture presents several advantages, and in particular the use of the well-controlled Al(Ga)As oxidation process.

Finally, several vertical emitting structures as IC-LEDs, RCLEDs and VCSELs are presented validating the assembly of the different parts previously studied.

Résumé

La disponibilité de VCSELs à pompage électrique à une longueur d'onde supérieure à 3 μm fonctionnant en régime continu au-dessus de la température ambiante est considérée comme une avancée pour des applications de détection optique. En effet, ces dispositifs sont peu coûteux, consomment peu et sont monomodes avec une accordabilité sans saut de mode. Ces propriétés idéales permettront une large utilisation de réseaux de capteurs photoniques.

Les VCSELs émettant dans le moyen infrarouge reposent sur des matériaux à base de GaSb. Mais entrer dans la gamme de longueurs d'onde comprise entre 3 à 5 μm nécessite de nouvelles approches pour la conception des zones actives et la technologie des dispositifs. Ainsi, l'objectif principal de cette thèse était d'étudier les éléments de base nécessaire pour développer de tels VCSELs.

Pour obtenir une émission efficace dans la gamme 3-4 μm , la zone active est basée des structures à cascade interbande (IC) avec des puits quantiques de type-II "W". Les principales propriétés des lasers utilisant ce type de zone active (ICL), telles que la longueur d'onde et le seuil laser, sont fortement influencées par la conception et la fabrication. En utilisant les conditions optimisées, nous avons réussi à fabriquer des ICLs émettant à 3,3 μm et fonctionnant en régime continue jusqu'à 80°C, ce qui confirme le potentiel des zones actives développées. Comme l'épaisseur des miroirs de Bragg (DBR) dépend de la longueur d'onde, nous avons utilisé une configuration VCSEL hybride avec un DBR semi-conducteur AlAsSb/GaSb dans la partie inférieure du dispositif et un DBR diélectrique ZnS/Ge dans la partie supérieure. Un autre problème dans la conception du VCSEL est la résistance électrique du DBR AlAsSb/GaSb qui entraîne la surchauffe du dispositif. Pour réduire les pertes ohmiques, nous avons utilisé un système d'injection intracavité. Ensuite, pour assurer un confinement électro-optique latéral efficace, nous proposons d'utiliser une ouverture d'oxyde de la même manière que les VCSELs sur GaAs. Cette approche est basée sur la croissance métamorphique et l'oxydation thermique sélective d'une hétéro-structure Al(Ga)As sur un demi-VCSEL à base de GaSb. Cette architecture présente plusieurs avantages, et en particulier l'utilisation du processus d'oxydation Al(Ga)As qui est bien contrôlé.

Enfin, plusieurs structures émettrices verticales comme les diodes électroluminescentes (LED), des LEDs à cavité résonantes (RCLEDs) et des VCSELs sont présentées, validant l'assemblage des différentes parties précédemment étudiées.